1987

Picosecond excited state dynamics and excitation transport in solution and on surfaces

Philip Arnold Anfinrud
Iowa State University

INFORMATION TO USERS

The most advanced technology has been used to photograph and reproduce this manuscript from the microfilm master. UMI films the original text directly from the copy submitted. Thus, some dissertation copies are in typewriter face, while others may be from a computer printer.

In the unlikely event that the author did not send UMI a complete manuscript and there are missing pages, these will be noted. Also, if unauthorized copyrighted material had to be removed, a note will indicate the deletion.

Oversize materials (e.g., maps, drawings, charts) are reproduced by sectioning the original, beginning at the upper left-hand corner and continuing from left to right in equal sections with small overlaps. Each oversize page is available as one exposure on a standard 35 mm slide or as a 17″ × 23″ black and white photographic print for an additional charge.

Photographs included in the original manuscript have been reproduced xerographically in this copy. 35 mm slides or 6″ × 9″ black and white photographic prints are available for any photographs or illustrations appearing in this copy for an additional charge. Contact UMI directly to order.

Accessing the World's Information since 1938

300 North Zeeb Road, Ann Arbor, MI 48106-1346 USA

Order Number 8805040

Picosecond excited state dynamics and excitation transport in solution and on surfaces

Anfinrud, Philip Arnold, Ph.D.

Iowa State University, 1987

U·M·I
300 N. Zeeb Rd.
Ann Arbor, MI 48106

Picosecond excited state dynamics and excitation transport in solution and on surfaces

by

Philip Arnold Anfinrud

A Dissertation Submitted to the
Graduate Faculty in Partial Fulfillment of the
Requirements for the Degree of
DOCTOR OF PHILOSOPHY

Department: Chemistry
Major: Physical Chemistry

Approved:

Signature was redacted for privacy.

In Charge of Major Work

Signature was redacted for privacy.

For the Major Department

Signature was redacted for privacy.

For the Graduate College

Iowa State University
Ames, Iowa

1987

TABLE OF CONTENTS

GENERAL INTRODUCTION

Radiationless transport of electronic excitations was first described in quantum mechanical terms by Förster in the late 1940s [1-3]. Since his pioneering work, this problem has received a significant amount of attention by both theorists [4-11] and experimentalists [12-15]. These and other studies have revealed the ubiquitous nature of excitation transport; the phenomenon is manifested in sensitized luminescence [16], concentration quenching of fluorescence [17], and time-dependent fluorescence line narrowing [18]. In addition, excitation transport occurs in the primary stages of photosynthesis to facilitate efficient light harvesting action [19].

The rate of excitation transport depends on the separation between and relative orientation of donor and acceptor. The dipole-dipole coupling mechanism for excitation transport operates over distances on the order of tens of angstroms, offering potential as a microscopic probe for determining the spatial or orientational distribution of molecules in diverse systems (e.g., amorphous solids, crystals, solutions, organized monolayers, micelles or polymer chains). The spatial and orientational dependence for various mechanisms of excitation transport has been characterized by Dexter [4].

While much of the earlier experimental work in excitation transport was performed under steady state conditions using the fluorecence quantum yield [12] or anisotropy [20] as an observable, it is clear that more information could be extracted from time-resolved measurements. Studies of excitation transport with picosecond time resolution became feasible only during this last decade through the development of mode-locked laser sources [21] which provide us with an opportunity to investigate excitation transport processes in greater detail. This study examines the time-resolved fluorescence decays for a variety of systems using the time-correlated single photon counting technique, and the transient absorption signal from submonolayer rhodamine 640 on various substrates using picosecond pump-probe spectroscopy. The goal of this work is to experimentally test current excitation transport theories and use these theories to elucidate the mechanisms and dynamics of excitation transport in various systems. It is hoped that such knowledge may enable one to probe the spatial or orientational distributions of molecules in various systems, and ultimately lead to the development of efficient artificial systems that mimic nature's photosynthesis.

This dissertation is organized into five sections. The theory of excitation transport in 2- and 3-dimensional disordered systems is the topic of Section I. The effect of

residual polarization on time-resolved fluorescence depolarization experiments is revealed in the manuscript which concludes this section. Section II includes descriptions of the experimental technique (time-correlated single photon counting), the apparatus, and the data analysis. The manuscripts from excitation transport studies in 3- and 2-dimensional systems are presented in in Sections III and IV, respectively. In addition to the time-resolved fluorescence work, a transient absorption study involving submonolayer rhodamine 640 on various substrates was accomplished. Section V contains two publications related to this work. The first presents details of the electronic apparatus used to achieve submonolayer sensitivity; the results of the transient absorption study are disclosed in the second.

SECTION I. THEORY OF EXCITATION TRANSPORT IN 2- AND 3-DIMENSIONAL DISORDERED SYSTEMS

RELATIONSHIP BETWEEN TIME RESOLVED OBSERVABLES AND THEORETICAL QUANTITIES

The spatial and orientational dependence for the rate of excitation transport from donor (D) to acceptor (A) can be readily derived beginning with the Fermi Golden Rule for the transition rate [22]

$$\omega_{A^*D \leftarrow AD^*} = \left[\frac{2\pi}{\hbar}\right] \rho(E) |\langle A^*D|H'|AD^*\rangle|^2 \qquad (1.1)$$

where $|AD^*\rangle$ corresponds to the wavefunction with A in the ground state and D in the excited state, $\rho(E)$ is the density of states in acceptor A as a function of energy E, and H' represents the perturbation due to the coulombic interactions between the electrons of A and D. H' may be expanded in powers of 1/R and for uncharged molecules assumes the form [4]

$$H' = \frac{e^2}{\kappa_d R^3} \{\hat{f}_A \cdot \hat{f}_D - 3(\hat{f}_A \cdot \hat{R})(\hat{f}_D \cdot \hat{R})\} \quad \text{(dipole-dipole)}$$

$$+ \frac{3e^2}{2\kappa_d R^4} \{ \qquad \} \quad \text{(dipole-quadrupole)}$$

$$+ \ldots \quad \text{(higher-order terms)} \qquad (1.2)$$

where $\hat{f}_A$ and $\hat{f}_D$ designate the dipole orientations of A and D respectively, $\hat{R}$ is the direction vector connecting A and D

and κ_d is the dielectric constant of the medium ($\kappa_d = 4\pi\varepsilon_o$ in SI units).

Dipole-dipole interactions dominate in systems where the transitions are dipole allowed. Since this work was limited to systems exhibiting dipole allowed transitions, all other terms in H′ will be neglected.

The orientation and distance dependence of the transition rate for dipole-dipole coupling may be extracted from Eqs. 1.1 and 1.2. The orientational transfer probability is [23]

$$\kappa^2 = \{\hat{f}_A \cdot \hat{f}_D - 3(\hat{f}_A \cdot \hat{R})(\hat{f}_D \cdot \hat{R})\}^2 \qquad (1.3)$$

where κ^2 is known as the orientation factor, and the distance dependence is proportional to $1/R^6$. It is convenient to rewrite the excitation transfer rate $\omega_{A^*D \leftarrow AD^*}$ as

$$\omega(R) = \frac{1}{\tau_D}\left[\frac{3\kappa^2(\Omega)}{2}\right]\left[\frac{R_o}{R}\right]^6 \qquad (1.4)$$

where τ_D is the excited state lifetime of D in the absence of excitation transport, $\kappa^2(\Omega)$ is the orientation factor as a function of the orientational coordinates Ω, and R_o is the Förster parameter. Dynamic averaging of $\kappa^2(\Omega)$ in an isotropic system yields $\langle\kappa^2\rangle = 2/3$. In this limit, R_o is the critical transfer distance for which the rate of

excitation transport is equal to the rate of intramolecular decay (i.e., the transport probability is 1/2). R_o may be defined in terms of experimental observables as [3]

$$R_o^6 = \frac{375(\ln 10)\phi_D}{8\pi^5 n^4 N} \int_o^\infty \frac{f_D(\bar{\nu})\varepsilon(\bar{\nu})}{\bar{\nu}^4} \, d\bar{\nu} \qquad (1.5)$$

where $\bar{\nu}$ is the wavenumber, $f_D(\bar{\nu})$ is the donor emission spectra (measured in quanta and normalized to unity on a wavenumber scale), $\varepsilon_A(\bar{\nu})$ is the molar decadic extinction coefficient, ϕ_D is the donor fluorescence quantum efficiency, n is the refractive index of the solvent, and N is Avagadro's number.

In contrast to most other definitions for R_o, the orientation factor was not included in Eq. 1.5 in order to highlight the role of κ^2 in the excitation transfer rate of Eq. 1.4. In the dynamic isotropic limit, Eq. 1.5 is equivalent to other reported definitions for R_o^6.

Excitation transport may proceed to two types of acceptors, donors (D) and traps (T). D→D transfer is generally reversible and results in migration of the excitation. D→T transfer is considered irreversible (since E(trap) < E(donor) normally) and the excitation is quenched. Both D→D and D→T transfer may occur in a given system resulting in migration assisted trapping; this situation is discussed briefly toward the end of Section I. Due to the complications involved with concurrent D→D and D→T

transport, this work is generally confined to systems where either D→T or D→D transport dominates.

D→T Excitation Transport

The theory of excitation transport between a donor and trap (D→T) was developed in the late 1940s by Förster [1-3]. In the limit of no D→D transport, the time-derivative of the probability that an excitation resides on an initially excited donor j surrounded by N traps is [1,2]

$$\frac{dp_j}{dt} = -\frac{p_j}{\tau} - \frac{1}{\tau}\sum_{k=1}^{N}\left[\frac{3\kappa^2(\Omega_k)}{2}\right]\left[\frac{R_o}{R_{jk}}\right]^6 p_j \qquad (1.6)$$

where the Ω_k are the relative orientational coordinates of trap k and donor j, and R_{jk} is the separation between trap k and donor j. The solution to Eq. 1.6 has the form

$$p_j = \exp\{ -\frac{t}{\tau} - \frac{t}{\tau}\sum_{k=1}^{N}\left[\frac{3\kappa^2(\Omega_k)}{2}\right]\left[\frac{R_o}{R_{jk}}\right]^6 p_j \} . \qquad (1.7)$$

Förster averaged Eq. 1.7 in the dynamic limit over randomly distributed traps in 3-dimensions to obtain the time-dependent probability that the excitation resides in the donor ensemble [2],

$$p_D(t) = \exp\{ -\frac{t}{\tau} - C_T\left[\frac{3\langle\kappa^2\rangle\pi t}{2\tau}\right]^{1/2}\} \quad \text{(dynamic)}, \qquad (1.8)$$

where C_T is the reduced trap concentration which is related to the trap number density ρ_T via [10]

$$C_T = \frac{4\pi}{3} R_0^3 \rho_T \ . \tag{1.9}$$

The dynamic limit associated with Eq. 1.8 requires that the molecular rotational period be short relative to the excited state lifetime. While the dynamic limit simplifies the solution to Eq. 1.7, it is more appropriate to consider the static limit where the molecules are frozen in space on the time scale of the excited state lifetime. It has been shown that solutions to Eq. 1.7 in the static and dynamic limit differ by only a scale factor γ (provided the spatial distribution of traps extends from zero to infinity) [23]

$$\gamma = \frac{\langle|\kappa|\rangle}{\langle\kappa^2\rangle^{1/2}} \ . \tag{1.10}$$

The static limit solution to Eq. 1.7 is given by

$$p_D(t) = \exp\{ - \frac{t}{\tau} - C_T\langle|\kappa|\rangle\left[\frac{3\pi t}{2\tau}\right]^{1/2}\} \qquad \text{(static)}. \tag{1.11}$$

For an isotropic distribution of dipoles in 3-dimensions $\langle\kappa^2\rangle = 2/3$, $\langle|\kappa|\rangle = .6901$, and $\gamma = .8452$. Since $\gamma < 1$, the excitation transport is slower in the static case.

It is clear from Eqs. 1.8 and 1.11 that $C_T = 0$ yields a fluorescence decay which is described by a single

exponential term. A non-zero value of C_T, however, introduces non-exponentiality into the fluorescence decay. The non-exponential character arises due to disorder in the trap distribution; excited donors which are remote relative to traps decay with a lifetime similar to the natural decay, while excited donors with nearby traps decay more quickly (Fig. 1.1).

Equation 1.8 and its 2-dimensional analog have been tested experimentally; the time-resolved emission was found to closely follow the appropriate form for 3-dimensions [13,14] and 2-dimensions [24,25].

D→D Excitation Transport

Unlike D→T transport, D→D excitation transport is generally reversible, a fact which greatly complicates the determination of the time-dependent probability that an excitation resides on an initially excited molecule. (D→D transport may not be completely reversible under experimental conditions where kT is significantly smaller than the donor inhomogeneous linewidth. In the low temperature limit, the quasi-reversible flow of excitation tends toward molecules which are lower in energy due to variations in their local environment. While dispersive excitation transport has recently attracted some interest [26,27], this work is confined to room temperature studies

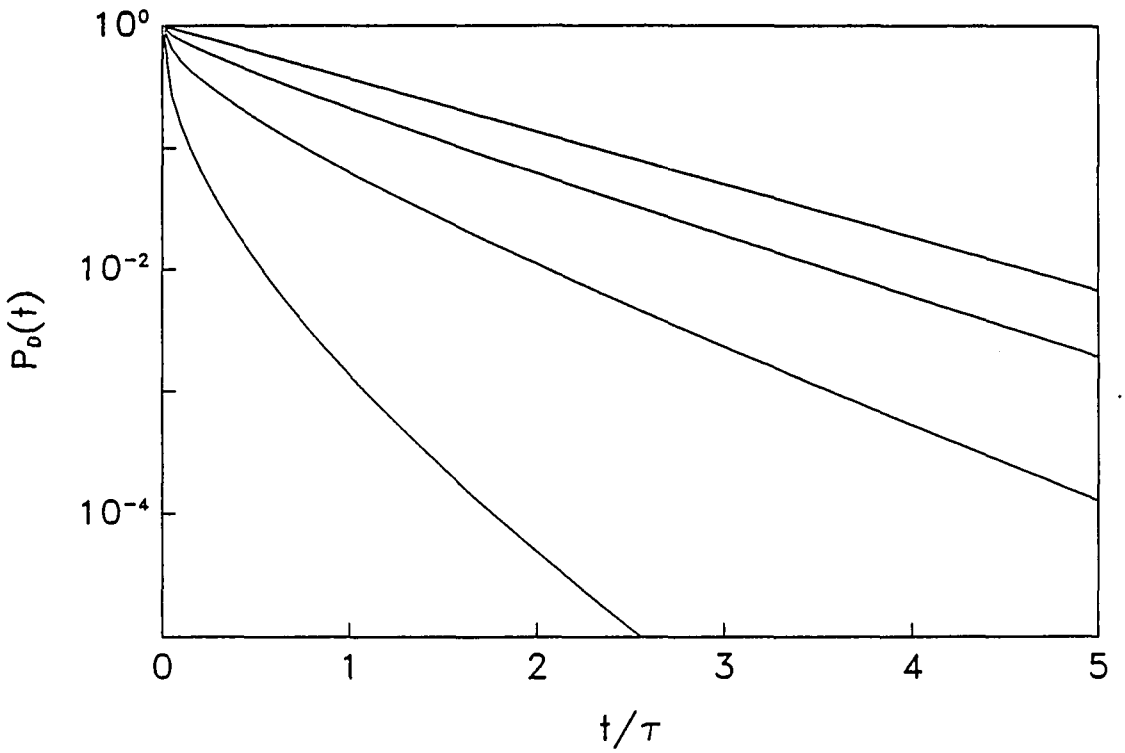

Fig. 1.1 3-dimensional Förster decay $p_D(t)$ plotted vs. t/τ in the dynamic limit for reduced trap coverages C_T = 0, .316, 1, and 3.16 (top through bottom, respectively)

with systems where dispersive effects may be neglected). The master equation describing the dynamics of excitation transport in a system of donors is

$$\frac{dp_j}{dt} = -\frac{p_j}{\tau} - \frac{1}{\tau}\sum_{k=1}^{N}\left[\frac{3\kappa^2(\Omega_k)}{2}\right]\left[\frac{R_o}{R_{jk}}\right]^6(p_k-p_j) \quad . \qquad (1.12)$$

Unfortunately, no closed form solution to Eq. 1.12 exists. Instead of seeking the probability that the excitation resides on an initially excited site as before, theorists generally prefer to estimate the probability $G^s(t)$ that the excitation resides on the initially excited site in the absence of intramolecular decay. The exact solution to $G^s(t)$ is related to $p_j(t)$ via

$$p_j(t) = \exp\left[-\frac{t}{\tau}\right]\cdot G^s(t) \quad , \qquad (1.13)$$

where τ is the fluorescence lifetime.

A model for $G^s(t)$ was proposed by Huber et al. [18,28] where interactions between pairs of molecules alone were considered (two-particle model). The exact configurational average appeared as a power series which was truncated to first order. The solution to this approximation yields an equation whose form is functionally identical to the Förster solution for D→T transport. Baumann and Fayer [23] recently developed a unified two-particle model for D→D and D→T excitation transport based on the first order term of the

exact configurational average expansion with the dimensionality generalized. Their static $G^s_{\Delta st}$ and dynamic $G^s_{\Delta d}$ results are

$$G^s_{\Delta st}(t) = \exp\{-C_\Delta \lambda^{\Delta/6-1}\left[\frac{3}{2}\right]^{\Delta/6} \langle|\kappa|^{\Delta/3}\rangle \Gamma(1-\Delta/6)\left[\frac{t}{\tau}\right]^{\Delta/6}\} \tag{1.14a}$$

$$G^s_{\Delta d}(t) = \exp\{-C_\Delta \lambda^{\Delta/6-1}\left[\frac{3\langle\kappa^2\rangle}{2}\right]^{\Delta/6} \Gamma(1-\Delta/6)\left[\frac{t}{\tau}\right]^{\Delta/6}\} \tag{1.14b}$$

$$\lambda = 1 \text{ for } D\rightarrow T \tag{1.15a}$$

$$\lambda = 2 \text{ for } D\rightarrow D \text{ transfer} \tag{1.15b}$$

$$\gamma = \frac{\langle|\kappa|^{\Delta/3}\rangle}{\langle\kappa^2\rangle^{\Delta/6}} \tag{1.16}$$

where Δ is the dimensionality (1, 2, or 3). (When the dimensionality is specified, the Δ subscript on the reduced concentration C_Δ is often replaced by a D or T to indicate the reduced donor concentration C_D, or the reduced trap concentration C_T, respectively).

The coefficients needed in Eqs. 1.14 and 1.16 are summarized in Table 1-1. Note that the excitation polarization in the static 2-dimensional ($\Delta = 2$) isotropic system influences the value of $\langle|\kappa|^{2/3}\rangle$. This is an expected result since perpendicular and parallel excitation polarizations preferentially excite dipoles oriented perpendicular and parallel to the 2-dimensional plane

Table 1-1. Coefficients in equations 1.14 and 1.16 for several combinations of spatial dimension and angular distributions in infinite systems [24]

			Dynamic		Static	
Dimension Δ	$\Gamma(1-\Delta/6)$	C_Δ	Angular distribution	$\langle\kappa^2\rangle$	Excitation polarization	$\langle\lvert\kappa\rvert^{\Delta/3}\rangle$	γ
3	1.772 45	$(4\pi/3)R_0^3\rho_3$	isotropic	2/3		0.6901	0.8452
2	1.354 12	$\pi R_0^2\rho_2$	isotropic	2/3	$\perp$ to plane	0.6909	0.7909
					$\parallel$ to plane	0.7641	0.8747
					uniform	0.7397	0.8468
			in-plane	5/4		0.9462	0.8784
1	1.128 79	$2R_0\rho_1$	isotropic	2/3	uniform	0.8305	0.8886

respectively, and dipoles oriented perpendicular to the plane lack the "head-to-head" orientation which is most efficient for dipole-dipole excitation transfer. The consequence is that excitation transport will be faster (larger $\langle|\kappa|^{2/3}\rangle$) when parallel polarization is used to excite an isotropic system.

Equations 1.14 for D→T transport ($\lambda = 1$) are identical to the expressions derived by Förster [2] for $\Delta = 3$, by Hauser et al. [29] and by Nakashima et al. [24] for $\Delta = 2$, and by Hauser et al. [29] for $\Delta = 1$. In addition, the D→D transport ($\lambda = 2$) result reproduces the 3-dimensional Huber expression [18,28]. While the unified treatment recovers the correct expressions for D→T transport, the two-particle D→D transfer equations are only accurate to first order in density [30]. The two-particle D→D transport result has been compared in 3-dimensions with the three-body GAF theory [7] which was shown to be accurate to second order in density [30]. Graphical comparison of these two levels of approximation revealed practically indistinguishable curves for concentrations up to $C_D = 5$ and times which are of significance in experiments [15,30]. This suggests that the two-particle theory provides a valid description for D→D excitation transport in 3-dimensions; it is expected to be accurate in lower dimensions as well. Since the two theories yield similar results, the compact expressions afforded by the two-particle theory are preferred to the

mathematical complexity represented in GAF theory [23]. Figure 1.2 illustrates the time-dependence of the two-particle approximation to $G_d^s(t)$ in various dimensions.

Equations 1.14 estimate the time-dependent probability $G^s(t)$ that an excitation resides on an initially excited molecule in the absence of intramolecular decay. While $G^s(t)$ cannot be measured directly as an experimental observable, it is related to the time-dependent decay in fluorescence anisotropy which can be measured. The relationship between $G^s(t)$ and fluorescence anisotropy will be illustrated in the following sections.

Theory of fluorescence polarization

Excitation of an isotropic ensemble of molecules with linearly polarized light generates an anisotropic excited state distribution. The anisotropy arises because the absorption probability for a linear oscillator is proportional to the square of the electric field component along the transition moment of the oscillator [31]. The anisotropic distribution of excited absorbers generally gives rise to polarized fluorescence (one exception occurs when the transition moments for the absorption and emission differ by 54.7° [32]; the role of this angle in fluorescence polarization will be discussed later). The degree of fluorescence polarization is calculated as follows:

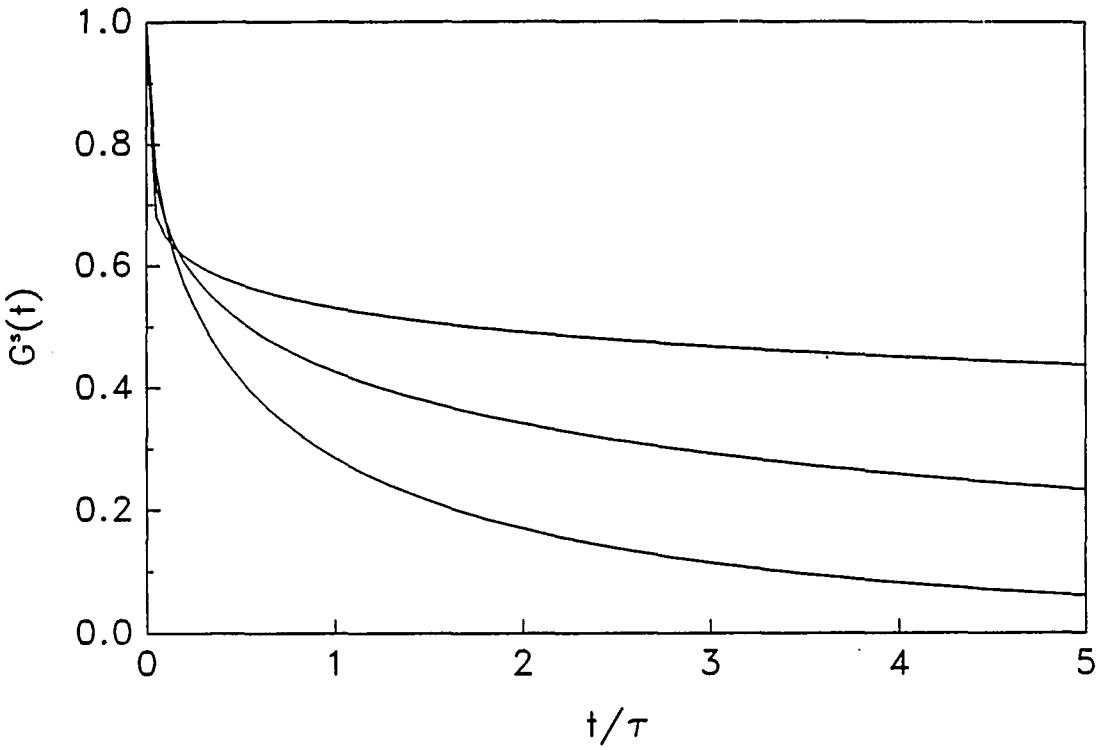

Fig. 1.2 $G^S(t)$ plotted vs. t/τ in the dynamic limit for Δ = 1, 2, and 3 (top through bottom, respectively) when C_Δ = 1 and λ = 2 (D→D limit)

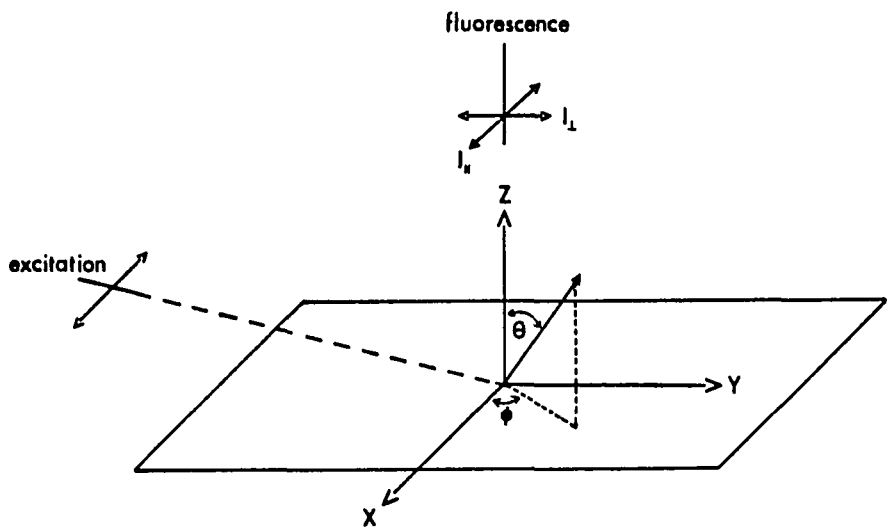

Fig. 1.3 Experimental geometry. The excitation is X-polarized, and the fluorescence is viewed along the Z-axis through an analyzer polarizer. The transition dipole orientation is defined by θ and ϕ

Consider a molecule with transition moment $\hat{p}$ excited with X-polarized light (Fig. 1.3),

$$\hat{p} = \begin{bmatrix} \sin\theta \cos\phi \\ \sin\theta \sin\phi \\ \cos\theta \end{bmatrix} \tag{1.17}$$

$$\hat{E}_{ex} = \begin{bmatrix} 1 \\ 0 \\ 0 \end{bmatrix} \tag{1.18}$$

where $\hat{E}_{ex}$ is the electric field direction for the excitation source. The absorption probability is proportional to the square of the electric field component of the excitation source along the transition moment $\hat{p}$ and is given by

$$(\hat{p}\cdot\hat{E}_{ex})^2 = \sin^2\theta \cos^2\phi \ . \tag{1.19}$$

Emission from $\hat{p}$ has polarization components along three orthogonal axes which are referred to as $\parallel$, $\perp$, and n where $\parallel$ and $\perp$ are parallel and perpendicular to the excitation polarization, and n is normal to both $\parallel$ and $\perp$. If the emission is viewed along the Z-axis, the three orthogonal components are

$$\hat{E}_{\parallel,em} = \begin{bmatrix} 1 \\ 0 \\ 0 \end{bmatrix} \tag{1.20a}$$

$$\hat{E}_{\perp,em} = \begin{bmatrix} 0 \\ 1 \\ 0 \end{bmatrix} \tag{1.20b}$$

$$\hat{E}_{n,em} = \begin{bmatrix} 0 \\ 0 \\ 1 \end{bmatrix} . \qquad (1.20c)$$

If the absorption and emission dipoles are parallel ($\hat{p} \| \hat{p}_{abs} \| \hat{p}_{em}$) the square of the electric filed component of $\hat{p}$ along each orthogonal polarization yields the corresponding emission intensity. They are

$$(\hat{p} \cdot \hat{E}_{\|,em})^2 = \sin^2\theta \cos^2\phi \qquad (1.21a)$$

$$(\hat{p} \cdot \hat{E}_{\perp,em})^2 = \sin^2\theta \sin^2\phi \qquad (1.21b)$$

$$(\hat{p} \cdot \hat{E}_{n,em})^2 = \cos^2\theta . \qquad (1.21c)$$

The emission probability for each polarization is proportional to the product of the absorption probability (Eqs. 1.19) and the corresponding emission intensity (Eqs. 1.21). Integrating this product over a sphere (isotropic distribution of $\hat{p}$) yields the total polarized fluorescence intensities $I_{\|}$, $I_{\perp}$, and I_n

$$I_{\|} = \int_0^{2\pi} \int_0^{\pi/2} (\sin^4\theta \cos^4\phi)\sin\theta \, d\theta \, d\phi = \frac{2\pi}{5} \qquad (1.22a)$$

$$I_{\perp} = \int_0^{2\pi} \int_0^{\pi/2} (\sin^4\theta \sin^2\phi \cos^2\phi)\sin\theta \, d\theta \, d\phi = \frac{2\pi}{15} \qquad (1.22b)$$

$$I_n = \int_0^{2\pi} \int_0^{\pi/2} (\sin^2\theta \cos^2\theta \cos^2\phi)\sin\theta \, d\theta \, d\phi = \frac{2\pi}{15} \qquad (1.22c)$$

where the extra sinθ term arises because the integration is carried out in spherical coordinates.

The degree of fluorescence polarization P_o is defined as [32]

$$P_o = \frac{I_{\parallel} - I_{\perp}}{I_{\parallel} + I_{\perp}} . \qquad (1.23)$$

Using Eqs. 1.22, we find that $I_{\parallel}/I_{\perp}=3$ and $P_o=1/2$, the maximum polarization possible for an isotropic system.

$I_{\parallel}$ and $I_{\perp}$ may be recovered experimentally by positioning an analyzer polarizer between the sample and the photodetector with orientation perpendicular and parallel to the excitation polarization respectively. While emission is often viewed along the Z-axis, Eqs. 1.22 apply to any viewing axis which is perpendicular to the excitation polarization. Note, however, that I_n can only be observed by viewing along the Y-axis (see Fig. 1.3).

Excitation transport depolarization

The orientation factor κ^2 (Eq. 1.3) permits excitation transport to acceptors with non-parallel dipole orientations. As a result, excitation transport tends to randomize the orientational distribution of excited molecules and destroys the anisotropy created with polarized excitation. Recall that $G^s(t)$ is the time-dependent probability that the excitation resides on the initially

excited site in the absence of intramolecular decay. If one excitation hop is sufficient to completely destroy the anisotropy (no residual polarization after one hop), then the anisotropy decays as $G^S(t)$. In order to find the relationship between $G^S(t)$ and the time-dependent polarized emission $I_{\parallel}$, $I_{\perp}$, and I_n, we recognize that in the limit of no residual polarization, the emission arises from two ensembles. The first consists of initially excited molecules whose time-dependent population is proportional to $P(t)\cdot G^S(t)$, where $P(t)$ is the isotropic decay (the decay observed in the absence of depolarization mechanisms). The second is comprised of molecules excited via one or more excitation hops whose time-dependent population is proportional to $P(t)\cdot[1 - G^S(t)]$. Emission from the first ensemble (initially excited sites) is polarized with $P_o = 1/2$, and the ratio of polarized components is $(3/5):(1/5):(1/5)$ for $I_{\parallel}$, $I_{\perp}$, and I_n respectively. Emission from the second ensemble is unpolarized with $P_o = 0$ so the ratio of polarized components is $(1/3):(1/3):(1/3)$. The time-dependent polarized emission is simply the sum of components from each ensemble [33]

$$I_{\parallel} = (3/5)P(t)G^S(t) + (1/3)P(t)[1 - G^S(t)]$$
$$= (1/3)P(t)[1 + .8G^S(t)] \qquad (1.24a)$$

$$I_{\perp} = (1/5)P(t)G^{S}(t) + (1/3)P(t)[1 - G^{S}(t)]$$
$$= (1/3)P(t)[1 - .4G^{S}(t)] \qquad (1.24b)$$

$$I_{n} = (1/5)P(t)G^{S}(t) + (1/3)P(t)[1 - G^{S}(t)]$$
$$= (1/3)P(t)[1 - .4G^{S}(t)] \; . \qquad (1.24c)$$

It is clear from Eqs. 1.24 that P(t) can be obtained by combining $(I_{\parallel} + 2I_{\perp})$. This may be accomplished experimentally by setting the analyzer polarizer (see Fig. 1.3) at the so-called "magic angle" where this linear combination obtains.

The transmission through a polarizer is proportional to $\cos^2\phi$ where ϕ is the angle between the incident polarization and the transmission axis of the analyzer polarizer [34]. Thus the magic angle, ϕ_{MA} is extracted from the equation

$$\frac{\sin^2\phi_{MA}}{\cos^2\phi_{MA}} = \tan^2\phi_{MA} = 2, \qquad \phi_{MA} = 54.7^{\circ} \qquad (1.25)$$

where ϕ_{MA} is defined relative to the parallel setting of the analyzer polarizer. Figure 1.4 illustrates experimentally obtained time-resolved polarized fluorescence profiles. Depolarization due to excitation transport is evident at 3×10^{-3} M where the polarized profiles converge at long times.

Two assumptions were made in writing Eqs. 1.24. The first required that the anisotropy be completely lost after

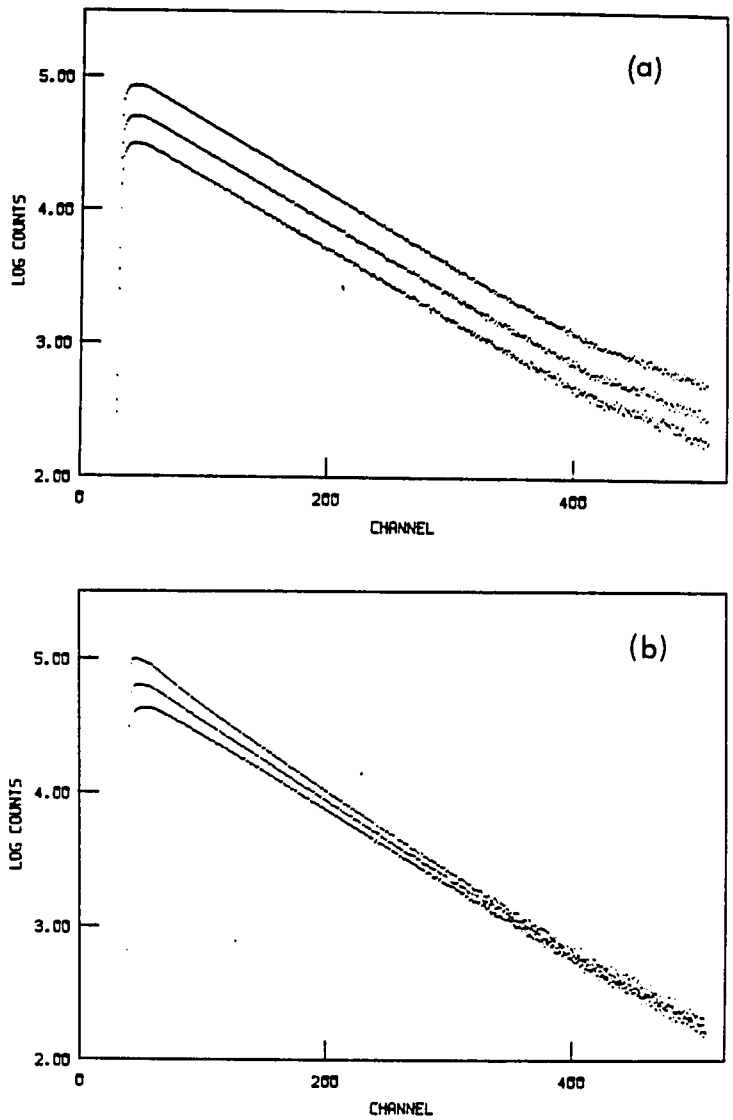

Fig. 1.4 Log plots of experimental time-resolved polarized emission profiles for 10^{-6} M (a) and 3×10^{-3} (b) DODCI in glycerol. Top to bottom are parallel, magic angle, and perpendicular profiles. The time calibration is 20 ps/channel

one excitation transfer. One excitation transfer is not sufficient to completely depolarize the fluorescence [35]; the effect of residual polarization after one hop on data analysis using Eqs. 1.24 has been discussed [36]. The second assumption required that the absorption and emission dipoles be parallel. Equations 1.24 may be generalized for non-parallel dipoles; this modification is discussed in the following section.

Other depolarization mechanisms

Excitation transport is one of several fluorescence depolarization mechanisms which include intrinsic depolarization, rotational diffusion, and self-absorption.

Intrinsic depolarization occurs when the absorption and emission dipoles are non-parallel. As a result, the emission originates from a dipole which is randomly displaced at an angle α about the absorption dipole axis. The randomness associated with the angular displacement in the emission dipole direction reduces the anisotropy. Equations 1.24 may be generalized to include the effects of intrinsic depolarization by scaling $G^S(t)$ with the factor $P_2(\cos\alpha)$ [32,37] so that

$$I_{\parallel} = P(t)[1 + .8P_2(\cos\alpha)\cdot G^S(t)] \qquad (1.26a)$$

$$I_{\perp} = P(t)[1 - .4P_2(\cos\alpha)\cdot G^S(t)] \qquad (1.26b)$$

$$I_n = P(t)[1 - .4P_2(\cos\alpha)\cdot G^S(t)] \qquad (1.26c)$$

$$P_2(\cos\alpha) = \frac{3\cos^2\alpha - 1}{2} \qquad (1.27)$$

where $P_2(\cos\alpha)$ is the second order Legendre polynomial in $\cos\alpha$. When $\alpha = 0$ (parallel dipoles), no intrinsic depolarization occurs and Eqs. 1.26 reduce to Eqs. 1.24. It is interesting to note that when $\alpha = 54.7°$ (the so-called "magic angle"), the anisotropy is completely lost (i.e., $I_{\parallel} = I_{\perp} = I_n$).

Rotational depolarization occurs when the molecule rotates on the time scale of the emission lifetime. The rotational motion randomizes the orientation of the excited dipoles and destroys the anisotropy created via polarized excitation. If the rotational motion is diffusive and if the rotor is spherical (degenerate rotational diffusion constants), the time-dependent polarized emission equations are

$$I_{\parallel} = P(t)[1 + .8\exp(-6Dt)] \qquad (1.28a)$$

$$I_{\perp} = P(t)[1 - .4\exp(-6Dt)] \qquad (1.28b)$$

$$I_n = P(t)[1 - .4\exp(-6Dt)] \qquad (1.28c)$$

where D is the diffusion constant for rotational motion.

The rotational depolarization equations are usually written using different notation [32,38]

$$I_{\parallel} = P(t)[1 + 2r(t)] \tag{1.29a}$$

$$I_{\perp} = P(t)[1 - r(t)] \tag{1.29b}$$

$$I_n = P(t)[1 - r(t)] \tag{1.29c}$$

where r(t) is called the anisotropy decay law. For an isotropic system, r(t) is defined as [32,38]

$$r(t) = \frac{I_{\parallel} - I_{\perp}}{I_{\parallel} + 2I_{\perp}} . \tag{1.30}$$

A comparison of Eqs. 1.28 and 1.29 reveals that r(t) = (2/5)exp(-6Dt) for spherical rotors. Eqs. 1.29 are also valid for non-spherical rotors, provided the appropriate form for r(t) is used. It has been shown that r(t) may contain as many as 5 exponential terms depending on molecular symmetry and the dipole orientation relative to the molecular axis [37]. Figure 1.5 illustrates the effect of rotational motion on the time-dependent decay for $I_{\parallel}$ and $I_{\perp}$. Fitting these data with the spherical rotor model recovers an estimate for the characteristic diffusion time 1/6D = 3.2 ns.

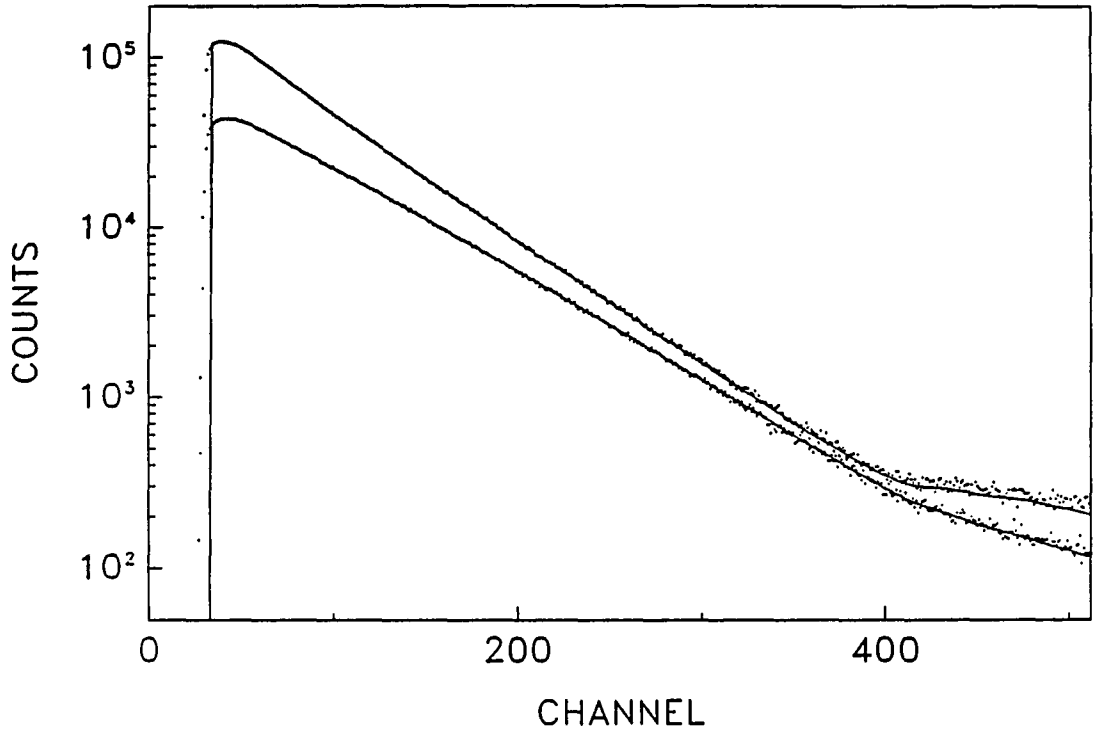

Fig. 1.5 Log plots of experimental time-resolved polarized emission profiles for 10^{-6} M DODCI in ethylene glycol. The solid lines represent the best fit (using Eqs. 1.28) to the parallel (top) and perpendicular (bottom) profiles. The fit recovered 1/6D = 3.2 ns. The time calibration is 20 ps/channel

Self-absorption occurs when the sample optical density is sufficient to permit reabsorption of sample emission. As in dipole-dipole excitation transport, the anisotropy is lost when emission arises from molecules that were not initially excited. In addition to depolarizing the emission, non-resonant radiative excitation transport (self-absorption) delays the emission thereby inflating the measured fluorescence lifetime. This is in contrast to resonant non-radiative excitation transport (e.g., dipole-dipole coupling) where no inflation of the fluorescence lifetime is observed.

The reabsorption probability a for an emitted photon depends on the overlap between the fluorescence and absorption spectra, the sample concentration, and the cell geometry. For emission originating at the center of a sphere [39,40],

$$a = \int_0^\infty f(\bar{\nu})(1 - 10^{-\varepsilon(\bar{\nu})cr})d\bar{\nu} \qquad (1.31)$$

where $f(\bar{\nu})$ is the fluorescence spectra (measured in quanta and normalized to unity), $\varepsilon(\bar{\nu})$ is the molar decadic extinction, $\bar{\nu}$ is the wavenumber, c is the concentration, and r is the radius. Hammond derived equations for a more practical experimental configuration where the sample is confined between parallel plates and the fluorescence is viewed head-on with respect to the excitation [39]. He

found the reabsorption probability a for rhodamine 6G fluoroborate in 95% ethanol to be about 7.7% for 10^{-6}M in a 1 cm path length cell [39]. This amount of reabsorption is sufficient to inflate the apparent fluorescence lifetime by about 7%. In order to minimize the effects of reabsorption (self-absorption depolarization and lifetime inflation) at milli-molar concentrations it may be necessary to construct sample cells with path lengths ~1 micron [15].

Excitation transfer studies are preferably carried out in systems where rotational depolarization can be neglected. It was recently discovered, however, that a solution as viscous as glycerol (954 cp at 25°C [41]) permits sufficient rotational motion of xanthene or carbocyanine dyes to affect the estimate for the reduced donor concentration C_D [42]. The error is most severe for $C_D < 0.5$. The depolarization arising from various sources may be properly accounted for with the following generalized time-dependent polarized emission equations

$$I_{\parallel} = P(t)[1 + 2P_2(\cos\alpha)\cdot G^S(t)\cdot r(t)] \qquad (1.32a)$$

$$I_{\perp} = P(t)[1 - P_2(\cos\alpha)\cdot G^S(t)\cdot r(t)] \qquad (1.32b)$$

$$I_n = P(t)[1 - P_2(\cos\alpha)\cdot G^S(t)\cdot r(t)] \qquad (1.32c)$$

(Note that the factors 0.8 and 0.4 were absorbed by r(t)).

Equations 1.32 take into account excitation transfer ($G^s(t)$), intrinsic ($P_2(\cos\alpha)$), and rotational ($r(t)$) depolarization. It is much more difficult, however, to generalize Eqs. 1.32 to include the effects of self-absorption depolarization. An analysis similar to that used in deriving Eqs. 1.24 suggests that self-absorption effects may be accounted for to first order by scaling $G^s(t)$ by $(1 - a)$, where a is the reabsorption probability. The parameter a is not a constant, however, because the reabsorption probability depends on the path length between the emission source and the cell window. This complication makes it highly desirable to minimize the effects of self-absorption by maintaining appropriately short path lengths.

Effect of orientational correlation

The time-dependent polarized emission results given in Eqs. 1.24 obtain when the residual polarization P_1 after one excitation transfer is negligible compared to the initial polarization P_o (i.e., one excitation transfer is sufficient to randomize the orientational distribution of the excitation). Galanin [35] found that $P_1 = 1/42$ (vs. $P_o = 1/2$) when excitation transport occurs between uncorrelated (randomly oriented) dipoles. While P_1 is not zero, the error incurred by using Eqs. 1.24 is small [36].

Suppose that orientational correlation occurs so that nearby molecules tend to align. P_1 is no longer independent

of the dipole separation R and becomes $P_1(R)$; the residual polarization $P_1(R)$ could range from 1/2 (perfect alignment) to 1/42 (uncorrelated case) as R varies from R_{min} to ∞, respectively (where R_{min} is the minimum molecular separation permissible). Since P_1 is not negligible when excitation transport occurs between molecules whose separation is $R \lesssim R_c$ (where R_c is the characteristic correlation length), Eqs. 1.24 fail. The failure is more severe at higher concentrations where an increasing fraction of the excitation transport occurs within R_c. If one was unaware of orientational correlation and attempted to fit experimental time-resolved polarized emission data with Eqs. 1.24, the reduced donor density C (from Eqs. 1.14) would be underestimated; the magnitude of the error would increase with concentration [42].

Orientational correlation can arise when local ordering in the host medium induces alignment of neighboring chromophores. For this to occur, the chromophore must interact with the medium via its coordination layer in a manner that favors alignment with the local structure of the medium. Therefore orientational correlation effects are not expected for spherical chromophores, chromophores which are large relative to R_c, or solution concentrations where $R_{mp} >> R_c$ (R_{mp} is the most probable separation between molecules).

The local ordering of the host medium is manifested by radial and orientational correlation among the molecules which make up the medium; the respective correlation lengths may differ significantly (e.g., orientational correlation extends beyond radial correlation in liquid crystals). While X-ray diffraction has revealed the extent of radial correlation for a variety of solvents, techniques for measuring orientational correlation are scarce.

The radial correlation functions obtained from X-ray analyses of liquid methanol and ethanol reveal little correlation beyond 5 to 6 Å [43]. In contrast, a similar study by Soltwisch and Steffen [44] using liquid glycerol at 250 and 350°K revealed correlation beyond 25 Å (Fig. 1.6). They reported that the details of the glycerol scattering intensity could be accounted for by assuming that the crystalline conformation of glycerol [45] predominates and orientational correlation persists even in the liquid phase.

While X-ray diffraction has proven useful in determining radial correlation in liquids, fluorescence concentration depolarization using appropriate chromophores offers potential as a sensitive probe of orientational correlation in liquids. To achieve this potential, the theory of fluorescence concentration-depolarization in the presence of orientational correlation must be developed.

The time-resolved polarized emission equations I (t) and I (t) (for the excitation and emission geometry previously

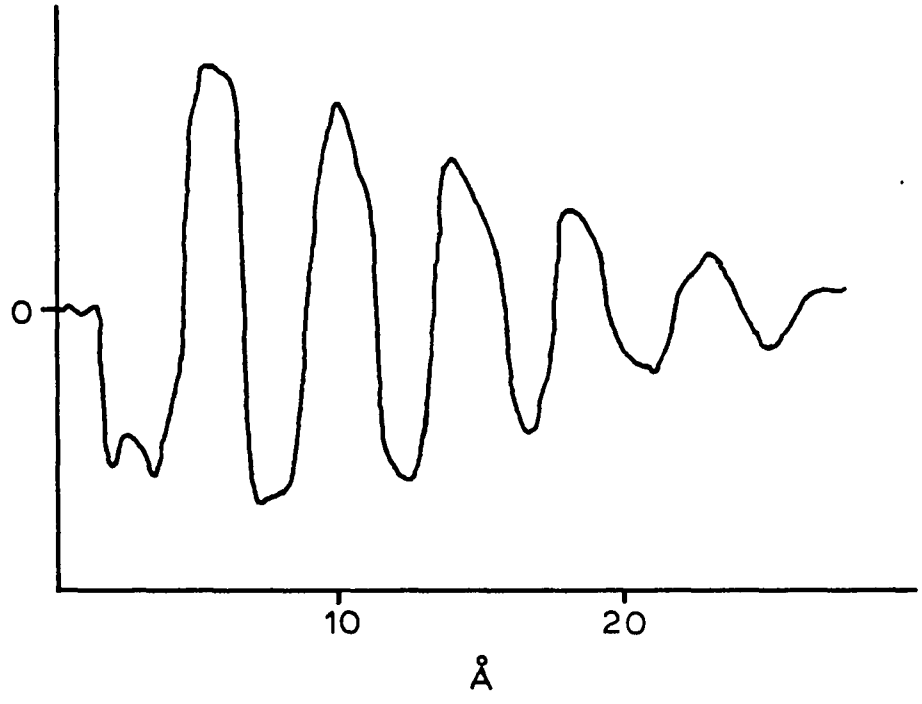

Fig. 1.6 The radial distribution function of liquid glycerol at 250 K [44]

considered) are

$$I_{\parallel}(t) = \langle \sum_j p_j(t) \sin^2\theta_j \cos^2\phi_j \rangle \tag{1.33a}$$

$$I_{\perp}(t) = \langle \sum_j p_j(t) \sin^2\theta_j \sin^2\phi_j \rangle \tag{1.33b}$$

where no other assumptions are made. The parameter $p_j(t)$ is the time-dependent probability that an excitation resides on dipole j at time t and represents the solution to Eq. 1.12. Unfortunately, no analytic solution to Eq. 1.12 exists even in the absence of orientational correlation. Orientational correlation complicates matters further by introducing a distance dependence to the orientational distribution and hence the orientation factor $\kappa^2(\Omega)$. Clearly, much theoretical work is required before one can generalize Eqs. 1.24 to include the effects of orientational correlation.

Knoester and Van Himbergen [46] recently attacked the problem of concentration depolarization in the presence of orientational correlations. Instead of deriving equations for $I_{\parallel}$ and $I_{\perp}$, they formulated their theory around the fluorescence emission anisotropy

$$A(t) = \frac{I_{\parallel} - I_{\perp}}{I_{\parallel} + 2I_{\perp}} \tag{1.34}$$

which may be rewritten in terms of Eqs. 1.33 as

$$A(t) = \frac{\langle \sum_j p_j(t)\sin^2\theta_j\ (1 - 2\sin^2\phi_j)\rangle}{\langle \sum_j p_j(t)\sin^2\theta_j\ (1 + \sin^2\phi_j)\rangle} \quad . \tag{1.35}$$

To make their theory more tractable, they neglected the distance dependence of the orientation factor. Since a distance dependent orientation factor (due to orientational correlation) yields enhanced excitation transport at shorter distances (where less depolarization occurs), their theory will overestimate the decay in anisotropy. They proceeded to derive an analytic expression for the time-dependent fluorescence anisotropy in the limit of no back transfer (Förster limit). Quantitative results from their theory required numerical integration. The theory was extended to allow for back transfer, but these results are much less tractable and require a numerical inverse Laplace transformation.

The effect of orientational correlation on the fluorescence anisotropy was illustrated via simulated decays [46]. The system under consideration was 2-dimensional with no back transfer, and the orientational correlation function was modeled with an exponential term. They found that the time-dependent anisotropy computed for C = 1 and a correlation length $R_C = R_O$ could be approximated with C = 0.3 and $R_C = 0$ (no correlation). It is clear that orientational correlations on the order of R_O can have a

significant impact on one's estimate for the reduced donor concentration C.

While the Knoester theory of fluorescence depolarization in the presence of orientational correlation does not account for the distance dependence of the orientation factor, it represents the most rigorous treatment currently available. This treatment, however, does not recover a facile expression relating R_c and C to the time-dependent polarized emission profiles $I_{\parallel}$ and $I_{\perp}$. A crude model which makes such a connection is now presented.

Suppose that orientational correlation is ignored and the time-dependent polarized emission profiles are fit with Eqs. 1.24 to recover an estimate for the reduced donor concentration C_D^{fit}. When the approximation for $G^S(t)$ is accurate in the absence of correlations, the estimate for C_D^{fit} will be less than or equal to the true reduced donor concentration C_D^{true}. The magnitude of the difference between C_D^{true} and C_D^{fit} depends on the correlation length R_c. In order to make the connection between (C_D^{true} - C_D^{fit}) and R_c, two assumptions are made. First, all dipoles found within R_c of the initially excited donor are parallel while those beyond R_c are randomly oriented. Second, excitation transport terminates after one hop (Förster limit). Within these approximations, depolarization arises only when excitation transport involves acceptors beyond the sphere of radius R_c. This implies that the fraction of the

total excitation transport occurring within R_c, $f(R_c)$, is equal to the fraction of dipoles that do not contribute to fluorescence depolarization $(C_D^{true} - C_D^{fit})/C_D^{true}$. In order to complete the task, a relationship between $f(R_c)$ and $(C_D^{true} - C_D^{fit})/C_D^{true}$ must be found. Toward that end, we recognize that the differential probability that a nearest neighbor resides at a distance R from a given molecule in a spatially random distribution is

$$dP(R) = 4\pi R^2 \rho \exp(-4\pi R^3 \rho/3) dR \qquad (1.36)$$

where ρ is the number density in the solution ($\rho \propto C_D^{true}$). The probability that excitation transport occurs within a sphere of radius R, S(R), is found by integrating the product of Eq. 1.36 and the distance dependent excitation transport probability. Therefore

$$S(R) = \int_0^R dP(R')/[1 + (R'/R_o)^6] \qquad (1.37)$$

where $1/[1 + (R'/R_o)^6]$ is the probability that excitation transport occurs between two molecules separated by R', and R_o is the critical transfer distance. Finally, the fraction of the total excitation transport that occurs within R is

$$f(R) = S(R)/S(\infty) \ . \qquad (1.38)$$

Hence the orientational correlation length R_c is simply the value of R which satisfies

$$f(R) = (C_D^{true} - C_D^{fit})/C_D^{true}), \qquad (1.39)$$

where the solution to Eq. 1.39 is found by numerical integration of Eq. 1.37. Though crude, this model facilitates the estimation of R_c using established excitation transport theories.

An improved estimate for R_c could be obtained using the theory of Knoester and Van Himbergen [46] for the time-dependent anisotropy A(t) in the presence of orientational correlations. The anisotropy function cannot be observed directly, however, and must be constructed from the polarized emission profiles $I_{\parallel}$ and $I_{\perp}$ using Eq. 1.34. This presents two problems in the analysis of the anisotropy and hence the recovery of R_c. First, the experimentally obtained polarized emission profiles are actually a convolution of the respective physical decay with the experimental instrument response function X (i.e., $X*I_{\parallel}$ and $X*I_{\perp}$ where * represents the convolution operator). While a convolute and compare nonlinear least squares analysis may be used to fit the experimental profiles $X*I_{\parallel}$ and $X*I_{\perp}$ (or $X*(I_{\parallel} \pm I_{\perp})$ since convolution is distributive), this type of analysis cannot be used to recover A(t) because A(t) is not trivially related to the convolutions of $I_{\parallel}$ and $I_{\perp}$ (i.e.,

$A(t) \neq X*(I_{\parallel} - I_{\perp})/X*(I_{\parallel} + 2I_{\perp}))$. One might attempt to deconvolve the experimental polarized emission profiles ($X*I_{\parallel}$ and $X*I_{\perp}$) to recover $I_{\parallel}$ and $I_{\perp}$ before constructing A(t). It has been reported, however, that "deconvolution as an information-improving device can easily become an exercise in self-delusion" [47]. The alternative is to ignore the early time behavior of the constructed anisotropy decay since this region alone is affected by the finite response time of the instrumentation. The second problem arises because A(t) is calculated from the sum ($I_{\parallel} + 2I_{\perp}$) and the difference ($I_{\parallel} - I_{\perp}$). Accurate recovery of A(t) requires high precision in obtaining $I_{\parallel}$ and $I_{\perp}$. Prior to constructing A(t), the two experimental profiles must be normalized with respect to excitation intensity, differential sensitivity to the emission polarization, and sample degradation; accurate normalization is difficult to achieve in any experiment when the data are not collected in parallel. While the time-dependent anisotropy is the quantity of interest in any depolarization study, comparison of theoretical A(t) with experimental data is indirect and difficult to effect. A better approach involves direct comparison between experimental and theoretical polarized emission decays. More theoretical work is necessary, however, to achieve compact theoretical expressions for $I_{\parallel}$ and $I_{\perp}$ which account for orientational correlation.

2-dimensional systems

For the sake of clarity, much of the preceding discussion focussed on 3-dimensional systems. The results obtained for the time-dependent polarized emission however, apply to all dimensionalities when the correct dimensional form for $G^S(t)$ is used, and when the orientational distribution is isotropic. While the orientational distribution in a solution is expected to be isotropic, experimental 2-dimensional systems (e.g., adsorption onto a solid surface, of confinement in a Langmuir-Blodgett monolayer) are generally anisotropic. The anisotropy arises when the physical (or chemical) forces that confine a chromophore to the plane tend to orient the molecule with respect to the surface normal. (The orientational distribution is generally assumed to be isotropic about the surface normal.) For example, Heinz et al. [48] and Di Lazzaro et al. [49] reported that xanthene dyes adsorb onto fused silica substrates with the long axis of the chromophore oriented at an angle of ~54° with respect to the surface normal. As a consequence, the time-dependent polarized emission results (Eqs. 1.24) must be modified to account for orientational anisotropy in 2-dimensional systems.

Previous work on anisotropic 2-dimensional systems assumed that the chromophore was oriented at a fixed angle θ^* with respect to the surface normal [50, 51]. This model

is now generalized to allow for dispersion about θ^* which is presently defined as the most probable orientation angle. Subsequent to this analysis, the orientation factor dependence on θ^* is calculated and the form for the rotational contribution to fluorescence depolarization in 2-dimensional systems is discussed.

To derive the time-dependent polarized emission equations for a 2-dimensional anisotropic system of donors, we again make the assumption that the polarization as defined in Eq. 1.23 is completely destroyed after one excitation transfer. Therefore, the emission arises from two ensembles: those initially excited via polarized light, and those excited after one or more excitation transfer steps. The orientationally averaged emission components arising from initially excited sites are $e_{\parallel}^{o}$, $e_{\perp}^{o}$, and e_{n}^{o}, while the three corresponding emission components due to uniformly excited dipoles (depolarized after one or more hops) are $e_{\parallel}^{1}$, $e_{\perp}^{1}$, and e_{n}^{1}. Therefore the time-dependent polarized emission equations are

$$I_{\parallel}(t) = P(t) \{e_{\parallel}^{o} G^{S}(t) + e_{\parallel}^{1} [1-G^{S}(t)]\} \qquad (1.40a)$$

$$I_{\perp}(t) = P(t) \{e_{\perp}^{o} G^{S}(t) + e_{\perp}^{1} [1-G^{S}(t)]\} \qquad (1.40b)$$

$$I_{n}(t) = P(t) \{e_{n}^{o} G^{S}(t) + e_{n}^{1} [1-G^{S}(t)]\} \qquad (1.40c)$$

where P(t) is the isotropic decay and $G^S(t)$ is the probability that the excitation resides on the initially excited site. It is convenient to rewrite Eq. 1.40 in a more familiar form:

$$I_{\parallel}(t) = e_{\parallel}^{1}\, P(t)\, [1 + d_{\parallel} G^S(t)] \tag{1.41a}$$

$$I_{\perp}(t) = e_{\perp}^{1}\, P(t)\, [1 + d_{\perp} G^S(t)] \tag{1.41b}$$

$$I_n(t) = e_n^{1}\, P(t)\, [1 + d_n G^S(t)] \tag{1.41c}$$

where

$$d_{\parallel} = \frac{e_{\parallel}^{o}}{e_{\parallel}^{1}} - 1 \tag{1.42a}$$

$$d_{\perp} = \frac{e_{\perp}^{o}}{e_{\perp}^{1}} - 1 \tag{1.42b}$$

$$d_n = \frac{e_n^{o}}{e_n^{1}} - 1 \quad . \tag{1.42c}$$

In our experimental geometry (see Fig. 1.3), the excitation polarization is parallel to the X-axis and the emission is along the Z-axis. Thus $e_{\parallel}$, $e_{\perp}$, and e_n are the polarized emission components along the X-, Y-, and Z-axes respectively. To complete the task, we must determine e^{o} and e^{1} as a function of the orientational distribution. Toward this end it is assumed that the orientational

distribution is isotropic about the Z-axis, and the emission dipole is parallel to the absorption dipole. The orientationally averaged polarization components arising from the initially excited sites are

$$e_{\parallel}^{\circ} = \int_0^{2\pi}\int_0^{\pi/2} (\sin^2\theta \cos^2\phi)(\sin^2\theta \cos^2\phi)\, g(\theta)\, d\theta d\phi \quad (1.43a)$$

$$e_{\perp}^{\circ} = \int_0^{2\pi}\int_0^{\pi/2} (\sin^2\theta \cos^2\phi)(\sin^2\theta \sin^2\phi)\, g(\theta)\, d\theta d\phi \quad (1.43b)$$

$$e_{n}^{\circ} = \int_0^{2\pi}\int_0^{\pi/2} (\sin^2\theta \cos^2\phi)(\cos^2\theta)\, g(\theta)\, d\theta d\phi \quad (1.43c)$$

where the first term in parentheses results from the absorption probability, the second term corresponds to the respective polarization component, and $g(\theta)$ is the orientational probability distribution function. The orientationally averaged polarization components arising from uniformly excited sites are

$$e_{\parallel}^{1} = A\int_0^{2\pi}\int_0^{\pi/2} (\sin^2\theta \cos^2\phi)\, g(\theta)\, d\theta d\phi \quad (1.44a)$$

$$e_{\perp}^{1} = A\int_0^{2\pi}\int_0^{\pi/2} (\sin^2\theta \sin^2\phi)\, g(\theta)\, d\theta d\phi \quad (1.44b)$$

$$e_{n}^{1} = A\int_0^{2\pi}\int_0^{\pi/2} (\cos^2\theta)\, g(\theta)\, d\theta d\phi \quad (1.44c)$$

where the terms in parentheses are the corresponding polarization components. The normalization factor A is

introduced to insure conservation of total emission intensity,

$$e_{\parallel}^{o} + e_{\perp}^{o} + e_{n}^{o} = e_{\parallel}^{1} + e_{\perp}^{1} + e_{n}^{1} \quad . \tag{1.45}$$

After integrating over ϕ, Eqs. 1.43 and 1.44 reduce to

$$e_{\parallel}^{o} = \frac{3\pi}{4} \int_{0}^{\pi/2} \sin^{4}\theta \; g(\theta) \; d\theta \tag{1.46a}$$

$$e_{\perp}^{o} = \frac{\pi}{4} \int_{0}^{\pi/2} \sin^{4}\theta \; g(\theta) \; d\theta \tag{1.46b}$$

$$e_{n}^{o} = \pi \int_{0}^{\pi/2} \sin^{2}\theta \cos^{2}\theta \; g(\theta) \; d\theta \tag{1.46c}$$

and

$$e_{\parallel}^{1} = \pi A \int_{0}^{\pi/2} \sin^{2}\theta \; g(\theta) \; d\theta \tag{1.47a}$$

$$e_{\perp}^{1} = \pi A \int_{0}^{\pi/2} \sin^{2}\theta \; g(\theta) \; d\theta \tag{1.47b}$$

$$e_{n}^{1} = 2\pi A \int_{0}^{\pi/2} \cos^{2}\theta \; g(\theta) \; d\theta \tag{1.47c}$$

Therefore

$$A = \frac{\int_{0}^{\pi/2} \sin^{2}\theta \; g(\theta) \; d\theta}{2\int_{0}^{\pi/2} g(\theta) \; d\theta} \tag{1.48}$$

Two limiting orientational distributions are considered. First, if the distribution of dipoles is isotropic, $g(\theta) = \sin\theta$ and Eqs. 1.41 become

$$I_{\parallel}(t) = \frac{2\pi}{9} P(t) [1 + 0.8\ G^S(t)] \qquad (1.49a)$$

$$I_{\perp}(t) = \frac{2\pi}{9} P(t) [1 - 0.4\ G^S(t)] \qquad (1.49b)$$

$$I_n(t) = \frac{2\pi}{9} P(t) [1 - 0.4\ G^S(t)] \qquad (1.49c)$$

which are within a constant of the results given in Eqs. 1.24. Second, if the dipoles are confined to a particular angle $\theta = \theta^*$, then $g(\theta) = \delta_{\theta,\theta^*}$ and the orientational distribution maps out cones on the surface. In this limit, Eqs. 1.41 reduce to

$$I_{\parallel}(t) = \frac{\pi}{2}\sin^4\theta^* P(t)[1 + 0.5\ G^S(t)] \qquad (1.50a)$$

$$I_{\perp}(t) = \frac{\pi}{2}\sin^4\theta^* P(t)[1 - 0.5\ G^S(t)] \qquad (1.50b)$$

$$I_n(t) = \pi \sin^2\theta^* \cos^2\theta^* P(t) \quad . \qquad (1.50c)$$

When 2-dimensional systems are not adequately described by either of the two limiting cases, a more general orientational distribution function is required. One such function allows dispersion in the dipole angle θ^*; modeling

the distribution with a Gaussian yields

$$g(\theta) = \sin\theta\, e^{-2.77\left(\frac{\theta - \theta^*}{\Gamma}\right)^2} \qquad (1.51)$$

where Γ is the dispersion Full-Width-Half-Max (FWHM), and θ^* is the most probable orientation angle. The limits of integration over θ ($0 \leq \theta \leq \pi/2$) imply a physical barrier to motion beyond these limits. This restriction is of no consequence when θ^* is set to 0, or $\pi/2$ due to symmetry. Even if these barriers to motion are unphysical, Eqs. 1.46 - 1.48 are expected to be accurate for small dispersions (i.e., such that $0 < (\theta^* \pm \Gamma) < 90°$).

The orientational probability distribution function given by Eq. 1.51 was used along with Eqs. 1.42 and 1.46 - 1.48 to obtain estimates for $d_{\parallel}$ and $d_{\perp}$. Figure 1.7 illustrate the effect of dispersion on $d_{\parallel}$ and $d_{\perp}$ for several angles θ^*. As the dispersion increase, $d_{\parallel}$ and $d_{\perp}$ diverge from the limiting values for dipoles along cones, and converge toward the limiting values for an isotropic distribution.

It is often useful to experimentally obtain a time-resolved profile which maps out the isotropic decay P(t). This is accomplished by viewing the fluorescence through an analyzer polarizer set at an angle such that the following linear combination obtains:

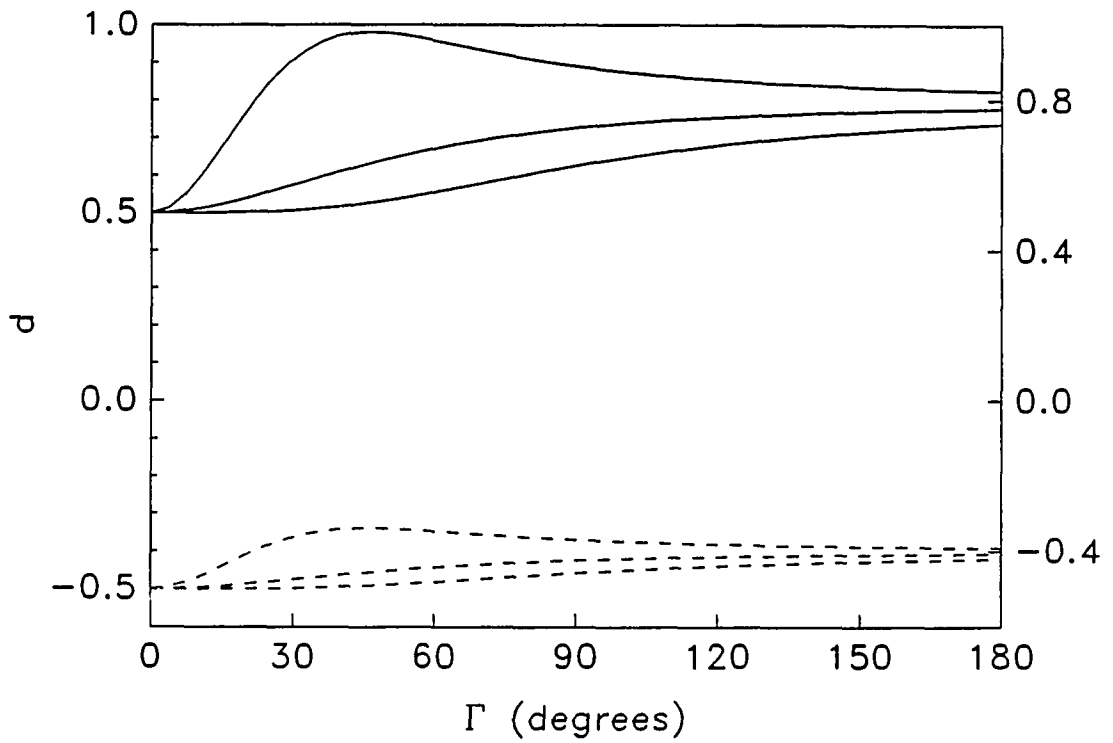

Fig. 1.7 Plot of $d_{\parallel}$ (solid lines) and $d_{\perp}$ (dashed lines) vs. dispersion (Γ) for θ^* = 30, 60, and 90 degrees (top through bottom, respectively). The dispersion about θ^* is modeled with Eq. 1.51

$$\cos^2\theta_{MA}\, I_{\parallel} + \sin^2\theta_{MA}\, I_{\perp} \propto P(t) \tag{1.52}$$

or

$$\cos^2\theta_{MA}\, d_{\parallel} + \sin^2\theta_{MA}\, d_{\perp} = 0 \tag{1.53}$$

then

$$\theta_{MA} = \tan^{-1}\sqrt{\frac{d_{\parallel}}{-d_{\perp}}} \quad . \tag{1.54}$$

Clearly, the appropriate angle θ_{MA} (Magic Angle) depends upon θ^* and Γ. This dependence is presented in Fig. 1.8 for three values of θ^*.

Dispersion in θ^* creates uncertainty in $d_{\parallel}$, $d_{\perp}$, and θ_{MA}. When the motivation for studying time-resolved fluorescence depolarization in 2-dimensions is to deduce an appropriate form for $G^s(t)$, it is desirable to minimize the uncertainty in the parameters $d_{\parallel}$ and $d_{\perp}$. This may be accomplished by selecting systems with little dispersion in θ^*, and/or systems with θ^* near 90 degrees. On the other hand, when $G^s(t)$ is known for a given system, it may prove possible to determine the dispersion in θ^*, provided θ^* and $P(t)$ can be independently determined.

Information related to the orientation angle θ^* may be obtained by measuring the total fluorescence intensity for excitation with p-polarized (normal to the plane) and

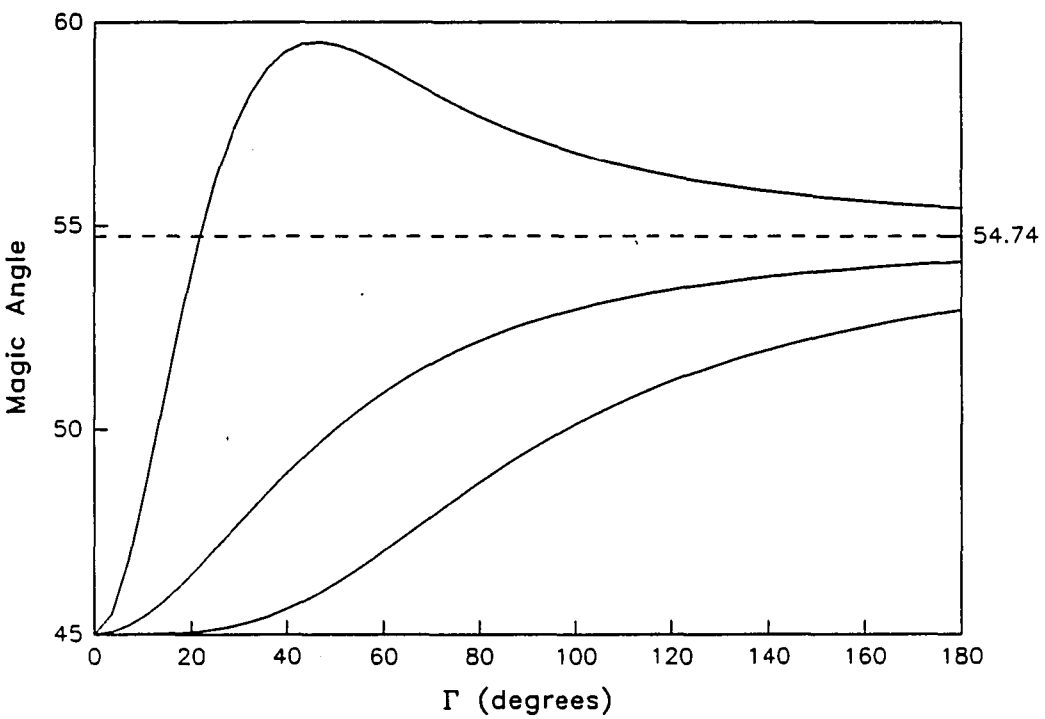

Fig. 1.8 Plot of the magic angle vs. dispersion (Γ) for θ^* = 30, 60, and 90 degrees (top through bottom, respectively). See Eq. 1.54

s-polarized (in the plane) light. The emission arising from s-polarized excitation is equal to $e^{o}_{\parallel} + e^{o}_{\perp}$ while the emission from p-polarized excitation is equivalent to $2e^{o}_{n}$. Thus

$$(I_s/I_p) = (e^{o}_{\parallel} + e^{o}_{\perp})/2e^{o}_{n} \tag{1.55}$$

where I_s and I_p are the total fluorescence intensities for excitation with s- and p-polarized light respectively. When there is no dispersion in θ^* (dipoles lie along cones) Eq. 1.55 reduces to

$$\theta^* = \tan^{-1}\sqrt{\frac{2I_s}{I_p}} \tag{1.56}$$

and the orientation angle θ^* may be found simply by measuring the ratio I_s/I_p. When there is dispersion, one cannot obtain a unique estimate for θ^*. Figure 1.9 illustrates the relationship between I_s/I_p and Γ for several values of θ^*. Note that I_s/I_p for large dispersion converges toward the value 2, which corresponds to the isotropic limit. It is clear from Fig. 1.9 that the measurement of I_s/I_p can only set limits on the range of θ^* (e.g., for $I_s/I_p = 0.5$, $0 < \theta^* < 45°$).

We now consider the orientation factor for the excitation transport probability. Table 1-1 contains the orientation factors $\langle\kappa^2\rangle$ and $\langle|\kappa|^{2/3}\rangle$ for two different

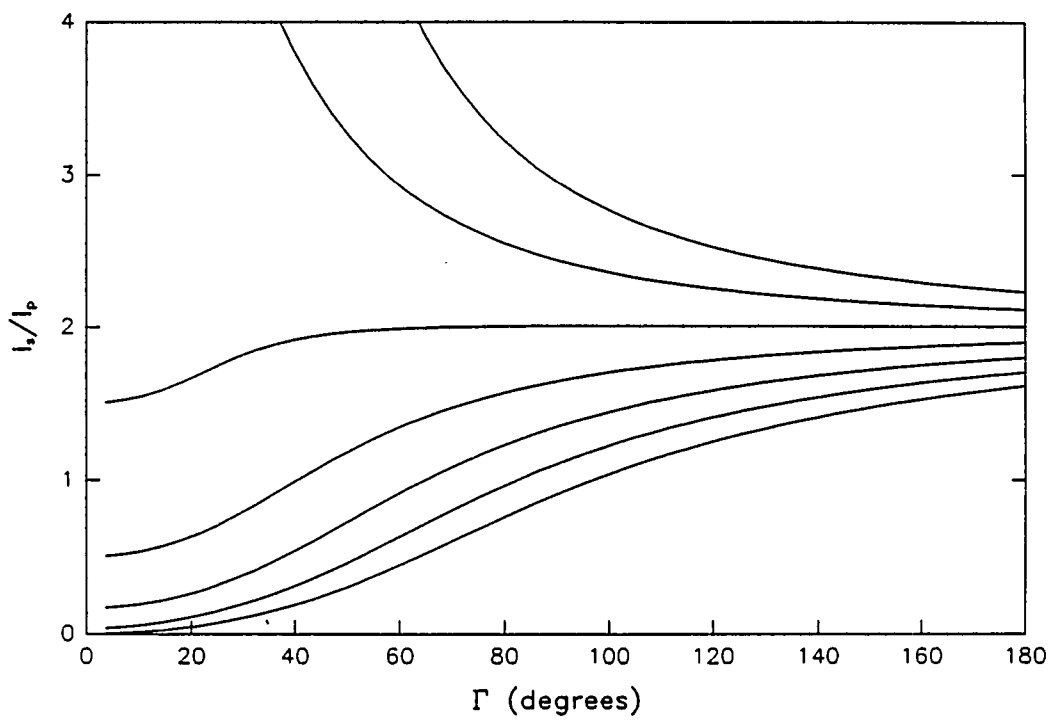

Fig. 1.9 Plot of I_S/I_p vs. dispersion (Γ) for θ^* = 0, 15, 30, 45, 60, 75, and 90 degrees (bottom through top, respectively). See Eq. 1.55

angular distributions in 2-dimensions: isotropic and in the plane [24]. A more general description confines the dipoles to a plane with the dipole direction fixed at an angle θ^* with respect to the surface normal (Fig. 1.10). The orientation factor associated with the dipole-dipole transport probability between $\hat{f}_D$ and $\hat{f}_A$ is given by Eq. 1.3. The present geometry yields

$$\hat{f}_D = \begin{bmatrix} \sin\theta^*\cos\phi_D \\ \sin\theta^*\sin\phi_D \\ \cos\theta^* \end{bmatrix} \tag{1.57a}$$

$$\hat{f}_A = \begin{bmatrix} \sin\theta^*\cos\phi_A \\ \sin\theta^*\sin\phi_A \\ \cos\theta^* \end{bmatrix} \tag{1.57b}$$

$$\hat{R} = \begin{bmatrix} \cos\phi \\ \sin\phi \\ 0 \end{bmatrix} \tag{1.57c}$$

Orientation averaging of κ^2 over ϕ_D, ϕ_A, and ϕ results in (see Fig. 1.11)

$$\langle\kappa^2\rangle = 5/4 \sin^4\theta^* + \cos^4\theta^* \quad . \tag{1.58}$$

When $\theta^* = 90$, the dipoles lie in the plane and $\langle\kappa^2\rangle$ becomes 5/4, the value found in Table 1-1. The static limit orientation factor $\langle|\kappa|^{2/3}\rangle$ is determined via numerical integration of Eq. 1.3 over ϕ_A and ϕ; the results are revealed in Fig. 1.12.

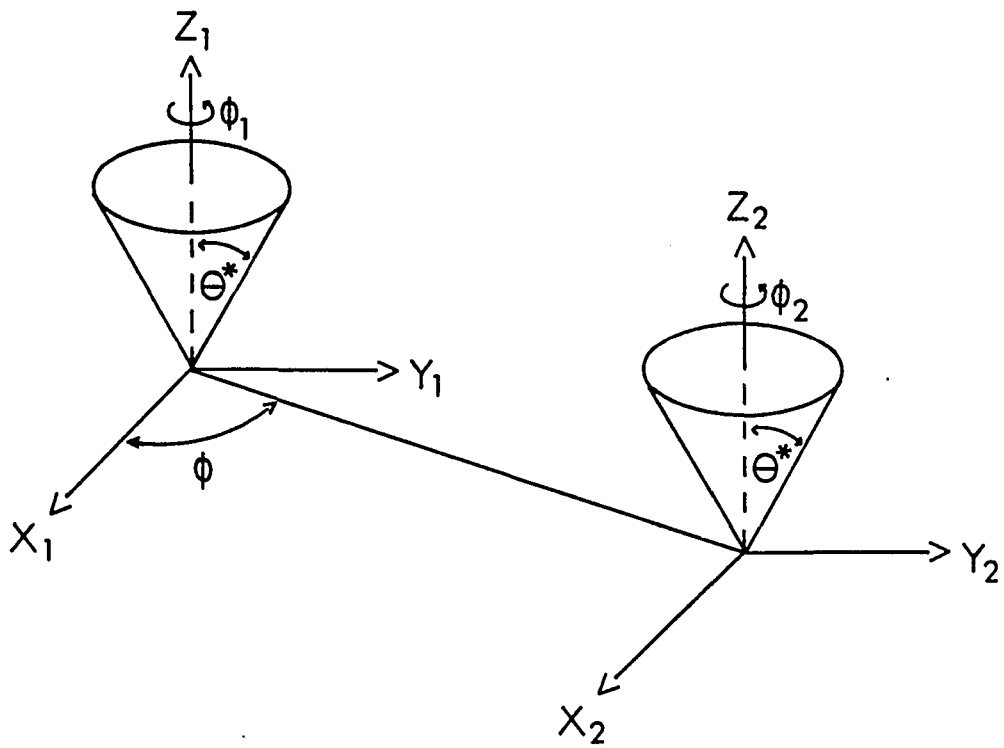

Fig. 1.10 Geometry for excitation transport between two dipoles confined within a plane

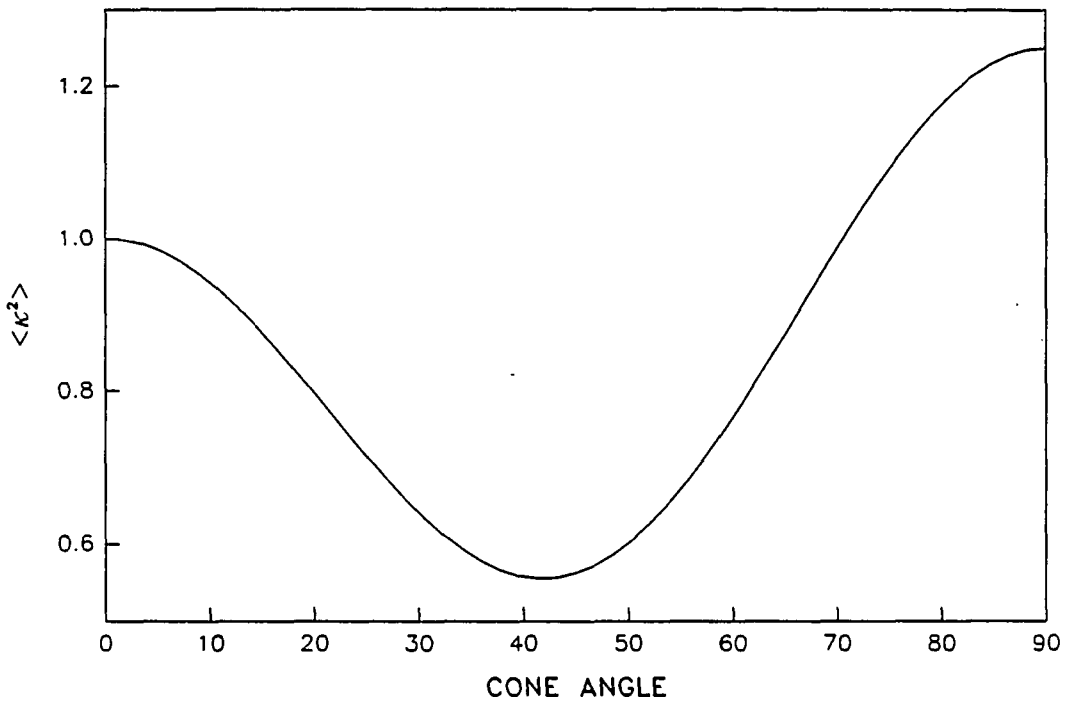

Fig. 1.11 Plot of the dynamic limit orientation factor $\langle \kappa^2 \rangle$ vs. cone angle θ^*. See Eq. 1.58

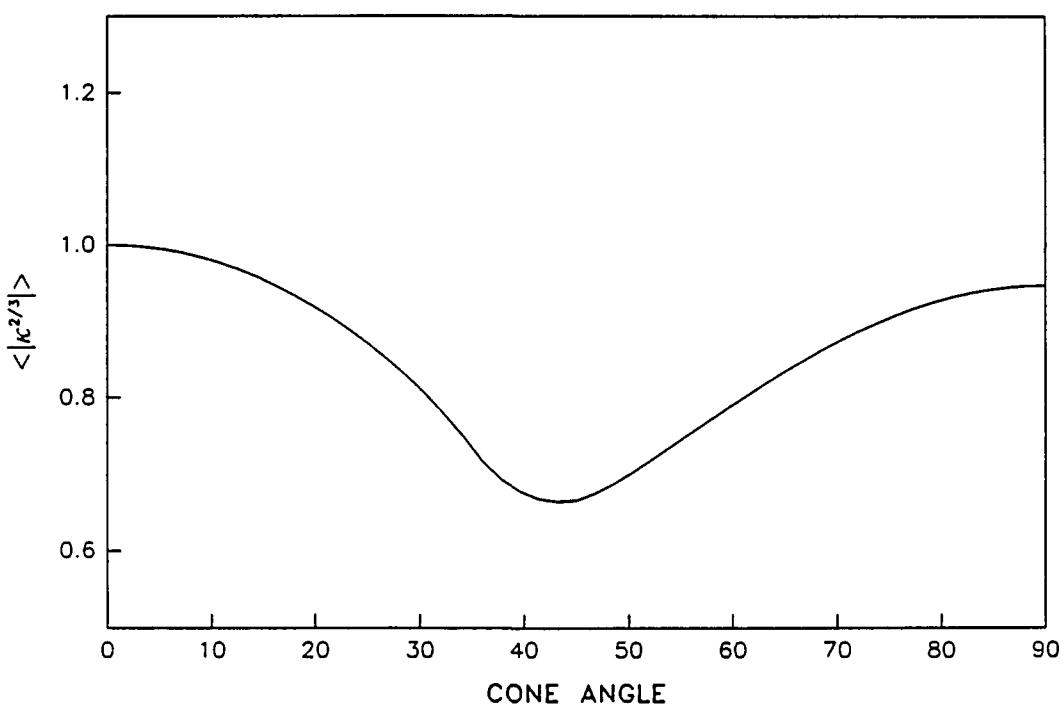

Fig. 1.12 Plot of the static limit orientation factor $\langle|\kappa|^{2/3}\rangle$ vs. cone angle θ^*

Finally, the rotational contribution to fluorescence depolarization in a 2-dimensional anisotropic system is considered. For this analysis, it is assumed that the dipoles are confined to a plane and are oriented at angle θ^* with respect to the surface normal. Two types of diffusional motion are possible: motion about and motion against the surface normal (i.e., ϕ and θ diffusion respectively). The excitation and emission geometry of Fig. 1.3 reveals that θ motion cannot depolarize the emission since this motion has no effect on the relative intensities of $I_{\parallel}$ and $I_{\perp}$. Diffusion about the surface normal, however, depolarizes the emission. If the dipole is free to rotate about the surface normal, the rotational anisotropy decay law is described by $r(t) \propto \exp(-6Dt)$ as before, where D is now the diffusion constant associated with this motion. The forces that impose an anisotropic distribution in a 2-dimensional system, however, may also hinder the rotational diffusion. The rotational depolarization is incomplete when the rotational diffusion is hindered; the limiting anisotropy, $A(t = \infty)$, is dependent upon the degree of restriction. A phenomenological model which accounts for restricted motion is given by

$$r(t) \propto [A_\infty + (1 - A_\infty) \exp(-6Dt)] \qquad (1.59)$$

(Equation 1.59 has been used in a different context to study

the restricted rotational diffusion of chromophores confined within the lipid bilayers of vesicle suspensions [52, 53, 54]. The analyses used by these authors, however, does not apply to our system where the chromophores are localized within a plane and the fluorescence is viewed along the surface normal.) The relationship between the limiting anisotropy, A_∞, and the degree of rotational freedom, Γ, can be obtained by assuming that the dipole orientation about the azimuth upon absorption is ϕ_o, and upon emission is $\phi_o + \beta$ where β is the rotation in the azimuthal angle due to diffusion. When there is no dispersion in θ^*, the polarized emission components $e_{\parallel}$ and $e_{\perp}$ become

$$e_{\parallel} = \sin^4\theta^* \int_0^{2\pi} \cos^2\phi_o \cos^2(\phi_o + \beta)\, d\phi_o \qquad (1.60a)$$

$$e_{\perp} = \sin^4\theta^* \int_0^{2\pi} \cos^2\phi_o \cos^2(\phi_o + \beta)\, d\phi_o \qquad (1.60b)$$

where Eqs. 1.43 were used. Integration of Eqs. 1.60 over ϕ_o yields

$$e_{\parallel} = \cos^2\beta\, e_{\parallel}^o + \sin^2\beta\, e_{\perp}^o \qquad (1.61a)$$

$$e_{\perp} = \sin^2\beta\, e_{\parallel}^o + \cos^2\beta\, e_{\perp}^o \qquad (1.61b)$$

where $e_{\parallel}^o$ and $e_{\perp}^o$ are defined in Eqs. 1.46. We must average $\sin^2\beta$ and $\cos^2\beta$ over all possible diffusion angles. To

effect these averages, it is assumed that the dipoles move freely about ϕ within the range Γ but cannot diffuse beyond this range. For example, if a dipole was in the middle of its range when absorption occurred, it could freely diffuse within the range $\phi_o \pm \Gamma/2$. We must also account for dipoles which are of either extreme when absorption occurs; their range would extend from ϕ_o to $\phi_o + \Gamma$, or ϕ_o to $\phi_o - \Gamma$. The average over all possible initial orientations is achieved by integrating over two variables, α and β so

$$\langle \sin^2\beta \rangle = \frac{1}{\Gamma^2} \int_0^{\Gamma} d\alpha \int_{-\Gamma+\alpha}^{\alpha} \sin^2\beta \, d\beta$$

$$= \frac{1}{2} \left(1 - \frac{\sin^2\Gamma}{\Gamma^2}\right) \qquad (1.62a)$$

$$\langle \cos^2\beta \rangle = \frac{1}{\Gamma^2} \int_0^{\Gamma} d\alpha \int_{-\Gamma+\alpha}^{\alpha} \cos^2\beta \, d\beta$$

$$= \frac{1}{2} \left(1 + \frac{\sin^2\Gamma}{\Gamma^2}\right) \qquad (1.62b)$$

and Γ is in radians. The final connection is made in realizing that the limiting anisotropy for the system under consideration is simply twice the polarization at long times.

$$A_\infty = 2 \left[\frac{e_\parallel - e_\perp}{e_\parallel + e_\perp}\right] = \frac{2\sin^2\Gamma}{\Gamma^2} \rho_o = \frac{\sin^2\Gamma}{\Gamma^2} \qquad (1.63)$$

For example, a diffusion range of Γ = 79.7 degrees (1.39 radians) accompanies a limiting anisotropy of A_∞ = 0.5. One could certainly use more sophisticated models to describe the distribution of β after randomization by rotational diffusion. The compact analytic expression of Eq. 1.63 is appealing, however, and may suffice when a rough estimate for the rotational freedom about ϕ in anisotropic 2-dimensional systems is desired.

It is worth mentioning that the self-absorption artifact which plagues excitation transport studies in 3-dimensional systems (at high concentrations) is absent in 2-dimensional systems. Perhaps the most conclusive test of excitation transport theories will be achieved in 2-dimensional systems.

Effect of excitation trapping on fluorescence depolarization

The time-resolved polarized emission equations derived thus far obtain when D→D excitation transport predominates (negligible D→T transport). These results may be extended to account for concurrent D→D and D→T excitation transport. To accomplish this, the following quantities are defined [52]:

$G^S(t, C_D, C_T)$ ≡ probability that the excitation is on the initially excited site,

$G^D(t, C_D, C_T)$ ≡ probability that the excitation resides in the donor ensemble,

$G^T(t, C_D, C_T)$ ≡ probability that the excitation is in the trap ensemble.

These probabilities depend on t, C_D, and C_T and are defined assuming an infinite lifetime for donor and trap. When the traps are non-fluorescent, the emission arises from two ensembles: those initially excited [$G^S(t)$], and those excited after one or more hops [$G^D(t) - G^S(t)$]. Hence the time-resolved polarized emission equations become

$$I_{\parallel} = \exp(-t/\tau) \{\tfrac{3}{5}G^S(t) + \tfrac{1}{3}[G^D(t) - G^S(t)]\} \qquad (1.64a)$$

$$I_{\perp} = \exp(-t/\tau) \{\tfrac{1}{5}G^S(t) + \tfrac{1}{3}[G^D(t) - G^S(t)]\} \qquad (1.64b)$$

which are rewritten in the more familiar form

$$I_{\parallel} = \tfrac{1}{3} \exp(-t/\tau)\, G^D(t) \left[1 + 0.8\, \frac{G^S(t)}{G^D(t)}\right] \qquad (1.65a)$$

$$I_{\perp} = \tfrac{1}{3} \exp(-t/\tau)\, G^D(t) \left[1 - 0.4\, \frac{G^S(t)}{G^D(t)}\right] \qquad (1.65b)$$

$$I_{MA} = \tfrac{1}{3} \exp(-t/\tau)\, G^D(t) \qquad (1.65c)$$

where I_{MA} is the isotropic decay observed by viewing the fluorescence through an analyzer polarizer oriented at the magic angle. The parameters C_D and C_T have been omitted for

clarity. When $C_T = 0$, $G^D(C_T = 0) = 1$ and Eqs. 1.65 reduce to Eqs. 1.24.

The Laplace transforms of $G^S(t)$ and $G^D(t)$ have been found within the 3-body approximation of LAF theory for excitation transport and trapping in 3-dimensional disordered systems [55]; their inverse Laplace was subsequently determined [11]. The analytic expressions for $G^S(t)$ and $G^D(t)$ found in reference [11] can be used in Eqs. 1.65 to account for trapping when it occurs in 3-dimensional fluorescence depolarization experiments.

RELATIONSHIP BETWEEN EXCITATION TRANSPORT AND FLUORESCENCE DEPOLARIZATION IN 2- AND 3-DIMENSIONAL DISORDERED SYSTEMS: EFFECT OF RESIDUAL POLARIZATION

Philip A. Anfinrud and Walter S. Struve

Department of Chemistry and Ames Laboratory - USDOE
Iowa State University, Ames, Iowa 50011

RELATIONSHIP BETWEEN EXCITATION TRANSPORT AND FLUORESCENCE DEPOLARIZATION IN 2- AND 3-DIMENSIONAL DISORDERED SYSTEMS: EFFECT OF RESIDUAL POLARIZATION

Introduction

Recent developments in the theory of dipole-dipole excitation transport in disordered systems [1-5] have been stimulated in part by the precision of time-resolved polarized fluorescence profiles afforded by current picosecond techniques. A frequently computed theoretical quantity is the time-dependent probability $G^S(t)$ that the excitation is found on the initially excited molecule. In the absence of excitation traps, $G^S(t)$ in 3-dimensional disordered systems is related to the fluorescence intensity components $I_{\parallel}(t)$ and $I_{\perp}(t)$ polarized along and normal to the excitation polarization by [6]

$$I_{\parallel}(t) = P(t)[1 + 0.8\ G^S(t)]$$
$$I_{\perp}(t) = P(t)[1 - 0.4\ G^S(t)] \qquad (1)$$

where P(t) is the isotropic decay function. Equations 1 are valid when the solvent or host is sufficiently viscous to inhibit rotational depolarization, when the molecular adsorption and fluorescence transition moments are linearly

polarized along the same axis, and when the excitation laser beam is so weak that the orientational distribution of unexcited molecules is random. Another assumption implicit in Eqs. 1 is that a single dipole-dipole excitation hop from the initial site to randomly oriented molecules yields a negligible average polarization

$$P_1 = (I_{\parallel} - I_{\perp})/(I_{\parallel} + I_{\perp}) \qquad (2)$$

Equations 1 have been used to analyze several time-resolved concentration depolarization experiments in solution [6-9].

Galanin has shown [10] that the actual polarization P_1 following a single dipole-dipole hop in 3-dimensional random systems is 1/42. This is small compared to the initial polarization ($P_0 = 1/2$) at $t = 0$. The error incurred by ignoring this residual polarization is obscured by experimental noise in most of the earlier time-resolved fluorescence experiments; it becomes barely detectable in our most recent work [8,9], and should be considered when comparing more precise fluorescence profiles with theory.

A similar situation arises in 2-dimensional systems. Molecules adsorbed on a flat surface with transition moments at a fixed angle θ^* from the surface normal (but with random azimuthal angles ϕ about the normal) will fluoresce with components parallel and normal to the excitation polarization

$$I_{\parallel}(t) = P(t)[1 + \tfrac{1}{2}G^{S}(t)]$$

$$I_{\perp}(t) = P(t)[1 - \tfrac{1}{2}G^{S}(t)] \qquad (3)$$

in the surface plane if emission is observed along the surface normal and if the residual polarization after one hop is negligible [11]. We show below that the polarization P_1 for $\theta^* = 90°$ (transition moments in the surface plane) and $\theta^* = 45°$ (the approximate adsorption angle of xanthene dyes on fused silica [12]) are 1/40 and 1/72, respectively. Hence, neglecting residual polarization for transition moments on the surface plane yields a level of approximation comparable to that in the 3-dimensional case; the approximation improves as θ^* is reduced.

In this work, we review Galanin's 3-dimensional calculation of P_1, because it has not been published in journals widely accessible to Western readers. We then generalize it to molecules adsorbed on a surface. We point out how Eqs. 1 and 3 can be approximately modified to account for residual polarization. We finally demonstrate the quantitative effects of neglecting residual polarization in realistic simulations of 3-dimensional transport experiments in solution.

Calculation of the Residual Polarization P_1

For dipole-dipole excitation transfer between molecules separated by the vector $\vec{r}$ with transition moments oriented along $\hat{d}_1$ and $\hat{d}_2$, the transfer probability contains the orientational factor [13]

$$K_{12}^2 = [3(\hat{d}_1 \cdot \hat{r})(\hat{d}_2 \cdot \hat{r}) - \hat{d}_1 \cdot \hat{d}_2]^2 \tag{4}$$

Using the notations $\cos\theta \equiv \hat{d}_1 \cdot \hat{r}$ and $\cos\chi = \hat{d}_1 \cdot \hat{d}_2$ and the fact that [10]

$$\hat{d}_2 \cdot \hat{r} = \sin\theta \sin\chi \sin\phi_1 \sin\phi_2 + \sin\theta \sin\chi \cos\phi_1 \cos\phi_2 + \cos\theta \cos\chi \tag{5}$$

(where ϕ_i is the azimuthal angle of dipole $\hat{d}_i$ about the intermolecular vector $\vec{r}$), one can average K_{12}^2 over θ, ϕ_1, and ϕ_2 for randomly oriented dipoles to obtain

$$\left\langle K_{12}^2 = \frac{3}{5} + \frac{1}{5}\cos^2\chi \right\rangle \tag{6}$$

Let the excitation laser be polarized along the z-axis; the fluorescence is observed along the y-axis. If the projections of $\hat{d}_1$ and $\hat{d}_2$ are $\cos\alpha_1$ and $\cos\alpha_2$ along the z-axis and $\cos\beta_1$ and $\cos\beta_2$ along the x-axis, the observed

fluorescence intensity components polarized along the z- and x-axes after one excitation hop will be

$$I_{\parallel} \propto \left\langle \cos^2\alpha_1 \cos^2\alpha_2 \left(\frac{3}{5} + \frac{1}{5}\cos^2\chi\right)\right\rangle$$

$$I_{\perp} \propto \left\langle \cos^2\alpha_1 \sin^2\alpha_2 \cos^2\beta_2 \left(\frac{3}{5} + \frac{1}{5}\cos^2\chi\right)\right\rangle \tag{7}$$

where the brackets indicate averaging over α_1, α_2, β_1, and β_2. Since

$$\cos\chi = \sin\alpha_1 \sin\alpha_2 \sin\beta_1 \sin\beta_2 + \sin\alpha_1 \sin\alpha_2 \cos\beta_1 \cos\beta_2 + \cos\alpha_1 \cos\alpha_2 \tag{8}$$

the averages in Eqs. 7 are readily found to be

$$I_{\parallel} \propto \frac{86}{1125}$$

$$I_{\perp} \propto \frac{82}{1125}$$

and the residual polarization is [10]

$$P_1 = \frac{I_{\parallel} - I_{\perp}}{I_{\parallel} + I_{\perp}} = 1/42 \tag{9}$$

We now treat the case of molecules adsorbed on a flat surface with transition moments aligned at a fixed angle θ^*

from the surface normal and at random azimuthal angles ϕ. The dipole-dipole transfer probability between molecules with molecules oriented along $\hat{d}_1$ and $\hat{d}_2$ is again proportional to K_{12}^2 as in Eq. 4, but with

$$\hat{d}_1 = (\sin\theta^*\cos\phi_1,\ \sin\theta^*\sin\phi_1,\ \cos\theta^*) \tag{10a}$$

$$\hat{d}_2 = (\sin\theta^*\cos\phi_2,\ \sin\theta^*\sin\phi_2,\ \cos\theta^*) \tag{10b}$$

$$\hat{r} = (\cos\phi,\ \sin\phi,\ 0) \tag{10c}$$

If the excitation laser is y-polarized, the surface occupies the xy-plane, and the fluorescence is observed along the surface normal, the fluorescence intensity components polarized parallel and normal to the exciting polarization will be

$$\begin{aligned} I_{\parallel} &\propto \left\langle \sin^4\theta^*\sin^2\phi_1\sin^2\phi_2 K_{12}^2 \right\rangle \\ I_{\perp} &\propto \left\langle \sin^4\theta^*\sin^2\phi_1\cos^2\phi_2 K_{12}^2 \right\rangle \end{aligned} \tag{11}$$

where the brackets denote averaging over ϕ_1, ϕ_2, and ϕ. The results are

$$I_{\parallel} \propto \sin^4\theta^*\left(\frac{41}{128}\sin^4\theta^* + \frac{1}{4}\cos^4\theta^*\right)$$

$$I_{\perp} \propto \sin^4\theta^*\left(\frac{39}{128}\sin^4\theta^* + \frac{1}{4}\cos^4\theta^*\right) \tag{12}$$

and

$$P_1 = \frac{\sin^4\theta^*}{40\sin^4\theta^* + 32\cos^4\theta^*} \tag{13}$$

for $\theta^* = 90°$ and $45°$, Eq. 13 yields $P_1 = 1/40$ and $1/72$, respectively.

Effect of Residual Polarization on Anisotropic Fluorescence Profiles

In a random 3-dimensional system in which the residual polarization P_1 cannot be neglected, Eqs. 1 for the polarized fluorescence components must be replaced by

$$I_{\parallel}(t) = P(t)\{1 + 0.8[G^S(t) + \alpha H(t)]\}$$

$$I_{\perp}(t) = P(t)\{1 - 0.4[G^S(t) + \alpha H(t)]\} \tag{14}$$

Here H(t) is the probability that excitation resides on a site excited by a single hop from the initially excited site. Equations 14 implicitly assume that the residual polarization P_2 after two excitation hops from the initial

site is negligible. The constant α is determined by recognizing that after one hop ($G^S \to 0, H \to 1$)

$$\frac{I_{\parallel} - I_{\perp}}{I_{\parallel} + I_{\perp}} = \frac{0.6\alpha}{1 + 0.2\alpha} = \frac{1}{42}$$

from which $\alpha = 1/25$. If the excitation transfer is limited to either a single hop to a site other than the laser-excited site, or to such a hop followed by back transfer to the initial site,

$$H(t) = 1 - G^S(t) \tag{15}$$

However, the site excited after one hop can also transmit its excitation to a third site. Accordingly, H(t) will become to first order a convolution of the rate $-dG^S(t)/dt$ that the second site is excited by transfer from the first site, with the probability $G^S(t - t')$ that the excitation remains on the second site after the latter becomes excited at time t'. Instead of Eq. 15, the function H(t) then becomes

$$H(t) = - \int_0^t \left[\frac{dG^S(t)}{dt}\right]_{t=t'} G^S(t - t')dt' \tag{16}$$

For realizable dye concentrations in viscous alcohols and for measurable fluorescence time windows, the Huber et al. [1] and Gochanour-Andersen-Fayer (GAF) 3-body [2] theories

predict nearly identical decay in $G^S(t)$ in 3-dimensional random systems [8]. The analytic Huber theory, which closely approximates the experimental decay of $G^S(t)$ for DODCI in ethylene glycol [9], yields the expression

$$G^S(t) = \exp\left(-C\sqrt{\frac{\pi t}{2\tau}}\right) \equiv \exp(-\beta\sqrt{t}) \tag{17}$$

Here τ is the isotropic intramolecular lifetime and C is the dimensionless reduced dye concentration [2]

$$C = \frac{4}{3}\pi R_o^3 \rho \tag{18}$$

which depends on the dye molecule number density ρ and the Förster parameter R_o, which characterizes the strength of the dipole-dipole coupling responsible for the transport [13]. The convolution integral for H(t) becomes

$$H(t) = \frac{\beta}{2}\int_o^t \frac{1}{\sqrt{t'}}\exp[-\beta(\sqrt{t'} + \sqrt{t - t'})]dt' \tag{19}$$

Simpson's rule was used to evaluate H(t). Due to the integrand's singularity at $t' = 0$, the integration region was broken up into four intervals (0, 0.001t), (0.001t, 0.01t), (0.01t, 0.1t), and (0.1t, t); each of these was subdivided into N integration steps. The singularity was avoided by neglecting the first integration step at $t' = 0$. It was found that N = 10 yielded values of H(t) within 0.5%

of those obtained with $N = 10^3$, and $N = 10$ was used in this work. In Figure 1, we show H(t) curves computed from Eq. 19 for seven reduced concentrations C ranging from 0.150 to 4.76. For these calculations, we used the DODCI lifetime $\tau = 1.7$ ns in glycerol [8]. While $G^S(t)$ decays monotonically from the value 1.0 at $t = 0$ [2], H(t) passes through a maximum and then decays.

To test the effect of this residual polarization on anisotropic fluorescence profiles, model $I_{\parallel}(t)$ and $I_{\perp}(t)$ profiles were first calculated by convoluting Eqs. 14 with an actual experimental photon-counting instrument function (~ 47 ps fwhm) generated in our laboratory [8,9]. The isotropic decay P(t) was modeled by a single-exponential function with a 1.7 ns lifetime; $G^S(t)$ was computed using the Huber theory (Eq. 17). These pairs of model profiles were computed for each of the reduced concentrations for which H(t) was evaluated (Fig. 1). They were augmented with Gaussian noise simulating the photon-counting statistics of our most recent work [8,9], where 10^5 counts were typically accumulated in the peak channel of $I_{\parallel}(t)$ (S/N ~ 300). These profiles were then fitted with Eqs. 1 (which ignore the effects of residual polarization) using a Marquardt nonlinear least-squares algorithm [8,9]. The isotropic decay P(t) was held to the identical form used to generate the model profiles, and a second experimental instrument function was used in the deconvolution. The lifetime τ in

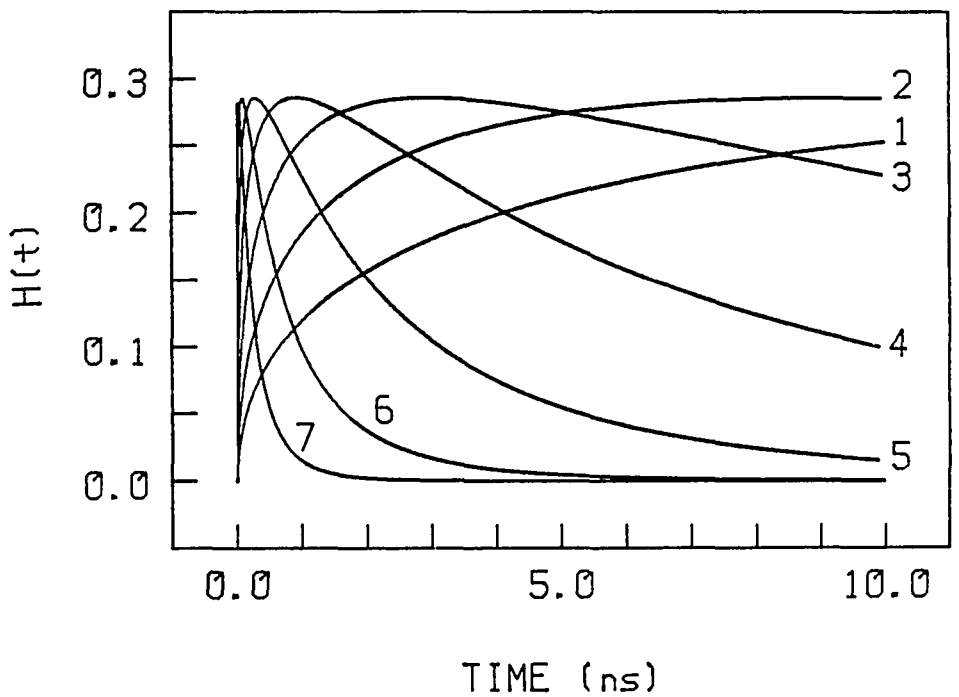

Figure 1. Plots of H(t) generated by numerical integration of Eq. 19 for reduced concentrations C equal to (1) 0.150, (2) 0.268, (3) 0.476, (4) 0.846, (5) 1.504, (6) 2.675, and (7) 4.757. The isotropic lifetime τ is 1.7 ns

$G^S(t)$ (Eq. 17) was frozen at 1.7 ns, the value used in the model profiles. The effect of neglecting residual polarization is then manifested by the difference between the optimized reduced concentrations (from fitting the model profiles using Eqs. 1) and the true reduced concentrations (from which the model profiles were initially computed using Eqs. 14). These differences are shown in Table I, which also shows the reduced χ^2 computed for both the original model profiles (with Gaussian noise) and the fitted profiles. The fractional differences between the true and fitted reduced concentrations are small, and amount to 5.6% in the worst case (C = 0.268). The reduced χ^2 are larger for the fitted than for the original model profiles, but by an amount which is barely perceptible under present statistics (which typify the most precise photon-counting transport work that has been done to date [8,9]). In Fig. 2, we show the model profiles for $I_{\parallel}(t)$ and $I_{\perp}(t)$ at C = 0.268 (the worst case) as discrete points; the fitted convolutions of Eqs. 1 with the instrument function are continuous curves. The inset plots show the autocorrelations of residuals for the latter fits; these are dominated by the Gaussian noise. Under present technology, experimental autocorrelations of residuals are clearly unlikely to reveal the systematic deviations which result from ignoring residual polarization. In Fig. 3, we plot the optimized reduced concentrations C versus the true reduced

Table I. Parameters for Fitting of Model Profiles with Equations 1 [a]

C(true)	C(fitted)	% difference	χ_r^2 (true)	χ_r^2 (fitted)
0.150	0.145	-3.3	1.032	1.170
			0.995	1.069
0.268	0.253	-5.6	0.972	1.034
			1.042	1.134
0.476	0.456	-4.2	0.998	1.083
			1.051	1.178
0.846	0.823	-2.7	1.037	1.092
			1.039	1.129
1.504	1.468	-2.4	1.075	1.228
			0.999	1.028
2.675	2.604	-2.6	1.050	1.204
			1.035	1.114
4.757	4.635	-2.6	0.951	1.044
			1.029	1.143

[a] For each reduced concentration, the first line under χ_r^2 is for $I_{\parallel}(t)$ and the second line is for $I_{\perp}(t)$.

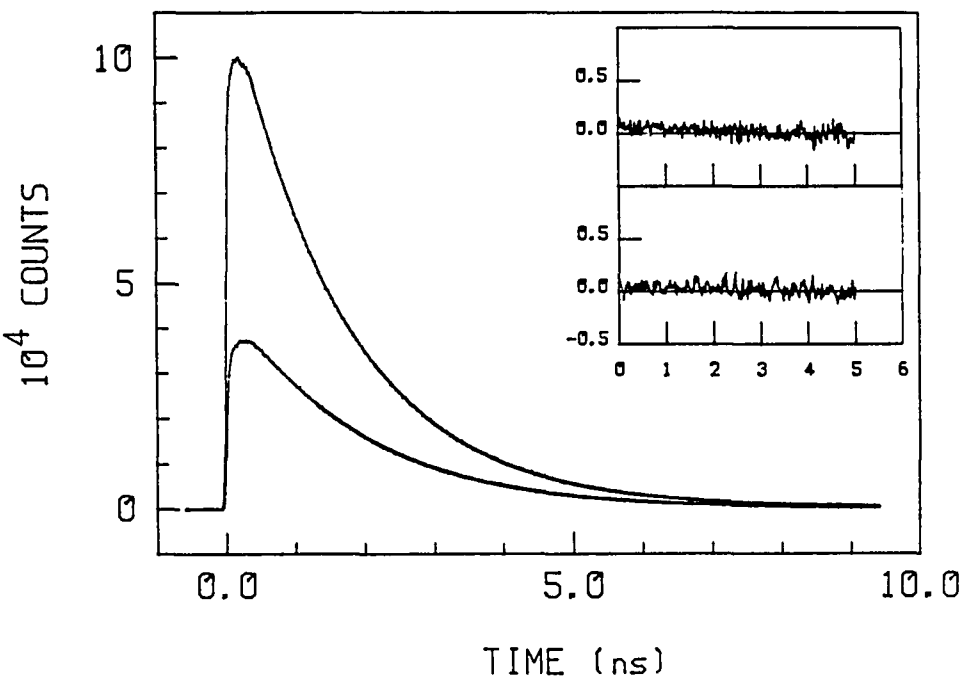

Figure 2. Model profiles for $I_{\parallel}(t)$ and $I_{\perp}(t)$ for C = 0.268, calculated by convolution of experimental instrument function [7,8] with Eqs. 14 (discrete points); $I_{\parallel}(t)$ and $I_{\perp}(t)$ profiles fitted by optimization of Eqs. 1, which ignore residual polarization (continuous curves). Top and bottom insets show autocorrelations of residuals for fitted $I_{\parallel}(t)$ and $I_{\perp}(t)$ profiles, respectively

concentrations. If the error due to neglect of residual polarization were negligible, these points would lie on a straight line. This very nearly is what occurs in Fig. 3. The errors shown here are far smaller that the discrepancies we have observed between current transport theories and fluorescence profiles for DODCI in glycerol [8], and are smaller than the discrepancies observed for DODCI in ethylene glycol [9]. The discrepancies observed in glycerol are likely a consequence of long-range ordering in the liquid's structure [14], causing nonrandomness in DODCI orientations which does not occur in glycol and most other alcohols at room temperature.

This analysis can readily be extended to residual polarization effects in anisotropic fluorescences from 2-dimensional transport. Since these effects are comparable in magnitude to those in 3-dimensional transport (Section II) and since existing work has been performed with considerably less favorable statistics ($\sim 10^4$ counts/peak channel) than in solution, they cannot account for the discrepancies observed between our experimental rhodamine 3B/fused silica work [11] and 2-dimensional transport theories. More precise 2-dimensional experiments are currently being conducted using octadecylrhodamine B chromophores in Langmuir-Blodgett monolayers in our laboratory.

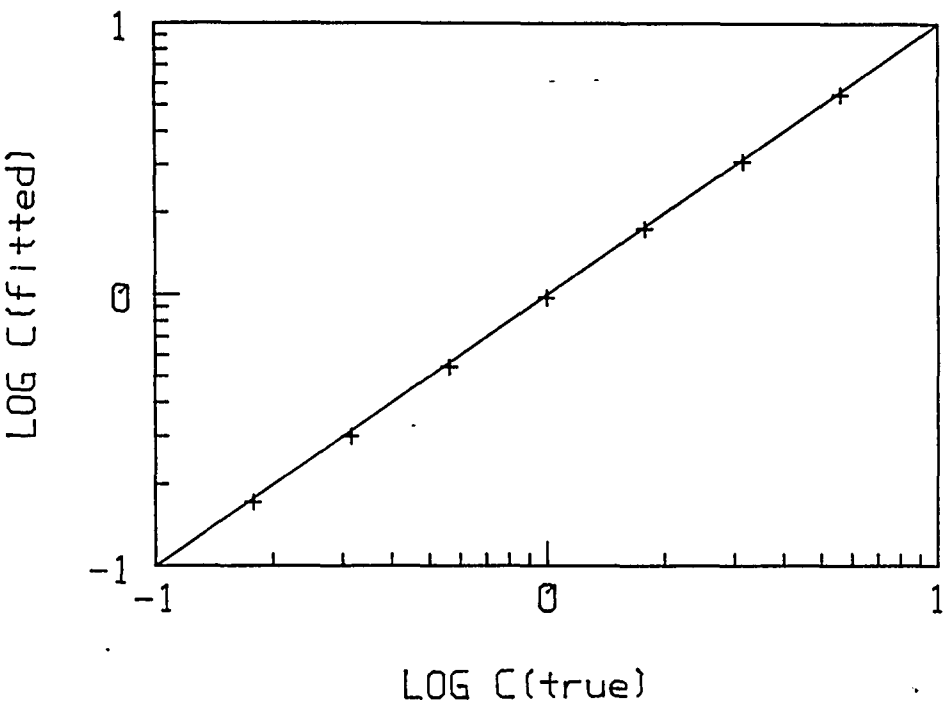

Figure 3. Optimized reduced concentrations C_D (fitted) versus true reduced concentrations C_D (true), from Table I. This Figure may be compared with Fig. 5 of Ref. 8 and with Fig. 4 of Ref. 9. These C_D values are related to the reduced concentrations C in text by $C_D = C/0.846$; this factor arises from orientational averaging of the dipole-dipole transfer rate in 3 dimensions [6]

Acknowledgements

The Ames Laboratory is operated for the U.S. Department of Energy by Iowa State University under Contract No. W-7405-Eng-82. This work was supported by the Office of Basic Energy Sciences.

References

1. Huber, D. L.; Hamilton, D. S.; Barnett, B. Phys. Rev. 1977, B16, 4642.
2. Gochanour, C. R.; Andersen, H. C.; Fayer, M. D. J. Chem. Phys. 1979, 70, 4254.
3. Loring, R. F.; Andersen, H. C.; Fayer, M. D. J. Chem. Phys. 1982, 76, 2015.
4. Loring, R. F.; Fayer, M. D. Chem. Phys. 1984, 85, 149.
5. Fedorenko, S. G.; Burshtein, A. I. Chem. Phys. 1985, 98, 341.
6. Gochanour, C. R.; Fayer, M. D. J. Phys. Chem. 1981, 85, 1989.
7. Anfinrud, P. A.; Hart, D. E.; Hedstrom, J. F.; Struve, W. S. J. Phys. Chem. 1986, 90, 2374.
8. Hart, D. E.; Anfinrud, P. A.; Struve, W. S. J. Chem. Phys. 1987, 86, 2689.
9. Anfinrud, P. A.; Struve, W. S.; submitted to J. Chem. Phys.
10. Galanin, M. D. Trudy Fiz. Inst. 1950, 5, 339.
11. Anfinrud, P. A.; Hart, D. E.; Hedstrom, J. F.; Struve, W. S. J. Phys. Chem. 1986, 90, 3116.
12. Di Lazzaro, P.; Mataloni, P.; DeMartin, F. Chem. Phys. Lett. 1985, 114, 103.

13. Förster, T. Discuss. Faraday Soc. 1959, 27, 7.

14. Soltwisch, M.; Steffen, B. Z. Naturforsch. 1980, 36a, 1045.

SECTION II. EXPERIMENTAL

TIME-CORRELATED SINGLE PHOTON COUNTING

The high gain and fast response of a photomultiplier tube (PMT) enables the detection of individual photons. This "digital" form of light detection, known as single photon counting (SPC), can often be advantageously implemented in spectrophotometers where analog processing of the PMT current is commonly employed. The SPC method improves low light level sensitivity, enhances the signal to noise ratio by discriminating against "dark" current, offers a wider dynamic range, and is less sensitive to drift in photodetector supply voltage or temperature [56]. Successful application of the SPC technique, however, demands that the instrumentation possess pulse-pair resolving capability. Hence, sufficiently low light level operation must be maintained such that the time between detected photons is long relative to the PMT pulse width.

Time resolution in SPC is achieved by measuring the time correlation (delay time) between each detected photon and the excitation pulse from which the emission arose. Accumulation of the sorted counts (number of photons detected within each delay time interval) yields an histogram representation of the time-resolved emission intensity. This technique is known as time-correlated single photon counting (TCSPC).

The method of TCSPC offers many advantages over the conventional form of time-resolved measurements where the average PMT current is measured vs. time. These include enhanced sensitivity and time resolution, an expanded dynamic range, and finally, the ability to effectively deconvolute the data to digitally improve the time resolution.

Since TCSPC is a single photon counting technique, it is intrinsically sensitive; further comment is not particularly illuminating.

It is interesting to note that the time-resolution achieved in TCSPC is not limited to the PMT anode pulse width (as in conventional time-resolved measurements), but is in principle limited only by the PMT transit time jitter. (The time between photoelectron generation at the PMT cathode and arrival of the resulting electrical pulse at the PMT anode is the transit time.) The transit time jitter can be an order of magnitude less than the anode pulse width in PMTs optimized for TCSPC.

The dynamic range available in TCSPC is clarified in a discussion of photon counting statistics. The number of photons detected in a particular time interval is an estimate to the mean μ. The probability distribution about μ is predicted by the Poisson distribution where the statistical variance is related to the number of counts by [57]

$$\sigma^2 = N. \qquad (2.1)$$

For example, a TCSPC profile collected to 10^6 counts in the peak region would exhibit ~.1% uncertainty (one statistical standard deviation σ) in the peak counts. This decay could be followed over 4 decades to 10^2 counts where the uncertainty is still only ~10%. Thus the dynamic range for TCSPC is in principle limited only by patience and/or practicality. This performance is unparalleled in schemes requiring analog processing of the PMT current. In practice, researchers generally accumulate data to $10^4 \rightarrow 10^5$ counts in the peak region.

The experimentally observed time resolved profile I(t) is not the true time-dependent emission p(t), but is actually a convolution of the true decay p(t) with the instrument response X(t) to the excitation pulse, so [58]

$$I(t) = \int_0^t X(t')\, p(t-t')dt'. \qquad (2.2)$$

The precision available in TCSPC facilitates accurate recovery of X(t) simply by viewing a scattering sample instead of a fluorescent one. Hence, TCSPC lends itself to a convolute-and-compare nonlinear least squares analysis where p(t) decay times shorter than the instrument response FWHM may be accurately estimated [58]. The shortest lifetime which can be reliably recovered using the

convolute-and-compare analysis was estimated to be one tenth the instrument response FWHM for a single exponential decay and one fifth for double exponentials [59].

The sensitivity, dynamic range, and time resolution achievable in TCSPC measurements enables a detailed analysis of the emission decay dynamics. These characteristics obtain when TCSPC is used with high repetition rate sources where acceptable signal to noise can be achieved in a reasonable amount of time. The TCSPC method becomes inefficient, however, when long lived decays (e.g., phosphorescence) are observed since the light source repetition rate must be reduced to allow complete sample recovery between pulses. For these situations, analog detection schemes may be preferred.

The apparatus used in our laboratory to effect TCSPC is illustrated in the schematic diagram of Fig. 2.1. The function of the various components is presently outlined; a detailed description is reserved for the remaining portion of Section II.

The excitation source is derived from an actively mode-locked argon ion laser which synchronously pumps a cavity dumped rhodamine 6G dye laser. The cavity dumper repetition rate is generally set to ~5 MHz, providing an excitation pulse periodicity of ~200 ns. The cavity dumped output is partitioned via a beam splitter. One portion is divided a second time before being routed to a real time

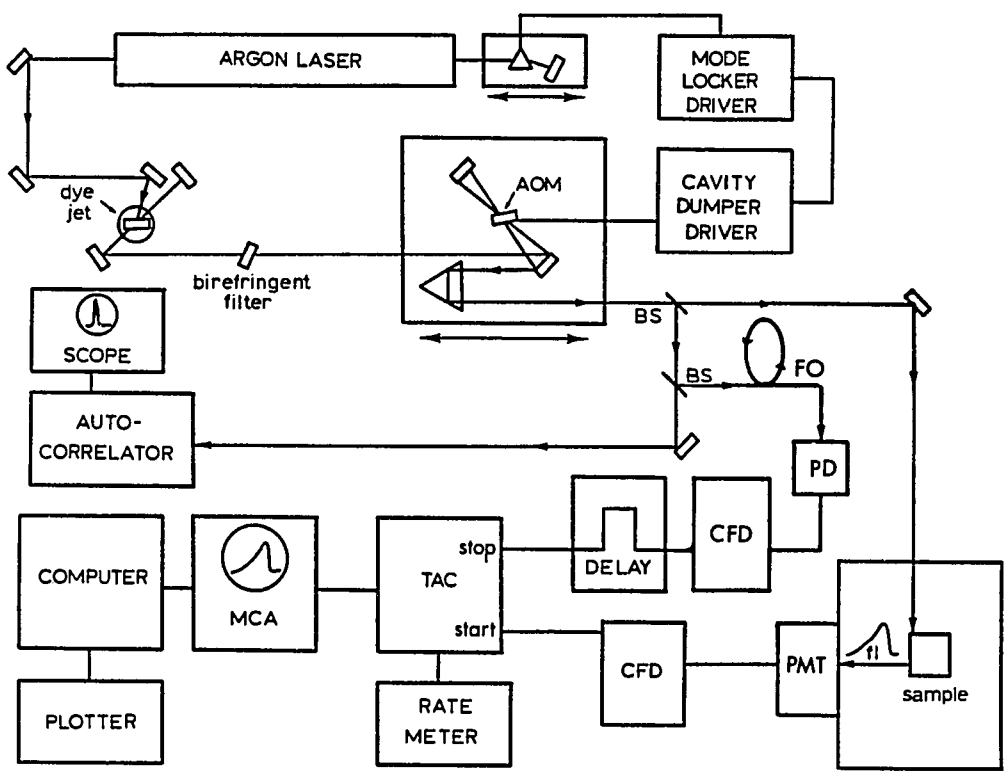

Fig. 2.1 Experimental apparatus for TCSPC. AOM, acousto-optic modulator; BS, beam splitter; FO, fiber optic delay; PD, photodiode; CFD, constant fraction discriminator; PMT, photomultiplier tube; TAC, time-to-amplitude converter; MCA, multichannel analyzer

autocorrelator. The autocorrelator provides a visual monitor of the pulse power and duration, thereby facilitating optimization of these parameters. The other split and delayed portion (coupled through a 15m fiber optic bundle) is used to drive a fast rise time photodiode to provide a low jitter reference signal at the cavity dumped repetition rate. The remaining portion is directed to the sample whereupon the emission is viewed with a PMT. The outputs of both PMT and photodiode are processed with constant fraction discriminators to provide a timing signal which is in principle independent of pulse amplitude. The processed PMT response and photodiode reference are routed to a time-to-amplitude converter (TAC) where the correlation time is measured. The TAC operates like a gated integrator viewing a constant voltage where the gating function is initiated by a START, and terminated with a STOP pulse. The integrated voltage is therefore proportional to the gate time, which is equivalent to the time difference between the START and STOP pulse. The integrated voltage for each processed event is passed along as an analog pulse to a multichannel analyzer (MCA) which sorts each signal according to its height and adds one count to a digital memory location corresponding to the appropriate delay time interval. (The MCA divides the delay time window in to N intervals; N is 512 for our measurements.) Hence, the MCA accumulates the time-resolved emission profile in histogram

form. A rate meter is also connected to the TAC to provide an on-line estimate for the experimental count rate. The accumulated counts are ultimately routed to a computer for data analysis.

Many of the components and methodologies used in our TCSPC system have evolved over the past few years of operation. The details are presented under three headings: Excitation Source, Electronics, and Data Analysis.

Excitation Source

Laser system

An argon ion laser (5-watt Coherent Innova 90) is actively mode-locked by modulating the cavity Q with an acousto-optic modulator (Harris Corp. H-401). The acousto-optic modulator consists of a piezoelectric transducer bonded to one parallel side of a quartz Brewster prism. (The prism also selects the operating wavelength for the laser.) About 500 mW of radio frequency (rf) power is used to excite the transducer at a prism resonance in order to establish a standing acoustic wave within the prism. The modulation in refractive index of the material due to the acoustic wave serves to diffract intensity out of the cavity. This loss is periodic, however, due to the build-up, collapse, and reversal of the standing wave. When the argon ion cavity length is set such that the inverse round

trip time exactly equals twice the rf frequency (the cavity Q is modulated at twice the rf frequency since an acoustic wave of either phase introduces a loss), the laser becomes optimally mode-locked. A simple interpretation of this phenomenon views the AOM as an optical shutter from which laser light emerges; only the emission that is in phase with the opening of the shutter can experience gain, and hence the laser output becomes pulsed at twice the rf frequency. Alternatively, the periodic loss forces all longitudinal modes to oscillate in phase; the inverse Fourier transform of a Gaussian frequency distribution with all phases locked to zero yields a Gaussian pulse whose temporal width Δt is given by [21]

$$\Delta t = \frac{2\pi\ (0.441)}{\Delta w} \qquad (2.3)$$

where Δw is the spectral bandwidth. The spectral bandwidth about the 514.5 nm argon ion laser line (due to inhomogeneous broadening) is sufficient to generate ~100 ps pulse widths. The mode-locked argon ion output is used to synchronously pump a cavity dumped dye laser (Coherent Model 590). Synchronization is achieved by matching the dye laser cavity length to the optimized argon ion cavity length. The home-built cavity dumper head is mounted on a translation stage to provide the necessary adjustment.

The pulse width emerging from an optimized synchronously-pumped dye laser may be as much as 100 times shorter than the pump-pulse duration [21]. The pulse shortening mechanism is readily explained in a qualitative sense. The modulation in the dye gain due to periodic excitation forces the dye pulse to circulate in synchrony. Thus the dye pulse arrives in the gain medium as the gain is increasing beyond threshold and amplification occurs. The gain is quickly extracted from the medium, however, and amplification of the trailing edge of the pulse is terminated. The increasing gain on the rising edge of the pulse combined with depletion (gain saturation) on the trailing edge effectively minimizes the pulse duration [60]. The steady state pulse width is limited by the dispersive forces found in the dye cavity [21] and by the available frequency bandwidth. The bandwidth permitted with the 3-plate birefringent tuning element used in our dye laser accommodates pulse widths down to ~5ps.

The cavity dumper is employed solely to lower the repetition rate of the dye laser output. The reduced rate, in principle, permits studies involving decays which are longer than the ~10 ns period of the synchronously pumped dye laser. In addition, TAC linearity appears to be significantly improved when the TAC STOP pulse repetition rate is reduced to 5 MHz or lower. These advantages favor cavity dumped systems in spite of the loss of average power.

All mirrors in the cavity dumped dye laser are ~100% reflective; output is accomplished via diffraction from an intracavity AOM (Harris Model H-106) positioned at a beam waist and oriented at Brewster's angle. This AOM is driven by a pulsed rf source whose carrier frequency is locked to a multiple (8x) of the mode-locker frequency (Harris Model H-102). The rf pulse is timed via an electronic delay to provide coincidence between the pulsed acoustic wave and the intracavity light pulse. The transient index modulation diffracts ("dumps") a portion of the intracavity pulse for external use. The cavity dumper repetition rate is selectable, but the maximum dump rate (every 20 light pulses) is generally used. Unfortunately, the rejection of adjacent pulses is rather poor for this system; intensities may be as large as a few percent of the main pulse. Hence, our TCSPC studies have been confined to a 10 ns (the periodicity of intracavity pulses) window. This limitation disappears when second harmonic generation (SHG) is employed to frequency double the excitation source. This is due to the power dependence of the SHG conversion efficiency (proportional to peak power squared [61]) which serves to further suppress the relative intensities of adjacent pulses.

Mode-locker

The quality of picosecond pulses generated with synchronously-pumped cavity dumped dye lasers depends critically on the mode-locked pump laser stability. The key elements affecting the pump stability are the rf drive and the acousto-optic modulator (AOM). Fleming [60] reported that the rf frequency stability must be better than one part per million to achieve pulse widths as short as 5 ps. This stability is readily achieved with crystal oscillators or frequency synthesizers. Klann et al. [62] demonstrated that optimum mode-locking often requires rf power on the order of 1 watt. Maintenance of resonant AOM operation at such power levels is problematic, however, due to the temperature dependence of the acoustic resonance. The thermal load placed on the AOM leads to temperature variations large enough to make resonant operation elusive. This fact is readily understood. The fraction of rf power delivered to the modulator as acoustic energy is frequency dependent; the fraction is maximized when the drive frequency is precisely tuned to an acoustic resonance. When operating on resonance, however, any temperature fluctuation which cools the modulator also shifts the acoustic resonance away from the drive frequency; less rf power is coupled into the modulator and the cooling trend is perpetuated. As a consequence of the positive thermal feedback, stable mode-locker operation cannot be achieved on an acoustic

resonance. Stable operation may be attained by tuning the rf drive frequency slightly below the acoustic resonance where negative thermal feedback obtains. This may compromise the mode-locking quality, however.

An elegant solution to this problem was first reported by Klann et al. [62] where active feedback was used to stabilize resonant mode-locker operation. A schematic of their circuit is presented in Fig. 2.2 The amplified rf is routed through a bidirectional coupler to the acousto-optic modulator whereupon a fraction of the incident power is reflected. The magnitude and phase of the reflected rf is dependent on the location of the acoustic resonance relative to the drive frequency (the reflected power is minimized and the phase passes through zero at resonance). The incident and reflected rf are sampled via the bidirectional coupler and fed into a phase detector where a dc voltage proportional to the phase error is generated. The amplified error signal modulates the nominal rf power (and hence, the AOM temperature) in order to minimize the phase error. As a consequence, the acoustic resonance is actively pulled into alignment with the drive rf and resonant operation is achieved.

Our mode-locker driver (Harris Corp. H-102) was rebuilt to enable active stabilization of the mode-locker acoustic resonance. The basic H-102 unit already provided three of the functions outlined in Fig. 2.2: frequency synthesis

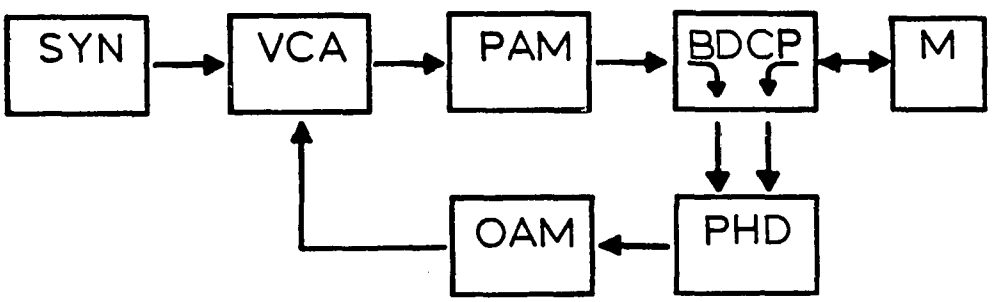

Fig. 2.2 Schematic of the mode-locker active stabilization system [62]. SYN, rf synthesizer; VCA, voltage controlled attenuator; PAM, power amplifier; BDCP, bidirectional coupler; M, mode-locker; PHD, phase detector; OAM, operational amplifier

(SYN), voltage controlled attenuation (VCA), and power amplification (PAM). Implementation of active stabilization simply required three additional components: a bidirectional coupler (BDCP), a phase detector (PHD), and two operational amplifiers (OAM).

The active stabilization circuit used in our mode-locker driver is depicted in Fig. 2.3. A portion (-10 dB) of the incident and reflected rf is sampled via a 10 dB bidirectional coupler (Merrimac #BC-10-50) and routed through impedance matched (50Ω) attenuators to the local oscillator (LO) and radio frequency (RF) inputs of the phase detector (Mini-Circuits #RDP-1), respectively. The pi resistor networks reduce the signals to an appropriate level (~7 dBm) before processing with the phase detector; their design provides 12.3 dB and 9.5 dB attenuation for the incident and reflected signals, respectively [63]. Concomitant with a phase dependent dc voltage at the IF port is an undesired ac component at twice the input frequency. The low pass RC filter effectively terminates the sum frequency into 50 Ω. The remaining dc component is proportional to the phase difference between the LO and RF inputs. The measured phase can differ from the true phase at the AOM input, however, due to unequal propogation delays for the incident and reflected signals. Consequently, the delay loop in the path of the sampled incident of signal must be adjusted to meet two criteria: the measured phase

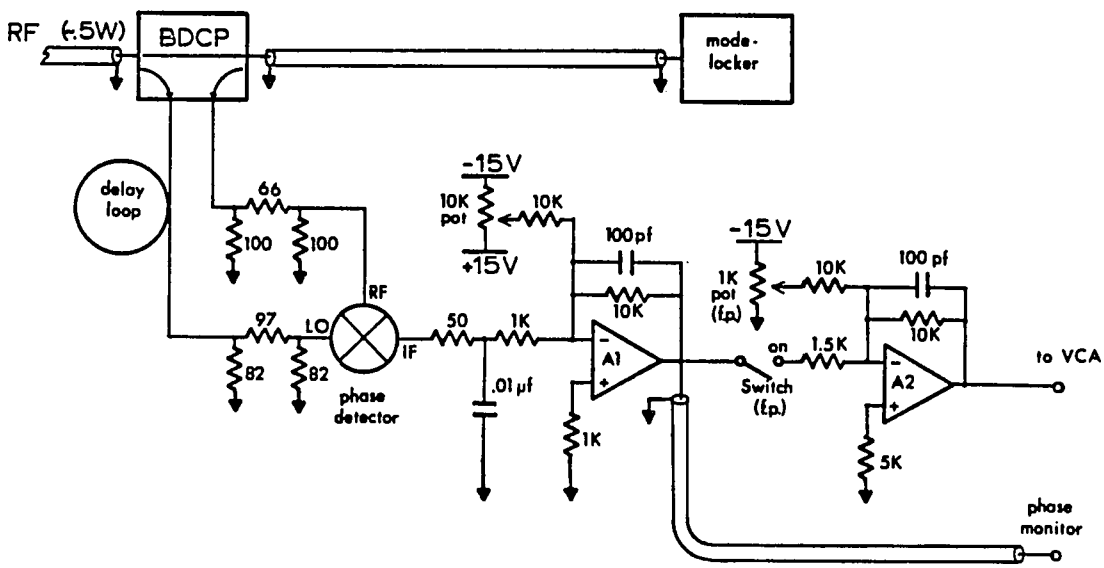

Fig. 2.3 Active stabilization circuit used in the H-102 mode-locker driver. BDCP, bidirectional coupler; LO, local oscillator input; RF, radio frequency input; IF, intermediate frequency output; VCA, voltage controlled amplifier; f.p., front panel

should be zero on resonance, and the slope of the phase near resonance must have the correct sign to provide negative feedback. Since the propogation delay in a coaxial cable is about 1.5 ns/ft, 48 MHz operation could require a delay loop as long as ~7 ft (this length would shift the phase by ~180 degrees). Instead of fabricating a delay cable to the exact dimension required, a close match was found (~2 ft for our system) and the resulting offset voltage was nulled via summing amplifier A1. This adjustment was made while operating on resonance as determined by monitoring the reflected rf power through a rear panel BNC connector (not shown in Fig. 2.3). The ten-fold gain (inverting) of A1 provides a phase calibration of ~10°/volt which is monitored via a rear panel BNC connector. In the original design, the front panel rf power potentiometer (1K pot) developed a control voltage which was routed directly to the VCA. For this circuit, the control voltage is first passed through the summing amplifier A2 (the polarity of the potentiometer supply voltage is reversed since A2 is configured as an inverting amplifier). The phase error from A1 is amplified further by A2 to provide ~1 db/degree rf power gain [62] (due to the nonlinear response of the VCA, this gain obtains only when the nominal rf power is ~.5 W). When the front panel automatic stabilization switch is closed (on), the amplified phase error sums with the front panel rf power setting to actively adjust the rf power and pull the

acoustic resonance into alignment with the drive rf. The operational amplifiers A1 and A2 (National Semiconductor LF-356) are equipped with feedback capacitors to limit their frequency bandwidth to ~150 kHz and thereby prevent high frequency oscillation.

The mode-locking AOM is housed in a temperature stabilized oven to minimize drift in the acoustic resonance due to environmental temperature fluctuations. Consequently, the actual frequency for an acoustic resonance depends not only on the selected rf power, but also on the oven temperature setting. The appropriate drive frequency for a given rf power and oven temperature is found by slowly raising the drive rf toward the acoustic resonance (starting from ~20-40 kHz below) until the phase monitor registers zero volts. Resonant operation is achieved and no further adjustment is necessary. If the automatic stabilization is disabled (switch opened), resonant operation will be lost within a few seconds.

Frequency synthesis in the H-102 is accomplished via several phase-locked loops. This method of frequency generation is inferior to direct synthesis schemes or simple crystal controlled oscillators because the phase-locked loop (PLL) introduces phase noise to the rf signal. While the PLL derived average frequency is precisely maintained (relative to a crystal controlled reference) fluctuations in the instantaneous frequency cannot be wholly eliminated.

The resulting phase noise may compromise the mode-locking quality. After failing for the second time in as many years, the frequency synthesis portion of the H-102 was shut down and replaced with a crystal controlled oscillator. The oscillator board was based on the Ames Laboratory Instrumentation Group design #ALE 1978 (see Fig. 2.4). The transistor is powered from a zener regulated +12 V supply. The crystal was custom manufactured to provide a resonance at 48.07 MHz (Oklahoma Crystal Manufacturing, Oklahoma City, OK). The variable capacitor C_3 tunes the oscillator to obtain maximum rf power while minimizing the harmonic content of the sine wave. The rf signal is tapped between L1 and L2 and routed through a series resonant circuit (L3C5) which is tuned to pass the fundamental. This signal is finally attenuated in an impedance matched T pad to a level compatible with the rf input of the H-102 (~.5 V_{p-p} into 50 Ω).

While resonant operation can be achieved at any rf power level/oven temperature combination by selecting an appropriate drive frequency, fixed frequency operation at a given power level requires temperature tuning of the AOM. To achieve resonant operation under fixed frequency control, the rf power and the oven temperature are adjusted for maximum output with the automatic stabilization circuit disabled. The phase error can be seen to vary as temperature rises. A rapid phase reversal is observed,

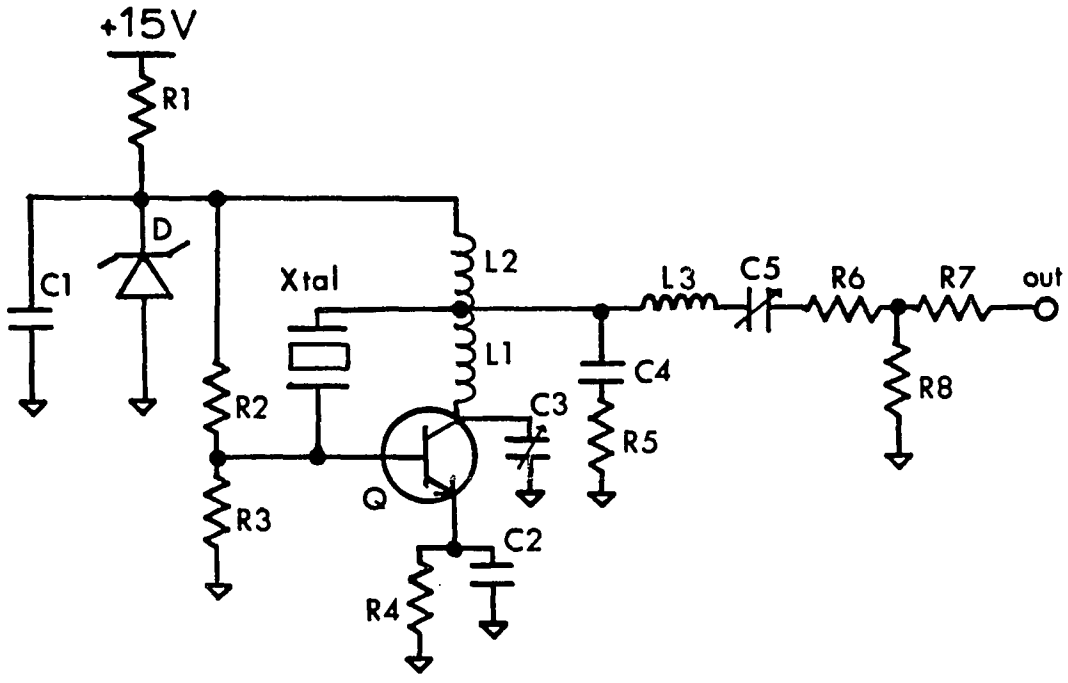

R1 = 150	R6, R7 = 18
R2 = 4.7K	R8 = 62
R3 = 1 K	C1 = .1
R4 = 330	C2, C4 = .01
R5 = 47	C3, C5 = 10→100 pf

L1 = 15 turns of #24 wire on a 1/4" round
L2 = 20 turns of #24 wire on a 1/4" round
L1 = 12 turns of #24 wire on a 1/4" round

Fig. 2.4 Crystal controlled oscillator circuit. Resistance and capacitance values are in ohms and microfarads, respectively, unless otherwise stated. D, 12V zener diode (1N963B); Q, transistor (2N3643); Xtal, 48.07 MHz crystal

however, when the acoustic resonance passes through the drive frequency. After this state is achieved, the oven temperature and rf power settings may be returned to normal and the feedback circuit enabled. Once the AOM temperature has stabilized, the oven temperature can be fine tuned to null the phase error.

Since the AOM is temperature tuned over a limited range, it is important to select an appropriate crystal frequency for a given rf power setting. To facilitate the selection, the H-102 was modified to readily accommodate an external variable frequency source. This was achieved by equipping the rear panel of the H-102 with a rf input BNC connector. (A second BNC connector, rf output, was connected to the internal fixed frequency oscillator; internal frequency control is attained by interconnecting the rf input and rf output with an external coaxial cable.) Frequency control was temporarily taken over by a frequency synthesizer (Programmed Test Sources 160). With the oven temperature set for normal operation and the rf power set to .5 W, the optimum frequency was found to be ~48.07 MHz. (Note that the front panel rf power calibration applies when using sources with the same signal power level as the internal oscillator.) A commercially obtained 48.07 MHz crystal was installed in the oscillator circuit of Fig. 2.4. After optimization, the actual operating frequency is 48.078656 MHz, and the long term stability is ~$\pm$2 Hz.

Autocorrelator

A synchronously pumped cavity dumped dye laser is capable of generating a train of short duration (<10 ps) with excellent pulse-to-pulse reproducibility. This performance, however, depends critically on the laser alignment. May et al. [64] reported that a dye laser cavity which is too long (relative to the pump laser) generates broadened pulses with substructure. Dye pulses from a cavity which is too short not only exhibit structure but are also accompanied by a secondary pulse. Clearly, dye laser optimization could be greatly facilitated by monitoring the output pulses.

The electrical bandwidth demanded by picosecond pulse measurements outstrips even the fastest photodetectors and sampling oscilloscopes. Time resolution down to ~1 ps can be achieved, however, with a synchroscan streak camera [64] but such exotic technologies are found in few laboratories. Alternatively, the autocorrelation technique using second harmonic generation (SHG) provides an indirect yet effective method for monitoring the pulsed output.

The second harmonic is generated by combining replica light pulses from each arm of a Michelson interferometer in a nonlinear crystal. The nonlinear electro-optical properties of the medium can be used to convert a portion of the combined fundamental laser light to the second harmonic provided the crystal is oriented such that the phase

matching condition obtains. Two experimental geometries may be used to provide "zero background" SHG (i.e., the SHG intensity is zero where there is no temporal overlap) [21, chapter 3]. Type II doubling utilizes orthogonally polarized light pulses which are collinearly focussed into the nonlinear medium; SHG is generated only when the two pulses overlap temporally. In type I doubling, two similarly polarized light beams are combined in a noncollinear geometry; SHG resulting from temporal overlap travels along their bisector (Fig. 2.5). In either case, the SHG intensity is measured as a function of optical delay to obtain the second order autocorrelation of the light pulse with sub-picosecond time resolution. The zero background type I scheme is most popular among CW mode-locked laser users.

The variable optical delay depicted in Fig. 2.5 may be achieved with a motor driven translation stage. The time necessary to complete a single scan, however, makes dye laser optimization a laborious process. A "real time" monitor of the laser pulses can be attained by replacing the translation stage with a rapidly varying optical delay, and by viewing the SHG intensity (PMT current) on an oscilloscope display. This greatly simplifies dye laser alignment and optimization.

Rapidly varying optical delays have been constructed using three different approaches. They include a sine

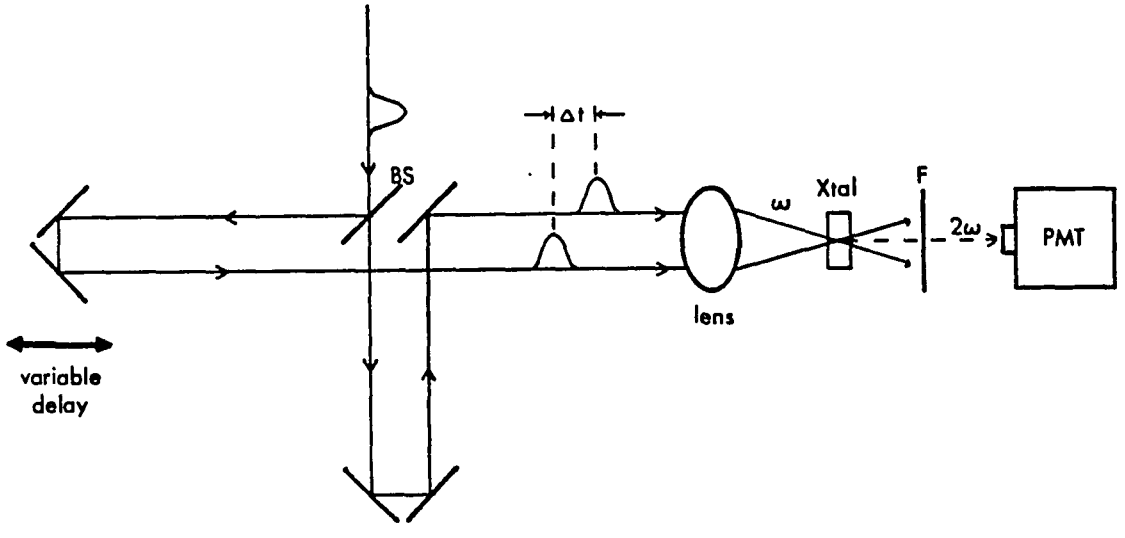

Fig. 2.5 Interferometer for "zero background" type I SHG. BS, beam splitter; Xtal, nonlinear crystal; ω, fundamental frequency; 2 ω, second harmonic frequency; F, UV-transmitting filter; PMT, photomultiplier tube

driven audio speaker (with an attached retro-reflector) [65], a rotating rooftop prism [66], and a rotating pair of mirrors [67].

We constructed a real time autocorrelator using the scheme of Yasa and Amer [67]. The rotating pair of mirrors is illustrated in Fig. 2.6. A light beam that is intercepted by both mirrors in the rotator experiences an optical delay which is determined by the rotation angle θ. Yasa and Amer showed that for small θ, the optical path difference Δl as a function of the rotation angle is

$$\Delta l(\theta) \simeq 4R\theta \tag{2.4}$$

where R is the radius of rotation (Fig. 2.6). The optical delay range $\Delta\tau$ and the scan nonlinearity NL (over the entire range) are approximated by

$$\Delta\tau \simeq \sqrt{2}\, d/c \tag{2.5}$$

and

$$NL \simeq d/(8R), \tag{2.6}$$

respectively, where d is the mirror diameter, and c is the speed of light. Finally, the time calibration (optical delay/time interval) is given by

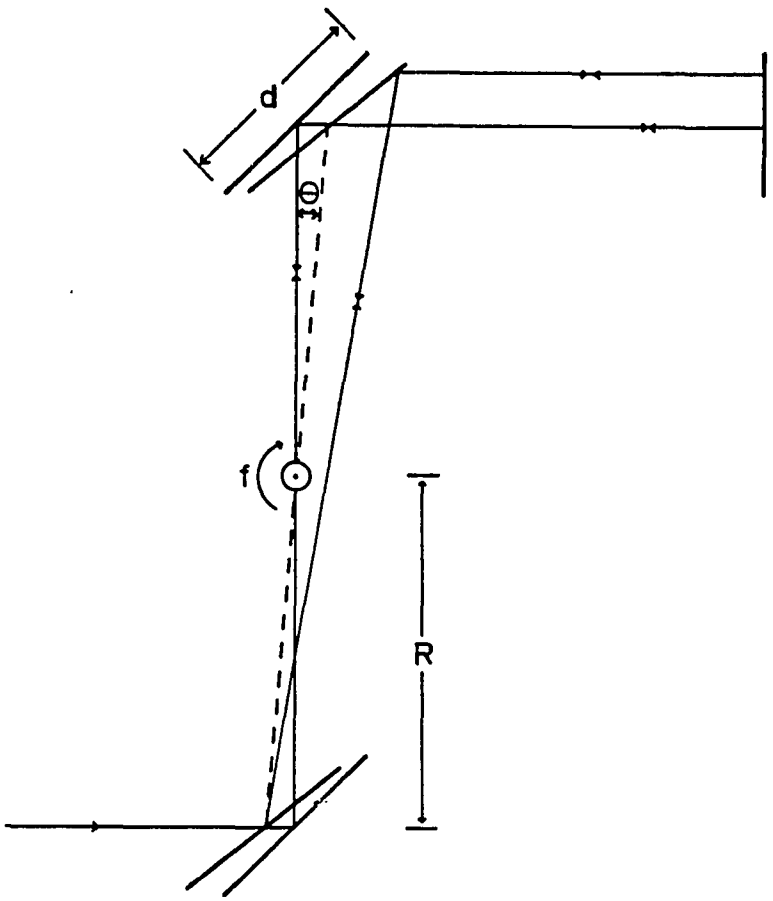

Fig. 2.6 Rotator geometry used by Yasa and Amer [67]. The dashed line connects the mirrors after rotation by θ degrees (the mirrors are oriented at 45 degrees relative to the rotator arm). f, rotational frequency; d, mirror length; R, radius of rotation

$$(\Delta\tau/\Delta t) = 8\pi Rf/c \qquad (2.7)$$

where f is the rotational frequency.

Many so-called "real time" autocorrelators actually operate below ~25 Hz (the experimental setup of Yasa and Amer operated a 5 Hz). The oscilloscope sweep at such frequencies is discontinuous. This compromise is often made in order to enhance the scan range, and/or linearity by increasing the mirror and/or rotor dimensions (Eqs. 2.5, 2.6). It may be impractical (motor size) or even dangerous to operate a large rotator at higher frequencies.

Our autocorrelator is driven by a 30 Hz synchronous AC motor (TRW Glove #138A2014). In addition to providing a flicker free real time display, this rotational frequency enables line trigger synchronization of the oscilloscope sweep. (An appropriately positioned photodiode is often used to trigger the oscilloscope sweep [67].) The rotator was designed to accommodate 1/2" round by 1/4" thick mirrors. A time calibration of 50 ps (optical delay)/ms (time interval) was achieved by making R = 1.988 cm (Eq. 2.7). These dimensions provide a maximum scan range of ~60 ps (Eq. 2.5) and a scan nonlinearity of <8% (Eq. 2.6). This scan range is more than adequate for viewing the mode-locked dye laser output whose pulse autocorrelation width is typically <15 ps FWHM. Since the magnitude of the nonlinearity is scan range dependent, the FWHM estimates are

generally accurate to better than 8%. The rotor was machined from a single piece of aluminum to tolerances normally achieved with a quality mill and lathe. The design parameters including the mirror parallelicity are not particularly critical. Care must be taken, however, in mounting the mirrors to the rotor; distortion due to mounting stress will compromise the pulse autocorrelation measurement.

In contrast to other rotation mirror layouts, we replaced the stationary mirror in Fig. 2.6 with a pair of orthogonally positioned mirrors. Hence, the returning ray is displaced (into the page of Fig. 2.6), and can be reflected toward the nonlinear medium without additional losses. The alternative is to sample the variably delayed light beam from the beam splitter. The extra loss at the beam splitter reduces the autocorrelator sensitivity by about a factor of two.

Alignment of the autocorrelator is relatively simple. The reflector in the static arm of the interferometer (Fig. 2.5) is positioned so that the optical delays in the two arms are similar (within $\pm$.5 cm). The two light beams must be made parallel prior to focussing to insure spatial overlap at the focus; redirecting the beams to a distant plane facilitates this adjustment. When the variable delay is set in motion, one is assured of spatial and temporal (modulated) overlap at the focus. The nonlinear crystal

(typically KDP or $LiIO_3$) is housed in a gimbal mount which is located at the lens focus. The phase matching condition for SHG is found by rotating the crystal about the laboratory Z-axis with the oscilloscope set to auto-trigger. When a pulse is observed (SHG is detected with the PMT), the oscilloscope can be set back to line trigger. It may be necessary to adjust the trigger slope and level to position the pulse and the center of the oscilloscope sweep. If the pulse is not near the center of the autocorrelator scan range, either stationary mirror may be moved. After optimization of the crystal orientation, the autocorrelator is ready for use.

The time resolution of the autocorrelator can easily be compromised by the electrical portion of the autocorrelator. This fact is presently explained. A coaxial cable contributes ~30 pf/foot of capacitance to the oscilloscope input. The scope rise time (10-90%) is then related to the cable length (connecting the PMT and oscilloscope) by

$$t_r \sim (.35)\ 2\pi R_{in}\ (C_{in} + 30 \times 10^{-12} X) \qquad (2.8)$$

where R_{in} and C_{in} are the scope input resistance and capacitance, respectively, and X is the cable length in feet. The factor .35 arises from the 10-90% rise time - bandwidth product [63, p. 455]. A ten foot cable connecting the PMT to a typical oscilloscope (R_{in} = 1 MΩ, and C_{in} = 20

pf) yields τ_r ~ 700 μs. Given our time calibration of 50 ps (optical delay)/ms (time interval), this cable length limits the effective optical pulse rise time to ~35 ps. Since t_r is proportional to R_{in}, this situation can be remedied by terminating the scope input with a resistor much smaller than R_{in}. (One must be mindful of the sensitivity limitations when the terminating resistor is too small, i.e., V = iR.) The 20 KΩ termination resistor used in our apparatus provides subpicosecond time resolution while retaining adequate sensitivity for real time optimization of our synchronously pumped dumped dye laser.

The instrument response function for TCSPC experiments was found to be somewhat insensitive to the dye laser cavity length provided the cavity was slightly long. The base of the instrument response function was noticeably affected, however, when the cavity length was too short because a secondary dye pulse appears. Hence, the dye laser is routinely operated with the cavity slightly long (as determined via the real time autocorrelator) so that environmental changes have little effect on the instrument response function.

Optics

The cavity dumped output (~10 mW at 570 nm, 5 MHz) is routed through a beamsplitter where ~80% of the intensity is extracted to be shared between the real time autocorrelator

and the timing reference photodiode. The remaining ~20% is directed toward the sample which is housed within a black enclosure (~2 ft in each dimension) equipped with entrance and exit baffle tubes. The polarization of the incoming light is purified with a "clean up" polarizer (Oriel 2730) aligned parallel to the sample plane (Fig. 2.7). The "clean up" polarizer mount was constructed to facilitate continuous and discreet (90 degree) rotation. Polarizer alignment is achieved by minimizing the Brewster reflection from a fused silica substrate positioned in lieu of the sample. The discreet settings allow accurate exchange between the two orthogonal polarizations. (The vertically polarized dye laser output is rotated ~45° via a quarter wave plate to enable selection of either polarization without loss of intensity.) When focussing is desired, the lens is positioned in front of the "clean up" polarizer to avert scrambling of the polarization state from residual birefringence in the focussing lens [68].

The sample emission is collected along the laboratory Z-axis (normal to the sample plane, see Fig. 2.7); it is successively transmitted through an analyzer polarizer (Promaster Spectrum 7) and sharp cut absorption filters (Schott OG-590 and/or RG-610) prior to collimation with a 5 or 10 cm focal length fused silica lens. The collected emission is focussed through a home-built variable rectangular aperture before impinging upon the photocathode

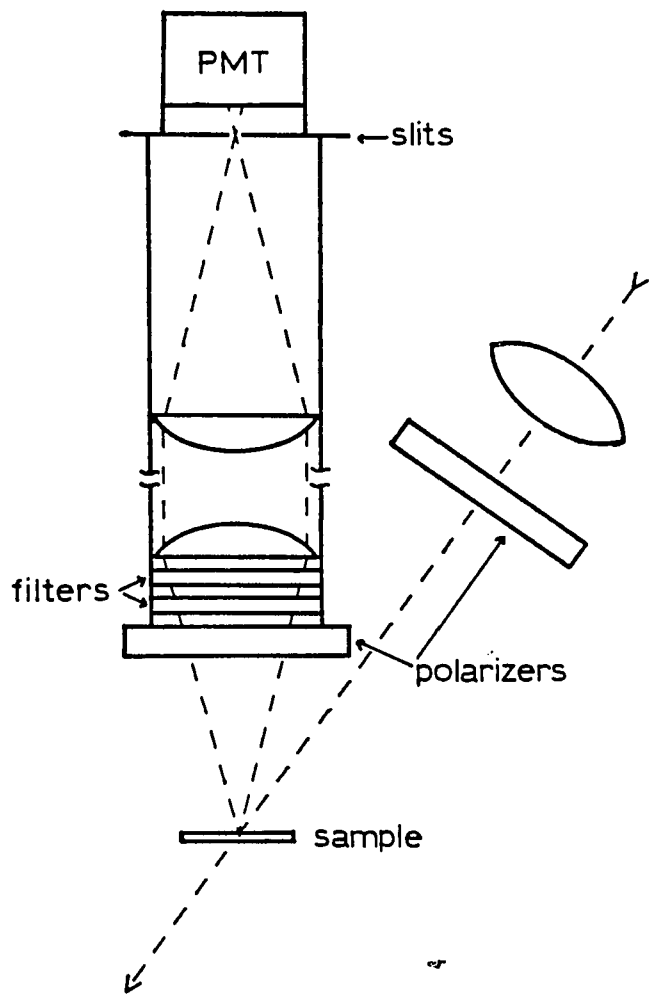

Fig. 2.7 Optical arrangement for collection of sample emission

of the PMT. Like the "clean up" polarizer mount, the analyzer polarizer could be set at discreet settings including 0, 45, 54.7, and 90 degrees. Alignment with respect to the incident polarization is achieved by seeking a null in the transmitted intensity from a surface reflection. Selection of parallel, perpendicular, and magic angle (54.7 degrees in isotropic systems or 45 degrees for 2-dimensional systems with dipoles oriented along cones) settings is therefore accurately achieved. To attain the level of precision available with TCSPC, it is necessary to effectively eliminate emission from sources other than the sample. When 570 nm excitation is used, two RG-590 sharp cut filters (3 mm each) are sufficient to completely absorb the scattered fundamental. Since these filters function by absorption (interference filters operate by reflection) filter fluorescence may occur. The spatial discrimination achieved by the rectangular slits (when the filter is placed near the collimating lens) minimizes this contribution to the detected intensity. Raman shifted light, however, is difficult to filter; this instrument response limited emission component may be subtracted experimentally, or digitally by incorporation in the fitting model. One last source arises from spontaneous emission from the dye laser; it can be observed as the portion of the laser output (tuned to 570 nm) which is transmitted through two OG-590 filters. The time resolved scattered spontaneous emission reveals the

population density in the dye jet. This complication is eliminated by dispersing the laser beam with a prism placed near the output; a circular aperture positioned near the sample rejects the spectrally broad spontaneous emission.

Competition from emission sources other than sample fluorescence were usually evident only when the full laser intensity was used; excitation transport studies were typically executed with the laser beam attenuated by one to two orders of magnitude.

Electronics

Photodetectors

A stable timing reference for time-to-amplitude conversion is commonly derived from a fast photodiode which samples a portion of the pulsed laser output [69]. The appropriate logic for the timing reference is generated via a threshold or constant fraction discriminator. Very fast photodiodes are demanded of threshold discrimination since amplitude fluctuations in the laser intensity appear as jitter in the timing reference. Timing jitter down to ~5-10 ps may require photo-response rise times of <100 ps depending on dye laser stability. Satisfactory performance can also be achieved from a fast photodiode (~1 ns rise time) coupled to a constant fraction discriminator. The constant fraction circuitry generates a timing pulse at a

point corresponding to a given fraction of the peak amplitude. Hence, the timing signal is in principle independent of pulse amplitude and low jitter discrimination is achieved.

Our apparatus utilizes an EG&G FOD-100 photodiode (~1 ns rise time) which is coupled to one channel of a quad constant fraction discriminator. Besides economy, the FOD-100 offers a large active area (~4 mm^2); the excitation source may be monitered without focussing.

The time resolution achievable in TCSPC is currently limited by PMT technology. Conventional PMTs optimized for timing applications (e.g., Philips XP2020Q) can provide time resolution down to ~235 ps (instrument response FWHM) [70]. The microchannel plate photomultiplier (MCP-PMT), while quite expensive ($\gtrsim$8 K), improves the time resolution to ~47 ps [15, 70].

The most important contribution to timing jitter in TCSPC is from the PMT transit time spread, i.e., the distribution of observed delay times between ejection of a photoelectron and the appearance of an electrical pulse at the PMT anode. The major contribution to the transit time spread apparently arises from the distribution of normal component velocities (in the direction of the first dynode) of the ejected photoelectrons. (Since the initial photoelectron energy is wavelength dependent, one would also expect a wavelength dependence for the transit time and the

transit time jitter.) Bebelaar [70] proposed that the dispersion in the transit time (Δt) is related to variations in the normal component of the initial photoelectron velocity Δv_n by

$$\Delta t = -m\ \Delta v_n / eE \qquad (2.9)$$

where m and e are the electron mass and charge, respectively, and E is the strength of the accelerating electric field (between the photo cathode and first dynode). Hence, high field strengths between the photocathode and first dynode are required in order to minimize the transit time jitter and the phototube wavelength dependence. (The wavelength dependence of the timing characteristics is particularly problematic when the observed emission is spectrally broad; convolute-and-compare analyses cannot be accurately conducted since the instrument response function is measured at a single wavelength.)

The XP2020Q, a 12-stage PMT, is commonly used for timing applications. It provides a current gain of ~2×10^6 - 3×10^7, a transit time of ~25 - 31 ns, and a pulse rise time of ~1.5 - 1.7 ns (these parameters depend on the voltage divider network and the operating voltage) [71]. The construction includes an accelerating grid located between the photocathode and the first dynode which enhances the electric field strength E by a factor of ~4.2 over

otherwise identical PMTs [70], thereby improving the timing characteristics. While our earliest experimental work utilized an XP2020Q PMT, we soon replaced it with a MCP-PMT.

The MCP-PMT is constructed (Fig. 2.8) from a bundle of glass capillaries whose inner walls are coated with a secondary electron emissive material [72]. The capillary diameter and length are typically ~10 μm and less than 1 mm respectively. When a primary electron strikes the channel wall with sufficient kinetic energy, secondary electrons are produced. An electric field accelerates the secondary electrons (Fig. 2.8) along parabolic trajectories (determined by their initial velocities) until they again impact the channel wall thereby providing additional secondary electrons. Hence, each capillary acts as an independent electron multiplier which is capable of generating up to 10^4 current gain with 1 kV applied voltage [72]. When additional gain is required, two MCPs can be stacked together.

The temporal characteristics of a two-stage PMT are impressive. We use a Hamamatsu Model R1564U whose transit time is only ~550 ps, and the pulse rise time is merely ~220 ps [73]. Moreover, the close proximity of the photocathode and the entrance channels (~3 mm, [72]) facilitates electric field strengths ~21 times greater than the accelerating potential of the XP2020Q [70]. As a result, the transit time spread and the wavelength

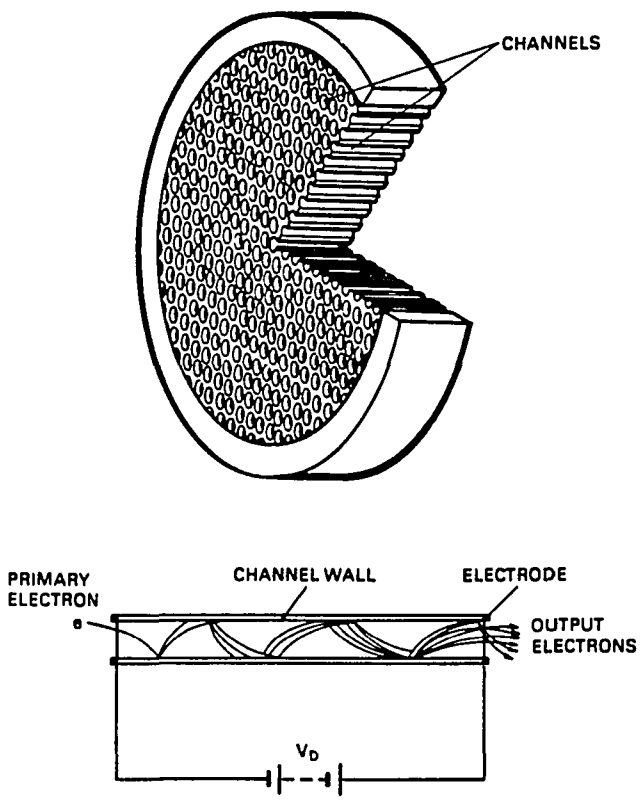

Fig. 2.8 MCP-PMT construction and attendant operation

dependence are significantly reduced.

The current gain achieved in a two-stage MCP ($\sim 5 \times 10^5$) is not sufficient for effective single photon counting applications. A three-stage MCP could be employed but this compromises the transit time spread. Instead, the two-stage MCP-PMT anode pulse is routed through an amplifier ($\gtrsim$20 dB gain) prior to processing with a constant fraction discriminator. The amplifier selection must be approached judiciously, however, due to the temporal characteristics of the MCP-PMT anode pulse and due to the nature of the signal source.

A rise time (t_r) of 200 ps (10-90%) requires a -3 dB bandwidth (Bw) of ~1.75 GHz ($Bw_{-3\ dB} \sim .35/t_r$, [63, p. 455]). Amplifiers with smaller bandwidths yield pulse broadening which may compromise the time resolution in TCSPC. On the other hand, amplifiers possessing a significantly broader bandwidth might introduce noise on the rising edge of the anode pulse; timing jitter in the constant fraction discriminator may result. In principle, amplification of the MCP-PMT anode pulse requires a frequency bandwidth of DC→2 GHz. The 1/f noise at lower frequencies, however, leads to false triggering of the constant fraction discriminator. This difficulty is avoided by utilizing an ac-coupled amplifier whose low end frequency response is around 10→100 kHz. This compromise is of no consequence provided the time between anode pulses is long compared to

the pulse width (generally true when operating TCSPC apparatus in the low light level limit).

The output of the PMT appears to be a light intensity controlled current source. This fact is often overlooked when amplifying the output of a MCP-PMT with an ac-coupled amplifier. The ac-coupled input provides no direct pathway for current to be dissipated to ground potential. As a consequence, the PMT current builds up a charge at the input; if this charge cannot be dissipated through a parasitic resistance, the resulting bias voltage may continue to build until the amplifier blows. (Many Hewlett-Packard 8447D amplifiers (26 dB, .1 MHz - 1.3 GHz) have been sacrificed in this fashion.) This problem is readily averted by supplying the PMT output with a terminating resistor ($50\Omega << R < 1M\Omega$).

Our TCSPC apparatus employs a 10 kHZ→3.15 GHz 21 dB gain inverting amplifier (B&H Electronics Co., Model AC 3011) which is equipped with a 10 kΩ input terminating resistor and input protection circuitry. (A BNC to SMA adapter allows direct connection between the MCP-PMT output and amplifier input.) The amplifier must not be driven into saturation (gain compression) or the pulse shape will be modified; effective constant fraction discrimination is dependent on pulse shape uniformity. The power output at 1 dB gain compression for our amplifier occurs at +4 dBm,

corresponding to a pulse response of ~.5 V. With the MCP-PMT operated at 3 kV, the amplified output is well below .5 V.

Constant fraction discriminator

The time resolution in TCSPC is ultimately limited by the PMT transit time spread. This lower limit is only approximately achieved due to other sources of timing jitter. The extent to which these additional sources can compromise the time resolution is evident by contrasting the reported TCSPC instrument response function FWHM for the same MCP-PMT (Hamamatsu Model R1564U) in different laboratories: 43 ps [74], 47 ps [15, 70], and 60 ps [69]. The major contribution to the timing jitter (beyond transit time dispersion) arises from discrimination of the PMT output pulses; it is difficult to generate a timing signal which correlates precisely with the arrival of the PMT anode pulse when the pulse to pulse amplitude fluctuates over a broad dynamic range. While this difficulty was overcome, in principle, with the advent of the constant fraction discriminator (CFD), successful application of the CFD method to short duration pulses from the MCP-PMT requires special attention.

As the name implies, a constant fraction discriminator develops a timing signal at a point on the leading edge which corresponds to a fixed fraction of the pulse

amplitude. This timing point is independent of pulse height provided the pulse shape is an amplitude invariant. The operating principle for constant fraction timing is revealed in Fig. 2.9. The input pulse is first split into two portions. The larger of the two is delayed, inverted, then summed with the smaller portion to generate a bipolar signal. The CFD timing pulse is generated at the zero crossing of the bipolar signal which occurs at a point corresponding to a fixed fraction of the delayed pulse amplitude.

The CFD circuitry itself contributes to the timing jitter when the slope of the bipolar signal at the zero crossing is not large relative to the noise on the input of the zero crossing detector. Hence, it is important to find the fraction f (f is the ratio of undelayed to delayed pulse amplitude) and delay t_d which maximize the slope at the zero crossing. Clearly, optimum constant fraction discrimination of a Gaussian pulse obtains when $f \approx 1$ (identical pulse amplitudes) and when t_d equals the pulse FWHM. The PMT output, however, is asymmetric (the rise and fall times for our MCP-PMT are 206 and 688 ps, respectively). Optimum performance in this case generally requires a fraction $f < 1$ and a delay $t_d <$ FWHM (pulse).

The analysis leading to optimized f and t_d for asymmetric pulses is greatly simplified by assuming that the zero crossing occurs at the peak of the undelayed pulse

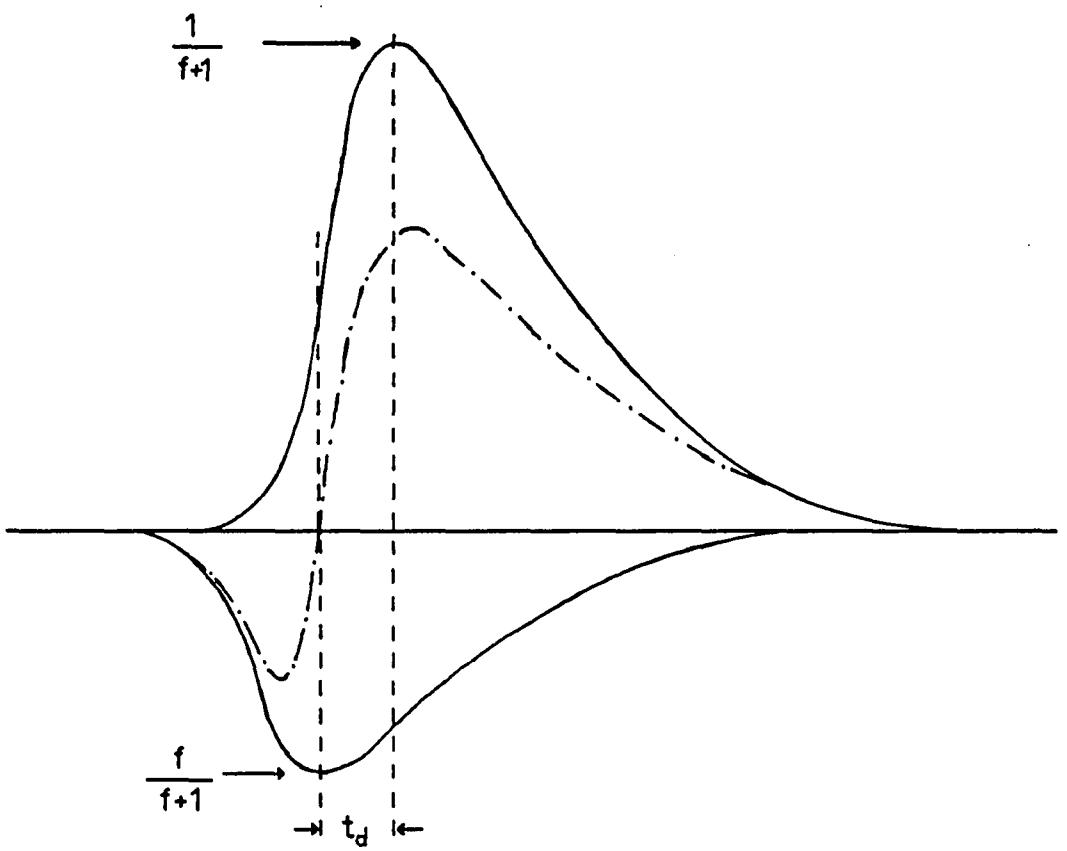

Fig. 2.9 Synthesis of a bipolar signal for constant fraction discrimination

(this restriction is of no consequence when the rise time is much faster than the fall time). Under this assumption, the slope at the zero crossing is determined solely by the delayed pulse. Moreover, the zero crossing occurs when the delayed pulse attains fraction f of its height. If the rising edge of the delayed pulse is modeled wih a Gaussian,

$$g = \exp[-1.42(t/t_r)^2] \tag{2.10}$$

where t_r is the pulse rise time (10-90%), the slope of the delayed pulse (within a scale factor) becomes

$$\frac{dg}{dt} = \frac{2.84t}{t_r^2} \exp[-1.42(\frac{t}{t_r})^2]$$

$$= \frac{2.84}{t_r} \sqrt{\frac{-\ln g}{1.42}}\ g \tag{2.11}$$

where Eq. 2.10 was used twice. Since g = f at the zero crossing, the properly scaled slope becomes

$$\left[\frac{1}{1+f}\right] \left.\frac{dg}{dt}\right|_{\substack{\text{zero-}\\ \text{crossing}}} = \left[\frac{1}{1+1/f}\right] \frac{2.84}{t_r} \sqrt{\frac{-\ln f}{1.42}} \tag{2.12}$$

where the factor (1/(1+f)) is the amplitude of the delayed pulse. Eq. 2.12 is maximized when f = .478. The appropriate delay as a function of f is found by modeling the bipolar signal bp with

$$bp = \left[\frac{1}{1+f}\right] \exp\left[-1.42\left(\frac{t-t_d}{t_r}\right)^2\right] - \left[\frac{f}{1+f}\right] \exp\left[-1.42\left(\frac{t}{t_r}\right)^2\right].$$

The bipolar signal is zero when t = 0 (the peak of the undelayed pulse) so

$$t_d = t \sqrt{\frac{-1nf}{1.42}} \quad ; \tag{2.14}$$

when f = .478, t_d = .72 t_r. When selecting a delay for discrimination at a particular fraction f, it may be wise to choose a delay cable sightly longer than t_d; the slope at the zero crossing is compromised when t_d is too short.

Commercially available CFDs are usually equipped to discriminate at f = 0.2. At best, optional modules can be obtained which enable discrimination at f = 0.1 or 0.3 [75]. The slope at the zero crossing with f = 0.478, however, is ~30% greater than the slope achieved when f = 0.2. Consequently, we modified our CFD (Tennelec TC 455) to accomodate f = 0.5. This was accomplished by changing two resistors in the fraction select module; the 10 and 250Ω resistors of an f = 0.2 module were replaced with 25 and 100Ω resistors, respectively.

The CFD contribution to timing jitter due to noise on the input of the zero crossing detector was evaluated. An external frequency generator was used to drive one channel of the quad CFD. One of the three outputs (~1 ns rise time,

<5 ns FWHM) was used to start the TAC. A second output was routed through a switchable attenuator (Kay Model 439A) before discrimination in another channel of the CFD which was optimized for f = 0.5; the discriminated output became the STOP pulse for the TAC. The time correlation information was accumulated on a MCA. The response FWHM (timing jitter) was found by modeling the profile with a Gaussian function; the results are presented in Fig. 2.10. The timing jitter is less than 10 ps provided the pulse amplitude is >100 mV. Since the critical factor is the slope through the zero crossing (not the actual pulse amplitude) we conclude that the CFD timing jitter is negligible when the slope is $\gtrsim$100 mV/ns. Since our MCP-PMT rise time is ~200 ps, jitter free discrimination should be possible down to ~20 mV pulse amplitudes. (It was found that pulse amplitudes within ~1-2 dB of the threshold setting were not discriminated effectively regardless of the threshold level. This arises due to the method used to gate the zero crossing detector output of the TC455. While this section of the CFD should be redesigned, it compromises the performance only when the pulse height distribution is concentrated near the threshold setting.)

We found that CFD optimization always required a delay t_d which was longer than that predicted by Eq. 2.14. This discrepancy is not a result of the approximation used to

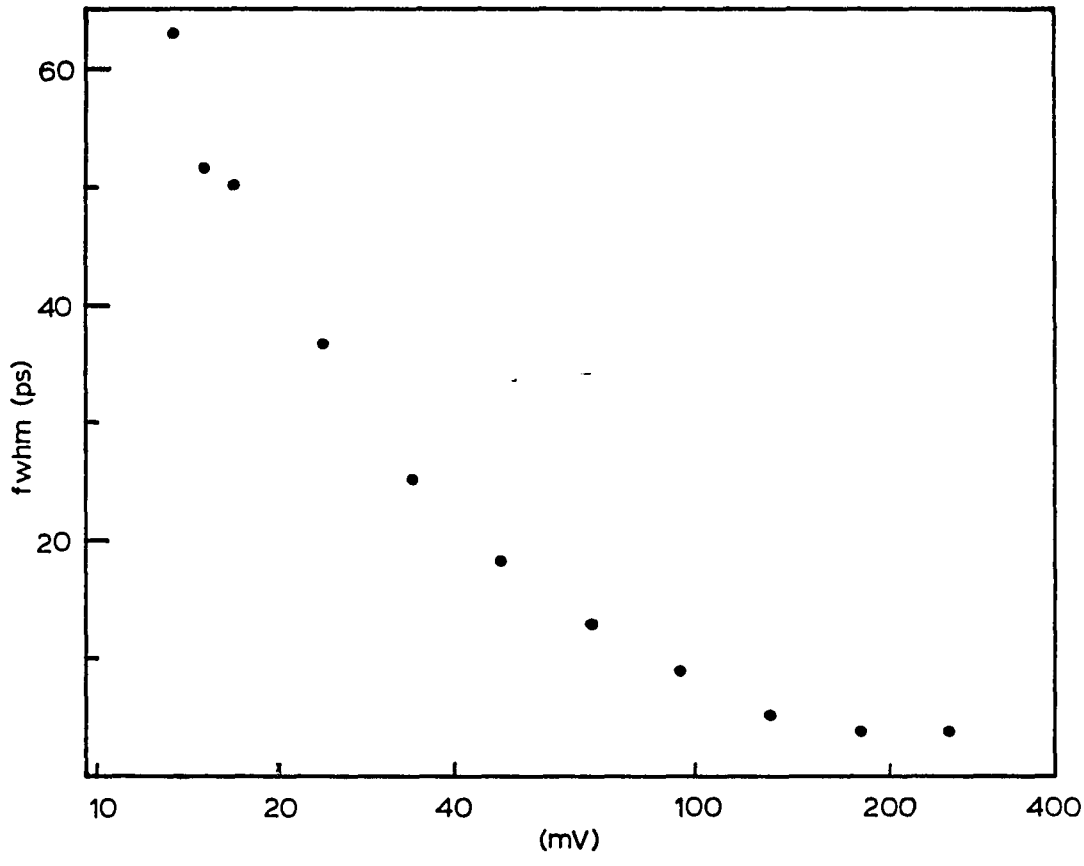

Fig. 2.10 Timing jitter (FWHM) in the CFD circuitry due to noise on the input of the zero crossing detector. The abscissa corresponds to the log of the input pulse amplitude (input pulse rise time, ~1 ns; FWHM, <5 ns)

derive Eq. 2.14, instead it arises because the Tennelec TC455 cannot follow the fast rise times supplied by the MCP-PMT. This fact becomes clear when an equivalent circuit for the TC455 zero crossing detector is considered (Fig. 2.11). The input pulse is split into two portions via an impedance matched divider. The fraction f determines R_1 and R_2 (e.g., when f = 0.5, R_1 = 25Ω and R_2 = 100Ω). The delayed and undelayed portions are routed to the 50Ω terminated inverting and non-inverting inputs of a fast differential amplifier (Plessey SP9687). The two inputs are subtracted by the differential amplifier whose outputs change state when the "zero crossing" occurs (i.e., when the voltage level at the non-inverting input exceeds the voltage level of the inverting input). Parasitic capacitance (C_p) at each input introduces an RC time constant which modifies (slows) the rising edge of the pulse. Contributing to the parasitic capacitance are the differential amplifier inputs (specified as 3 pF) and a pair of reverse biased input protection diodes (1N4154). The latter were removed to speed up the response time. The 3 dB bandwidth for the resulting low pass RC filter network (i.e., the frequency where the capacitive impedance reduces the voltage level at the input by the factor .70 f) is given by

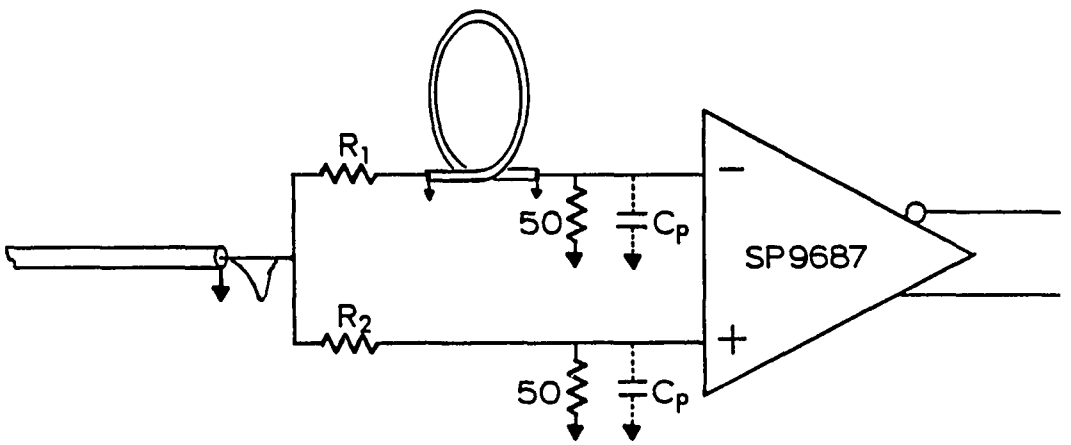

Fig. 2.11 CFD input circuitry and zero crossing detector

$$f_{3dB} = \frac{1}{2\pi C_p}\left[\frac{.4124}{R} + .00825\right] \qquad (2.15)$$

where f_{3dB} is the frequency at the 3 dB point, R is the resistance between the source and the input (i.e., R_1 or R_2), and C_p is the parasitic capacitance. The minimum rise time (10-90%) that each input can follow is finally determined from the rise time - bandwidth product [63, p. 455]. When using f = 0.5, R_1 = 25Ω, and R_2 = 100Ω, the minimum rise times for the inverting (delayed) and non-inverting (undelayed) inputs are ~270 and ~534 ps, respectively. Clearly, the non-inverting input cannot follow the ~200 ps MCP-PMT rise time. Consequently, a delay longer than the value t_d predicted by Eq. 2.14 is required. (Due to the CFD rise time limitations, the benefits of a 3.15 GHz amplifier bandwidth is questionable. The 1.3 GHz (~270 ps rise time) HP 8447 amplifier may work equally well.)

The time resolution currently reported by us (47 ps, [15]) was achieved after a number of modifications were made to the CFD. The input protection diodes were removed to minimize the capacitance at the zero crossing comparator inputs. The standard 0.2 fraction module and corresponding pc board sockets were replaced with directly mounted resistors which formed a 0.5 fraction network. Reflections due to an impedance mismatch at the input attenuator module were minimized by replacing the module and corresponding pc

board sockets with a 0.1" stripline. The delay cable (RG-174U) was permanently installed within the CFD. An appropriate length (~10-14 cm) was found by trial and error. (Care had to be exercised in routing the delay cable; when positioned too close to the zero crossing comparator IC, rf feedback occurred and the timing precision was adversely affected.) The most difficult modification enabled discrimination of positive going pulses (we are unaware of any inverting transformer which matches the 3.15 GHz bandwidth of our amplifier). This was accomplished by switching the inverting and non-inverting inputs of the zero crossing and threshold comparators, and by reversing the polarity of the reference voltage for the threshold detector. While seemingly straightforward, the compact circuit layout of the TC455 makes the latter modification difficult.

Two channels of the quad CFD were used in our TCSPC system: the top channel processed the MCP-PMT output and the bottom channel generated a timing reference from the photodiode signal. Cross-talk occurred between the two channels of the quad when they processed events which were nearly coincident. Interference need not be confined to channels within the quad, however, as independent discriminators powered in the same NIM bin also suffered from cross-talk. This interference was manifested as nonlinearity in the TAC response; it was eliminated by

delaying the arrival of the timing reference (photodiode) pulse by ~50 ns so that discrimination of both signals would be initiated from a quiescent state (the discriminator settling time was <<50 ns). When the required delay was generated via a fiber optic cable, the extrinsic source of TAC nonlinearity disappeared. Use of a coaxial cable delay (bundled within an rf shield) was not as successful. While the nonlinearity due to nearly coincident events was eliminated, a new source of nonlinearity was introduced. This nonlinearity exhibited a periodicity similar to the cavity dumper rf. It is believed to be caused by rf pickup or a ground loop problem.

Time-to-amplitude converter

Time-resolved emission profiles collected with TCSPC are unsurpassed in linearity and dynamic range. Consequently, this method is ideally suited to studies where detailed comparisons between experimental decays and theories are demanded. When every PMT detected photon is processed (undergoes time-to-amplitude conversion), the TCSPC performance is limited only by intrinsic TAC nonlinearity. (Our Ortec 457 TAC is specified as having $<\pm 2\%$ differential and $<\pm 0.1\%$ integral nonlinearity.) The TAC, however, is capable of processing only the first detected photon within each excitation cycle. Since discrimination against late arrivals distorts the data (pulse pile-up distortion), the

time resolved emission profiles must be acquired under conditions which minimize the probability of detecting two or more photons per excitation cycle. This requires that the count rate (detected photons/sec) be significantly lower than the laser repetition rate (excitation cycles/sec). The count to repetition rate ratio μ required to achieve statistically limited performance is revealed through an analysis of pulse pile-up distortion.

The probability of detecting a photon within a particular time interval i per excitation cycle is P_i. Since the TAC responds only to the first photon in a given excitation cycle, the probability of processing that photon is equal to P_i times the probabilities that no photons are detected in each preceding time interval. Hence,

$$N_i = N P_i \prod_{j=1}^{i-1} (1 - P_j) \qquad (2.16)$$

where N_i is the number of photons processed (observed) in interval i when the total number of excitation cycles is N [76]. Equation 2.16 is equivalent to the more useful form

$$P_i = N_i/(N - \sum_{j=1}^{i-1} N_j) \qquad (2.17)$$

where P_i (the true emission probability per excitation cycle) can be easily evaluated in terms of experimental N

and N_i. The relative error that accompanies an experimental profile is then given by

$$\delta_i = \frac{N_i - NP_i}{NP_i} = -\frac{1}{N} \sum_{j=1}^{i-1} N_j. \qquad (2.18)$$

It is clear from Eq. 2.18 that the relative error is most severe at the tail of the time-resolved decay; it is approximated by

$$\delta_{max} \sim -\mu \qquad (2.19)$$

where μ is the count rate divided by the laser repetition rate (equivalent to $\Sigma N_j/N$). Equation 2.19 predicts that ~1% precision in the tail of a time resolved decay requires $\mu \lesssim 0.01$. Under these conditions, an emission profile can be followed down to ~100 counts (where 10% statistical precision obtains) with negligible pulse pile-up distortion.

Experimental time-resolved profiles may be mathematically corrected for pulse pile-up distortion via Eq. 2.17 provided the detected events are negligible in duration relative to the TAC time window. This criterion is not met in our experimental studies where the MCP-PMT pulse width (~.6 ns FWHM) is not small compared to the 10 ns TAC window. The situation is even worse with the XP2020Q PMT whose pulse width is ~3.7 ns FWHM. Consequently, a second photon detected within a given excitation cycle almost

certainly influences the constant fraction timing of the first. The resulting timing signal error cannot be mathematically corrected. The distortion is most severe near the peak of the response where the emission probabilities are maximized. (In contrast, normal pulse pile-up distortion is worse at the tail of the decay.) This distortion can be problematic since it affects the data in the region which is most precisely determined (~10^5 peak counts provides ~.3% precision). A convolute and compare analysis is suspect when pulse pile-up occurs since the distortion is count rate and profile shape dependent. These problems are averted by reducing μ to a level where the probability of detecting two (or more) photons per excitation cycle is suitable small. When μ is much less than one, the Poisson distribution [57, page 37]

$$P(n,\mu) = \frac{\mu^n}{n!} e^{-\mu} \qquad (2.20)$$

predicts the probability of n events occurring during a given excitation cycle when the mean probability is μ. Hence, the ratio of the probabilities $P(2,\mu)/P(1,\mu)$ is $\mu/2$. When $\mu<.02$, the probability that a second event would interfere with the first is <1%. Clearly, minimization of pulse pile-up distortion requires that $\mu \lesssim .01$.

Two experimental configurations have been utilized to accomplish time-to-amplitude conversion: normal and

inverted. the normal geometry derives the START pulse from the timing reference (excitation pulse). The START pulse initiates a conversion which may or may not be terminated by an emission derived (detected photon) STOP pulse. When no photon is detected, the TAC recycles and awaits the next START pulse. The TAC recycle time limits its operation to $\lesssim$150 kHz. The nearest cavity dumped frequency available with our TCSPC apparatus is ~100 kHz. Consequently, minimization of pulse pile-up distortion with the normal TAC geometry requires a count rate $\lesssim$1 kHz.

The inverted geometry is much more efficient. The START pulse is derived from the emission so that a conversion is initiated only when a photon is detected. Hence, excitation rates well above 150 kHz are permitted. Since we use ~5 MHz excitation rate, count rates as high as 50 kHz should be allowed without distortion from pulse pile-up. A count rate dependence to the instrument function width was discovered, however, when using the inverted TAC geometry; the width broadened with increasing count rate. This rate dependence was traced to the TAC. Apparently, the TAC integrating capacitor does not fully discharge during the recycle time. In fact, ~100 μs are required to effectively dissipate the charge. Consequently, the voltage attained in a time-to-amplitude conversion is affected by the dwell time between it and the previous conversion. The period between conversions at low count rates ($\lesssim$1 kHz) is long enough to

discharge the TAC integrating capacitor so minimum width instrument response functions are obtained. Significant broadening is observed at higher count rates, however, where dispersion in the dwell time yields jitter in the conversion. While compromising the time resolution, this TAC rate dependence also renders the convolute-and-compare analysis invalid unless the count rate for the data collection and instrument response are identical. (This problem does not arise with the normal TAC geometry due to periodic conversion.) This situation is rectified by disabling the TAC after a conversion for a period long enough to allow complete discharge of the integrating capacitor. This is accomplished by gating the TAC off for ~125 μs with a pulse derived from the TAC true START output. The ~125 μs period sets an upper limit to the data collection count rate of ~8 kHz. With this modification, we routinely accumulate data at ~4-5 kHz processed counts (~20 kHz actual counts) with no detectable rate dependence. Hence, the inverted TAC geometry provides ~5 times improved throughput over the normal configuration while minimizing pulse pile-up distortion.

Gated intensity integrator

A variety of experimental situations arise where the relative amplitudes of several time-resolved profiles are desired. For example, when the emission from several

sources are additive, the difference between profiles with and without the fluorophore of interest recovers the desired time-resolved emission. In addition, it is often useful to reproduce the relative amplitude of polarized emission profiles; such information is necessary when one attempts to accurately recover the time-resolved anisotropy from these profiles. Proper normalization is difficult to achieve, however, when the profiles are collected at different times and when the excitation intensity is not necessarily a constant. A method which accumulates the profiles for a given integrated laser intensity is required.

Cross and Fleming [38] devised an excitation intensity integrator based on a voltage controlled oscillator (VCO). The VCO was driven by a PMT which viewed a portion of the excitation intensity. The intensity dependent VCO frequency was counted to a preset number whereupon the MCA was disabled. When the sample is light stable, and when the photodetector efficiency is constant, this intensity integrator method should, in principle, recover the relative amplitudes of various profiles. This method fails, however, to account for the dead time which arises in both TAC and MCA (each device rejects all input signals while processing an event). Since the dead time is count rate dependent, the intensity integrator circuit functions properly only when the count rates for all profiles are identical. This severely restricts the applicability of this circuit.

We have developed a gated intensity integrator circuit which averts the difficulty due to dead time in the electronics. Figure 2.12 depicts a block diagram for this circuit. A photodiode (EG&G FOD-100) was used to monitor a split portion of the laser intensity. A current to voltage converter with gain (10^4-10^7 volts/amp) was constructed from two LF-356 operational amplifiers. The intensity dependent voltage was routed to a VCO (Burr-Brown VFC 320) which provided 100 kHz/volt gain with better than 1% linearity from 0.1 to 10 volts. The frequency output was directed to an input on a gatable monostable multivibrator (74121); the inhibit input followed the dead time. The computer controlled counter (Commodore C64) was unable to respond to frequencies above a few hundred kilohertz, so the gated VCO output was divided in a ÷10 counter (7490) prior to processing. The MCA was enabled by the computer until a preset number of pulses were counted, corresponding to a given integrated laser intensity while the apparatus was "live".

The dead time for our apparatus is determined by the gating pulse used to avert the TAC rate dependence. The same pulse (~125 μs) is used to gate the VCO output off via the monostable multivibrator. The precision achieved in accounting for dead time is determined by the number of VCO pulsed per dead time period. Since we generally operate the VCO at ~700 kHz, the precision is ~1%. Note that the

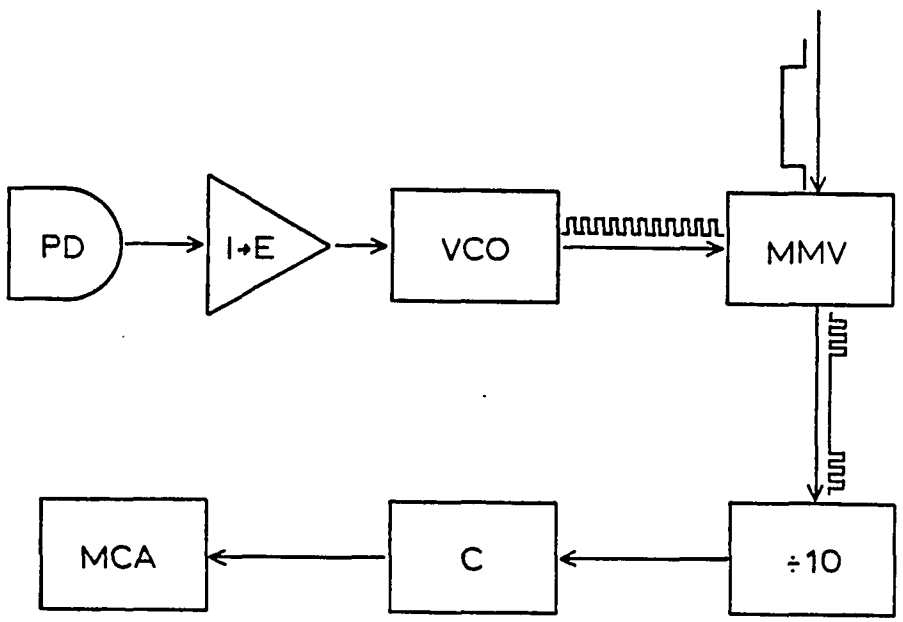

Fig. 2.12 Gated intensity integrator circuit. PD, photodiode; I→E, current to voltage amplifier; VCO, voltage controlled oscillator; MMV, monostable multivibrator; ÷10, divide by ten counter; C, computer controlled counter; MCA, multichannel analyzer

lengthy dead time (~125 μs) imposed by the TAC gating procedure facilitates precise accounting for dead time with readily achieved ($\lesssim$1 MHz) VCO frequencies.

Data Analysis

The time-resolved profiles I(t) obtained with TCSPC are actually a convolution of the true time dependent emission p(t) with the instrument response function X(t) (Eq. 2.2). Since X(t) can be recovered with great precision, the mathematical convolution of the model function with X(t) may be fitted to I(t); parameter optimization is achieved via a Marquardt based [77] nonlinear least squares convolute-and-compare analysis. Care must be exercised in calculating the convolution. The model p(t) is usually analytic while X(t) is an histogram, i.e., the counts recorded in a particular MCA channel i is the integral of the number of counts detected within the interval i-1/2 to i+1/2. The convolution formula often reported and formerly used by us is

$$F_n = \sum_{i=0}^{n} X(i)\, p(n-i) \qquad (2.21)$$

where p(t) is evaluated at the point in time corresponding to the center of MCA channel n-i, and F_n is the convolution at channel n. When the instrument response function is many

channels wide, Eq. 2.21 provides a satisfactory approximation to the convolution. When the instrument response function is narrow (e.g., our MCP-PMT yields a response ~2 channels wide when the time scale is 20 ps/channel) Eq. 2.21 overestimates the convolution near the peak region. Given our experimental parameters, the peak of a 100 ps decay component is overestimated by ~12%. This error is minimized by replacing p(t) in Eq. 2.21 with

$$H_p(i) = \int_{(i-1/2)\Delta t}^{(i+1/2)\Delta t} p(t)\, dt \qquad (2.22)$$

and

$$H_p(0) = \int_{o}^{\Delta t/2} p(t)\, dt \qquad (2.23)$$

where Δt is the time per interval and $H_p(i)$ is the histogram representation of the analytic function. The integrals are evaluated analytically (for multiexponential decays) or are approximated using a modification of Simpson's rule (for Förster or other functions with no analytic integral).

The nonlinear least squares fitting routine was generalized to accommodate multiexponential, Förster (Eq. 1.8), or Förster plus exponential decay models, and was used to fit magic angle time-resolved emission profiles. the Marquardt based program minimizes the weighted χ^2

$$\chi = \sum_n w_n (I_n - F_n)^2 \qquad (2.24)$$

where w_n is the statistical weight for channel n (for photon counting statistics, $w_n = 1/I_n$ [58, p. 172]). When the model accurately describes the data, the reduced chi-squared (χ^2_ν) is expected to be near 1.00. This number should not be used as the sole criterion upon which the quality of the fit is judged. For example, errors in the convolution due to a coarse instrument response function, while limited mostly to the rising edge of the response, may account for a significant portion of the estimated χ^2_ν. A more relevant criterion is whether the fitting model exhibits systematic deviations relative to the experimental profile. For this determination, the autocorrelation of the weighted residuals was devised [78]. The autocorrelation function is

$$A_n = \frac{2N'}{(N-M)} \frac{\sum_{i=1}^{(N-M)/2} w_i^{1/2}(I_i - F_i) w_{i+n}^{1/2}(I_{i+n} - F_{i+n})}{\sum_{i=1}^{N'} w_i (I_i - F_i)^2} \qquad (2.25)$$

where the data range from M to N, and N′ is the total number of channels. When no systematic deviations are present (within the counting statistics), A_n is randomly distributed about zero. A poor fit, however, betrays itself as a modulation in the autocorrelation of the weighted residuals.

The autocorrelation approach is very powerful, in particular when the data are collected to ~10^4 peak counts. For peak counts ~10^5, systematic deviations appear in the autocorrelation function which arise from TAC nonlinearity. It is difficult to separate this contribution from systematic deviations due to the fitting model, however. For data sets collected to this level of precision, the quality of fit may be effectively judged simply by inspecting a plot of the data and fitted curves.

The quantity of interest in any fluorescence depolarization study is the time-dependent anisotropy. While the anisotropy cannot be observed directly, it can be constructed from experimentally obtained parallel and perpendicular profiles using Eq. 1.34. While most workers attempt to fit the anisotropy, we believe it is more fruitful to generalize the fitting model to account for both polarized profiles and fit them simultaneously (see pp. 39-40). Toward this end, we modified our Marquardt nonlinear least squares routine to enable simultaneous minimization of the χ^2 for both polarized profiles while providing an option for linking any or all of the fitting parameters [79]. Linked deconvolution facilitates accurate recovery of the linked fitting parameters [80] by suppressing sensitivity to experimental artifacts. This suppression arises because the fitting parameter C_D (excitation transport depolarization) or τ_{rot} (rotational depolarization) affects the polarized

profiles oppositely (see Eqs. 1.24 or Eqs. 1.28), while experimental artifacts affect the profiles similarly. In contrast, attempts to fit one of the two polarized profiles leads to greater uncertainty in the estimate of the parameters since the least squares routine is allowed to fit the true decay plus any superimposed artifact.

When high precision magic angle profiles (P(t) ≡ isotropic decay) are obtained in viscous solvents (e.g., glycerol or ethylene glycol), single exponential emission is the exception rather than the rule. This nonexponentiality must be properly accounted for when attempting to fit the polarized emission profiles.

Solvent reorganization occurs when an $S_1 \leftarrow S_0$ transition is accompanied by a sudden dipole moment change. Concomitant with the solvent rearrangement is a dynamic red shift of the fluorescence emission spectra (lowering of energy) [81]. When the dynamic shift moves the emission band away from optional overlap with the photodetector spectral bandpass, the time-resolved decay appears to be biexponential with positive preexponents. A shift toward optimal alignment also appears to be biexponential but with a negative preexponent [15]. Excitation trapping also leads to nonexponential P(t). Unless the trapping is severe, a biexponential model with positive preexponents is usually sufficient to describe the decay.

If the nonexponential character of P(t) is not taken into account when fitting the polarized profiles, the parameters C_D or τ_{rot} will not be properly determined. We avoid this pitfall by collecting three polarized profiles, one of which is obtained at the magic angle. P(t) is determined by fitting the magic angle profile with a flexible model (generally biexponential); these results are then used to fix P(t) in the polarized profile fit. Hence, one fits the differences between polarized and isotropic profiles, which should arise solely from the anisotropy.

SECTION III. TIME-RESOLVED EXCITATION TRANSPORT STUDIES IN 3-DIMENSIONAL DISORDERED SYSTEMS

FLUORESCENCE DEPOLARIZATION OF RHODAMINE 6G IN GLYCEROL: A PHOTON-COUNTING TEST OF 3-DIMENSIONAL EXCITATION TRANSPORT THEORY

Philip A. Anfinrud, David E. Hart, John F. Hedstrom, and Walter S. Struve

Department of Chemistry and Ames Laboratory - USDOE
Iowa State University, Ames, Iowa 50011

FLUORESCENCE DEPOLARIZATION OF RHODAMINE 6G IN GLYCEROL: A PHOTON-COUNTING TEST OF 3-DIMENSIONAL EXCITATION TRANSPORT THEORY

Introduction

It has been long recognized that accurate modeling of fluorescence concentration depolarization in solution is a formidable theoretical problem. Early attempts to describe the influence of Förster dipole-dipole excitation transport [1] on fluorescence depolarization frequently assumed that transfer was limited to one or two excitation hops from the initially excited molecule [2, 3], or that excitation was exchanged only between nearest and next-nearest neighbor molecules in solution [4-6]. To our knowledge, the first realistic calculations of the probability $G^S(t)$ that excitation is found on the initially excited molecule at time t were provided by Gochanour, Andersen, and Fayer [7], who worked out diagrammatic Green's function expansions of solutions to the excitation transport master equation [8] and obtained successive self-consistent approximations to $G^S(t)$. The latter Green's function is related to the fluorescence depolarization in solution by [9]

$$G^S(t) = \frac{I_{\parallel}(t) - I_{\perp}(t)}{I_{\parallel}(t) + 2I_{\perp}(t)} \qquad (1)$$

where $I_{\parallel}(t)$ and $I_{\perp}(t)$ are the fluorescence intensity components polarized parallel and normal to the excitation polarization. (This equation holds if the solvent is viscous enough to inhibit rotational depolarization during the fluorescence lifetime, if the molecular absorption and emission transition moments coincide, and if the excitation pulse energy is small enough so that the orientational distribution of unexcited molecules is random.) Gochanour and Fayer [9], (hereafter GF) tested their second-lowest (three-body) self-consistent approximation to $G^s(t)$ by measuring the experimental time-dependent fluorescence components

$$\begin{aligned} I_{\parallel}(t) &= Ae^{-t/\tau}\,[1 + 0.8G^s(t)] \\ I_{\perp}(t) &= Ae^{-t/\tau}\,[1 - 0.4G^s(t)] \end{aligned} \qquad (2)$$

for rhodamine 6G (rh6G) in glycerol. By computing the three-body Green's function $G^s(t)$, which depends on the known rh 6G concentration and on the isotropic dye lifetime τ (which they measured at sufficiently high dilution so that $G^s(t) \to 1$ for all t), they were able to check experimental fluorescence intensities against convolutions of their Gaussian experimental response function with theoretical profiles generated from Eqs. 2. Excellent visual agreement was obtained, with divergences of $\lesssim 5\%$ for times up to $\sim 2.5\tau$ ($\sim$8 ns).

GF obtained their fluorescence profiles by KDP sum-frequency mixing of rh 6G fluorescence with variably delayed 1.06 μm pulses from a CW mode-locked Nd:YAG laser, and the resulting 390-nm up-converted pulses were detected by a cooled photomultiplier and lock-in amplifier. In this paper, we use time-correlated photon counting to obtain time-dependent fluorescences for rh 6G in glycerol. This technique [10] offers far superior data statistics, and autocorrelation functions of the residuals [11] can elicit systematic deviations between data and theoretical profiles which are too small to observe using sum-frequency mixing. Our data analysis (Experimental Section) provides a check on whether the polarized fluorescence components actually exhibit the form of Eqs. 2, or whether the single-exponential factors are distorted, e.g., by excitation trapping at rh 6G dimers, which accelerates fluorescence decay and renders it nonexponential in highly concentrated solutions. Our analysis also avoids parameter correlation (covariance) between the rh 6G concentration (which influences $G^S(t)$) and τ in Eqs. 2, so that it is unnecessary to rely on independent low-concentration measurements to obtain the isotropic dye lifetime τ. This advantage is important, because τ varies significantly with rh 6G concentration even in 10 μm path length fluorescence cells due to self-absorption [12] and (at the higher

concentrations) excitation trapping. It develops that because the absorption and fluorescence spectra of rh 6G overlap so much near 540 nm [12], self-absorption cannot be even approximately suppressed in such thick cells at the millimolar concentrations over which excitation transport competes efficiently with intramolecular decay. At the lowest rh 6G concentrations, our fluorescence decay profiles prove to be indistinguishable from theoretical profiles calculated using the three-body Green's function $G^S(t)$ in Eqs. 2 when the autocorrelation of residuals are examined. Nonstatistical autocorrelations are obtained at higher rh 6G concentrations, but these differences are shown to arise largely from nonexponentiality in the isotropic decay function (i.e., excitation trapping by rh 6G dimers) and from self-absorption, rather than from inaccuracies in the three-body Green's function.

Experimental Section

An acousto-optically mode-locked argon ion laser (Coherent Innova 90 with 5 W plasma tube operated at 26 A) pumped a cavity-dumped rhodamine 590 dye laser (Coherent CR-599-01 tuned with three-plate birefringent filter) to produce tunable picosecond pulses which exhibited zero-background autocorrelations with ~8 ps fwhm. The mode locker was a Harris Corporation H-401 unit driven at 48 MHz.

The 4.8-MHz cavity dumper included a Harris Corporation H-100 acousto-optic modulator and H-102 driver, with folding reflectors mounted on Newport Research Corporation beam directors and Line Tool Co. translators. Laser performance was monitored and optimized with a rotating-mirror real-time autocorrelator [13].

Commercial rhodamine 590 chloride (rh 6G) was obtained from Exciton; the unpurified dye showed only one TLC spot using Analtech silica gel G plates and three different solvent systems (ethanol/acetone, ethanol/acetic acid, and 1-propanol/formic acid). Fluorescence cells were formed from $\lambda/4$ fused quartz flats by compressing a drop of solution between two flats. Optical density measurements on rh 6G solutions of known concentration in such cells showed that this procedure typically yielded solutions with ~10μm path length. Thinner cells (~2 - 4μm) could be obtained by etching the Al coating from a ~ 4mm diameter circular area of an optically flat front-surface reflector, and then bounding the sample between a surface so treated and a fused quartz flat.

Horizontally polarized 575 nm dye laser pulses were incident on the horizontal rh 6G cell surface at ~75° from normal. Fluorescence was collected vertically with a 5 cm focal length quartz lens and was focused by a 10 cm focal length lens through a variable rectangular aperture prior to detection by a Hamamatsu 1564U microchannel plate phototube

(MCP) with bialkali photocathode and borosilicate glass window. The MCP exhibited ~6 x 10^5 gain at 3000 V, 500 nm and a transit time spread of 76 ps at 3200 V. Laser scatter and filter fluorescence were minimized by two 3 mm Schott OG-590 filters and a 3 mm Schott RG-610 filter. Excitation pulses were focused with a 10 cm focal length quartz lens to ~0.1-mm diameter at the cell surface. The excitation and analyzer polarizers were Promaster Spectrum 7 photographic polarizers; the analyzer was placed between the cell and the collecting lens. The differential detector sensitivity to fluorescence photons polarized parallel and normal to the excitation polarization was conservatively less than 2%.

MCP photocurrent pulses were amplified and inverted using a B&H Electronics AC3011 MIC (3.15 GHz) 21 dB preamplifier and an EG&G IT100 inverting transformer. Amplified pulses were passed through a Tennelec TC455 quad constant-fraction discriminator (CFD) and served as START pulses in an Ortec 457 time-to-amplitude converter (TAC). An EG&G FOD-100 photodiode operating in the photoconduction mode sampled dye laser pulses; its signal was processed through an Ortec 934 quad CFD to provide STOP pulses. TAC output was stored in a Canberra Series 30 MCA operated in the PHA mode to yield 5.0, 10.0, or 20.0 ps channel resolution. Instrument functions for deconvolution of raw data were obtained by scattering 575-nm laser pulses from a clean quartz substrate, and typically exhibited ~80 ps fwhm.

After transfer to a Digital Equipment Corporation MINC-23 system with dual floppy disk drive operating in an RT-11 environment with FB monitor, fluorescence profiles were analyzed with a Marquardt nonlinear regression [14] program.

Data Analysis

For a given fluorescence decay law N(t), the convolute-and-compare analysis forms the convolution C_n in the nth channel of N(t) with the instrument function x(t),

$$C_n = \sum_{i=1}^{N} x(i - s)N(n - i) \tag{3}$$

where s is a variable, integral shift parameter. For the trial function N(t), we use $I_s(t)$ or $I_d(t)$ in Eqs. 2, with the three-body approximation [9] to the Green's function given by the numerical inverse Laplace transform [15] of

$$G^s(\varepsilon) = \tau\{(\pi^2\gamma^2C^2/4\ [1 - [1 + (32/\pi^2\gamma^2C^2)^2](\varepsilon\tau - 0.1887\gamma^2C^2)]^{1/2} + 4(\varepsilon\tau - 0.1887\gamma^2C^2)\}/[4(\varepsilon\tau - 0.1887\gamma^2C^2)^2] \tag{4}$$

Here $\gamma = 0.846$ is a constant which arises from the dipole-dipole orientational dependence of the excitation transfer probability [9], and the reduced concentration

$$C = \frac{4}{3}\pi R_o^3 \rho \tag{5}$$

depends on the dye molecule number density ρ and on the Förster parameter R_o which characterizes the excitation hopping rate w_{jk} between molecules with transition moments oriented along d_j and d_k separated by distance R_{jk},

$$\begin{aligned} w_{jk} &= \frac{3}{2\tau}\left(\frac{R_o}{R_{jk}}\right)^6 K_{jk}^2 \\ K_{jk} &= \hat{d}_j \cdot \hat{d}_k - 3(\hat{d}_j \cdot \hat{R}_{jk})(\hat{d}_k \cdot \hat{R}_{jk}) \end{aligned} \tag{6}$$

Since $G^S(t)$ depends on the reduced concentration C and on the isotropic lifetime τ, convolutions of the model functions in Eqs. 2 with the instrument function contain four adjustable parameters: A, τ, C, and s. (Cavity-dumping at 4.8 MHz made it unnecessary to include the base line as an adjustable parameter, or to build the mode-locked laser pulse periodicity into the modeling function as was done in earlier work [16].) These four parameters can be simultaneously optimized in the nonlinear regression program to minimize the statistically weighted χ^2

$$\chi^2 = \sum_{i=M}^{N} (C_i - Y_i)^2 / Y_i \tag{7}$$

where Y_i is the number of fluorescence counts accumulated in channel i and (M, N) is the channel range used in the analysis. Our 80 ps fwhm instrument function was not wide compared to the 20 ps channel spacing. Since the convolute-and-compare analysis was restricted to integral shift parameters s, choosing M = 1 produced disproportionate contributions to χ^2 from the rising-edge portion of the fluorescence profiles. Channel M was instead typically placed on the rising edge at 90% peak counts, and the continuous curves representing optimized fits to our data profiles (Results and Discussion Section) begin with channel M.

Covariance can compromise the uniqueness of fits based on simultaneous variation of C and τ, because increases in C can be compensated by increases in τ to yield a Green's function which is nearly unchanged over the analyzed channel range. The isotropic lifetime τ was therefore extracted from single-exponential fits to magic-angle fluorescence profiles, which were accumulated at all rh 6G concentrations with an analyzing polarizer aligned at 54.7° from the excitation polarization to yield profiles proportional to $I_{\parallel}(t) + 2I_{\perp}(t)$. The results of such single-exponential fits to magic-angle profiles are summarized in Table I for five rh 6G concentrations between 1.43×10^{-5} and 4.12×10^{-3} M. The cell thickness in all cases was 10 μm. The visual quality of the fits is shown for four of the samples in

Table I. Magic-angle fits of rhodamine 6G fluorescence profiles

Sample	Concentration, M	τ, ns	χ^2_r
1	1.43×10^{-5}	3.40	1.180
2	6.29×10^{-4}	3.56	1.944
3	1.62×10^{-3}	3.72	2.306
4	2.45×10^{-3}	3.78	3.237
5	4.12×10^{-3}	3.32	3.782

Figure 1. Reduced χ^2 values tend to increase with concentration, and they range from ~1.1 to 3.8. The relative inaccuracy of the single-exponential fit in the latter case arises from nonexponential decay behavior introduced by excitation trapping [17] by rh 6G dimers, which are more numerous at the higher concentrations. The autocorrelations of residuals [13]

$$A_n = \frac{2N'}{(N - M)} \frac{\sum_{i=1}^{(N-M)/2} Y_i^{1/2}(C_i - Y_i)Y_{i+n}^{1/2}(C_{i+n} - Y_{i+n})}{\sum_{i=1}^{N'} Y_i(C_i - Y_i)^2} \qquad (8)$$

with N′ equal to the number of channels comprising the fluorescence profile, provide a more discriminating test for quality of fit. The nearly statistical autocorrelation which is shown for the lowest concentration in Figure 1 shows that the magic-angle profile is nearly indistinguishable from single-exponential decay under present counting statistics.

Of particular interest in Table I is the marked variation of the optimized lifetime τ with rh 6G concentration. Though all of the magic-angle profiles in this table were obtained with 10 μm fluorescence cells, self-absorption (which dilates the fluorescence lifetime without sensibly affecting its exponentiality [12])

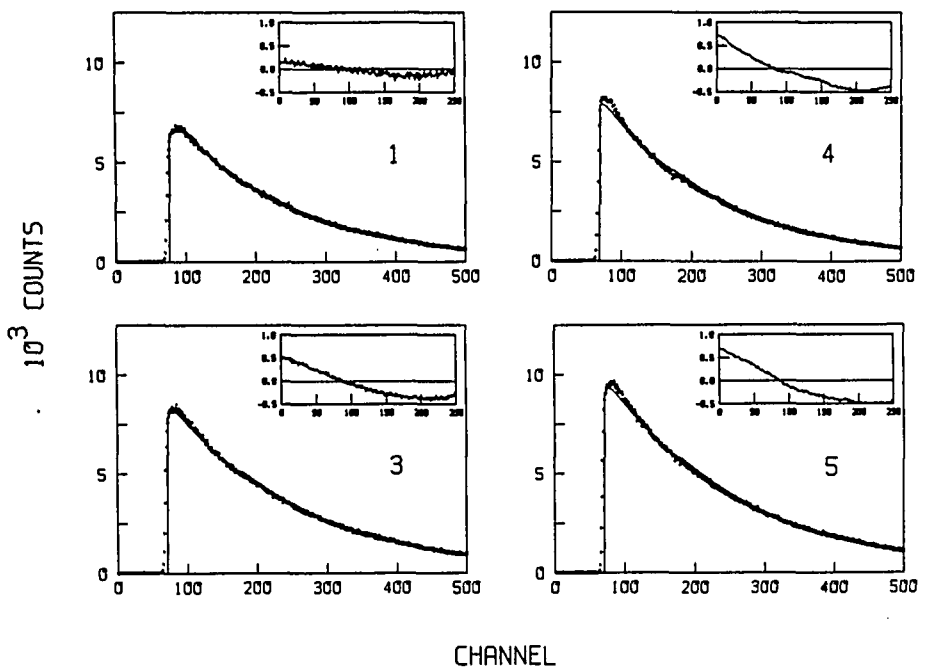

Figure 1. Magic-angle fluorescence profiles for samples 1, 3, 4, and 5 in Table 1. Continuous curves are optimized convolutions of single-exponential decay functions with the instrument function Inset plots show autocorrelations of residuals. Time calibration is 20 ps per channel. Cell thickness was 10 μm in each case

increases τ from 3.40 to 3.78 ns in samples 1 - 4; excitation trapping reduces τ to 3.32 ns at the highest concentration (sample 5). Much larger τ variation with rh 6G concentration (up to 4.83 ns at 2.45×10^{-3} M) was observed in a 100-μm cell. Following Hammond [12], the isotropic lifetimes τ may be converted into lifetimes τ_c corrected for self-absorption via

$$\tau_c = \tau(1 - aQ_o) \tag{9}$$

with

$$aQ_o = 2.65cl \int_o^\infty \varepsilon_F E(\lambda)(0.0039 - \log A_F)\, d\lambda \tag{10}$$

$E(\lambda)$ is the rh 6G emission spectrum normalized to the fluorescence quantum yield Q_o, ε_F is the rh 6G absorption coefficient at the fluorescence wavelength, A_F is the sample absorbance at the fluorescence wavelength, c is the solution concentration, and l is the cell length. Using values of ε_F, $E(\lambda)$, and Q_o for rh 6G in ethanol [12], one obtains the lifetimes τ_c corrected for self-absorption in Table II. For the four lowest concentrations, τ_c is between 3.32 and 3.39 ns; this mutual consistency strongly suggests that self-absorption is the primary origin of lifetime dilation in samples 1-4, and that a 10-μm cell is not thin enough to

Table II. Lifetime corrections for self-absorption

Sample	Path length, μm	a	τ, ns	τ_C, ns
1	10	0.003	3.40	3.39
2	10	0.058	3.56	3.37
3	10	0.106	3.72	3.35
4	10	0.131	3.78	3.32
5	10	0.160	3.32	2.82

completely remove this artifact at any of these concentrations. The correction is almost negligible ($\lesssim$0.3%) in sample 1, but amounts to ~12% in sample 4. For sample 5, τ_c is ~500 ps shorter than those found at lower concentrations, indicating that trapping is rapid at 4.12×10^{-3} M.

The magic-angle profile analyses provide initial τ values for deconvolution of the $I_{\parallel}(t)$ and $I_{\perp}(t)$ profiles using Eqs. 2 and 4 as model functions. Both of these profiles are deconvoluted simultaneously, with C and τ linked by minimization of their combined χ^2 [18]. This procedure effectively eliminates parameter correlation, because the effects of changing C (or τ) have opposite sign in $I_{\parallel}(t)$ and $I_{\perp}(t)$ according to Eqs. 2. This was demonstrated in trial deconvolutions of simulated profiles, computed by convoluting a 100 ps fwhm Gaussian instrument function with $I_{\parallel}$ and $I_{\perp}$ decay laws calculated using Eqs. 2 and 4 with C = 0.5 and τ = 4.0 ns. Independent deconvolution of these simulated $I_{\parallel}$ and $I_{\perp}$ profiles yielded optimized lifetimes of 4.016 and 4.008 ns, and optimized reduced concentrations of 0.535 and 0.468, respectively (Table III). In the linked deconvolution, the common values of τ and C converge to 3.996 ns and 0.5008 instead. Table III also shows that considerably larger fractional differences in C are obtained between independent and linked deconvolutions when C = 0.1 instead of C = 0.5 is used to

Table III. Deconvolutions of simulated $I_{\parallel}$ and $I_{\perp}$ profiles

	τ = 4.000 ns, C = 0.500			
	independent		linked	
	$I_{\parallel}$	$I_{\perp}$	$I_{\parallel}$	$I_{\perp}$
A	0.1129	0.3049	0.1122	0.3025
τ, ns	4.0156	4.0077	3.9961	3.9961
C	0.5349	0.4684	0.5008	0.5008
χ_r^2	1.024	1.022	1.032	1.032

	τ = 4.000 ns, C = 0.100			
	independent		linked	
	$I_{\parallel}$	$I_{\perp}$	$I_{\parallel}$	$I_{\perp}$
A	0.1092	0.3206	0.1085	0.3188
τ, ns	4.0305	4.0257	3.9960	3.9960
C	0.1311	0.0797	0.0998	0.0998
χ_r^2	1.024	1.023	1.032	1.032

simulate the data profiles; this occurs because $G^S(t)$ is less sensitive to C when the latter is small. In each of these tests, Gaussian noise was added to the simulated profiles.

Covariance can thus be ruled out as a source of artifacts in our data analysis. The magic-angle analyses we have described show that excitation trapping by dimers considerably distorts the isotropic decay behavior at the highest concentration, and that lifetime dilation by self-absorption is difficult to suppress in rh 6G solutions. These phenomena affect the fluorescence anisotropy (and the measured Green's function $G^S(t)$) in ways which are difficult to correct for rigorously. Excitation trapping reduces the fluorescence depolarization and the apparent value of C, because excitation transport is interrupted at a lifetime shorter than the intramolecular lifetime τ_D. Self-absorption leads to inflated values of the measured reduced concentration, because absorption and reemission of fluorescence in solution contributes an additional mechanism for depolarization. A realistic assessment of these effects is important in a careful experimental test of excitation transport theory.

Results and Discussion

The polarized fluorescence profiles are displayed with the optimized convolutions of Eqs. 2 with the instrument function for samples 1, 3, 4, and 5 in Figure 2. These profiles exhibit the expected trend from slight to strong fluorescence depolarization over the rh 6G concentration range 1.43×10^{-5}, 4.12×10^{-3} M within the displayed time period of ~10 ns. In Table IV, we list the final fitting parameters for these $I_{\parallel}(t)$ and $I_{\perp}(t)$ profiles. The visual fits, the reduced χ^2 values in Table IV, and the autocorrelations of residuals shown in Figure 2 all tend to worsen at the highest rh 6G concentrations. The origin of part of these discrepancies is clearly the fact that the magic-angle profiles are not precisely single-exponential (Figure 1), especially at the highest concentrations, so that the single-exponential isotropic factors in Eqs. 2 cannot represent the true decay behavior. The least-squares program attempts to compensate for this nonexponentiality by adjustment of the parameters in $G^S(t)$ when fitting $I_{\parallel}(t)$ and $I_{\perp}(t)$, with the result that the autocorrelations in some cases (samples 2 and 3) are markedly better for the $I_{\parallel}(t)$ profile than for the magic-angle profile. The trend in optimized reduced concentrations C vs. rh 6G molarity M is summarized in Figure 3 for samples 1-5, with additional data points added for a sample with $M = 1.76 \times 10^{-4}$ M. Solutions

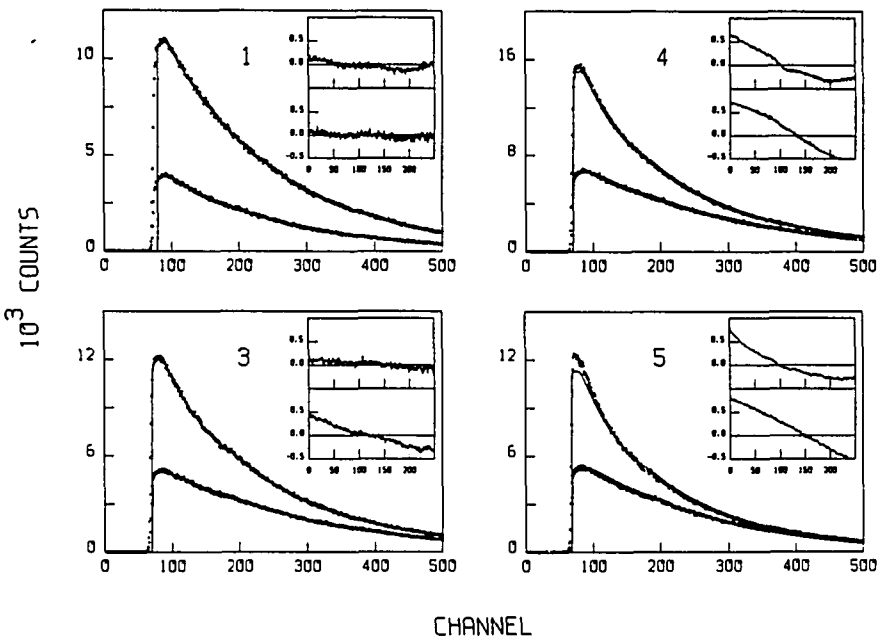

Figure 2. Fluorescence profiles $I_{\parallel}(t)$ and $I_{\perp}(t)$ for samples 1, 3, 4, and 5 in Table 1. Continuous curves are optimized convolutions of model functions computed from Eqs. 2 and 4 with the instrument function. Upper and lower inset plots show autocorrelations of residuals for $I_{\parallel}(t)$ and $I_{\perp}(t)$, respectively. Time calibration is 20 ps per channel; cell thickness was 10 μm in each case

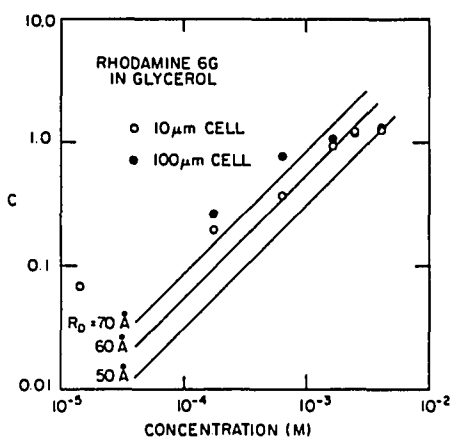

Figure 3. Optimized reduced concentrations C of rh 6G solutions, from nonlinear least-squares fits to $I_{||}(t)$ and $I_{\perp}(t)$ profiles of model functions calculated from three-body Green's function $G^S(t)$. Data points are included for solutions in 10-μm cell (O) and 100-μm cell (●). Straight lines give actual reduced concentration vs. rh 6G solution molarity for dyes with Förster parameters R_O = 50, 60, and 70 Å

Table IV. Fitting parameters for anisotropic fluorescence profiles

$$I_{\parallel}(t) = Ae^{-t/\tau}[1 + 0.8G^{S}(t)]$$

$$I_{\perp}(t) = Ae^{-t/\tau}[1 - 0.4G^{S}(t)]$$

Sample		τ, ns	C	χ^2_r
1	∥	3.41	0.0675	1.141
	⊥			1.172
2	∥	3.68	0.368	1.318
	⊥			1.926
3	∥	3.77	0.927	1.270
	⊥			2.153
4	∥	3.69	1.22	3.006
	⊥			4.501
5	∥	3.22	1.26	6.170
	⊥			5.268

with cell thicknesses of both 10 μm and 100 μm (the 100 μm sample profiles and fitting parameters are not shown) are included in this plot. C should in principle be proportional to M through Eq. 5, this is approximately obeyed only by the 10-μm samples over the limited concentration range 6×10^{-4}, 2.4×10^{-3} M, where the proportionality factor corresponds to R_o ~60 Å. At higher concentrations, C values obtained in both 10-μm and 100-μm cells level off due to excitation trapping, which artificially depreciates the apparent reduced concentration. The separations between the 10-μm and 100-μm data points at the other concentrations are a consequence of greater self-absorption in the thicker samples, and they show that this effect can materially influence the measured fluorescence anistropy as well as the isotropic lifetimes in our samples (Table II).

Our method of data analysis formally differs from that of GF in that these authors varied C to most closely match their profiles with convolutions of Eqs. 2 at one concentration (2.6×10^{-3} M, comparable to that of our sample 4). This optimized value of C (0.83) was used to infer that R_o = 50 Å, and this value of the Förster parameter was used to calculate theoretical decay profiles for comparison with their data obtained at other concentrations, yielding visually excellent results. If they were so handled, our data would have yielded similar

results, but with a somewhat larger empirical value of R_o between 50 and 60 Å (Figure 3). What our present analysis shows is that the apparently small differences between the calculated and experimental profiles arise primarily from self-absorption and excitation trapping artifacts, rather than from discrepancies between the three-body and true Green's functions $G^S(t)$. Avoiding such artifacts would require better sample design: thinner sample cells and more effective inhibition of rh 6G aggregation. GF employed cells ranging from 300 to 5 μm in thickness, and we used 10 μm cells at all of our concentrations. Figure 3 and Table II together suggest that cells thinner than ~2μm should be used, at least at the highest concentrations. We constructed such cells by etching 4mm diameter areas of Al coating from $\lambda/4$ glass substrates using HF solution, only to find that the substrate material itself fluoresced in the red under 575 nm laser excitation. Experiments with well-constructed cells ~1μm thick are planned in our laboratory. Excitation trapping is clearly a more persistent problem, particularly in the dynamically interesting high-concentration regime in which breakdowns in any self-consistent approximation to $G^S(t)$ will first become apparent. Self-absorption can be minimized in well-designed transient-grating experiments [19] to test the excitation transport theory. Such experiments do not offer data with the statistical quality available in photon counting, and

their results are similarly influenced by excitation trapping if the latter is not properly taken into account.

Our data points for the two lowest concentrations in Figure 3 lie significantly higher than would be expected for physically reasonable Förster parameters R_o. Self-absorption is not likely to contribute significantly at such concentrations; the large divergences are in part a consequence of the relative insensitivity of $G^s(t)$ to C for $t \leq 2\tau$ when $C \lesssim 0.1$.

Very recently, Fedorenko and Burshtein [20] demonstrated that the inverse Laplace transform of Eq. 4 can be inverted analytically, and compared the long-time asymptotic behavior of the three-body $G^s(t)$ with the known asymptotic behavior [21] of the true Green's function. Considerable emphasis was placed on the fact that the three-body theory exhibits incorrect long-time behavior. In "static-quenching" situations in which the reduced dye concentration C is negligible compared to the reduced trap concentration C_T, $G^s(t)$ is given exactly by [22]

$$G^s(t) = \exp[-C_T(\pi t/\tau)^{1/2}] \qquad (11)$$

It is readily shown in such cases (cf. Fig. 1 in Ref. 20) that the three-body Green's function is a very good approximation to the true $G^s(t)$ for $C_T \lesssim 1$ when $t \lesssim 2\tau$ (the experimental time regime investigated by GF and by us), but

progressively worsens at longer times. It seems reasonable a priori that the three-body $G^S(t)$ will exhibit similar behavior in the present systems ($C_T << C$), for which exact Green's functions have not been calculated. Indeed, our rigorous least-squares analysis of polarized photon-counting fluorescence profiles from rh 6G in glycerol shows that differences between the theoretical and experimental decay curves are dominated by trapping and self-absorption artifacts, rather than by errors in the three-body approximation. These differences are not very large (especially when viewed on a linear scale as in Figure 2), and in this sense the 3-body Green's function does provide a very good approximation.

It is obviously of interest to explore these systems' fluorescence profiles at longer times where the three-body approximation breaks down, since no current theory describes this regime accurately. This can be achieved using longer counting times in sample cells short enough to inhibit dynamic self-absorption effects, provided excitation trapping can be suppressed by minimizing dye aggregation. Such experiments are being developed in our laboratory.

Acknowledgements

The Ames Laboratory is operated for the U.S. Department of Energy by Iowa State University under Contract No. W-7405-Eng-82. This work was supported by the Office of Basic Energy Sciences. We thank Professor Michael Fayer for valuable discussions, and are indebted to Robert Crackel for his help with the corrections for self-absorption.

References

1. Förster, T. Discuss. Faraday Soc. 1959, 27, 7.
2. Galanin, M. D. Trudy Fiz. Inst. 1950, 5, 339.
3. Vavilov, S. I. Zh. Eksp. Teor. Fiz. 1943, 13, 13.
4. Craver, F. W.; Knox, R. S. Mol. Phys. 1971, 22, 385.
5. Craver, F. W. Mol. Phys. 1971, 22, 403.
6. Ore, A. J. Chem. Phys. 1959, 31, 442.
7. Gochanour, C. R.; Andersen, H. C.; Fayer, M. D. J. Chem. Phys. 1979, 70, 4254.
8. Förster, Th. Ann. der Phys. 1948, 6, 55.
9. Gochanour, C. R.; Fayer, M. D. J. Phys. Chem. 1981, 85, 1989.
10. O'Connor, D. V.; Phillips, D. "Time-correlated Single Photon Counting", Academic Press: New York, 1984.
11. Grinvald, A.; Steinberg, I. Z. Anal. Biochem. 1974, 59, 583.
12. Hammond, P. R. J. Chem. Phys. 1979, 70, 3884.

13. Yasa, Z. A.; Amer, N. M. Opt. Commun. 1981, 36, 406.

14. Marquardt, D. W. J. Soc. Ind. Appl. Math. 1963, 11, 431.

15. Stehfest, H. Commun. ACM 1970, 13, 47.

16. Anfinrud, P.; Crackel, R. L.; Struve, W. S. J. Phys. Chem. 1984, 88, 5873.

17. Loring, R. F.; Andersen, H. C.; Fayer, M. D. J. Chem. Phys. 1982, 76, 2015.

18. Knutson, J. R.; Beechem, J. M.; Brand, L. Chem. Phys. Lett. 1983, 102, 501.

19. Miller, R. J. D.; Pierre, M.; Fayer, M. D. J. Chem. Phys. 1983, 78, 5138.

20. Fedorenko, S. G.; Burshtein, A. I. Chem. Phys. 1985, 98, 341.

21. Vugmeister, B. E. Phys. Status Solidi 1978, 906, 711.

22. Förster, Th. Z. Naturforsch., A: Astrophys., Phys. Phys. Chem. 1949, 4A, 321.

EXCITATION TRANSPORT IN SOLUTION: A QUANTITATIVE COMPARISON BETWEEN GAF THEORY AND TIME-RESOLVED FLUORESCENCE PROFILES

Philip A. Anfinrud, David E. Hart, and Walter S. Struve

Department of Chemistry and Ames Laboratory - USDOE
Iowa State University, Ames, Iowa 50011

EXCITATION TRANSPORT IN SOLUTION: A QUANTITATIVE COMPARISON BETWEEN GAF THEORY AND TIME-RESOLVED FLUORESCENCE PROFILES

Introduction

There has been a resurgence of interest in the problem of electronic singlet excitation transport in solution, where the transport rates are governed by Förster dipole-dipole coupling [1]. One of the properties which characterizes transport in a system of N identical molecules which are randomly distributed in space is $G^S(t)$, the time-dependent probability that the excitation resides on the molecule which was initially excited at t=0. The calculation of $G^S(t)$ is a challenging theoretical problem: excitation can return to the initial site via hopping trajectories with unlimited length and topology, and an infinite-order density expansion must be summed to evaluate $G^S(t)$ exactly.

Gochanour, Andersen, and Fayer [2] (hereafter GAF), formulated diagrammatic expansions of the Laplace transform $\hat{G}^S(\varepsilon)$ of $G^S(t)$ in powers of ε. Using a series of self-consistent approximations, they obtained compact analytic expressions for infinite-order partial sums of the $\hat{G}^S(\varepsilon)$ expansions. These approximations to the Laplace transform were inverted numerically for selected molecule number

densities to obtain the two lowest-order self-consistent approximations (the 2-body and 3-body approximations) to $G^s(t)$. An intriguing feature of the GAF theory was the relative simplicity of its expressions for $\hat{G}^s(\varepsilon)$, since no assumptions limiting either the number of excitation hops [3, 4] or the number of neighboring molecules involved [5] were made. The 2-body and 3-body approximations both yielded mean-squared displacements $\langle r^2(t)\rangle$ approaching 6Dt at long times, where the diffusion coefficent D exhibited a correct number density dependence. D itself varied with t at early times, suggesting that the self-consistent approximations can at least qualitatively describe the transition from the nondiffusive (short-time, low-density) to diffusive (long time, high density) regimes.

There is no guarantee that the series of self-consistent approximations converges rapidly to the true Green's function $G^s(t)$. Fedorenko and Burshtein [6] recently analyzed the 2- and 3-body theories by showing that $\hat{G}^s(\varepsilon)$ can be inverted analytically. They demonstrated that while the exact Green's function must behave as [7]

$$G^s(t) \rightarrow \left[\frac{2\tau}{\pi C^2 t}\right]^{3/2} \qquad (1)$$

for times $t >> 18\tau/\pi C^2$ (where τ is the isolated-molecule excited state lifetime and C is a dimensionless molecule number density defined in Experimental Section and Data

Analysis Section), the 3-body Green's function behaves as

$$G^S(t) \rightarrow \frac{8}{\pi^{1}/2}\left[\frac{8\tau}{\pi^2 C^2 t}\right]^{3/2}\exp(-0.1197C^2t/\tau) \qquad (2)$$

at long times. The asymptotic 2-body Green's function differs from this only in the substitution of 0.3084 for the number 0.1197 in Eq. 2, so that the 3-body theory does not substantially correct the 2-body theory in this regime. The basic validity of the self-consistent equation used for generating the partial sums has also been questioned [8].

From the experimental perspective, the pertinent time regime is not so much the asymptotic region where Eq. 1 applies ($t \gtrsim 6\tau$ for $C = 1$, where the fluorescence count rate falls to $< 2 \times 10^{-3}$ times the peak count rate), but rather the physically interesting regime where $G^S(t)$ is falling violently during the transition from nondiffusive to diffusive behavior. In the absence of excitation traps (the "migration limit"), there is no expression for $G^S(t)$ whose accuracy has been confirmed at such times. In 3-dimensional disordered systems, $G^S(t)$ is related to the fluorescence intensity components $I_{\parallel}(t)$ and $I_{\perp}(t)$ polarized along and normal to the laser excitation polarization by [9]

$$I_{\parallel}(t) = P(t)[1 + 0.8\ G^{S}(t)],$$

$$I_{\perp}(t) = P(t)[1 - 0.4\ G^{S}(t)] \qquad (3)$$

when the solvent is viscous enough to inhibit rotational depolarization, when the absorption and fluorescence transition moments are parallel, and when the exciting beam is sufficiently weak not to perturb the random orientational distribution of transition moments in unexcited molecules. P(t) is the isotropic decay function, which is single-exponential in the absence of excitation trapping of other artifacts. Gochanour and Fayer [9] measured polarized fluorescence profiles for rhodamine 6G in glycerol, and compared them with convolutions of their experimental response function with the 3-body approximation to $G^{S}(t)$. They obtained excellent visual agreement for $t<2.5\tau$ and concentrations up to 5.3×10^{-3} M. Anfinrud et al. [10] obtained a more stringent test of the 3-body theory for rhodamine 6G in glycerol using time-correlated photon counting, which can afford higher S/N ratios than profiles generated by KDP frequency-mixing of dye fluorescence with delayed 1.06 μm pulses from a Q-switched mode-locked Nd:YAG laser [9]. The photon-counting profiles were closely simulated using Eqs. 3 with the 3-body $G^{S}(t)$ for dye concentrations between 1.7×10^{-4} and 2.4×10^{-3} M. However, the experimental profiles proved to be strongly

distorted by self-absorption [11] (which dilates the measured isotropic lifetime τ and artificially inflated the observed depolarization) and by excitation trapping (which renders the isotropic decay nonexponential and truncates the depolarization). These artifacts dominated the differences between the experimental and optimized theoretical profiles.

In this work, we report photon-counting profiles for DODCI in glycerol. The large overlap between the absorption and fluorescence spectra in xanthene and carbocyanine dyes requires the use of fluorescence cells $\lesssim 2$ μm thick to avert self-absorption effects a millimolar concentrations [11]; cell thicknesses of 10 μm [10] and 5 to 300 μm [9] were used in earlier work. DODCI has a shorter isotropic lifetime τ than rhodamine 6G in glycerol (~1.7 vs. ~3.4 ns), giving an expanded dynamic range for testing $G^S(t)$ with our observation window (~10 ns). Longer counting times were employed to yield ~10^5 counts (S/N ~ 300) in the peak channel. With these modifications, the residuals between the experimental and 3-body theoretical profiles are no longer dominated by either self-absorption or trapping effects at concentrations below ~10^{-3} M.

It should be stressed here that extremely high precision is needed to achieve meaningful tests of transport theories using polarized fluorescence profiles. For illustration, we show convolutions in Fig. 1 of an instrument response function (generated by numerical convolutions of a 100 ps

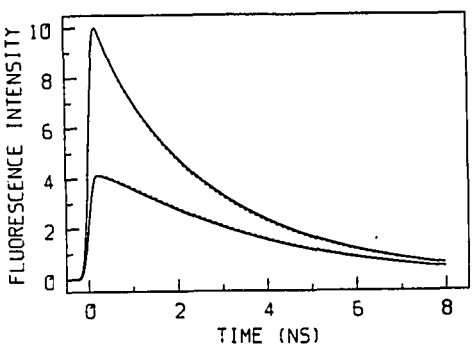

Figure 1. Convolutions of a model instrument function (generated by numerical convolution of a 100 ps FWHM Gaussian function with a 140 ps FWHM Gaussian function) with Eqs. 3 for $I_{\parallel}(t)$ and $I_{\perp}(t)$. The GAF 2-body and 3-body approximations are used for $G^{s}(t)$. From top to bottom, the plotted curves are 3-body $I_{\parallel}(t)$, 2-body $I_{\parallel}(t)$, 2-body $I_{\perp}(t)$, and 3-body $I_{\perp}(t)$. The reduced concentration C and isotropic lifetime τ are 0.83 and 3.1 ns, respectively

FWHM Gaussian excitation pulse with a 140 ps FWHM Gaussian detection pulse to simulate the experimental conditions reported by Gochanour and Fayer [9]) with Eqs. 3 for $I_{\parallel}(t)$ and $I_{\perp}(t)$ using the 2-body and 3-body approximations to $G^{s}(t)$ with C = 0.83, τ = 3.1 ns. It is clear that earlier tests of GAF theory [9, 10] were barely precise enough to differentiate between the 2-body and 3-body theories for C~1, let alone test details of the 3-body theory. In our earlier photon-counting work [10] we accumulated ~10^4 counts in the peak channel, yielding S/N$\lesssim 10^2$; larger fluctuations characterized the profiles generated by frequency-mixing gating [9]. This underscores the need for a careful study of possible experimental artifacts. In addition to self-absorption and trapping, we have considered and eliminated intrinsic depolarization, 2-dimensional (thin-cell) effects, solvent reorganization, scattered light, background emission, filter fluorescence, polarizer alignment, and rate dependence in the photon counting time-to-amplitude converter as important contributions to the differences between our experimental and theoretical profiles.

Experimental Section and Data Analysis

The mode-locked argon ion laser, synchronously pumped rhodamine 590 laser, and cavity dumper produced tunable pulses with ~8 ps FWHM and 4.8 MHz repetition rate as

described previously [10]. Commercial DODCI was obtained from Excitation. A $\lambda/20$, 2.5 cm dia fused silica substrate was commercially coated with Al and MgF_2 overcoat (CVI Laser Corporation); a 9mm dia region of this coating was removed by etching with HF solution. Solutions of DODCI in glycerol were compressed between this optic and an uncoated $\lambda/20$ fused silica substrate. Absorption spectra of rhodamine 6G solutions in this cell (in which the unetched Al/MgF_2 coating served as a spacer), combined with the absorption coefficient derived from spectra of standard rhodamine 6G solution in a 1 cm cell, indicated that the ultrashort cell thickness was between 1.5 and 2.0 μm.

In the first set of fluorescence experiments reported in this paper, the optics and photon-counting electronics were nearly identical to those used in the rhoodamine 6G work [10]. Horizontally polarized dye laser pulses entered the ultrashort cell at ~75° incidence from the surface normal, and fluorescence was collected along the normal with a 10 cm focal length quartz lens. Two 3mm Scott OG-590 filters and one CVI multilayer dielectric sharp-cutoff filter (hereafter referred to as filter combination A) screened lased scatter from the detector. The fluorescence detection and photon-counting system were built around Hamamatsu 1564U microchannel plate phototube (MCP), a B&H Electronics AC3011 MIC (3.15 GHz) 21dB preamplifier, Tennelec TC 455 and Ortec 934 quad constant-fraction discriminators (CFDs), and an

Ortec 457 time-to-amplitude converter (TAC). Since the discriminators accepted only negative-going pulses, an EG&G IT100 inverting transformer processed the positive-going output from the B&H preamplifier. The TAC output was stored in a Canberra Series 30 multichannel analyzer operated in the pulse height analysis mode with 20 ps/channel resolution. The excitation wavelength was 575 nm. Instrument functions for deconvolution were obtained by scattering 575 nm pulses from a clean silica substrate, and were typically ~80 ps FWHM.

In a second series of fluorescence experiments, several modifications were incorporated in the optics and electronsic. One channel of the Tennelec TC455 constant-fraction discriminator was modified to accept positive-going input pulses directly from the preamplifier, obviating the EG&G IT100 inverting transformer used in earlier work. The input circuitry leading to the zero-crossing comparator in the TC455, designed for triggering by pulses with ~1 ns rise time, was rebuilt to accommodate the somewhat faster rise time pulses from the MCP/preamplifier. Time-to-amplitude conversion in the TAC proved to be influenced by the count rate, causing instrument function broadening that could be minimized by restricting the count rate to below ~1kHz [12]. A 125 μs gating pulse was derived from the true START output of the TAC using a Tektronix PG501 pulse generator, and was used to gate the TAC off for this time

period. This effectively eliminated TAC rate dependence for count rates up to ~8kHz, the limit imposed by the 125 μs gating period. Shorter gating periods produced detectable instrument function broadening at count rates $\gtrsim$ 1kHz; omission of gating yielded ~15 ps broadening at 10 kHz count rate. Discrimination of START and STOP pulses was accomplished using two channels of the Tennelec TC455 CFD, rather than one channel in each of the Ortec 934 and Tennelec TC455 discriminators. With these changes, a ~47 ps FWHM instrument function was obtained which was independent of count rate. The latter was typically ~5 kHz. DODCI samples in this series were excited at 570 rather than 575 nm, and 3 mm Schott filters (filter combination B) superseded the filters (combination A) used in the first series. The instrument function sharpening and the change in excitation wavelength had minimal effects on the measured fluorescence dynamics. Altering the filter combination produced observable changes; the experimental conditions pertinent to each data set are specified in what follows by naming the filter combination used.

For each DODCI sample, fluorescence profiles were accumulated with an analyzing polarizer (Promaster Spectrum 7) aligned in each of three positions: along the excitation polarization, normal to the excitation polarization, and at the magic angle θ = 54.7° from the excitation polarization. These yielded the experimental profiles $I_{\parallel}(t)$, $I_{\perp}(t)$, and

$I_{\parallel}(t)\cos^2\theta + I_{\perp}(t)\sin^2\theta \equiv P(t)$, respectively, according to Eqs. 3. The differential apparatus sensitivity to fluorescence photons polarized was less than 2%.

Fluorescence profiles were transferred to a DEC MINC-23 minicomputer equipped with Winchester and dual floppy disk drives operating in a TSX-Plus multiuser environment. The convolute-and-compare analysis employed Marquardt nonlinear least-squares regression [13] to minimize χ^2, the sum of weighted squares of residuals between the number of fluorescence counts in each channel n and the discrete convolution

$$C_n = \sum_{i=1}^{n} x(i - s)I(n - i) \qquad (4)$$

of the instrument function x(t) with the decay law I(t). Here s is an adjustable integer (the shift parameter), and I(t) is an arbitrary model function with an arbitrary number of adjustable parameters. For magic-angle profiles accumulated with filter combination A, a single-exponential model function $P(t) = A \exp(-t/\tau)$ with adjustable lifetime τ was initially used. Equations 3 were then used as model functions for the anisotropic profiles $I_{\parallel}(t)$ and $I_{\perp}(t)$, with $G^S(t)$ given in the GAF 3-body approximation by the inverse Laplace transform of

$$\hat{G}^S(\varepsilon) = \tau\{(\pi^2\gamma^2C^2/4)[1-[1 + (32/\pi^2\gamma^2C^2) \times (\varepsilon\tau - 0.1887\gamma^2C^2)]^{1/2}] + 4(\varepsilon\tau - 0.1887\gamma C^2)\}/[4(\varepsilon\tau - 0.1887\gamma C^2)^2]. \quad (5)$$

The constant $\gamma = 0.846$ results from the dipole-dipole orientation dependence of the transport probability w_{jk} between molecules j and k. C is the dimensionless reduced concentration

$$C = \frac{4}{3}\pi R_o^3\rho, \quad (6)$$

with ρ equal to the dye molecule number density and R_o equal to the Förster parameter [1] characterizing the transport probability

$$\omega_{jk} = \frac{3}{2\tau}\left[\frac{R_o}{r_{jk}}\right]^6[\hat{d}_j\cdot\hat{d}_k - 3(\hat{d}_j\cdot\hat{r}_{jk})(\hat{d}_k\cdot\hat{r}_{jk})]^2 \quad (7)$$

between dye molecules separated by $\vec{r}_{jk}$ and having transition moments along $\hat{d}_j$ and $\hat{d}_k$.

$G^S(t)$ depends on two parameters, the isotropic lifetime τ and the reduced concentration C. In the earlier experimental runs obtained with filter combination A, covariance between τ and C in fitting $I_{\parallel}(t)$ and $I_{\perp}(t)$ was effectively suppressed by first obtaining an initial value of τ at each concentration from single-exponential

convolute-and-compare analysis of the magic-angle profile. Using this initial choice for τ, the $I_{\parallel}$ and $I_{\perp}$ profiles could be deconvoluted in tandem by minimizing their combined χ^2 [10, 14] with respect to A, s, τ, and C. Tests of this fitting procedure on simulated polarized fluorescence data with Gaussian noise [10] indicate that it inhibits covariance because changes in τ (or C) have opposite effects on $I_{\parallel}(t)$ and $I_{\perp}(t)$ via Eqs. 3. The optimum shift parameter s was determined by fitting profiles over the entire MCA channel range. The final fit was then performed with fixed shift parameter over a range beginning with a channel on the rising edge at ~90% peak counts, since the discreteness of the 20 ps channel spacing otherwise resulted in artificially large contributions to χ^2 from earlier channels on the rising edge.

Apart from yielding τ values for deconvolution of the anisotropic profiles, analysis of the magic-angle profiles provides a useful diagnostic for data artifacts. Figure 2 shows a magic-angle profile for 2.28×10^{-3} M DODCI in glycerol, which typifies our counting statistics (72,000 - 120,000 peak channel counts) and quality of single-exponential fits. In Table I, we list the results of single-exponential fits to magic-angle profiles for DODCI concentrations between 1.19×10^{-5} and 2.49×10^{-3} M. For concentrations up to 1.23×10^{-3} M, the lifetimes vary insignificantly (<2%) from a mean of 1.72 ns - implying that

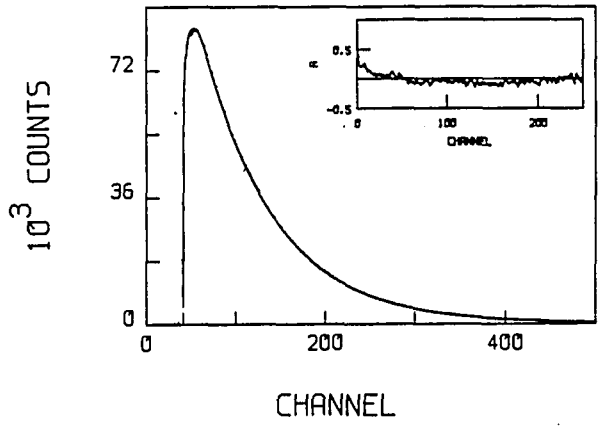

Figure 2. Magic angle fluorescence profile for 2.28×10^{-3} M DODCI in glycerol, obtained using 2μm cell length and filter combination A (see text). Continuous curve is optimized convolution of instrument function with single-exponential model function (τ = 1.61 ns, χ^2_r = 1.836). Inset shows autocorrelation of weighted residuals. Time calibration is 20 ps/channel

Table I. Magic angle fits of DODCI fluorescence profiles[a]

$I(t) = A \exp(-t/\tau)$

Concentration, M	τ,ns	χ_r^2
1.19×10^{-5}	1.71	2.407
	1.68	1.478
	1.69	1.354
1.63×10^{-4}	1.70	1.138
	1.72	1.320
	1.71	2.110
2.54×10^{-4}	1.72	1.734
3.88×10^{-4}	1.74	2.370
	1.74	2.721
5.85×10^{-4}	1.71	2.898
	1.73	4.406
1.23×10^{-3}	1.74	4.828
1.95×10^{-3}	1.67	3.297
2.28×10^{-3}	1.61	1.836
	1.61	2.009
2.49×10^{-3}	1.59	2.783
	1.60	2.317

[a]Accumulated using filter combination A (see the text).

effects of self-absorption on τ have been virtually eliminated at these concentrations by using 2 μm cell length. Quantitative calculation of the expected distortion in τ due to self-absorption [11], using the absorption and fluorescence spectra of DODCI in glycerol, predicts <3% dilation for concentrations as high as 10^{-3} M in a 2 μm cell. Much larger τ variation was observed in 10 μm rhodamine 6G solutions over a similar concentration range due to self-absorption [10]. At higher concentrations, τ becomes increasingly shortened by excitation trapping by dye aggregates whose density increases with dye concentration.

Figure 2 exemplifies an additional artifact, which shows up as a small discrepancy between the experimental magic-angle profile (discrete points) and the convolution of the optimized single-exponential decay law with the instrument function (continuous curve) over the first ~10 channels near the peak. This phenomenon is readily seen only under present of superior counting statistics. It arises from solvent reorganization: the first few solvent coordination layers react to the dipole moment change accompanying the $S_1 \leftarrow S_0$ transition and the fluorescence spectrum dynamically shifts [15], altering the fraction of the fluorescence spectrum transmitted by the cutoff filters. The inset plot in Fig. 2 displays the autocorrelation of weighted residuals [10, 16], which consists of statistical fluctuations about zero autocorrelation in the case of a perfect fit [17].

This autocorrelation is dominated by nonstatistical contributions in the first few channels. To confirm that these discrepancies arise from solvent reorganization, the filter combination A used in the first set of experiments was replaced with combination B. The accompanying change in spectral sensitivity is shown in Fig. 3, which contrasts the sensitivities of combination A and combination B when used with the Hamamatsu 1564U MCP photocathode. For comparison, we superimposed the DODCI fluorescence spectrum from 10^{-3} M glycerol solution in a thin cell (normalized to photocathode response and Jobin-Yvon H-20 monochromator transmission). The peak sensitivities using combination A (~645 nm) and combination B (~605 nm) lie considerably to the red and slightly to the blue, respectively, of the DODCI fluorescence maximum at ~610 nm. The nonexponential behavior detected in magic-angle profiles using both of these filter combinations was characterized by fitting them with the biexponential function $A_1 \exp(-t/\tau_1) + A_2 \exp(-t/\tau_2)$, in which the long-component lifetime τ_2 is similar to the single-exponential lifetimes τ in Table I and the preexponential factor A_1 is a measure of the early-time nonexponentiality. Negative A_1 were generally required for good biexponential fits to profiles accumulated with combination A (Table II): the fluorescence spectrum at early times is blue-shifted from the static spectrum shown in Fig. 3, and at such times the reduced overlap between the

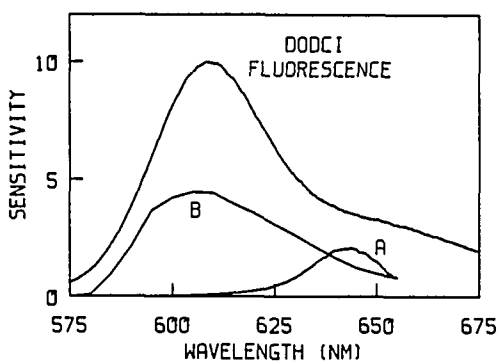

Figure 3. Spectral sensitivity of microchannel plate detector with (a) filter combination A and (b) filter combination B, superimposed on fluorescence spectrum of 1×10^{-3} M DODCI in glycerol. All spectra were evaluated using a Jobin-Yvon H20 monochromator ($\Delta\lambda$ = 0.5 nm) and Philips 56DUVP phototube; spectral sensitivity curves are corrected for MCP response using published sensitivities of MCP and 56DUVP phototubes

Table II. Magic angle fits of DODCI fluorescence profiles[a]

$$I(t) = A_1 \exp(-t/\tau_1) + A_2 \exp(t/\tau_2)$$

Concentration, M	A_1	τ_1,ns	A_2	τ_2,ns	χ_r^2
1.19×10^{-5}	-0.0624	0.252	1.062	1.70	0.9619
	-0.0060	0.927	1.006	1.68	1.479
1.63×10^{-4}	-0.0161	0.441	1.016	1.69	0.9859
	-0.0463	1.03	1.046	1.70	1.115
	-0.0514	0.899	1.051	1.69	1.394
2.54×10^{-4}	-0.0461	0.776	1.046	1.70	1.053
3.88×10^{-4}	-0.0543	0.640	1.054	1.72	0.9874
	-0.1027	1.15	1.103	1.70	2.197
5.85×10^{-4}	-0.0699	0.605	1.070	1.69	1.100
	-0.0834	0.495	1.083	1.70	1.133
1.23×10^{-3}	-0.1024	0.296	1.102	1.72	1.224
1.95×10^{-3}	-0.1090	0.146	1.109	1.66	1.190
2.28×10^{-3}	-0.1577	0.039	1.158	1.61	1.161
	-0.0482	0.065	1.048	1.61	1.857
2.49×10^{-3}	-0.0722	0.041	1.072	1.59	2.679
	-0.1093	1.14	0.8907	1.64	1.353

[a]Accumulated using filter combination A.

fluorescence spectrum and the spectral sensitivity depresses the photon counts. (This effect is apparent in the magic-angle profile of Fig. 2, which was obtained using combination A.) Optimal biexponential fits to profiles taken using combination B yielded positive A_1 (Table III), since the sensitivity of this combination overlaps the early-time blue-shifted spectrum somewhat more than it overlaps the static spectrum. In the latter case, near-perfect biexponential fits were obtained (χ_r^2 = 0.995 to 1.257, as compared to χ_r^2 = 1.1387 to 4.828 for the single-exponential fits in Table I). The long-component lifetimes τ_2 in Tables II and III exhibit trends similar to that of the lifetimes τ in Table I: τ_2 varies by less than 3% except at the highest concentrations, where the decay is significantly accelerated by trapping. At such concentrations, comparisons of our anisotropic fluorescence data with transport theory become suspect. In our view, the contrasting early-time deviations from exponentiality in magic-angle profiles obtained using the two filter combinations is convincing evidence that they originate from dynamic spectral shifts accompanying solvent reorganization. We have observed similar trends in nonexponentiality of isotropic profiles from rhodamine 640 in glycerol.

Table III. Magic angle fits of DODCI fluorescence profiles[a]

$$I(t) = A_1 \exp(-t/\tau_1) + A_2 \exp(t/\tau_2)$$

Concentration, M	A_1	τ_1,ns	A_2	τ_2,ns	χ_r^2
1.84×10^{-4}	0.0658	0.779	0.9342	1.651	0.995
3.25×10^{-4}	0.0528	0.8250	0.9472	1.662	1.148
5.70×10^{-4}	0.0708	1.043	0.9294	1.674	1.152
9.95×10^{-4}	0.2211	1.381	0.7789	1.690	1.044
1.78×10^{-3}	0.2135	1.195	0.7865	1.663	1.257
3.00×10^{-3}	0.1850	0.8561	0.8150	1.535	1.077

[a]Accumulated using filter combination B.

Results and Discussion

Results of convolute-and-compare analysis of the anisotropic fluorescence profiles using the 3-body Green's function for $G^S(t)$ are summarized in Tables IV and V for data accumulated using filter combination A and B, respectively. Profiles obtained using combination A were fitted with the functions $I_\parallel(t)$ and $I_\perp(t)$ in Eqs. 3, using the isotropic function $P(t) = b_1 \exp(-t/\tau)[1 - b_2 \times \exp(-t/\tau')]$. Only C, b_1, and τ were floated. The initial τ values were taken from the long-component lifetimes t_2 from the biexponential fits in Table II, while the τ' values were fixed at $(1/\tau_1 - 1/\tau_2)^{-1}$ and the b_2 values were fixed at A_1/A_2. For profiles obtained using combination B, the isotropic decay function P(t) in Eqs. 3 was represented by biexponential decay functions in which A_1, A_2, τ_1, and τ_2 were fixed at the values listed in Table III. Only C and a scaling parameter were allowed to vary for these profiles; the lifetime parameter τ in $G^S(t)$ [Eq. 5] was held at 1.665 ns, which well approximates τ_2 from biexponential fits to the isotropic profiles at all but the highest DODCI concentration (Table III). Representative plots of anistropic photon-counting profiles with optimized convolutions of the instrument function with Eqs. 3 are shown in Fig. 4 for two contrasting concentrations (1.63×10^{-4} and 2.28×10^{-3}M). The physical depolarization is

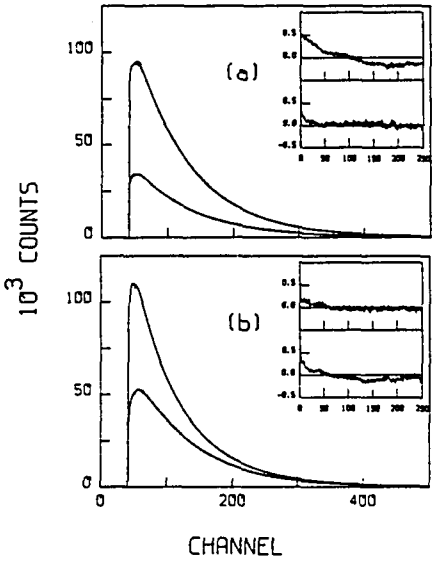

Figure 4. Fluorescence profiles $I_{\parallel}(t)$ and $I_{\perp}(t)$ for (a) 1.63×10^{-4} M and (b) 2.28×10^{-3} M DODCI in glycerol, obtained using 2 μm cell length and filter combination A. Continuous curves are optimized convolutions of Eqs. 3, using 3-body Green's function, with the instrument function. Upper and lower inset plots show autocorrelations of weighted residuals for $I_{\parallel}(t)$ and $I_{\perp}(t)$, respectively. Time calibration is 20 ps/channel

Table IV. Fitting parameters for anisotropic fluorescence profiles[a]

Concentration, M	τ,ns	C	χ_r^2
1.19×10^{-5}	1.71	0.079	2.270
	1.69	0.063	1.421
	1.68	0.056	2.081
1.63×10^{-4}	1.71	0.124	1.767
	1.72	0.116	1.702
	1.72	0.118	2.190
2.54×10^{-4}	1.72	0.163	2.590
3.88×10^{-4}	1.76	0.233	3.636
	1.75	0.226	2.402
5.85×10^{-4}	1.71	0.318	2.797
	1.74	0.307	4.931
1.23×10^{-3}	1.75	0.540	5.359
1.95×10^{-3}	1.67	0.691	3.572
2.28×10^{-3}	1.63	0.775	2.358
	1.61	0.726	2.197
2.49×10^{-3}	1.61	0.797	2.652
	1.61	0.819	2.694

[a]Accumulated using filter combination A.

Table V. Fitting parameters for anisotropic fluorescence profiles[a]

Concentration, M	C	χ_r^2 (combined)
1.84×10^{-4}	0.116	1.788
3.25×10^{-4}	0.212	1.841
5.70×10^{-4}	0.331	1.599
9.95×10^{-4}	0.492	1.463
1.78×10^{-3}	0.668	1.594
3.00×10^{-3}	0.846	1.472

[a]Accumulated using filter combination B.

noticeably more rapid at the higher concentration (Fig. 4b), where the $I_{\parallel}$ and $I_{\perp}$ profiles merge to within a standard deviation well before the end of the window. The quality of fit (as judged by the autocorrelations of weighted residuals in the inset plots) is not markedly different in Figs. 4a and b, because the residuals are dominated in the first 50 channels by solvent reorganization effects which appear independently of concentration. The reorganization artifacts were not apparent in our earlier rhodamine 6G work [10], in which ~12,000 peak channel counts were typically collected.

The optimized reduced concentrations $C \equiv (4/3)\pi R_0^3 \rho$ vary smoothly with actual DODCI concentration M, as shown in Fig. 5a and b for data obtained using filter combinations A and B, respectively. Data points for concentrations lower than 1.63×10^{-4}M are not included in this figure, because $\partial G^S(t)/\partial C$ became so small at such concentrations that the Marquardt algorithm does not converge with the present S/N ratios. The points at higher concentrations should ideally form a locus with constant Förster parameter R_0. The R_0 value computed [1] from DODCI absorption and fluorescence spectra and the refractive index of glycerol is ~64Å. The points in Fig. 5 lie near R_0 ~63 to 65Å at the lowest DODCI concentrations, but skew systematically toward smaller R_0 at higher concentrations. Since artificially small R_0 values are then required for the 3-body theory to replicate the

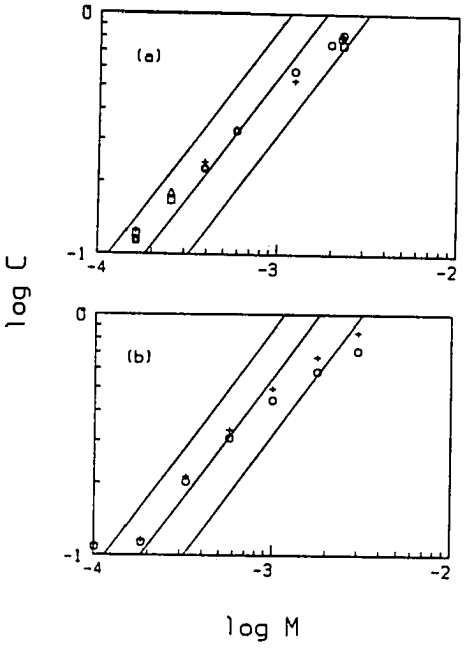

Figure 5. Optimized reduced concentrations C vs. actual DODCI concentrations M, from linked deconvolutions of $I_{\parallel}$ and $I_{\perp}$ profiles collected using (a) filter combination A and (b) filter combination B. Straight lines give loci of true reduced concentrations vs. M for (from left) R_o = 70, 60, and 50Å. In (a), different symbols represent 3-body fits to anisotropic profiles from different experimental runs. In (b), a single run at each concentration is analyzed using the 2-body (O) and 3-body (+) approximation to $G^s(t)$

experimental profiles, the observed decay in $G^S(t)$ is slower than that predicted by the 3-body theory by an amount which increases with dye concentration. This skewing trend is clearly unaffected by the filter combination used to accumulate the profiles. Since the nonexponential deviations attending solvent reorganization in the magic-angle profiles exhibit opposite signs for the two filter combinations, the similarity of Figs. 5a and b is evidence that the skewing is not a solvent reorganization artifact. The anisotropic profiles collected using combination A were also deconvoluted using single-exponential functions with floating τ for $P(t)$ in $I_{\parallel}(t)$ and $I_{\perp}(t)$. This procedure generated a plot similar to those in Fig. 5, implying that these results are not sensitive to details of modeling the isotropic decay. It should be noted that optimized reduced concentrations C are displayed in Fig. 5b for fits using the 2-body as well as 3-body approximation for $G^S(t)$. The C values for the 2-body fits are systematically lower than those for the 3-body fits, because the 2-body approximation to $G^S(t)$ decays more rapidly than the 3-body approximation by an amount which increases with C [2]. The skewing in Fig. 5 indicates that the true $G^S(t)$ in our DODCI solutions decays more slowly than either of these approximations. The distinctions which show up in Fig. 5(b) between the 2-body and 3-body fits would be difficult to measure with the S/N available in earlier depolarization experiments [9, 10].

The deviations exhibited at the higher concentrations in Fig. 5 are physically large, Since excitation trapping by DODCI aggregates visibly distorts the magic-angle profiles at the three highest concentrations in Table I and the two highest concentrations in Table III, the points extracted from anisotropic profiles at these concentrations in Figs. 5a and b respectively may be influenced by this artifact. However, appreciable skewing is evident at lower concentrations ($\lesssim 10^{-3}$M), where analyses of isotropic profiles show little distortion from self-absorption or trapping. Fitting the anisotropic profiles between ~10^{-4} and 6×10^{-4}M in Fig. 5a required adjustment of R_o from ~65 to ~60Å; this artificially decreases the strength of the Förster dipole-dipole interaction (which varies as R_o^6) by a factor of 1.6.

Another phenomenon considered as a source of artifacts was intrinsic depolarization, arising from noncoincidence between the directions of the absorption and emission transition moments in the dye. When these moments form an angle $\lambda \neq 0$, the function $G^s(t)$ in Eqs. 3 must be replaced [18] by $G^s(t)P_2(\cos\lambda)$, where $P_2(\cos\lambda)$ is the second-order Legendre polynomial in $\cos\lambda$. For a number of molecules, λ is small [15]; the value $\lambda = 7.4°$ has been reported for the $S_1 \leftarrow S_o$ transition in DPH [19]. Several of our anisotropic profiles were fitted using variable λ initially set at 10°. The nonlinear least-squares algorithm forced λ toward 0°

(final values of 0.02° to 0.09° were typical). Allowance for intrinsic depolarization did not improve the quality of the fits, nor did it materially influence the optimized C values. Residual emission and laser scatter from a solution cell filled with pure glycerol accumulated peak channel counts which were lower than those characteristic of our fluorescence profiles by factors of $\gtrsim 10^2$, indicating that emission sources other than DODCI contributed negligibly to our profiles. Analyzing polarizer alignment errors were minimal, because the alignment of the perpendicular polarization was accurately set by minimizing the transmission of the polarized laser beam reflected directly off a cell window, and because the alignment benchmarks for the parallel and magic angle positions were machined into the polarizer mount to within an accuracy of ~0.1°. Effects of reduced system dimensionality accompanying the use of 2 μm cells are unlikely, because this cell thickness corresponds to ~300 R_0 for DODCI in glycerol; this migration distance is not typically approached for our solutions during our photon-counting time window.

The 3-body theory is expected to exaggerate the rate of decay in $G^S(t)$ in principle, since it omits 4-body and higher-order processes by which excitation can be returned to the initial donor molecule. GAF compared the decay in $G^S(t)$ in the 2-body and 3-body approximations for $0<t<\tau$ and $C = 1.0, 5.0$; they found that the lower-order 2-body

approximation decays more rapidly. However, it can be argued that at our present concentrations the probability of four donors being close enough together to produce significant 4-body contributions to $G^s(t)$ is negligibly small [20]. Our discrepancies may not be caused by errors in the 3-body theory, but may arise because dye solutions do not resemble the model on which the theory is based. Since the dye tends to aggregate at millimolar concentrations, the probability of finding tightly grouped monomers may be significantly higher than in the random spatial distributions envisioned by the theory.

The question arises why one should focus on testing the GAF theory, because simpler theories for $G^s(t)$ are available. The long-time behavior [7] described in Eq. 1 is expected to become accurate for $t/\tau >> 6/C^2$, which translates into $t >> 10ns/C^2$ for DODCI. This regime is marginally reached at long times in our profiles for the highest concentrations and is not reached in the lower concentrations at all. At the short times where $t/\tau << 6/C^2$, Huber, Hamilton, and Barnett showed that $G^s(t)$ is expected to behave as [21]

$$G^s(t) \rightarrow \exp[- C(\frac{\pi t}{2\tau})^{1/2}]. \qquad (8)$$

In Fig. 6, we show comparative plots of Eq. 8 and the 3-body approximation to $G^s(t)$ for C = 1.0 (which exceeds the

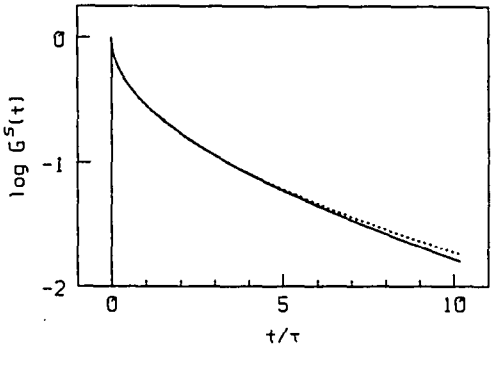

Figure 6. Comparison of the 3-body approximation to $G^S(t)$ (solid curve) and the short-time asymptotic expression (Eq. 8, dashed curve), computed for C = 1.0

highest concentration for which our data are valid) and times out to 10τ. The two functions are remarkably similar. Deconvolutions of representative data were repeated using Eq. 8 instead of the 3-body function for $G^S(t)$, and optimized C values nearly identical to those in Table IV were obtained. It appears fair to say that for the present experimental times and concentrations of interest ($t \lesssim 6\tau$, $C \lesssim 1.0$), Eq. 8 provides as accurate an approximation to $G^S(t)$ as the 3-body theory. The mutual agreement between these theories, coupled with their disagreement with our data, suggests that the discrepancies shown in Fig. 5 arise because real solutions of DODCI in glycerol are not well represented by the assumptions underlying the theories. We have obtained experimental plots similar to those in Fig. 5 for rhodamine 6G in glycerol [10], and thus such discrepancies may be a general property of cyanine and xanthene dyes in alcoholic solution.

Acknowledgements

The Ames Laboratory is operated for the U.S. Department of Energy by Iowa State University under Contract No. W-7405-Eng-82. This work was supported by the Office of Basic Energy Sciences. We thank Professor Michael Fayer and Shaul Mukamel for valuable discussions.

References

1. Förster, T. Discuss. Faraday Soc. 1959, 27, 7.
2. Gochanour, C. R.; Andersen, H. C.; Fayer, M. D. J. Chem. Phys. 1979, 70, 4254.
3. Galanin, M. D. Tr. Fiz. Inst. Akad. Nauk USSR 1950, 5, 339.
4. Vavilov, S. I. JETP 1943, 13, 13.
5. Craver, F. W.; Knox, R. S. Mol. Phys. 1971, 22, 385.
6. Fedorenko, S. G.; Burshtein, A. I. Chem. Phys. 1985, 98, 341.
7. Klafter, J.; Silbey, R. J. Chem. Phys. 1980, 72, 843.
8. Vodunov, E. N.; Malyshev, V. A. Fiz. Tverd. Tela (Leningrad) 1984, 26, 2990.
9. Gochanour, C. R.; Fayer, M. D. J. Phys. Chem. 1981, 85, 1989.
10. Anfinrud, P. A.; Hart, D. E.; Hedstrom, J. F.; Struve, W. S. J. Phys. Chem. 1986, 90, 2374.
11. Hammond, P. R. J. Chem. Phys. 1979, 70, 3884.
12. Bebelaar, D. Rev. Sci. Instrum. 1986, 57, 1116.
13. Marquardt, D. W. J. Soc. Ind. Appl. Math. 1963, 11, 431.
14. Knutson, J. R.; Beechem, J. M.; Brand, L. Chem. Phys. Lett. 1984, 88, 5873.
15. Lakowicz, J. R. "Principles of Fluorescence Spectroscopy", Plenum: New York, 1983; chapter 5.
16. Anfinrud, P.; Crackel, R. L.; Struve, W. S. J. Phys. Chem. 1984, 88, 5873.
17. Grinvald, A.; Steinberg, I. Z. Anal. Biochem. 1974, 59, 583.
18. Chuang, T. J.; Eisenthal, K. B. J. Chem. Phys. 1972, 57, 5094.

19. Shinitzky, M.; Barenholz, Y. J. Biol. Chem. 1974, 249, 2652.

20. Fayer, M. D. Dept. of Chem., Stanford University, private communication.

21. Huber, D. L.; Hamilton, D. S.; Barnett, B. Phys. Rev. B. 1977, 16, 4642.

COMPARISON OF DODCI FLUORESCENCE DEPOLARIZATION IN GLYCEROL AND ETHYLENE GLYCOL: EFFECT OF ORIENTATIONAL CORRELATION ON EXCITATION TRANSPORT

Philip A. Anfinrud and Walter S. Struve

Department of Chemistry and Ames Laboratory - USDOE
Iowa State University, Ames, Iowa 50011

COMPARISON OF DODCI FLUORESCENCE DEPOLARIZATION IN GLYCEROL AND ETHYLENE GLYCOL: EFFECT OF ORIENTATIONAL CORRELATION ON EXCITATION TRANSPORT

Introduction

Our laboratory has recently been assessing fluorescence concentration depolarization techniques as a means of testing electronic excitation transport theories for molecules in disordered systems [1-3]. Fluorescence depolarization measurements are not an inherently sensitive probe of transport, even in systems of randomly oriented molecules [2]. Polarized fluorescence profiles with S/N $> 10^2$ are typically required for meaningful tests of transport theories; small artifacts can easily invalidate such work. In our first study of excitation transport in solution [1], we exploited time-correlated photon counting to monitor fluorescence depolarization from rhodamine 6G at concentrations between 0.17 and 2.4 mM in glycerol. It was shown that artifacts arising from excitation trapping by dye aggregates and from fluorescence self-absorption [4] readily dominate the residuals between experimental fluorescence profiles and profiles calculated from current transport theories, such as the Gochanour-Andersen-Fayer (GAF) self-consistent 3-body theory [5]. These artifacts were minimized in subsequent experiments on DODCI in glycerol

[2], by housing sample solutions in fluorescence cells $\lesssim 2\mu m$ thick and by maintaining dye concentrations below ~ 3 mM to inhibit dye aggregation. Some 10^5 photon counts were typically accumulated in the peak channel of DODCI fluorescence profiles, as compared to ~ 10^4 counts in the rhodamine 6G experiments. Under these conditions, a subtle new artifact became discernible [2] during the first ~ 200 ps of each profile. Its origin was confirmed to be solvent reorganization, which originated from a disparity in dipole moments between the dye S_0 and S_1 electronic states and caused dynamic shifting of the DODCI fluorescence spectrum at early times. (DODCI profiles were monitored for ~ 9 ns, corresponding to ~ 5.3 S_1 state lifetimes in glycerol.) The algebraic sign of this early-time artifact could be manipulated by the choice of optical filter placed between the sample cell and fluorescence detector. In this manner, the solvent reorganization artifact was demonstrated to have little effect on multiparameter fitting of transport theories to our polarized fluorescence profiles.

For all of these precautions, the discrepancies observed between our DODCI profiles [2] and current transport theories [5-7] remained physically large. When randomly oriented, nonrotating molecules in 3 dimensions are excited by a weak, linearly polarized laser pulse, the emitted fluorescence components $I_{\parallel}(t)$ and $I_{\perp}(t)$ polarized parallel and normal to the excitation polarization are approximately

related to the probability $G^S(t)$ that the excitation is found on the initially excited molecule by

$$I_{\parallel}(t) = P(t)[1 + 0.8\ G^S(t)]$$
$$I_{\perp}(t) = P(t)[1 - 0.4\ G^S(t)] \qquad (1)$$

Here P(t) is the isotropic decay function, which is theoretically single-exponential for a sufficiently dilute, homogeneous dye solution. (P(t) was represented by biexponential functions in our earlier DODCI work to account for the solvent reorganization artifact [2].) The Green's function $G^S(t)$ was modeled by either the GAF 3-body theory [5] (which yields a complicated but analytic [6] expression for $G^S(t)$) or the 2-particle theory of Huber et al. [7]. The latter theory predicts that at sufficiently early times and/or low dye concentrations,

$$G^2(t) = \exp[-C(\frac{\pi t}{2\tau})^{1/2}] \qquad (2)$$

Both of these theories contain as parameters the intrinsic excited state lifetime τ and the dimensionless reduced dye concentration

$$C = \frac{4}{3}\pi R_0^3 \rho \qquad (3)$$

where ρ is the molecule number density and R_0 is the Förster parameter [8]. The GAF 3-body and Huber 2-particle theories yield nearly identical decay functions $G^S(t)$ for C = 1.0 and $t \lesssim 5\tau$ [2], so that these two theories are virtually indistinguishable for realizable dye concentrations in glycerol and for measurable time windows. The discrepancies between our polarized DODCI profiles and the Huber 2-particle theory are summarized in Fig. 1, which was generated by fitting data taken from ref. 2. Here the optimized reduced concentration C (obtained by fitting profiles with Eqs. 1, using either GAF 3-body or Huber theory for $G^S(t)$) are plotted versus the actual dye concentration. For a perfect theory, the points in Fig. 1 should fall on a straight line of constant R_0. Since these points skew systematically from $R_0 \sim 63$ Å to $R_0 \sim 53$ Å as M is increased from ~ 0.2 to 1.8 mM, the apparent strength of the dipole-dipole coupling (which scales as R_0^6 [8]) artificially increases by a factor of ~ 2.8. (Detection of even such a large discrepancy required fluorescence profiles with peak S/N ~ 300 ($= \sqrt{10^5}$). We were unable to explain this disagreement.

Since the publication of this work, several possible sources have been considered for the discrepancy. The use of Eqs. 1 to analyze fluorescence data rests on the assumption that the residual polarization

Figure 1. Optimized reduced concentrations C_D versus DODCI concentrations in glycerol, from linked deconvolution of $I_{\parallel}$ and $I_{\perp}$ fluorescence profiles [2] using Eqs. 1. The GAF 3-body and the Huber 2-particle theories for $G^S(t)$ yield similar results. (a) C_D vs. [T]. Straight lines give loci of true reduced concentrations versus monomer concentrations [M] for (from left) R_o = 70 Å, 60 Å, and 50 Å. (b) C_D vs. [T]. Points labeled (O) and (□) were obtained from data analyses considering and neglecting rotational depolarization, respectively. Straight lines correspond to (from left) R_o = 60 Å, 50 Å. (c) C_D versus [M]. Both rotational depolarization and dimerization equilibrium were taken into account. Straight lines correspond to (from left) R_o = 60 Å, 50 Å

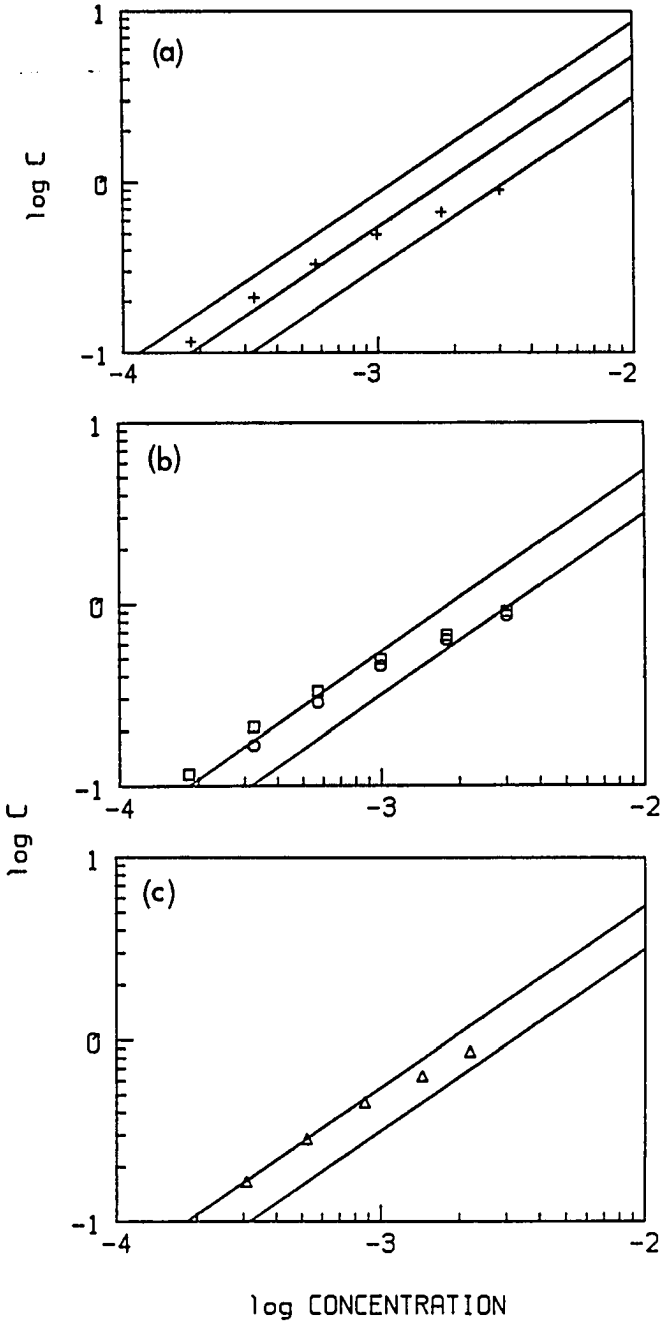
(a)
(b)
(c)
log C
log CONCENTRATION
1
0
-1
-4
-3
-2

$$P_1 = (I_{\parallel} - I_{\perp})/(I_{\parallel} + I_{\perp}) \qquad (4)$$

retained in an orientationally random solution after a single excitation hop from the initially excited molecule is zero. Galanin has shown that $P_1 = 1/42$ in a random 3-dimensional system [9]. We have reanalyzed our DODCI data accordingly [10], and have shown that consideration of this residual polarization barely affects the discrepancy in Fig. 1.

While rotational diffusion of DODCI in glycerol is slow compared to the intrinsic S_1 state decay, it does contribute slightly to the total fluorescence depolarization during our 9 ns time window. This rotational depolarization can be independently characterized in very dilute solution ($\sim 10^{-6}$ M), where excitation transport is negligible. The rotational diffusion component of the total fluorescence depolarization proves to be separable from the excitation transport component, so that transport theories can be tested even in the presence of rotational diffusion. Using an analysis described in the Data Analysis Section, we find that the rotational depolarization of DODCI in glycerol is well described by a single-exponential anisotropy function with lifetime $\tau_{rot} \sim 69$ ns. When the corresponding contribution to the fluorescence depolarization is separated from the transport component, fitting the latter with the Huber 2-particle theory yields the results shown as circles

in Fig. 1(b). For comparison with earlier analyses, this figure also shows the results obtained by neglecting rotational depolarization (squares). While failure to consider rotational diffusion affects all of the data points (particularly at the lower concentrations where transport depolarization is minor), the discrepancy remains large.

A third source of error arises because not all DODCI species exist as monomers in glycerol. The abscissas in Figs. 1(a-b), putatively the dye monomer concentration [M], are actually the total dye concentration $[T] \simeq [M] + 2[M_2]$. Equating [M] with [T] will skew the data points downward at higher concentrations, because the ratio $[M_2]/[M]$ will increase with [T]. We evaluated the dimerization equilibrium constant $K_d = [M_2]/[M]^2$ by obtaining DODCI absorption spectra at several concentrations in glycerol, and by measuring optical densities at the M and M_2 band maxima at 575 and 545 nm respectively. The inferred K_d depends on the values assumed for the absorption coefficients $\varepsilon_{max}(M)$ and $\varepsilon_{max}(M_2)$. A dilute DODCI spectrum yielded the former; the latter is bounded by $\varepsilon_{max}(M) \leq \varepsilon_{max}(M_2) \leq 2\varepsilon_{max}(M)$, depending on the vector addition of monomer transition moments in the dimer [11]. In the worst case [$\varepsilon_{max}(M) = \varepsilon_{max}(M_2)$], it is found that some 27% of DODCI molecules exist in dimers in glycerol when [T] = 3.0 mM. When both rotational depolarization and dimerization

are taken into account (assuming ε_{max} is identical for both M and M_2), the modified plot in Fig. 1(c) results. The data skewing is now significantly reduced, but it is still large.

Yet another possible origin for the discrepancy is nonrandomness in molecular orientations. Since the average separation between DODCI pairs is on the order of 30 Å in our most concentrated solutions, such nonrandomness would have to be a consequence of long-range ordering in the solvent structure. Such ordering is absent in most alcohols at room temperature (Results and Discussion Section). Glycerol has been used in previous fluorescence experiments on solution transport [1,2,12], because its large viscosity (954 cp at 25°C [13]) precludes large contributions to depolarization from rotational diffusion. In liquid glycerol, however, the radial distribution functions derived from X-ray structure factors obtained between 250° and 350° K exhibit coherent oscillations out to separations larger than 25 Å [14]. Hence, sufficiently concentrated DODCI solutions in glycerol are likely to exhibit appreciable orientational correlation between neighboring chromophores. If DODCI neighbors tend to have parallel transition moments, for example, a single excitation hop will produce less depolarization than in an orientationally random sample. The residual polarization P_1 will then become appreciable, rendering Eqs. 1 inapplicable. The nonrandom orientational distributions would also influence the calculation of $G^S(t)$.

The significance of this effect would increase with dye concentration, as the solvent ordering asserts itself at shorter chromophore separations.

In this work, we have obtained polarized fluorescence profiles for DODCI in ethylene glycol, a solvent which does not exhibit comparable long-range ordering at room temperature (Results and Discussion Section). The bulk viscosity of ethylene glycol (17.4 cp at 25°C [13]) is some two orders of magnitude smaller than that of glycerol, and rotational diffusion of DODCI in ethylene glycol contributes substantially to the total fluorescence depolarization observed in that solvent. DODCI dimerization is much less prevalent in ethylene glycol than in glycerol, however. When our DODCI profiles from glycol solutions are analyzed with due attention to rotational depolarization and the dimerization equilibrium, close agreement is obtained with the Huber and GAF 3-body theories (Results and Discussion Section). This result strongly suggests that orientational correlation accounts for most of the unexplained discrepancy exhibited by DODCI/glycerol in Fig. 1(c).

Experimental Section

The tunable picosecond excitation laser system [1], composed of a mode-locked argon ion laser, synchronously pumped rhodamine 590 laser, and cavity dumper, generated 570

nm pulses with ~ 7 ps FWHM at 4.8 MHz repetition rate. DODCI was supplied by Exciton; purified ethylene glycol was obtained from Fisher Scientific, and contributed no background counts to fluorescence profiles from DODCI solutions. DODCI emission was analyzed with a Promaster Spectrum 7 linear polarizer, passed through two 3 mm Schott OG-590 filters, collected with a 10 cm focal length quartz lens, and focussed through a variable rectangular aperture onto a Hamamatsu 1564U microchannel plate phototube (MCP). The time-correlated photon counting electronics [2] included a B&H Electronics AC3011 MIC 3.15 GHz preamplifier, a Tennelec TC455 constant-fraction discriminator (CFD, and an Ortec 457 time-to-amplitude converter (TAC). One channel of the TC455 CFD was modified to accept positive-going pulses from the preamplifier, and generated the START input for the TAC. The STOP input was provided by a second TC455 channel which processed negative-going pulses from an EG&G FOD-100 laser-monitoring photodiode. Cross-talk between the channels (which caused TAC nonlinearity) was eliminated by delaying the photodiode signal relative to the MCP signal in a 15 m fiber optic. Fluorescence profiles were accumulated in a Canberra Series 30 multichannel analyzer with 20 ps/channel resolution. The TAC was automatically gated off by a 125 μs gating pulse derived from the TAC's true START output, effectively eliminating count rate-dependence in time-to-amplitude conversion while allowing count rates up

to ~ 8KHz [2]. Fluorescence profiles were obtained at ~ 5KHz count rate; instrument functions (evaluated by detecting 570 nm laser pulses scattered from a roughened fused silica substrate in place of the sample housing) were ~ 47 ps FWHM.

Polarized DODCI fluorescence profiles were obtained using ethylene glycol solutions in specially designed optical cells with $\lesssim$ 2 μm path length to minimize self-absorption [2]. For excitation transport studies, the DODCI concentrations ranged between 0.315 and 5.61 mM. In separate calibration runs, the rotational diffusion of DODCI in ethylene glycol was studied by obtaining polarized profiles from 0.00098 mM solutions; 100 μm cells were used here without danger of incurring self-absorption artifacts. At the latter concentration, the decay in $G^S(t)$ due to transport is negligible during our ~ 9 ns time window. The ambient temperature during both sets of runs was 23.5°C.

Data Analysis

Fluorescence profiles were accumulated for each DODCI sample with the analyzing polarizer aligned at θ = 0°, 54.7°, and 90° from the laser polarization in order to obtain the experimental $I_{\parallel}(t)$, magic-angle, and $I_{\perp}(t)$ profiles respectively. The isotropic decay function P(t) from the magic-angle profile at each concentration was

fitted with a biexponential decay law using a Marquardt nonlinear least-squares program [15], with the results shown in Table I. The isotropic decay is dominated in all cases by a long component with lifetime τ_1 ~ 1.2 ns in ethylene glycol (vs. 1.7 ns in glycerol [2]). This lifetime is nearly constant for concentrations up to 1.78 mM, and shows no stretching due to self-absorption. At the highest two concentrations (3.14 and 5.61 mM) τ_1 drops to 1.151 and 1.022 ns respectively due to excitation trapping at aggregates. The small short component τ_2 (436 to 563 ps) arises chiefly from the solvent reorganization artifact [2] at the lower concentrations, but may also be influenced by excitation trapping at 3.14 and 5.61 mM. In the course of this work, it became recognized that the commonly used technique for calculating the discrete convolution

$$F(I) = \sum_{J=0}^{I} x(J)DEC(I-J) \tag{5}$$

of the apparatus instrument function X(J) with the fitted decay law DEC(I) is not strictly accurate. Since X(J) is a histogram (rather than continuous) representation of the instrument function, the convolution procedure requires that the discrete function DEC(I) be a histogram representation

$$DEC(I) \equiv \int_{I-1/2}^{I+1/2} DEC(x)dx \tag{6}$$

Table I. Magic angle fits of DODCI fluorescence profiles in ethylene glycol

$$P(t) = a_1 \exp(-t/\tau_1) + a_2 \exp(-t/\tau_2)$$

Concentration, mM	a_1	τ_1, ps	a_2	τ_2, ps	χ_r^2
0.00098	0.903	1297	0.097	563	1.256
0.315	0.898	1284	0.102	509	1.092
0.558	0.908	1271	0.092	436	1.222
0.988	0.905	1260	0.095	458	0.959
1.78	0.870	1237	0.130	508	1.067
3.14	0.838	1151	0.162	483	1.210
5.61	0.617	1022	0.383	504	1.430

of the continuous function DEC(x) instead of

$$DEC(I) = DEC(x)\big|_{x=I} \tag{7}$$

In fitting with the single-exponential decay law $DEC(x) = a\exp(-x/\gamma)$, for example, the discrete decay law should be

$$DEC(I) = a\int_{I-1/2}^{I+1/2} \exp(-x/\gamma)dx$$

$$= a\gamma\{\exp[-(I-1/2)/\gamma] - \exp[-(I + 1/2)/\gamma]\} \tag{8a}$$

$$DEC(0) = a\gamma\{1 - \exp[-1/2\gamma]\} \tag{8b}$$

instead of $DEC(I) = a\exp(-I/\gamma)$. For decay models which cannot be integrated analytically, Simpson's rule is used to generate the histogram representation of DEC(I). The numerical differences between this and earlier [1-3] calculations of the discrete convolution assume importance when DEC(x) changes rapidly during a single channel (20 ps in our work). Hence, the associated errors are concentrated in the peak regions at early times, and they primarily affect the short-component parameters in Table I. They do not materially influence the conclusions reached in earlier work [1-3], where the fitted excitation transport parameters largely depended on fluorescence depolarization evolving over several ns.

The polarized fluorescence profiles obtained at 0.00098 mM (the limit of zero excitation transport) were then fitted with the decay laws

$$I_{\parallel}(t) = a_{\parallel} P(t)[1 + 0.8e^{-6Dt}]$$

$$I_{\perp}(t) = a_{\perp} P(t)[1 - 0.4e^{-6Dt}] \qquad (9)$$

These expressions are applicable to rotational diffusion of a spherical rotor with angle $\lambda = 0°$ between absorption and fluorescence transition moments [16]. The DODCI transition moment lies essentially parallel to the long axis; earlier attempts to fit polarized DODCI profiles in glycerol by floating λ as a parameter [2] tended to force λ toward 0°. Rotational diffusion of an asymmetric rotor in 3 dimensions is characterized by five time constants in general [16]. However, DODCI rotation about the long axis is expected to cause negligible depolarization. The other two rotation axes in this highly prolate molecule will exhibit similar diffusion constants, which are represented by D in Eqs. 9. In fitting these equations to the low-concentration anisotropic profiles, the isotropic decay P(t) was simulated by a biexponential function with fixed parameters taken from the first line of Table I. As in earlier work [1,2], $I_{\parallel}(t)$ and $I_{\perp}(t)$ were fitted simultaneously by optimizing their combined χ_r^2. The only parameters varied were the scaling

factors $a_{\parallel}$, $a_{\perp}$ and the diffusion constant $D \equiv 1/6\tau_{rot}$; their final values are given in Table II. This linked deconvolution of $I_{\parallel}$ and $I_{\perp}$ yields the single reorientation time τ_{rot} = 3.223 ns; the relative qualities of fits are reflected by the values of χ_r^2 calculated separately for each profile following optimization of their combined χ_r^2. In Fig. 2, the experimental isotropic and anisotropic profiles of 0.00098 mM DODCI are compared with their fitted model functions. The isotropic profile P(t) is clearly well described by a biexponential decay law, and the pertinent autocorrelation of residuals [17] is dominated by statistical noise. The anisotropic fits are less good: χ_r^2 is 1.891 for $I_{\parallel}(t)$, as compared to 1.256 for the isotropic function P(t), and the autocorrelations for these fits exhibit nonstatistical deviations (Fig. 2). A more detailed orientational diffusion model than the spherical rotor may yield better anisotropic fits; we comment on the effects of these deviations on the interpretation of our transport data in the following Section.

In the presence of excitation transport at higher DODCI concentrations, Eqs. 9 for the anisotropic fluorescence intensities become superseded by

$$I_{\parallel}(t) = a\, P(t)[1 + 0.8\, G^S(t)\exp(-6Dt)]$$

$$I_{\perp}(t) = a\, P(t)[1 - 0.4\, G^S(t)\exp(-6Dt)] \qquad (10)$$

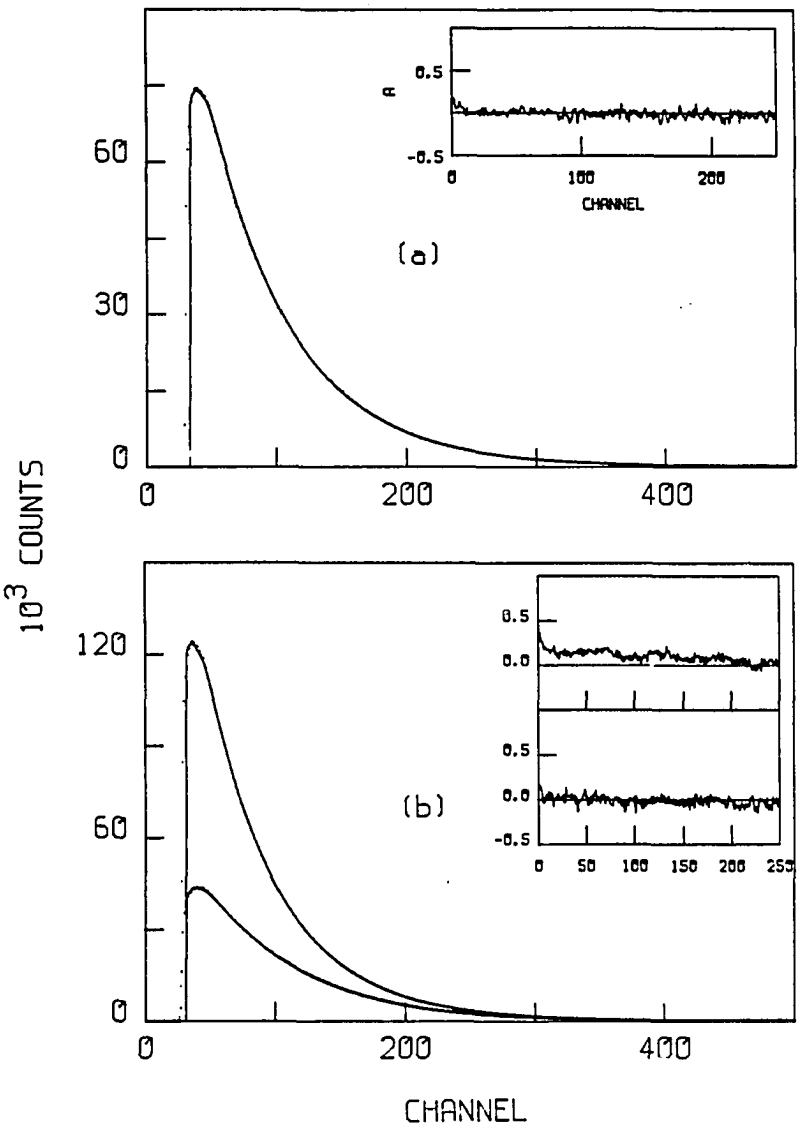

Figure 2. Fluorescence profiles of .00098M DODCI in ethylene glycol; (a) isotropic, and (b) anisotropic. Inset plots show autocorrelations of weighted residuals for (from top) P(t), $I_{\parallel}(t)$, and $I_{\perp}(t)$. Time calibration is 20 ps/channel

Table II. Results of linked deconvolution of 0.00098 mM anisotropic DODCI profiles in ethylene glycol

$$I_{\parallel}(t) = a_{\parallel}P(t)[1 + 0.8\exp(-6Dt)]$$

$$I_{\perp}(t) = a_{\perp}P(t)[1 - 0.4\exp(-6Dt)]$$

Profile	τ_{rot}, ns	χ_r^2
$I_{\parallel}(t)$	3.223	1.891
$I_{\perp}(t)$	3.223	1.225

if one assumes that the residual polarization P_1 after a single excitation hop is zero. In this limit, all of the polarization stems from excitation residing on the laser-excited molecule. The anisotropic profiles accumulated at DODCI concentrations from 0.315 to 5.61 mM were fitted using Eqs. 10. The isotropic decays P(t) were modeled using biexponential functions with fixed preexponential and lifetime parameters taken from Table I. The reorientation time τ_{rot} (= 1/6D) was maintained at 3.223 ns (Table II). The Huber 2-particle function (Eq. 2) was used for $G^s(t)$; the intrinsic lifetime τ was fixed at 1.300 ns, which closely approximates the long-component lifetime τ_1 = 1.297 ns found in the isotropic decay at 0.00098 mM (the low-concentration limit in which trapping artifacts in P(t) are negligible). Aside from $a_\parallel$ and $a_\perp$, the reduced concentration C in the 2-particle approximation to $G^s(t)$ was the only variable parameter in these fits.

Results and Discussion

The optimized reduced concentrations C and χ_r^2 are listed for the fitted anisotropic profiles in Table III. The two-particle formulation of $G^s(t)$ in Eq. 2 is derived from the orientationally averaged excitation transport rate from molecule i to molecule j,

Table III. Results of linked deconvolution of anisotropic DODCI profiles at higher concentrations in ethylene glycol

$$I_{\parallel}(t) = a_{\parallel}P(t)[1 + 0.8G^{S}(t)\ \exp(-6Dt)]$$

$$I_{\perp}(t) = a_{\perp}P(t)[1 - 0.4G^{S}(t)\ \exp(-6Dt)]$$

Concentration, mM	C	$C_D = C/\gamma$	$\chi^2_r(\parallel)$	$\chi^2_r(\perp)$
0.315	0.126	0.149	1.465	1.315
0.558	0.225	0.266	1.494	1.178
0.988	0.416	0.491	1.533	1.226
1.78	0.767	0.907	1.736	1.184
3.14	1.43	1.70	1.649	1.584
5.61	2.62	3.09	1.783	2.046

$$\frac{dp_i}{dt} = -\frac{1}{\tau}\left[\frac{R_o}{r_{ij}}\right]^6 p_i \qquad (11)$$

When the correct dipole-dipole orientation dependence of dp_i/dt is taken into account, one finds that the reduced concentration C in Eq. 2 must be replaced by γC, with $\gamma = 0.846$ [12]. This is reflected in the third column in Table III, which gives the physical reduced concentrations C_D corresponding to the optimized C parameters in our linked deconvolutions of anisotropic profiles. The quality of most fits at the higher concentrations is exemplified by our data for 0.988 mM in Fig. 3. The fluorescence depolarization (evidenced by the rate of coalescence of the $I_{\parallel}$ and $I_{\perp}$ profiles) is noticeably more rapid here than at 0.00098 mM in Fig. 2, because excitation transport furnishes an additional depolarization mechanism at the higher concentration. As in the 0.00098 mM solution (Fig. 2), the isotropic profile P(t) is well approximated by a biexponential decay law. The fit is less impressive for $I_{\parallel}(t)$, and in fact the nonstatistical autocorrelation of residuals for $I_{\parallel}(t)$ at 0.988 mM physically resembles that for $I_{\parallel}(t)$ at 0.00098 mM, where rotational diffusion dominates the anisotropy (Fig. 2). The autocorrelations at all other concentrations except 5.16 mM (where excitation trapping appreciably distorts P(t), Table I) are similar to those in Figs. 2 and 3. This suggests that at

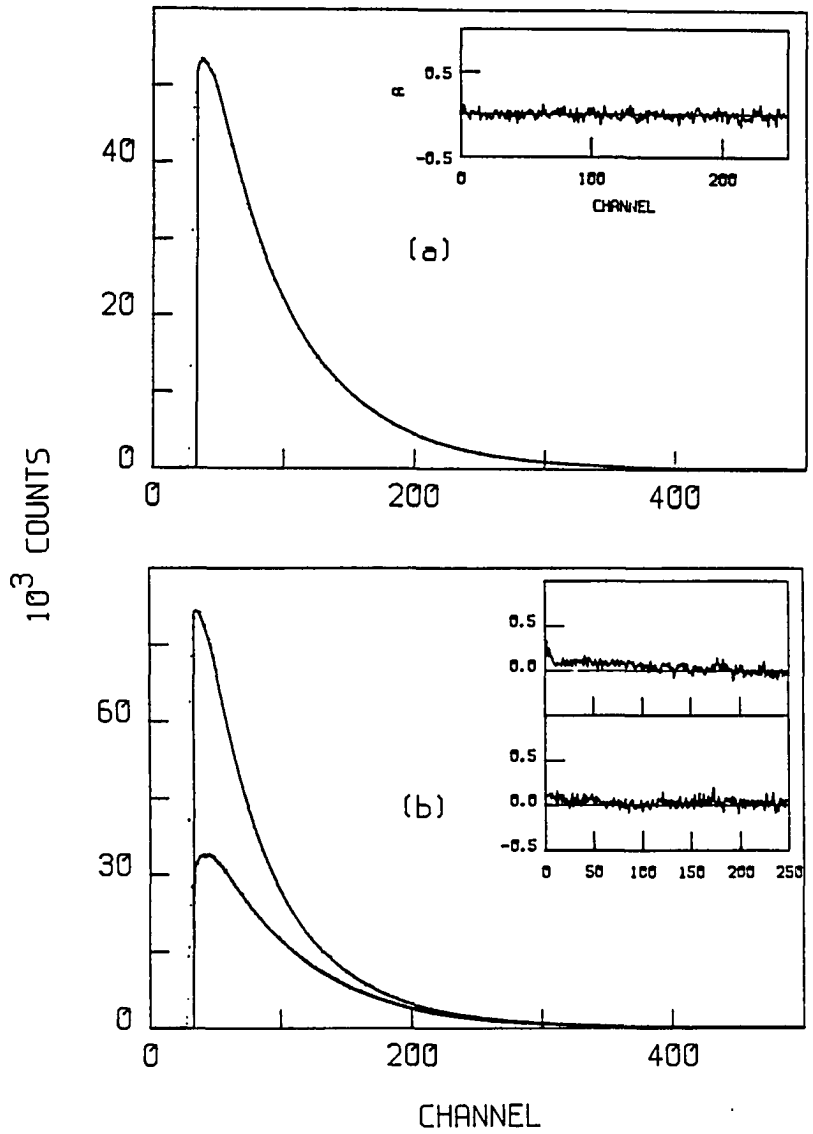

Figure 3. Fluorescence profiles of 0.988 mM DODCI in ethylene glycol; (a) isotropic, and (b) anisotropic. Inset plots show autocorrelations of weighted residuals for (from top) P(t), $I_{\parallel}(t)$, and $I_{\perp}(t)$. Time calibration is 20 ps/channel

concentrations other than 5.16 mM, the nonstatistical character in the autocorrelation functions originates primarily from the spherical rotor approximation in our rotational diffusion model, rather than from problems in our modeling of $G^S(t)$.

In Fig. 4, we plot the optimized reduced concentrations C_D from Table III versus the actual dye monomer concentrations [M]. The format of this Figure for ethylene glycol is identical to that of Fig. 1 for glycerol. The discrepancies between the experimental points and the theory are clearly far smaller in ethylene glycol than in glycerol. The experimental conditions of the present work were nearly identical to those in our earlier DODCI experiments in glycerol. The slight upward skewing shown in Fig. 4 for ethylene glycol at the higher concentrations may be due to trapping artifacts. A theory which ignores trapping (e.g., Eq. 2) tends to overestimate $G^S(t)$; the fitting procedure would then yield inflated values of C_D at concentrations where trapping is important. It is interesting that the discrepancies remain small up to 5.61 mM in ethylene glycol (R_0 varies by $\lesssim$ 2.5 Å), even though excitation trapping considerably distorts P(t) at this concentration (Table I). Hence, the Huber 2-particle theory (and by implication the GAF 3-body theory) appears to work well throughout this concentration range in ethylene glycol. This contrasts markedly with the situation in glycerol (Fig. 1(c)).

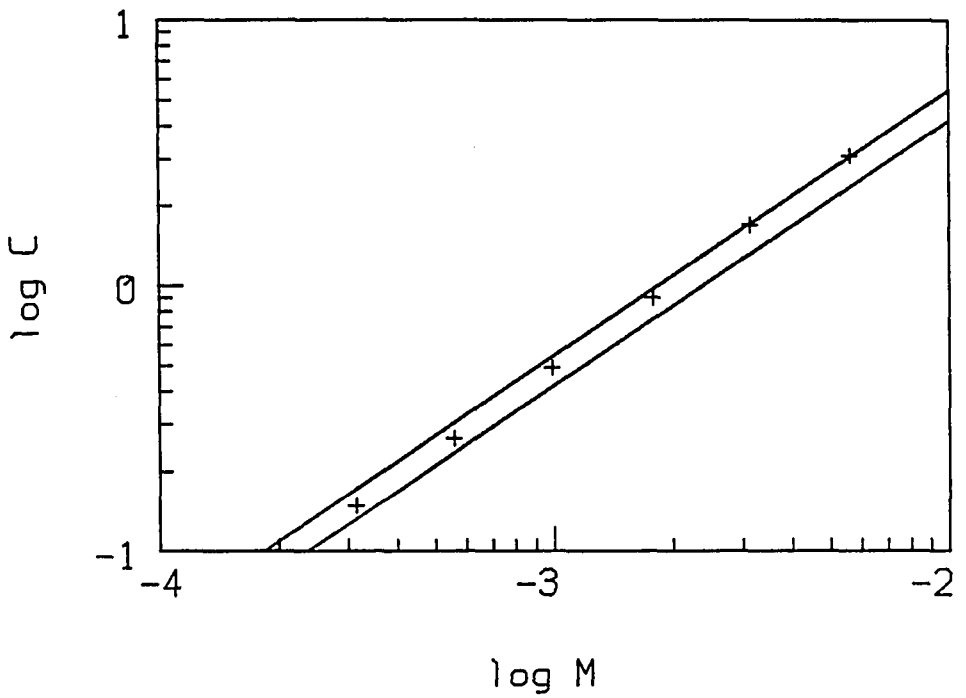

Figure 4. Optimized reduced concentrations C_D versus actual DODCI monomer concentrations [M] in ethylene glycol, from linked deconvololution of $I_{\parallel}$ and $I_{\perp}$ fluorescence profiles using Eqs. 10 (see text). The Huber 2-particle theory is used for $G^S(t)$, and the rotational diffusion parameter is taken from Table II. Straight lines give loci of true reduced concentrations versus [M] for (from left) R_o = 60 Å and 55 Å

The microstructure of liquid alcohols has received increased attention in recent years. Monte Carlo simulations of liquid methanol [18] and ethanol [19] indicate that near 25°C these alcohols consist of irregularly winding chains of sequentially hydrogen-bonded monomers. Distinct peaks attributable to nearest-neighbor and second nearest-neighbor molecular pairs appear in the radial correlation functions generated by such simulations. Like the correlation functions obtained from X-ray analyses of liquid methanol and ethanol [20], these theoretical functions exhibit little radial correlation beyond separations of 5 to 6 Å. Similar conclusions are obtained using the RISM integral equation approach to simulate methanol [21]. In such solvents, essentially random orientations may be expected for dye molecules separated by tens of Å.

The crystal structure of solid glycerol ($CH_2OHCHOHCH_2OH$) at -75°C was reported by van Koningsveld [22]. It crystallizes in the orthorhombic space group $P2_12_12_1$ ($Z = 4$) with six hydrogen bonds in a unit cell ($a = 7.00$ Å, $b = 9.96$ Å, $c = 6.29$ Å). As shown in Fig. 5 (plotted using the atomic coordinates reported by van Koningsveld together with the $P2_12_12_1$ equivalent positions), the molecular conformation in solid glycerol is the αα-staggered conformation in the Bastiansen nomenclature [23]. This conformation is also found to predominate in liquid glycerol

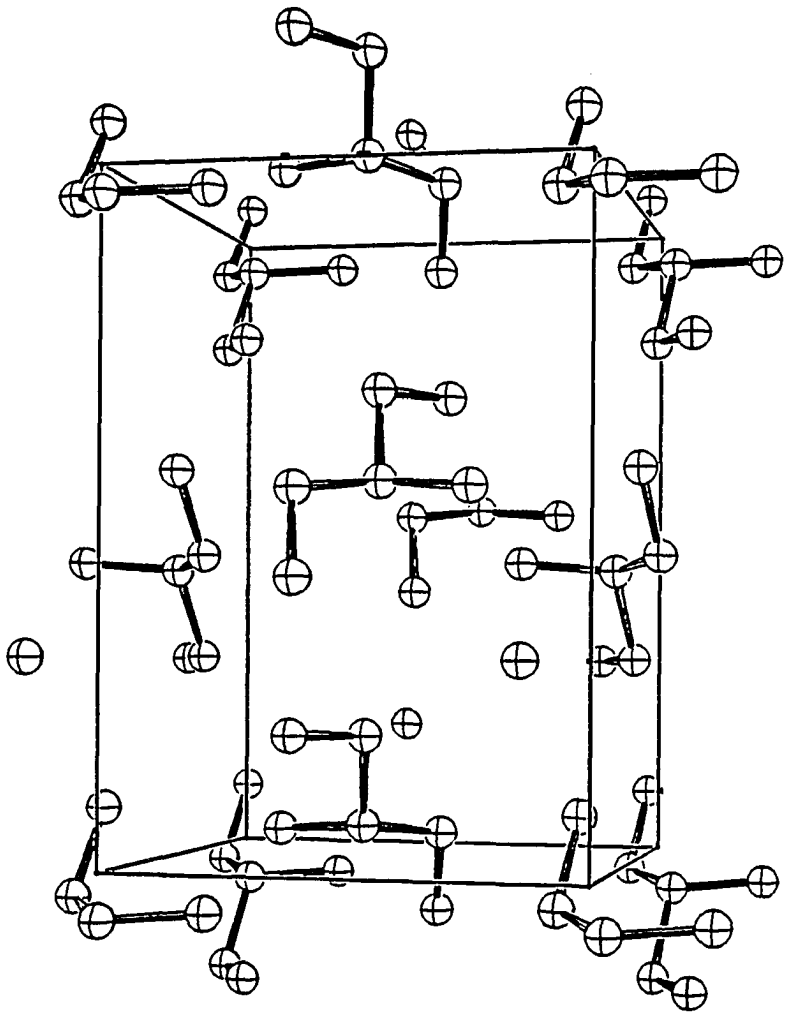

Figure 5. Crystal structure of orthorhombic glycerol ice, $CH_2OHCHOHCH_2OH$ (calculated from atomic positions and space group symmetry given in ref. 21). Hydrogen atom positions are not shown. The a- and b- axes are horizontal and vertical respectively

[14], where the radial correlation function computed from the Fourier-transformed X-ray scattering intensity distribution exhibits strong coherent peaks out to more than 25 Å (several unit cell dimensions). Such long-range solvent ordering is likely to contribute to orientational correlation among nonspherical guest chromophores for nearest-neighbor distances in the tens of Å. The sign of the discrepancies in Fig. 1 is consistent with an increased predominance of parallel neighbors at higher concentrations; no depolarization attends excitation transport in the limit of parallel chromophores, and so the apparent reduced concentration C becomes depressed relative to its true value as the concentration increases. There is little evidence of comparable ordering in the liquid structure of pure ethylene glycol. Several conformations, including intramolecularly hydrogen-bonded molecules of gauche geometry as well as trans molecules, appear to be important in the liquid [24,25]. There is indirect evidence of 2-dimensional structure in ethylene glycol methyl ether [26]. Time-resolved orientational diffusion experiments have demonstrated that tetracene rotates comparatively much more rapidly in its molecular plane in glycol than in 1-dodecanol [27]; this supports the existence of a locally layered microstructure in glycol. Unlike a number of other alcohol ices of low molecular weight (e.g., methanol, ethanol, glycerol), glycol ice has no entry in the comprehensive

NBS-JCPDS Crystal Data compilations as of 1981 [28]. We are not aware of any published glycol liquid structure factor determination, despite its important commercial uses in solvents, coolants, and as an intermediate in polymer production. Hence, the long-range radial correlations in liquid glycerol [14] appear to be absent in glycol, and orientational correlation is a likely origin for the contrast in transport behavior between these two solvents.

Quantitative consideration of the orientational correlation required to produce the discrepancies shown in Fig. 1(c) raises interesting questions about the microstructure in glycerol. At the highest concentration used (~ 3 mM), the optimized reduced concentration C_D is ~ 59% of the actual C_D value (computed using R_o ~ 64Å for DODCI in glycerol [2]) if ε_{max} (M) = ε_{max} (M_2). Some 41% of the DODCI chromophores are thus presumably hidden by orientational correlation at this concentration when transport is monitored by fluorescence depolarization. The differential probability that a nearest neighbor resides at separation R from a given DODCI molecule in a spatially random distribution is [29]

$$dP(R) = 4\pi R^2 \rho \exp(-4\pi R^3 \rho/3) dR \qquad (12)$$

where ρ is the DODCI number density in the solution. The most probable nearest-neighbor separation is then

$$R_{mp} = (2\pi\rho)^{-1/3} \tag{13}$$

At 3 mM, R_{mp} becomes 44Å. The probability Q(R) that a particular DODCI molecule has a nearest neighbor lying within separation R is

$$Q(R) = \int_0^R P(R')dR' = 1 - \exp(-4\pi R^3\rho/3) \tag{14}$$

At our highest concentration, 11.2% of the DODCI molecules then have nearest neighbors within R = 25Å if the molecules are randomly distributed. The fraction of the total dipole-dipole excitation transport occurring at distances $\leq$ R is

$$f(R) = S(R)/S(\infty) \tag{15}$$

where

$$S(R) = \int_0^R dP(R')/[1 + (R'/R_0)^6] \tag{16}$$

if orientationally averaged transition rates are used. When f(R) is evaluated in this manner, one finds that 15% of the total transport is expected to occur at separations shorter than 25Å when the concentration is 3 mM. Equation 16 is easily modified to accommodate nonrandom orientational distributions: f(R) may be computed under the crude assumption that all DODCI molecules separated by $R \leq R_c$ have

mutually parallel transition moments, but have uncorrelated orientations for $R > R_c$. (So defined, R_c represents an orientational "correlation length".) The value of the correlation length R_c which then renders $f(R_c)$ equal to the observed fraction 0.41 of "orientationally hidden" molecules is 39.9 Å. If ε_{max} (M_2) is assumed to be 2 ε_{max} (M) instead of ε_{max} (M), R_c becomes 41.9 Å.) This orientational correlation length is appreciably greater than the decay length of ~ 25 Å shown by the radial correlation function from X-ray scattering in liquid glycerol [14]. Our results therefore suggest that either orientational correlations in liquid glycerol persist to considerably longer separations than radial correlations (as in liquid crystals), or the spatial distribution of DODCI molecules becomes increasingly nonrandom at higher concentrations. Experimental techniques for measurement of orientational correlations in liquids are scarce, and fluorescence concentration depolarization using nonspherical chromophore molecules offers a potentially sensitive probe for this aspect of liquid structure.

Acknowledgements

The Ames Laboratory is operated for the U.S. Department of Energy by Iowa State University under Contract No. W-7405-Eng-82. This work was supported by the Office of

Basic Energy Sciences. We thank Professors Michael Fayer and Robert Jacobson for valuable discussions.

References

1. Anfinrud, P. A.; Hart, D. E.; Hedstrom, J. F.; Struve, W. S. J. Phys. Chem. 1986, 90, 2374.

2. Hart, D. E.; Anfinrud, P. A.; Struve, W. S. J. Chem. Phys. 1987, 86, 2689.

3. Anfinrud, P. A.; Hart, D. E.; Hedstrom, J. F.; Struve, W. S. J. Phys. Chem. 1986, 90, 3116.

4. Hammond, P. R. J. Chem. Phys. 1979, 70, 3884.

5. Gochanour, C. R.; Andersen, H. C.; Fayer, M. D. J. Chem. Phys. 1979, 70, 4254.

6. Fedorenko, S. G.; Burshtein, A. I. Chem. Phys. 1985, 98, 341.

7. Huber, D. L.; Hamilton, D. S.; Barnett, B. Phys. Rev. 1977, B16, 4642.

8. Förster, Th. Disc. Far. Soc. 1959, 27, 7.

9. Galanin, M. D. Tr. Fiz. Inst. Akad. Nauk USSR 1950, 5, 339.

10. Anfinrud, P. A.; Struve, W. S. J. Phys. Chem. in press.

11. Chambers, R. W.; Kajiwara, T.; Kearns, D. R. J. Phys. Chem. 1981, 78, 380.

12. Gochanour, C. R.; Fayer, M. D.; J. Phys. Chem. 1981, 85, 1989.

13. Weast, R. C., Ed., "Handbook for Chemistry and Physics"; CRC Press: Cleveland, 1975.

14. Soltwisch M.; Steffen, B. Z. Naturforsch. 1981, 36a, 1045.

15. Marquardt, D. W. Commun. ACM 1970, 13, 47.

16. Chuang, T. J.; Eisenthal, K. B. J. Chem. Phys. 1972, 57, 5094.

17. Grinvald, A; Steinberg, I. Z. Anal. Biochem. 1974, 59, 583.

18. Jorgensen, W. L.; J. Am. Chem. Soc. 1981, 103, 341.

19. Jorgensen, W. L.; J. Am. Chem. Soc. 1981, 103, 345.

20. Wertz, D. L.; Kruh, R. K. J. Chem. Phys. 1967, 47, 388.

21. Pettitt, B. M.; Rossky, P. J. J. Chem. Phys. 1983, 78, 7296.

22. van Koningsveld, H. Rec. Trav. Chim. Pays Bas 1968, 87, 243.

23. Bastiansen, O. Acta Chem. Scand. 1949, 3, 415.

24. van Duin, M.; Baas, J. M. A.; van de Graaf, B. J. Org. Chem. 1986, 51, 1298.

25. Podo, F.; Nemethy, G.; Indovina, P. L.; Radics, L.; Viti, V. Mol. Phys. 1974, 27, 521.

26. Tenenbaum, A. E.; Kaporovskii, L. M.; Shcherbina, E. I. Zh. Fiz. Khim. 1978, 52, 180.3

27. Sanders, M. J.; Wirth, M. J.; Chem. Phys. Lett. 1983, 101, 361.

28. Mighell, A. D.; Stalick, J. K., Eds. "Crystal Data: Determinative Tables", 3rd Ed. (U.S. Dept. of Commerce, National Bureau of Standards, and JCPDS - International Centre for Diffraction Data, Washington 1983).

29. Knox, R. S. Physica 1968, 39, 361.

SECTION IV. TIME-RESOLVED EXCITATION TRANSPORT STUDIES IN 2-DIMENSIONAL DISORDERED SYSTEMS

EXCITATION TRANSPORT AND TRAPPING IN A TWO-DIMENSIONAL DISORDERED SYSTEM: CRESYL VIOLET ON QUARTZ

Philip A. Anfinrud, Robert L. Crackel, and Walter S. Struve

Department of Chemistry and Ames Laboratory - USDOE
Iowa State University, Ames, Iowa 50011

EXCITATION TRANSPORT AND TRAPPING IN A TWO-DIMENSIONAL DISORDERED SYSTEM: CRESYL VIOLET ON QUARTZ

Introduction

Energy transport and trapping processes involving organic dye molecules are relevant to the efficiency of dye sensitizers on semiconductor surfaces in liquid-junction solar energy cells [1], and have received considerable recent theoretical study in two-dimensional [2, 3] and three-dimensional [4-8] systems. Coating ultra-violet-bandgap semiconductors such as TiO_2 with a visibly absorbing dye has been proposed for extending solar cell photoconductivity response to overlap the solar blackbody spectrum [1]. Similar sensitization of visible photoconduction in organic molecular crystals has yielded sensitive probes of electrolyte-dissolved dyes at the picogram level [9]. For such dye coatings, photoejection of an electron from an electronically excited dye monomer into the solid is expected to compete with (a) radiative decay of the S_1 state of surface-absorbed monomers, (b) intramolecular nonradiative decay of S_1 state monomers, (c) resonant electronic excitation transport between adsorbed S_1 state and S_0 state monomers due to Förster-type dipole-dipole interactions [10], and (d) nonresonant excitation

transport from S_1 state monomers to dye dimers and/or oligomers.

It is logical to focus on the dynamics of processes (a) through (d) by examining time-resolved fluorescence profiles of dyes adsorbed onto insulators into which the electron photoinjection channel is energetically closed. Kemnitz et al. [11] have recently carried this out for submonolayers of rhodamine B on naphthalene and on glass. The resulting fluorescence profiles exhibited more rapid decay at higher surface coverages, were invariably nonexponential, and could sometimes be simulated with a biexponential decay law. At higher coverages, excitation transport and trapping was clearly the primary decay route for fluorescing S_1 state rhodamine B monomers. The details of the experimental profiles were found to be consistent with the existence of two distinct monomer surface adsorption geometries, which exhibited phenomenological fluorescence lifetimes differing by a factor of ~4. At the highest dye coverages, an additional, rapidly decaying single-exponential component appeared whose intensity increased with dye coverage; this was attributed to rhodamine B dimer fluorescence.

In an earlier study, Liang et al. [12] examined the fluorescence decay for rhodamine B on glass at ~0.5 monolayer coverage. Like Garoff et al. [13], who studied rhodamine B on silica, they found that the adsorbed dye fluorescence lifetimes were far shorter than for rhodamine B

in dilute solution, presumably in consequence of excitation trapping by dye aggregates.

In this paper, we report a picosecond photon counting fluorescence study of cresyl violet (oxazine 9 [14], hereafter CV) adsorbed onto fused quartz. We address the following questions: (i) What are the number and identities of dye species which fluoresce? (ii) To what extent can a careful analysis of the fluorescence profiles differentiate among the accuracies of alternative model functions for the time-dependent fluorescence intensity? (iii) How uniquely can the final fluorescence decay parameters be determined from such an analysis without resort to independent knowledge of, e.g., the dye monomer surface number density? The total CV surface coverages are systematically varied over more than two orders of magnitude. A comparison of absorption spectra for CV on quartz with those of CV in dilute ethylene glycol solution indicates that CV dimers are far more prevalent on quartz than in alcoholic solution (viz. Experimental Section), and much of the laser absorption necessarily produces electronic excitation in CV dimers rather than monomers. We also obtained fluorescence profiles for rose bengal and rhodamine B on quartz. CV was chosen for detailed experiments, because the substantial overlap between its 600-nm monomer $S_1 \leftarrow S_0$ absorption band and our rhodamine 590 laser tuning bandwidth afforded higher fluorescence signal-to-noise ratios, and thus a much broader

surface coverage range, than was possible with the other dyes. The surface deposition techniques - substrate coating with dye solution, followed by centrifugation and evaporation [15] - are similar to those used in recent surface-adsorbed dye fluorescence experiments [11-13]. This approach prepares a surface coating in which the CV species are imbedded in solvent and air multilayers, rather than adsorbed onto clean, well-characterized surfaces in the ultrahigh vacuum sense. Our purpose in following established coating techniques is to facilitate comparisons between our results and the earlier work [11-13]. It is expected that the surface cleanliness of the insulators will have little influence on the energy transport/trapping dynamics on insulators, since the transport processes depend primarily on the dye Förster interaction parameters rather than on dye-surface interactions.

If the profiles of fluorescence components from individual emitting species can be separated, they may be compared with theoretical time-dependent excited-state populations N(t) corresponding to two-dimensional excitation transport and trapping. Several levels of approximation to the exact solutions $N_E(t)$ to the energy transport and trapping master equation [4] are available for disordered systems. The two-body approximations $N_2(t)$ to $N_E(t)$ may be obtained for <u>arbitrary</u> times and monomer and trap coverages from a Dyson equation in which the self energy has been

approximated by a sum of two-site graphs in the diagrammatic expansion of the Green function solution [5] to the master equation. Higher n-body approximations $N_3(t)$, etc. may be analogously obtained and are expected to converge to $N_E(t)$ in the limit of large n. The two-body approximations $N_2(t)$ are readily obtained in terms of inverse Laplace transforms of closed-form expressions in both three [5] and two [3] dimensions, while the three- and higher n-body approximations are much more involved [4, 5].

When the trap coverages greatly exceeds the monomer coverage, so that negligible monomer-monomer excitation transfer occurs, the Förster limit [10] is obtained in which the excited-state population is given exactly in two dimensions by [2]

$$N_F(t) = A \exp[-t/\tau - 1.354C_T(t/\tau)^{1/3}] \qquad (1)$$

where τ is the fluorescence lifetime of isolated monomers and C_T is the reduced trap coverage (section III). Kemnitz et al. [11] found that many of their fluorescence profiles for rhodamine B on naphthalene and glass were consistent with a sum of two expressions of the form of Eq. 1 for two independently decaying excited dye monomer species, or with Eq. 1 plus a single, rapidly decaying exponential term.

The two-body approximations $N_2(t)$ to the master equation solutions $N_E(t)$ break down at high trap coverages and long

times in three- [5] and two- [3] dimensional systems [5, 16] but is very ill-behaved in two-dimensional systems [17]. It is therefore pertinent to ask whether among the monomer and trap coverages studied here there are regimes in which the Förster limit supplies a better description of the transport/trapping dynamics than, say, the two-body approximations $N_2(t)$ to the master equation solutions, and conversely whether such a low-order approximation can simulate the fluorescence decay where the Förster limit expression $N_F(t)$ fails.

Finally, at long times both the Förster population $N_F(t)$ in Eq. 1 and the two-body approximation $N_2(t)$ [3] become indistinguishable from single-exponential decay. When fluorescence is emitted by two independent species with excited-state populations decaying by trapping processes, the apparent decay law will be biexponential in the photon counting instrument function profile obscures the early-time nonexponentiality in $N_F(t)$ of $N_2(t)$. The resulting variety of possible decay laws, coupled with the number of possible emitting species - monomers adsorbed onto surface with different configurations [11], dimers, etc. - requires a detailed analysis of model function fits for fluorescence profiles in order to differentiate among alternative assignments of even the most prominent fluorescence components to particular dye species.

Experimental Section

An acousto-optically mode-locked argon ion laser pumped a synchronous dye laser containing rhodamine 590 to produce tunable picosecond pulses whose fwhm was shown by zero-background autocorrelation [18] to be ~15 ps. The ion laser was a Control Laser Model 553-A with 6-W plasma tube operated at 26-A current, modulated by a Harris Corporation H-401 mode-locker with H-402 RF driver to yield 5145 Å pulses with a 47.614 MHz repetition rate and 170 mW average power. The dye laser was a Coherent Radiation Model CR-599-01 tuned with a three-plate birefringent filter. Its output coupler was replaced by an extended cavity 95% reflector mounted on a Line Tool Co. translator for synchronization with the argon laser pulse repetition rate. Conversion efficiencies from argon to dye laser wavelengths averaged ~15% at 5850 Å, the wavelength used for most of the CV fluorescence experiments.

Fluorescence from CV samples on quartz was collected at a right angle from the laser beam with a 5-cm focal length quartz lens and focussed through a variable rectangular slit before impinging on a Philips XP2020Q photon counting phototube with DU photocathode. A 3-mm Schott RG-610 filter and a CVI dichroic filter (optical density ~2 at 5850 Å, <0.1 at 6300 Å) screened 5850-Å laser scatter from the phototube. Laser pulses were focussed with a 15-cm focal

length quartz lens to a diameter of ~0.1 mm at the substrate surface, which was enclosed in a ~2 ft x 2 ft x 2 ft dark chamber with entrance and exit baffle tubes ~1 ft. long. The dye laser polarization was purified with an Oriel 2730 linear polarizer prior to striking the coated substrate, which was oriented at Brewster's angle. With this arrangement, scattered laser light contributed negligibly to the measured fluorescence profile at all times for all CV samples.

Photocurrent pulses from the phototube were amplified and inverted with a Hewlett-Packard 8447D 26 dB preamplifier and EG & G IT100 inverting transformer. Fluorescence profiles were obtained by picosecond time-correlated photon counting [19]. Amplified photocurrent pulses were passed through an Ortec 583 constant fraction discriminator before serving as start pulses in an Ortec 457 time-to-pulse height converter (TAC). Stop pulses for the TAC were derived by processing mode-locker driver synchronization output pulses through an Ortec 934 updating discriminator, and adjusting their delay with respect to incidence of start pulses with an Ortec 425A nanosecond delay box. TAC-processed output pulses were stored as fluorescence profiles in a Canberra Industries, Inc. Series 30 multichannel analyzer (MCA) operated in the PHA mode. Depending on the CV fluorescence decay time scale, profiles were stored in 511 MCA channels with a channel resolution of 6.25, 12.5, or 25 ps.

Instrument functions for deconvolution raw data were obtained by measuring time-correlated profiles of 612-nm laser pulses scattered from a clean quartz substrate and were typically 275-300 ps fwhm (the major contribution arising from electron transit spread in the phototube). Fluorescence profiles were transferred to a Digital Equipment Corporation MINC-23 minicomputer system with dual floppy disk drive operating in an RT-11 environment with FB monitor. They were normalized for TAC nonlinearity and then analyzed with a Fortran IV convolute-and-compare algorithm built around the Marquardt nonlinear regression technique [20], which is capable of fitting data sets with an arbitrary mathematical model. Single-exponential, biexponential, and Förster-limit decay fits to CV fluorescence profiles were efficient on the MINC-23 (~3 min. per six iteration deconvolution in the bioexponential case), but the nonanalytical Loring-Fayer-type decay fits typically required ~180 min. per deconvolution.

The cresyl violet was a commercially obtained laser dye from Exciton and was used without further purification. The absorption spectrum of CV in dilute diethylene glycol solution, given in Figure 1a, nearly replicates the one reported by Drexhage for CV in ethanol [14]. Surface substrates were optically polished fused quartz with $\lambda/4$ flatness obtained from George Behm and Sons, Dayton, OH. Coating these substrates by placing drops of methanolic CV

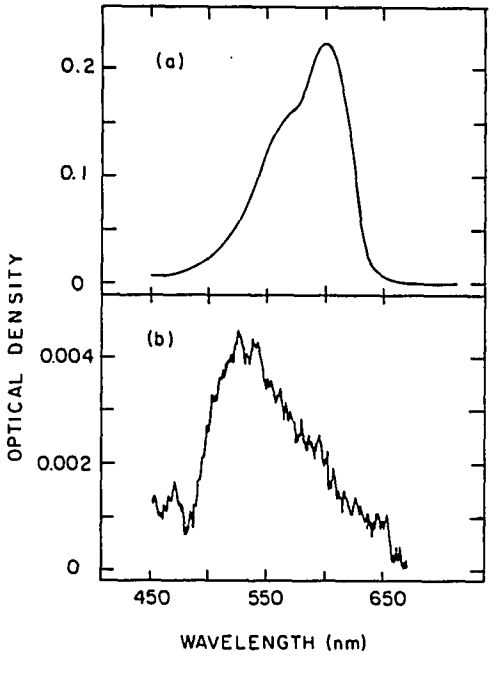

Figure 1. Absortion spectra of cresyl violet;
(a) 3.04 x 10^{-6} M in diethylene glycol, 1-cm path length; (b) on quartz, sample 1 of Table I

Table I. Cresyl violet sample characteristics

Sample	Concentration in diethylene glycol coating solvent (M)	Surface optical density ±0.0005	Surface number density (cm^{-2})
1	6.78×10^{-4}	0.0033	1.9×10^{13}
2	3.81×10^{-4}	0.0024	1.4×10^{13}
3	1.84×10^{-4}	0.0015	8.8×10^{12}
4	1.41×10^{-4}	0.0010	5.9×10^{12}
5	1.13×10^{-5}	--	--
6	3.04×10^{-6}	--	--

solution on the substrate and permitting evaporation [12] resulted in macroscopically fluctuating CV surface coverages with large variations in fluorescence decay times. Use of ethylene glycol as coating solvent and substrate centrifugation during evaporation [12] reduced the point-to-point variations in phenomenological time constants τ to <10% in most samples for τ comparable to or larger than the instrument function width (section IV); sample inhomogeneity effects on fluorescence profiles were further minimized by the small size of the focussed laser beam diameter.

For all but the lowest two CV surface coverages studied, the adsorbed CV absorption spectrum was measurable on a Perkin-Elmer 320 UV-visible dual-beam spectrophotometer (optical density threshold ~0.0005) with uncoated quartz as reference. The adsorbed CV optical densities at 5300 Å, the concentrations of CV solutions in ethylene glycol used for substrate coating, and estimated CV surface number densities (vide infra) for the studied samples are listed in Table I. Within the considerable scatter in measured adsorbed-CV optical densities, the latter correlate monotonically with the concentrations of coating solutions. A typical adsorbed-CV absorption spectrum is given in Figure 1b. The substantial blue shift from ~6010 to ~5300 Å of the CV spectrum upon adsorption, along with the appearance of a long-wavelength tail not present in the spectrum of CV in ethylene glycol, render Figure 1b analogous to the solution

absorption spectra of dye dimers reported for rhodamine B, sulforhodamine B [21], eosin, fluorescein [22], rhodamine 6G [23], and rose bengal [24]. The blue-shifted bands of such dimers have been interpreted [25-27] as arising from $\psi_+ \leftarrow \psi_0$ transitions from the ground state dimer to the higher-energy component of two split excitonic states which result from strong mixing of degenerate ground-state monomer-excited-state monomer states by the electric dipole-dipole interaction. Effects of vibronic coupling on dimer absorption spectra have been discussed by Chambers et al. [21].

We show in Figure 2 the absorption spectrum of 2.96×10^{-6} M CV in water, which resembles the spectrum in Figure 1b apart from a ~100 Å solvent shift. The identities of the principal absorbing dye species in alcoholic rhodamine B solutions have been demonstrated to be protonated and unprotonated monomers in acid-base equilibrium [28-29] rather than monomers and dimers as reported earlier [23]. Dimers have been found to be more prevalent in aqueous solutions of rhodamine B [21, 30] than in alcohols. In our case, addition of Triton X-100 to an aqueous CV solution exhibiting the spectrum of Figure 2 recovered a CV monomer spectrum which peaked near 6000 Å (similar to Figure 1a), and the CV monomer fluorescence count rate was increased thereby by a factor of $\sim 10^2$. It is thus probable that a monomer-dimer rather than an acid-base equilibrium accounts

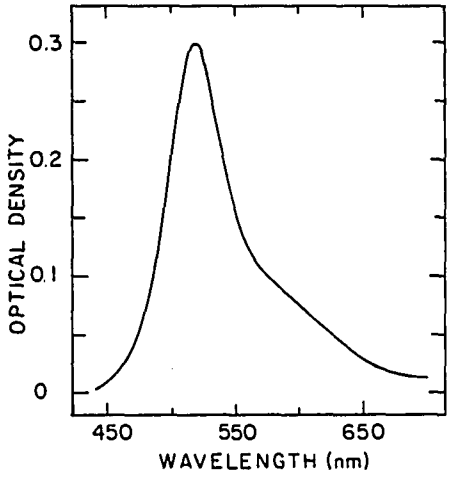

Figure 2. Absorption spectrum of 2.96×10^{-6} M aqueous cresyl violet solution, 1-cm path length

for the differences between the CV absorption spectra in Figures 1a and 2. If essentially complete dimerization is assumed in water, we obtain $\varepsilon_{max} = 1.04 \times 10^5$ L/(mol·cm) at 5200 Å for CV dimers (vs. $\varepsilon_{max} \sim 7 \times 10^4$ L/(mol·cm) at 6010 Å for CV monomers in ethanol [14]). This value, which is a lower limit for ε_{max} of CV dimers in water, is used to estimate CV number densities for the samples whose optical densities are listed in Table I. The largest CV number density in Table I is ~1 order of magnitude smaller than required for monolayer CV coverage on a flat surface, so the dye coating on amorphous quartz may be regarded as a two-dimensional disordered system for all experimental conditions used here. The absorption spectra of adsorbed CV in samples 1-4 of Table I, which all exhibit intense 5200 Å bands without prominent features near 6010 Å (the CV monomer band position in ethanol [14]), clearly indicate that the surface densities of CV dimers in these higher-density samples are considerably larger than those of CV monomers. The moderate spectral broadening of the 5300-Å band in Figure 1b relative to the shape of the $\psi_+ \leftarrow \psi_0$ dimer band in solution (Figure 2) may be evidence of the formation of higher oligomers on the surface.

Convolute-and-Compare Analysis

For an assumed fluorescence decay law N(t), the convolute-and-compare algorithm forms the discrete convolution C_n of N(t) in the nth channel

$$C_n = \sum_{i=1}^{n} x(i-s)N(n-i) \qquad (2)$$

where x(k) is the value of the instrument response function stored in the kth MCA channel obtained by using laser light scattered from a clean quartz substrate. The shift parameter s arises primarily from the laser tuning wavelength dependence of the laser pulse phase shift relative to the arrival time of stop pulses derived from the mode-locker synchronization output. Besides the Förster limit decay law $N_F(t)$ (Eq. 1), we used as initial trial decay functions the single- and biexponential forms

$$N_e(t) = A \exp(-t/\tau) \qquad (3)$$

$$N_b(t) = A_1 \exp(-t/\tau_1) + A_2 \exp(-t/\tau_2) \qquad (4)$$

as well as the decay law for a single emitting species which obeys the Loring-Fayer two-body approximation [5] to the master equations for two-dimensional energy transport and trapping [3]

$$N_2(t) = A \exp(-t/\tau) G^D(t) \tag{5}$$

Here $G^D(t)$ is the inverse Laplace transform of

$$\hat{G}^D[0,\varepsilon] = \frac{[\hat{G}^S(\varepsilon)]^2}{\hat{G}^S(\varepsilon) - \tilde{\Delta}_2[0,\hat{G}^S(\varepsilon)]} \tag{6}$$

with

$$[\hat{G}^S(\varepsilon)]^{1/3} =$$

$$\left[\frac{1}{2\varepsilon} + \frac{1}{4\varepsilon^2} + \frac{C^3}{27\varepsilon^3}^{1/2}\right]^{1/3} + \frac{1}{2\varepsilon} - \frac{1}{4\varepsilon^2} + \frac{C^3}{27\varepsilon^3}^{1/2}\Bigg]^{1/3} \tag{7a}$$

$$\tilde{\Delta}_2[0,\hat{G}^S(\varepsilon)] = 2^{1/3}\frac{\pi C_M[\hat{G}^S(\varepsilon)]^{4/3}}{3^{3/2}\tau^{1/3}} \tag{7b}$$

$$C = \frac{2\pi}{3^{3/2}\tau^{1/3}}(2^{-2/3}C_M + C_T) \tag{7c}$$

$\hat{G}^D[0,\varepsilon]$ is inverted numerically by using the Stehfest algorithm [31]. It contains three adjustable parameters: the isolated-monomer lifetime τ and the reduced monomer and trap surface densities

$$C_M = \pi(R_0^{MM})^2 \rho_M \tag{8a}$$

$$C_T = \pi(R_0^{MT})^2 \rho_T \tag{8b}$$

The monomer and trap surface number densities are ρ_M and ρ_T; R_0^{MM} and R_0^{MT} are parameters which characterize the

orientationally averaged Förster monomer-monomer and monomer-trap excitation transfer rates [10]

$$w_{jk} = \frac{1}{\tau_M}\left[\frac{R_0^{MM}}{r_{ij}}\right]^6 \tag{9a}$$

$$w_{jk} = \frac{1}{\tau_M}\left[\frac{R_0^{MT}}{r_{ij}}\right]^6 \tag{9b}$$

The decay laws $N_\varepsilon(t)$, $N_b(t)$, $N_F(t)$, and $N_2(t)$ nominally contain two, four, three, and four adjustable parameters, respectively. The additional parameters s and the zero-fluorescence base line are introduced in the calculation of the convolution C_n in Eq. 2. When the fluorescence decay was not strictly rapid compared to the 10.50 ns laser pulse spacing, the 95.228 MHz periodicity was built into the modeling function to account for small contributions to the fluorescence profile from molecules excited by the laser pulse which preceded the one which appeared in the TAC window.

A Marquardt nonlinear regression [20] program was used to minimize

$$\chi^2 = \sum_i w_i(C_i - Y_i)^2 \tag{10}$$

with respect to the adjustable parameters. Y_i denotes the number of counts accumulated in channel i, and the weight w_i

in channel i was equated to $1/Y_i$. For slow decays, the final χ^2 was improved by assigning the base line as an adjustable parameter, rather than estimating it from the portion of the TAC window for early times prior to excitation.

For single- and biexponential fits, the convolute-and-compare procedure converged to unique final parameter sets which were insensitive (<1% variation in lifetimes for τ appreciably longer than the instrument function width, ~5% for τ comparable to the instrument function width) to initial parameter choices. (Biexponential fits with τ_2/τ_1 ~ 1 are a well-known exception to this uniqueness property [32].) χ^2 minimization using simultaneous variation of all parameters in $N_F(t)$ and $N_2(t)$, however, tended to produce convergence to local minima whose locations depended on initial parameter choice. This occurred in $N_F(t)$ because C_T and τ are coupled in the product $C_T(t/\tau)^{1/3}$ in Eq. 1; for $N_2(t)$, the problem arose from the nearly symmetrical appearance of C_T and C_D in Eq. 7. Initial Förster-limit fits using $N_F(t)$ and $N_2(t)$ were therefore guided by setting τ at a physically reasonable value corresponding to a fluorescence lifetime of CV in solution.

Results

Fluorescence profiles are shown in Figure 3 for each of the samples listed in Table I. Increasing the CV surface coverage on quartz accelerates the overall decay, in analogy to the fluorescence behavior reported by Liang et al. [12] and by Kemnitz et al. [11] for rhodamine B on insulators. Each of the trial functions $N_F(t)$, $N_e(t)$, $N_b(t)$, and $N_2(t)$ [Eq. 1 and 3-7] was tested on most of the profiles. Of these model functions, only $N_b(t)$ yielded convolutions of the instrument function which were consistently good fits to the fluorescence profiles in Figure 3 ($1.1 < \chi^2 < 5.9$); these optimized convolutions are plotted as continuous lines in Figure 3. The final parameters for the biexponential fits are reported in Table II for the profiles analyzed in Figure 3. It should be noted that the derived short- and long-component lifetimes τ_1 and τ_2 are generally disparate by one order of magnitude, so that the final lifetimes obtained from minimization of χ^2 in these cases are relatively insensitive to initial parameter choice. The ratio $A_1\tau_1/A_2\tau_2$ of integrated fluorescence profiles for the long and short components varies from 0.020 (at the lowest CV coverage) to the order of 2.0. The fluctuations in this ratio at high coverages arise because in this limit, where τ_1 becomes much shorter

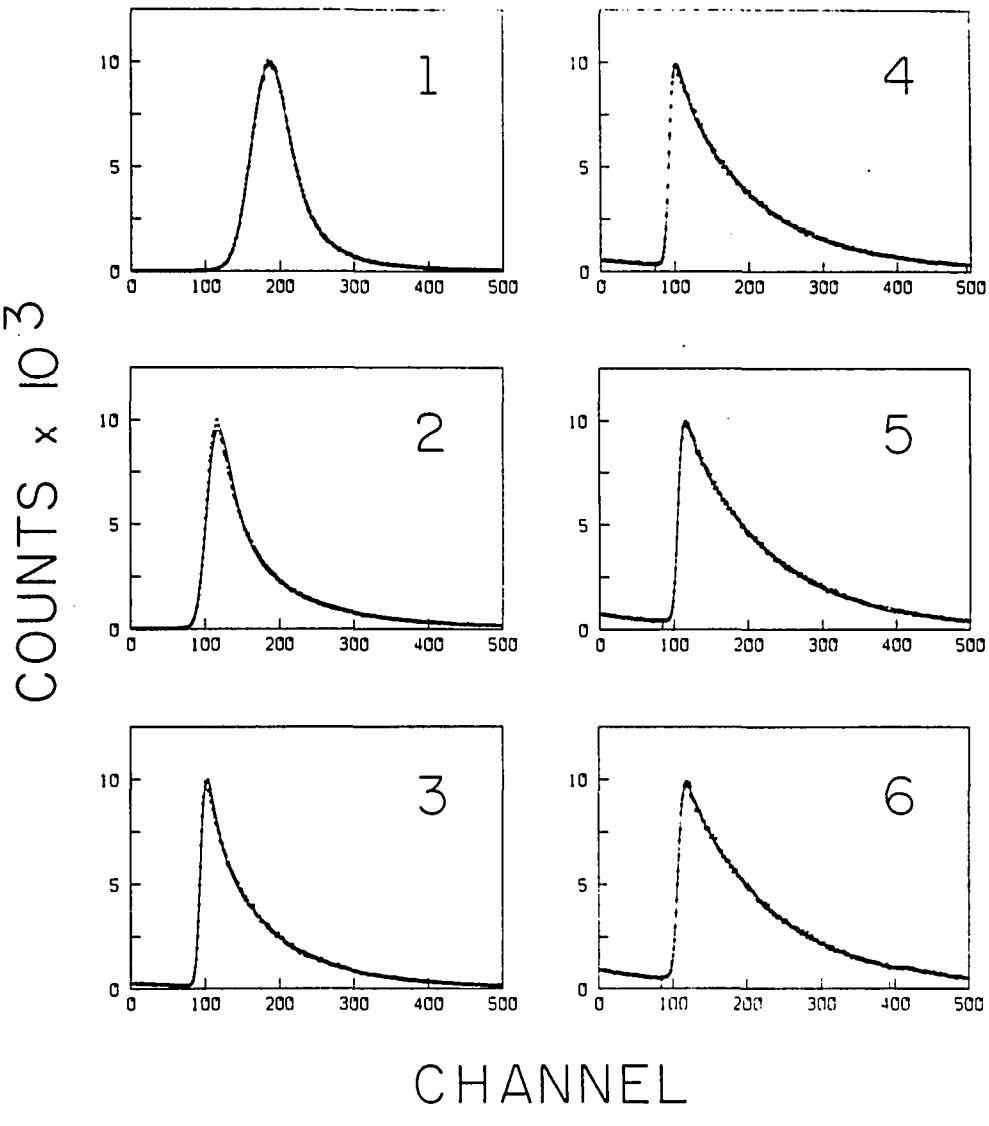

Figure 3. Typical cresyl violet fluorescence profiles from samples 1-6 of Table I. The channel calibrations are 6.25 and 12.5 ps/channel for samples 1 and 2, respectively, and 25.0 ps/channel for samples 3-6. 10^4 counts were accumulated in the peak channel in each case. Continuous curves are biexponential fits, with optimized parameters listed in Table II

Table II. Biexponential fitting parameters

$$N_b(t) = A_1 \exp(-t/\tau_1) + A_2 \exp(-t/\tau_2)$$

Sample	A_1	τ_1, ps	A_2	τ_2, ps	$A_1\tau_1/A_2\tau_2$	χ^2
1	0.235	20.2	0.00519	392	0.428	1.42
2	0.0548	192	0.173	1143	2.04	5.89
3	0.0499	312	0.0522	2150	0.139	2.16
4	0.0349	220	0.0626	2653	0.0463	1.57
5	0.0320	185	0.0657	2862	0.0315	1.28
6	0.0183	216	0.0665	2927	0.0203	1.27

Table III. Local variations in biexponential fitting parameters

Sample	A_1	τ_1' ps	A_2	τ_2' ps	χ^2
6	0.0203	216	0.0183	2927	1.27
	0.0264	176	0.0288	2941	1.14
	0.0314	120	0.0477	2945	1.28[a]
	0.0255	90	0.0533	2876	1.21
4	0.0291	336	0.0614	2660	1.35
	0.0328	276	0.0607	2642	1.76[a]
	0.0291	318	0.0615	2666	1.40
	0.0349	220	0.0626	2652	1.57

[a]Continued laser exposure of same substrate location as profile yielding parameters listed on previous line.

than the instrument function width, the fractional uncertainty in τ_1 becomes large.

Since our CV deposition method produced nonuniform coverages on quartz, Table III gives the variations in final biexponential decay parameters for several randomly selected points on samples 4 and 6 of Table I. While the point-to-point variations in τ_2 are substantial, they are smaller than the sample-to-sample variations of the average τ_2 for a given sample. Also included for both samples in Table III are biexponential fitting parameters for consecutive fluorescence profiles taken with the same 0.1-mm-diameter region exposed to the laser beam for counting periods of less than 6 min. The derived long-component lifetimes τ_2 are not significantly affected by these exposures (although the fluorescence count rate typically decreased 10% per counting period on sample 4, and 70% on sample 6), so the collected profiles show little evidence of contributions from photoproduct emission.

The inability of the elementary decay laws $N_e(t)$, $N_F(t)$, and $N_2(t)$ to reproduce the experimental profiles in Figure 3 suggests the existence of at least two emitting species. The conclusion of several emitting species was reached by Kemnitz et al. [11] for fluorescence from rhodamine B adsorbed on naphthalene and on glass. These workers used an expression of the form

$$N_{eF}(t) = A_1 \exp(-t/\tau_1) + A_2 \exp[-t/\tau_2 - 1.354C_T(t/\tau_2)^{1/3}] \quad (11)$$

to simulate some of their decays. This model function would correspond to two independently emitting dye ensembles: one decaying intramolecularly with lifetime τ_1, and the second decaying via excitation trapping in addition to intramolecular relaxation with lifetime τ_2. Such a mechanism for decay in the second ensemble would be applicable in the Förster limit where the reduced number density of the second emitting species is negligible compared to C_T, the reduced number density of species responsible for trapping of excitation in the second species. The decay law in Eq. 11 exhibits a high degree of parameter correlation in that changes in χ^2 in Eq. 10 attending variations in one parameter are readily compensated by variations in the remaining parameters. Initial fits of Eq. 11 to the profiles in Figure 3 were therefore performed with τ_2 fixed at 3000 ps, which approximates typical fluorescence lifetimes of CV monomers in dilute alcoholic solution [33]. The optimized parameters from the initial fits guided the choice of initial parameters in final fits, in which all of the parameters (including τ_2) were simultaneously varied in $N_{eF}(t)$. The values of the final parameters for the resulting fits, based on Eq. 11, are given in Table IV. The optimized χ^2 values

Table IV. Fitting parameters for

$$N_{eF}(t)=A_1\exp(-t/\tau_1)+A_2\exp[-t/\tau_2-1.354C_T(t/\tau_2)^{1/3}]$$

Sample	A_1	τ_1' ps	A_2	τ_2' ps	C_T	χ^2
1	0.282	15.7	0.00770	436	0.377	1.39
2	0.252	8.8	0.0879	2432	1.97	1.55
3	0.119	22.2	0.118	3231	0.980	1.09
4	0.133	21.3	0.0866	3280	0.418	1.06
5	0.0700	38.6	0.0832	3381	0.306	1.04
6	0.0329	90.8	0.0776	3425	0.226	1.09

vary between 1.04 and 1.55 and are in most cases not significantly different from χ^2 for the biexponential fits. The corresponding convolutions of Eq. 11 with the instrument function, if plotted on the scale of Figure 3, would be nearly indistinguishable in most cases from the displayed biexponential convolution.

The qualities of fits based on the decay models $N_b(t)$ and $N_{eF}(t)$ may be differentiated by evaluating the respective autocorrelations of the residuals [32]

$$A_n = \frac{N}{M} \frac{\sum_{i=1}^{M} w_i^{1/2} (C_i - Y_i) w_{i+n}^{1/2} (C_{i+n} - Y_{i+n})}{\sum_{i=1}^{N} w_i (C_i - Y_i)^2} \qquad (12)$$

Here N is the number of channels which comprise the fluorescence profile, and M is taken to be half the number of channels used in the convolute-and-compare fit. A_1, the autocorrelation in channel 1, is unity. For good quality fits, the autocorrelation function in channels for other n is dominated by random statistical fluctuations symmetrically scattered about $A_n = 0$. Systematic deviations $(C_i - Y_i)$ which alternate in sign between contiguous channel spaces (in consequence of using a functionally incorrect model N(t) produce an autocorrelation function with well-defined low-frequency periodicity. We show in Figure 4 the autocorrelation functions computed for n up to 250 channels

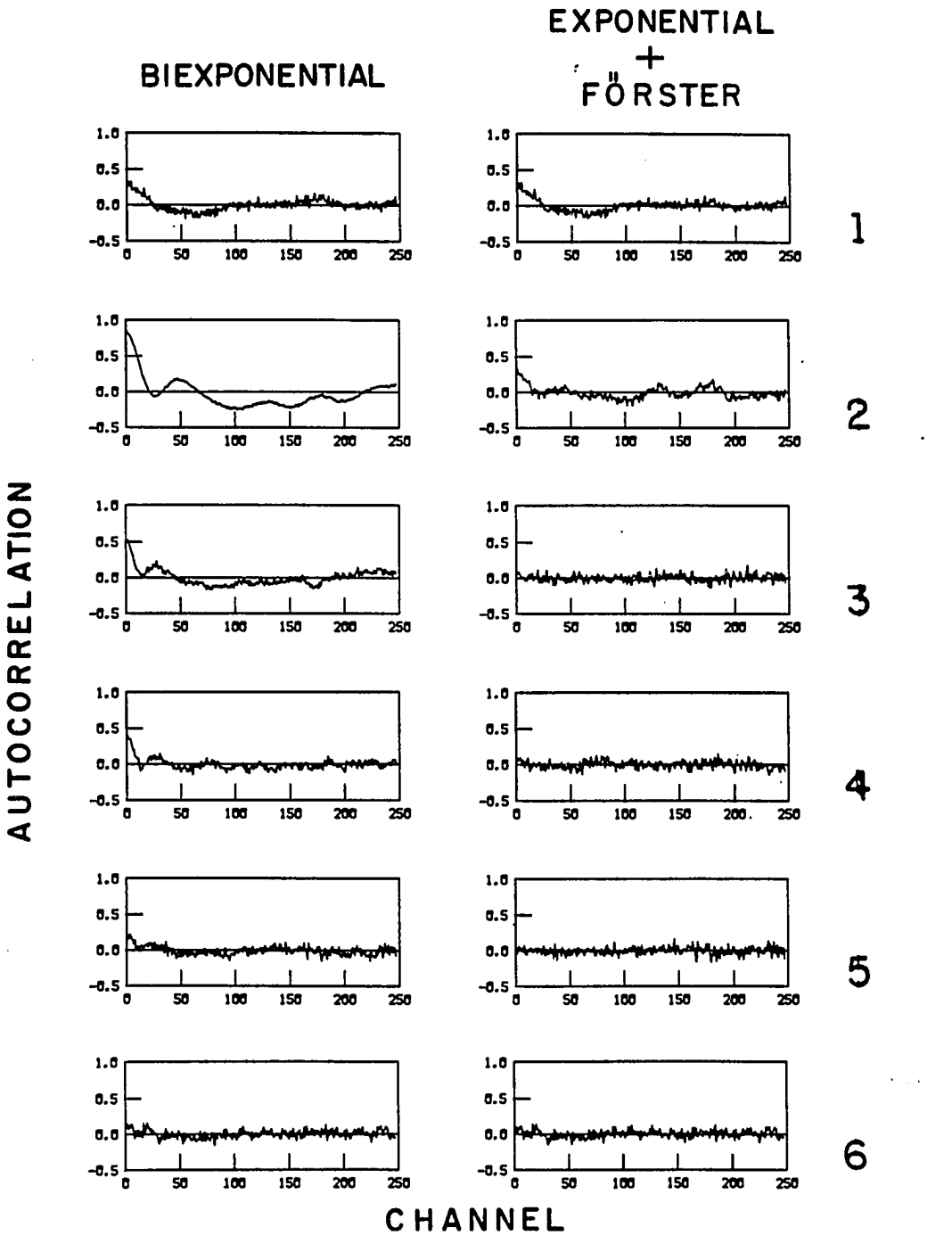

Figure 4. Autocorrelation functions for biexponential and exponential plus Förster fits to profiles 1-6 in Figure 3

for the $N_b(t)$ and $N_{eF}(t)$ fits to each of the profiles of Figure 3. At the lowest CV coverage, the autocorrelation functions from both models are similar, implying that in this limit they provide similarly valid approximations to the data. For the four intermediate coverages (samples 2 through 5), the $N_{eF}(t)$ autocorrelations are markedly better than those from $N_b(t)$. Each of the profiles in Figure 3 exhibits similar counting statistics, since 10^4 counts were always accumulated in the peak channel. Hence, the normalization of A_n in Eq. 12 implies that the rms noise amplitude for an autocorrelation function in Figure 4 will be larger for the higher-quality fits, as is the case for the $N_{eF}(t)$ fits to the profiles from samples 2 through 5. At the highest coverage (sample 1), neither fit yields a statistical autocorrelation. In high-coverage profiles in which the decay is rapid relative to the instrument function width, the calculated convolutions are highly sensitive to the evaluation of the instrument function. The details of the latter are necessarily suspect because the phototube electron transit time distributions depend on the detected photon wavelength, and because the autocorrelation functions for both models in Figure 4 tend to worsen at higher coverages, where the instrument function becomes critical. The autocorrelation functions for $N_{eF}(t)$ fits with τ_2 fixed at 3000 ps (not shown in Figure 4) were intermediate in quality between those shown in Figure 4 for $N_b(t)$ and the

fully optimized $N_{eF}(t)$. Since $N_{eF}(t)$ has the same number of adjustable parameters (with τ_2 fixed) as $N_b(t)$, the better autocorrelations from $N_{eF}(t)$ at intermediate coverages are not an artifact of higher functional flexibility, particularly since τ_2 varies little for the full-optimization fits in this coverage range (Table IV). Finally, we give the fluorescence profile, single-exponential fit using $N_e(t)$ and autocorrelation function obtained from 5.0×10^{-6} M CV in aqueous solution in Figure 5. This profile was obtained with an analyzing polarizer inclined 54.7° from the laser polarization [34] in order to remove the fluorescence anisotropy $\tau(t)$ due to orientational relaxation [35], thereby rendering the measured profiles single exponential. The autocorrelation in Figure 5 exemplifies the limiting quality of fits attainable with our apparatus [36]. Hence, the nonstatistical character of the autocorrelations for the $N_b(t)$ fits for samples 2-5 in Figure 4 does not arise from instrumental factors such as residual TAC nonlinearity or instrument function error.

Fluorescence spectra were evaluated for the samples in Table I, using a J-Y H20 scanning monochromator operated with 0.5-nm bandpass and detecting the fluorescence with an Amperex 56D-UVP photomultiplier behind a Schott 3-mm RG610 filter. A typical fluorescence spectrum for adsorbed CV is shown in Figure 6; no evolution was observed in this spectrum, whose band maximum fluctuated between 6230 and

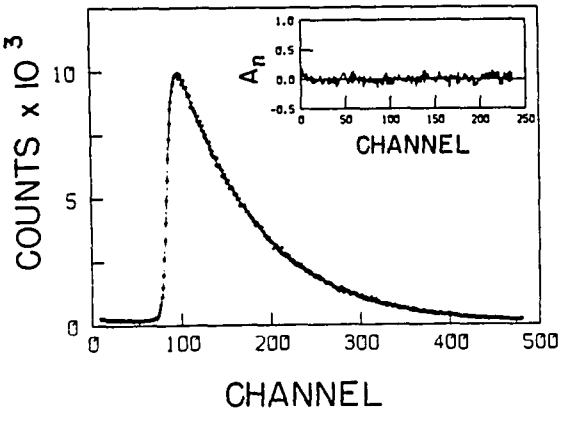

Figure 5. Fluorescence profile and autocorrelation function for single-exponential fit for 5.0×10^{-6} M aqueous cresyl violet solution with orientational fluorescence anisotropy suppressed. The optimized lifetime is 2235 ps, vs. 2390 ps reported in ref 28 for isotropic lifetime decay. Channel calibration is 25 ps

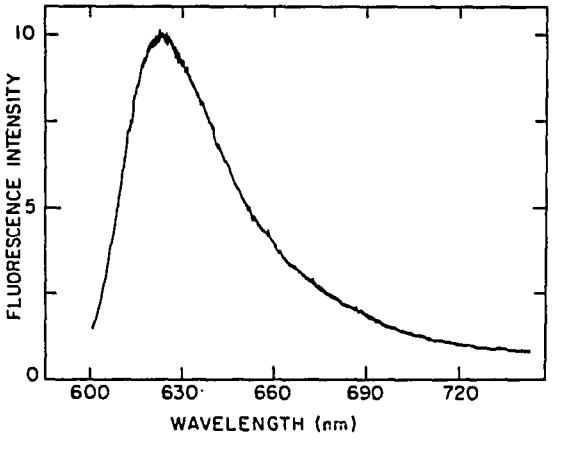

Figure 6. Fluorescence spectrum, uncorrected for instrumental response, for cresyl violet on quartz, sample 1 of Table I

6290 Å over the coverages listed in Table I. However, the biexponential fitting parameters in Table II predict that the time-integrated fluorescence intensity $A_1\tau_1$ for the short-lifetime component should become comparable to $A_2\tau_2$ at high concentrations, meaning the fluorescence spectrum should vary with coverage if the τ_1 and τ_2 components are emitted by species with different fluorescence spectra and similar oscillator strengths. The $N_{eF}(t)$ fitting parameters in Table IV, however, predict, in agreement with our fluorescence spectra, that the short-component fluorescence should be masked by the long-component spectrum at all coverages if the short component does not exhibit a much larger transition moment than the long component. The position of the fluorescence band maximum in Figure 6 nearly coincides with that reported by Drexhage [14] for dilute CV solution in ethanol.

For all but the highest coverages, the two-species decay law $N_{eF}(t)$ is sufficient for yielding nearly statistical autocorrelations of the residuals. We attribute the long-component decay to CV monomer fluorescence because (i) the τ_2 parameter in the phenomenological biexponential fits of Table II, which yields a statistical autocorrelation at the very lowest coverage (sample 6), converges in this limit to a value of ~3000 ps, within the range of solvent-dependent fluorescence lifetimes τ_f of CV in solution [33] and (ii) fits based on the $N_{eF}(t)$ model yield nearly statistical

autocorrelations with τ_2 between 3200 and 3450 ps at most coverages. The identity of the promptly emitting short-component species is more problematic. A priori, several of the possibilities are fluorescences from directly excited impurities, directly excited dimers/oligomers, or directly excited CV monomers adsorbed onto the quartz with a different configuration than that of the CV species responsible for the long component τ_2, in analogy to the assignment suggested for one of the emission components from rhodamine B on insulators [11]. Impurity fluorescences are unlikely because we obtain good statistical autocorrelations for single-exponential fits for CV in dilute ethanol and water solutions and because thin-layer chromatography of our CV solutions in ethanol yielded no extraneous bands. The lifetimes τ_1 of the short component extracted from the $N_{eF}(t)$ fits (Table IV) are in the range 8.8-90.8 ps. These are subject to large statistical error because they amount to three channel widths at most, but they are so short compared to the CV monomer solution lifetimes that it is difficult to attribute them to CV monomers having special adsorption geometry. Another possible assignment is emission from the ψ_+ exciton component of CV dimers [21], which would be consistent with the large $\psi_+ \leftarrow \psi_0$ oscillator strength in CV (Figure 2). Picosecond $\psi_+ \leftarrow \psi_-$ internal conversion (IC) of the emitting ψ_+ state to a nonfluorescing ψ_- CV dimer state would be consistent with the observation

that $S_n \rightarrow S_1$ IC is an ultrafast process in the majority of aromatic molecules [37]. Prompt emission by CV dimers is also favored by the predominance of dimer absorption in our adsorbed CV adsorption spectra, which are typified by the spectrum in Figure 1b. However, no dimer fluorescence appears in the aqueous CV profile in Figure 5 (which exhibits a statistical autocorrelation function with the single-exponential model $N_e(t)$), although this solution exhibits the CV dimer absorption spectrum in Figure 2. This indicates that in aqueous solution the ψ_+ state is so short-lived that its fluorescence profile is effectively swamped by fluorescence from a small concentration of CV monomers. If the relative CV monomer densities were similar in water and on quartz, it would be necessary to hypothesize that $\psi_+ \leftarrow \psi_-$ IC is appreciably slower on a quartz surface than in solution in order to attribute our short emission component to CV dimers. While conceivable, such an assignment requires further proof.

Still another possibility is that orientational diffusion of adsorbed CV monomers on quartz, rather than a second CV species, produces the short emission component. In the presence of three-dimensional orientational diffusion, the detected fluorescence intensity would become [34]

$$I(t) = I_{\parallel}(t) + 2I_{\perp}(t) = \left[\frac{2}{3} + \frac{1}{3} r(t) \right] \quad N(t) \qquad (13)$$

where r(t) is the time-dependent fluorescence polarization anisotropy. For isotropic rotational diffusion with diffusion coefficient D

$$r(t) = \frac{2}{5}e^{-6Dt} \tag{14}$$

The fluorescence intensity for a CV monomer ensemble which undergoes orientational diffusion as well as Förster trapping decay will then obey

$$I(t) = \left[\frac{2}{3} + \frac{2}{15}\exp(-6Dt)\right] N_F(t) =$$

$$\left[\frac{2}{3} + \frac{2}{15}\exp(-6Dt)\right] A \exp\left[-t/\tau - 1.35C_T(t/\tau^{1/3}\right] \tag{15}$$

Equation 15 is valid only if negligible monomer-monomer excitation hopping occurs during the monomer fluorescence profile, since such excitation transfer destroys orientational correlation in the emitting ensemble. This is exactly the regime in which the Förster limit applies. When the anisotropy function, proportional to exp(-6Dt), decays rapidly compared to $N_F(t)$, the decay law in Eq. 15 will closely resemble $N_{eF}(t)$ (Eq. 11), particularly when the reciprocal of 6D spans only a few MCA channels. The $\exp(-t/\tau_1)$ term in $N_{eF}(t)$ would then phenomenologically represent the $\exp(-6Dt)N_F(t)$ term in Eq. 15, with the consequence that τ_1 would shorten with increased CV coverage

(owing to the more rapidly decaying $N_F(t)$ factor for larger C_T) when the profiles are fitted with the $N_{eF}(t)$ model. This behavior is exhibited by τ_1 in Table IV, although excessive significance should not be attached to this trend because τ_1 is never wider than three channels. Chuang and Eisenthal [35] have shown that, for completely anisotropic rotational diffusion ($D_x \neq D_y \neq D_z$), r(t) contains five distinct exponential decay times. It is likely that adsorbed CV would rotate about one axis at most, yielding an essentially single-exponential anisotropy function.

We searched for effects of orientational diffusion by obtaining profiles using an analyzing polarizer aligned 0°, 54.7°, and 90° from the laser polarization. The three profiles were evaluated sequentially with unshifted laser beam exposure on two samples with CV coverages similar to those of samples 3 and 4. In both cases, analyses of the profiles yielded no polarization dependence commensurate with that predicted for orientational diffusion (e.g., the r(t) term in I(t) should drop out entirely when the 54.7° polarizer is used). The foregoing discussion is based on three-dimensional orientational diffusion and adsorbed CV molecules may be constrained to rotate about axes with special orientations relative to the surface. The anisotropy function r(t) would then be different than in the three-dimensional case, but the fluorescence profiles would still exhibit a polarization dependence if r(t) were

responsible for the rapidly decaying component. Hence contributions from orientational diffusion can be ruled out.

The possibility that the short-lifetime component is scattered laser fundamental light was checked and discounted by testing the effect of an additional RG-610 filter (optical density >2 at 585 nm) on the profiles.

In summary, the biexponential decay law fortuitously yields fits with low χ^2, but gives integrated fluorescence ratios A_1r_1/A_2r_2 which would be expected to cause observable spectral evolution in fluorescence emitted by samples 1-6. For profiles in which the decay is slow over the instrument function width, the $N_{eF}(t)$ model yields fitted functions whose deviations from the data points are smaller than the rms statistical noise. The long decay component in $N_{eF}(t)$ is CV monomer emission. The origin of the fast decay component is unproven, but it is not orientational diffusion, impurity fluorescence, or laser scattering. We caution that instrument function errors may contribute substantially to the fast component under the present resolution: we have observed large fluctuations in the preexponential factors of the first (but not the second) term of $N_{eF}(t)$ from run to run using similar samples. We expect to resolve this question by incorporating a microchannel plate phototube with an instrument function of <80ps in our apparatus.

It is unnecessary to postulate more than two emitting CV species to account for our profiles. The fact that CV, unlike rhodamine B [14], exhibits an inherently rigid skeletal structure may account for the apparent absence of absorption geometrical effects on CV fluorescence lifetimes, since Kemnitz et al. [11] attributed their rhodamine B lifetime dichotomy to contrasting rigidities of dye monomers adsorbed in different ways on the surface.

Excitation Transport and Trapping

We have shown that, at all but the highest CV surface coverages, the fluorescence profiles are described within photon counting error by the model function $N_{eF}(t)$, the sum of a rapidly decaying single-exponential term and a term representing intramolecular plus Förster-type excitation trapping decay, whose lifetime approaches the fluorescence lifetime of CV monomers at low coverage. The Förster limit expression (Eq. 1) for monomer excitation trapping is valid when the reduced monomer density is negligible compared to the reduced trap density, $C_T/C_M>>1$ [2]; under this qualification, it will hold for arbitrary C_T. In the presence of trapping by CV dimers, the Förster limit is likely to be approximately obeyed in all samples listed in Table I for which absorption spectra were obtained, since the latter are all strongly dominated by the 520-nm $\psi_+ \leftarrow \psi_0$

dimer band. The reduced trap densities C_T derived from the N_{eF} fits to the fluorescence profiles (Table IV) extend from 0.226 to 1.97. For samples 2-4 (the ones for which approximate values of ρ_T are available in Table I and for which instrument function uncertainty is less critical to the accuracy of the fluorescence profile), C_T varies roughly linearly with p_T as predicted by Eq. 8b. The derived R_0^{MT} parameter varies from 15 to 21 Å.

We now consider whether the Loring-Fayer two-body master equation solutions for transport and trapping in a two-dimensional disordered system can model the fluorescence profiles when combined with a rapidly decaying single exponential term

$$N_{e2}(t) = A_1 \exp(-t/\tau_1) + A_2 \exp(-t/\tau_2)G^D(t) \qquad (16)$$

To compare the properties of this model function with those of $N_{eF}(t)$, we plot $[G^D(t) - f(t)]/f(t)$ vs. times for various C_T in Figure 7, where $f(t) = \exp[-1.354C_T(t/\tau)^{1/3}]$. This shows that when $C_M = 0$ and $t<2\tau$ the two-body function is a good approximation to the exact Förster expression for $C_T \lesssim 0.20$, and then fails badly for larger C_T. It is thus anticipated that Eq. 16 should yield a fit of fair statistical quality to the profile from sample 6 (and of poorer quality for the others). In practice, the number of independent parameters in convolutions of $N_{e2}(t)$-A_1, A_2, τ_1,

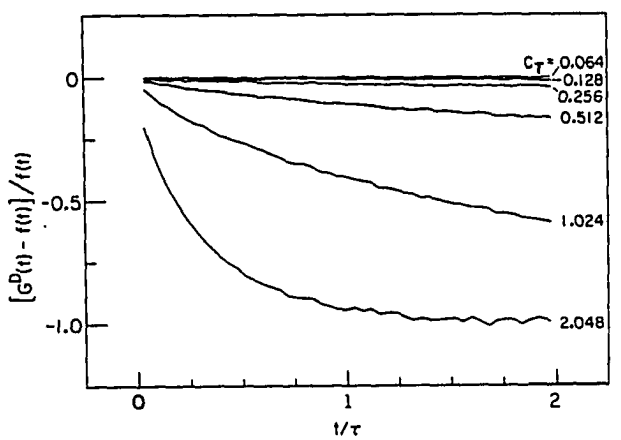

Figure 7. Comparison of the Loring-Fayer two-body approximation to $G^D(t)$ with $f(t) = \exp[-1.354C_T(t/\tau)^{1/3}]$. The time axis is calibrated in units of the monomer lifetime τ

τ_2, C_M, C_T, s, and the base line parameter yield eight in all -leads to severe convergence problems in the convolute-and-compare analysis. The "true" optimized parameters are difficult to find even in samples in which $N_{e2}(t)$ yields a fair approximation to $N_{eF}(t)$, e.g., sample 6. Further, we found that in sample 3 an analysis based on $N_{e2}(t)$ fortuitously led to a low χ^2 (=1.22) and a fair autocorrelation function, even though the $N_{eF}(t)$ analysis for sample 3 yields C_T = 0.980 (Table IV). For such C_T, $N_2(t)$ is a poor approximation to $N_F(t)$, as shown in Figure 7. Hence, the final parameters from that analysis (C_M = 0.037, C_T = 0.679, τ_1 = 56 ps, τ_2 = 3.20 ns) must be regarded with suspicion. It is interesting to note that if the final parameters from the $N_{eF}(t)$ fits are simply substituted into $N_{e2}(t)$ and if C_M is set equal to 0, convolutions of $N_{e2}(t)$ yield computed decay curves with χ^2 = 149, 11.2, and 2.20 for samples 3, 4, and 6, respectively. Since the corresponding reduced trap concentrations are 0.980, 0.418, and 0.226, these χ^2 reflect on the quality of the two-body approximation to $N_F(t)$. Even for the latter fit (sample 6), the autocorrelation function is poorer than any of the ones shown in Figure 4.

The Förster limit expression for the monomer excitation decay fails when monomer-monomer excitation transport becomes important, i.e., when $C_M \gtrsim C_T$. This situation is evidently not reached in any of the samples studied here, as

the $N_{eF}(t)$ decay model provides a statistical-limit fit to the emission profiles even for samples prepared from the most dilute coating solutions used (3.2×10^{-6} M). Hence, the Förster limit model satisfactorily accounts for the monomer excitation trapping decay in all of our cases (except possibly at the highest coverage - sample 1 - where instrument function uncertainty becomes important). There is no regime among the samples of Table I in which the Loring-Fayer two-body approximation to N(t) provides a uniquely accurate description of the trapping dynamics; such a regime would likely be one in which C_M and C_T are comparable and less than ~0.20. For larger reduced surface coverages, higher-order master equation solutions would be required if C_M were not negligible compared to C_T.

Huber has calculated $G^D(t)$ for excitation trapping in three-dimensional disordered systems in which C_T is much lower than C_M [6]. His results correspond approximately to the three-dimensional two-body approximation [4] (and somewhat more closely to the three-body approximation) in this regime. Since CV dimers are the overwhelmingly predominant species on quartz at all coverages, the Huber limit does not apply here. Very recently, Loring et al. have extended their excitation transport and trapping theory to the case of dilute traps randomly substituted on a regular lattice [38]. Our profiles, emitted by CV monomers on amorphous quartz, are well fit by the continuum model

$N_{e2}(t)$ at trap coverages C_T for which $N_2(t)$ is a good approximation to the Förster limit $N_F(t)$. The substituted lattice model may be necessary for dyes adsorbed on single-crystal naphthalene [11].

Conclusions

For the fluorescence profiles emitted by cresyl violet adsorbed onto quartz, our conclusions are as follows:

(i) The bulk of the observed fluorescence from samples 1-6 is emitted by CV monomers whose excitation decays via trapping by dimers in the Förster limit, $C_T >> C_M$. The fast-component emission is unassigned and may be an artifact of the instrument function uncertainty. It is not emitted by impurities but may be CV dimer fluorescence. However, no CV dimer fluorescence is observed in an aqueous CV solution, even though CV dimers absorb strongly at the laser excitation wavelength.

(ii) The autocorrelation functions (Figure 4) readily differentiate the qualities of the biexponential and single-exponential plus Förster decay models, although both models yield similar χ^2 in optimized fits. In samples 3-6, the $N_{eF}(t)$ fits yield autocorrelation functions of statistical quality. More flexible model functions (e.g., postulating more than two emitting species) are unnecessary for replicating the decay dynamics.

(iii) The final fluorescence decay parameters for fits based on $N_2(t)$, $N_{eF}(t)$, and $N_e(t)$ [the latter for aqueous CV] correspond to well-defined convergences in the convolute-and-compare analyses. For $N_{eF}(t)$, the extracted C_T and τ_2 values in samples 3-6 (which are less subject to instrument function uncertainty) prove to be physically reasonable (Table IV). Analyses based on the single-exponential plus two-body approximation function $N_{e2}(t)$ will require independent knowledge of some of the parameters, such as C_M and C_T; these are considerably more difficult to ascertain for dye submonolayers on surfaces than for dyes in solution.

Acknowledgements

We thank Professor Duane Smith and Dennis Jensen for their help in the computer analysis of the fluorescence profiles. The Ames Laboratory is operated for the U.S. Department of Energy by Iowa State University under Contract No. W-7405-Neg-82. This work was supported by the Office of Basic Energy Sciences.

References

1. Fox, M. A; Nobs, F. J.; Voynick, T. J. Am. Chem. Soc. 1980, 102, 4029. Hohman, J. R.; Fox, M. A. J. Am. Chem. Soc. 1982, 104, 401.

2. Nakashima, N.; Yoshihara, K.; Willig, F. J. Chem. Phys. 1980, 73, 3553.

3. Loring, R. F.; Fayer, M. D. Chem. Phys. 1982, 70, 139.

4. Gochanour, C. R.; Andersen, H. C.; Fayer, M. D. J. Chem. Phys. 1979, 70, 4254.

5. Loring, R. F.; Andersen, H. C.; Fayer, M. D. J. Chem. Phys. 1982, 76, 2015.

6. Huber, D. L. Phys. Rev. B. 1979, 20, 2307, 5333.

7. Haan, S. W.; Zwanzig, R. J. Chem. Phys. 1978, 68, 1879.

8. Ediger, M. D.; Fayer, M. D. J. Chem. Phys. 1983, 78, 2518.

9. Mulder, B. J. Philips Res. Rep. 1967, 22, 553.

10. Förster, Th. Ann. Phys. (Leipzig) 1948, 6, 55.

11. Kemnitz, K.; Murao, T.; Yamazaki, I.; Nakashima, N.; Yoshihara, K. Chem. Phys. Lett. 1983, 101, 337.

12. Liang, Y.; Ponte Goncalves, A. M.; Negus, D. K. J. Phys. Chem. 1983, 87, 1.

13. Garoff, S.; Stevens, R. B.; Hanson, C. D.; Sorenson, G. K. J. Lumin. 1981, 24, 773.

14. Drexhage, K. H. In "Topics in Applied Physics"; Schäfer, F. P., Ed.; Springer-Verlag: West Berlin; 1973.

15. Wokaun, A.; Lutz, H. P.; King, A. P.; Wild, U. P.; Ernst, R. R. J. Chem. Phys. 1983, 79, 509.

16. Miller, R. J. D.; Pierre, M.; Fayer, M. D. J. Chem. Phys. 1983, 78, 5138.

17. Fayer, M. D., Dept. of Chem., Stanford University, private communication.

18. Ippen, E. P.; Shank, C. V. Appl. Phys. Lett. 1975, 27, 488.

19. Beddard, G. S.; Fleming G. R.; Porter, G.; Searle, G. F. W.; Synowiec, J. A. Biochim. Biophys. Acta 1979, 545, 165.

20. Marquardt, D. W. J. Soc. Ind. Appl. Math. 1963, 11, 431.

21. Chambers, R. W.; Kajiwara, T.; Kearns, D. R. J. Phys. Chem. 1974, 78, 380.

22. Förster, Th.; König, E. Z. Elektrochem. 1957, 61, 344.

23. Selwyn, J. E.; Steinfeld, J. I. J. Phys. Chem. 1972, 76, 762.

24. Rohatgi, K. K.; Mukhopadhyay, A. K. Photochem. Photobiol. 1971, 14, 551.

25. McRae, E. G.; Kasha, M. J. Chem. Phys. 1958, 28, 721.

26. McRae, E. G.; Kasha, M. "Physical Processes in Radiation Biology"; Academic Press: New York, 1964.

27. Kasha, M.; Rawls, H. R.; Ashraf-Bayoumi, M. Pure Appl. Chem. 1965, 11, 371.

28. Sadkowski, P. J.; Fleming, G. R. Chem. Phys. Lett. 1978, 57, 526.

29. Faraggi, M.; Peretz, P.; Rosenthal, I.; Weinraub, D. Chem. Phys. Lett. 1984, 103, 310.

30. Lopez-Arbeloa, I.; Ruiz Ojeda, P. Chem. Phys. Lett. 1982, 87, 5560.

31. Stehfest, H. Commun. ACM 1970, 13, 47.

32. Grinvald, A.; Steinberg, I. Z. Anal. Biochem. 1974, 59, 583.

33. Beddard, G. S.; Doust, T.; Meech, S. R.; Phillips, D. J. Photochem. 1981, 17, 427.

34. Tao, T. Biopolymers 1969, 8, 609.

35. Chuang, T. J.; Eisenthal, K. B. J. Chem. Phys. 1972, 57, 5094.

36. The autocorrelation functions for CV fluorescence in solution are particularly sensitive to the alignment of the 54.7° analyzer. A misalignment of ~5° yielded poor single-exponential autocorrelations for CV in ethanol and glycol but gave statistical biexponential autocorrelations; the resulting biexponential lifetimes τ_1 and τ_2 for CV in ethanol were similar to those reported by Beddard et al.[33]

37. Avouris, P.; Gelbart, W. M.; El-Sayed, M. A. Chem. Rev. 1977, 77, 793.

38. Loring, R. F.; Andersen, H. C.; Fayer, M. D. Chem. Phys. 1984, 85, 149.

EXCITATION TRANSPORT AND FLUORESCENCE ANISOTROPY OF RHODAMINE 3B ON AMORPHOUS QUARTZ

Philip A. Anfinrud, David E. Hart, John F. Hedstrom, and Walter S. Struve

Department of Chemistry and Ames Laboratory - USDOE
Iowa State University, Ames, Iowa 50011

EXCITATION TRANSPORT AND FLUORESCENCE ANISOTROPY OF RHODAMINE 3B ON AMORPHOUS QUARTZ

Introduction

Electronic excitation transport and trapping in disordered systems have provided challenging problems to theorists interested in predicting time-dependent observables such as excited state populations, fluorescence depolarization, and the transient grating effect [1]. Such properties may be extracted from solutions to the couples master equations which govern the set of probabilities p_j that electronic excitation resides on molecule j at time t. In the absence of excitation trapping, these master equations assume the form [2]

$$dp_j/dt = \sum_k^N w_{jk}(p_k - p_j) - p_j/\tau_D \qquad (1)$$

for a system of N identical donor molecules with intramolecular excited state lifetime τ_D. The coefficients w_{jk} are Förster dipole-dipole transition rates [3]

$$w_{jk} = \frac{3}{2\tau_D}\left[\frac{R_o}{r_{jk}}\right]^6 \left[\hat{d}_j\cdot\hat{d}_k - 3(\hat{d}_j\cdot\hat{r}_{jk})(\hat{d}_k\cdot\hat{r}_{jk})\right]^2 \qquad (2)$$

where $\vec{r}_{jk}$ is the position of molecule j relative to that of molecule k, $\hat{d}_j$ and $\hat{d}_k$ are unit vectors along the respective

transition moments, and R_0 is the intermolecular separation at which excitation transport and intramolecular decay have equal probability. Since excitation can migrate from molecule to molecule in sequences with unlimited length and topology, exact solutions to the master equations have not been achieved for arbitrary donor molecule number densities in system of any dimensionality. Early attempts to approximate the master equation solutions tended to assume either that one or two excitation migrations occurred at most during the donor excited state lifetime [4, 5] or that excitation sharing was limited to nearest [6] or nearest and next-nearest neighbors [7].

Beginning in 1979, Andersen, Fayer, and their co-workers developed Green's function expansions of the master equation solutions [8-11] to yield successive self-consistent approximations to $G^S(t)$, the time-dependent probability that electronic excitation will be found on the photon-excited donor molecule. $G^S(t)$ is experimentally observable using the transient grating effect [12], and is also related to the time-dependent fluorescence depolarization [13] by

$$G^S(t) = 2.5\frac{I_{\parallel}(t) - I_{\perp}(t)}{I_{\parallel}(t) + 2I_{\perp}(t)} \qquad (3)$$

in three-dimensional systems, where $I_{\parallel}(t)$ and $I_{\perp}(t)$ are the fluorescence intensity components polarized parallel and normal to the linearly polarized excitation. It has been verified [13] that the next-lowest (three-body) self-

consistent approximation to $G^s(t)$ in three dimensions [8] yields calculated fluorescence polarization components in excellent agreement with those observed in concentrated dye solutions, and the master equation has been considered essentially solved for three-dimensional disordered systems.

For two-dimensional systems (e.g., molecules adsorbed onto a flat surface), comparable master equation solutions are not available because in two dimensions the three-body Green's function $G^s(t)$ fails to converge at long times [14]. The lowest order, two-body approximation [11] is expected to be less reliable in two than in three dimensions, because density expansions tend to converge less rapidly in systems with lower dimensionality. No experimental measurements of two-dimensional $G^s(t)$ have been reported to our knowledge. In this work, we have measured fluorescence anisotropies for rhodamine 3B (R3B) adsorbed onto optically flat fused quartz. Our experimental fluorescence components $I_{\parallel}(t)$ and $I_{\perp}(t)$ are deconvoluted with model decay functions which incorporate the two-dimensional, two-body Green's function $G^s(t)$ for donor molecules randomly distributed on a flat surface. At very low coverages, we find that essentially no fluorescence depolarization occurs within several donor lifetimes (or equivalently that $G^s(t) \to 1$ for all t); this implies that dye reorientation contributes negligibly to the observed fluorescence depolarization, which then arises exclusively from excitation transport among motionless,

adsorbed donors. R3B was chosen for the donor species because it dimerizes much less in our surface coating procedure than many dyes (including cresyl violet [15]), is free of acid-base equilibria which complicate the fluorescence profiles of rhodamine B [16, 17], and exhibits an $S_1 \leftarrow S_0$ absorption band (ε_{max} ~1.2 x 10^5 at 555 nm in ethanol; ~10 nm red shift on quartz) which can be pumped by a rhodamine 590 synchronously pumped dye laser.

The relationship between $G^S(t)$ and the fluorescence components $I_{\parallel}(t)$ and $I_{\perp}(t)$ depends on the angular distribution of fixed donor transition moments on the surface [18], so a knowledge of this distribution is important to the data analysis. It is possible a priori that R3B molecules adsorbed on $\lambda/4$ fused quartz can experience microscopic surface roughness with a mean periodicity small enough to produce transition moments which are nearly randomly oriented in three dimensions. Second-harmonic anisotropy measurements on "optically flat fused quartz" substrates coated with less than one monolayer of xanthene dyes (rhodamine 6G, rhodamine B, and acidic fluorescein [19, 20])have implied that the transition moments in these systems form characteristic fixed angles θ^* from the macroscopic surface normal (Figure 1), with random distributions in the azimuthal adsorption angle ϕ. The derived adsorption angles (e.g., $\theta^* = 52 \pm 4°$ and $55 \pm 4°$ for the long-axis polarized $S_1 \leftarrow S_0$ transitions in rhodamine

6G and rhodamine B respectively) support the hypothesis that adsorption occurs through bonding of the -COOH or -COOR groups to the fused silica substrate. Since these substrates are not absolutely flat on a molecular scale, our transition moment distributions cannot actually be restricted to single, sharp cones of half-angle θ^*. This is demonstrated in Figure 2a, which compares fluorescence profiles (obtained by techniques described in the Experimental Section) horizontally and vertically polarized laser pulses. The fluorescence was collected along the vertical surface normal in both cases without an analyzing polarizer. The two profiles should exhibit identical time dependence if the transition moments are restricted to a single cone with its symmetry axis parallel to the surface normal. They would differ materially if the transition moments were randomly oriented in three dimensions, and they would then correspond to $I_{\parallel}(t) + I_{\perp}(t)$ and $2I_{\perp}(t)$ in the three-dimensional notation of Eq. 3. Since the profiles in Fig. 2a in fact do not coincide, they give dynamic evidence that the dye transition moments are not adsorbed at a uniform angle θ^* from the excited fluorescence profiles collected from the same R3B/quartz sample (i) with an analyzing polarizer oriented perpendicular to the excitation polarization (Fig. 1) and (ii) with no analyzing polarizer. Since the difference between the pair of profiles in Figure 2b is much larger than that in Figure 2a, fluorescence

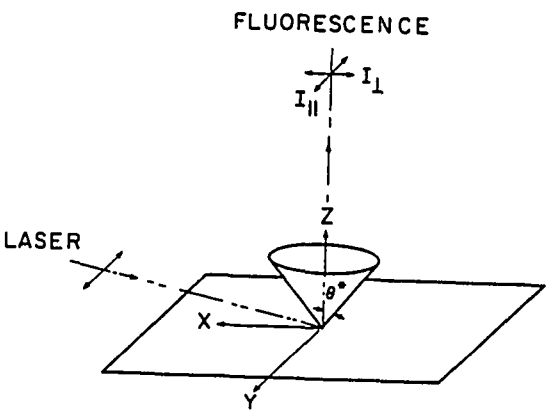

Figure 1. Experimental geometry. The surface lies in the xy plane. Laser pulses are y-polarized in most of this work, and fluorescence is observed along the z axis. For analysis, dye transition moments are assumed to be randomly distributed on a cone of half-angle θ^* from surface normal

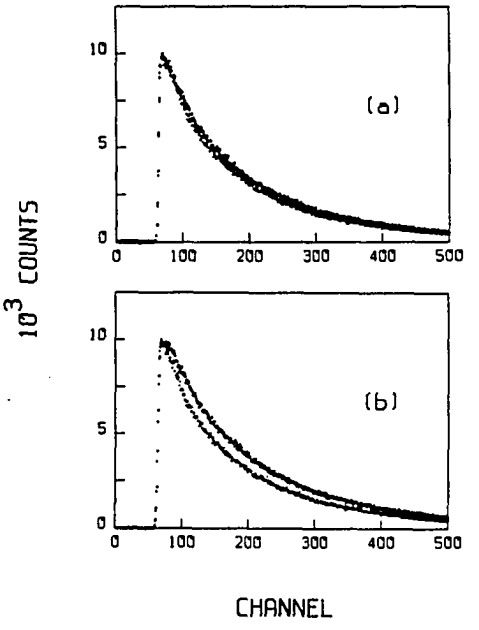

Figure 2. Fluorescence profiles from R3B on optically flat quartz, viewed along surface normal (a) without analyzing polarizer for out-of-plane (upper) and in-plane (lower) laser polarizations and (b) for in-plane laser excitation with a perpendicular analyzing polarizer (upper) and with no analyzing polarizer (lower). Counting times were adjusted to yield 10^4 peak counts in each profile. R3B coverage is similar to that of sample 3 in Table I. Time calibration is 20 ps/channel

depolarization in our R3B/quartz systems is dominated by changes in the azimuthal adsorption angle ϕ attending excitation transport, rather than by ensemble variations in the orientation of the cone axis. A a first approximation, it will therefore be assumed that the R3B transition moments are restricted to lie on the surface of a single cone of half-angle θ^* (whose value does not enter in the relationship between $G^s(t)$ and the time-dependent fluorescence polarization components) aligned parallel to the macroscopic surface normal.

In the Calculation Section, we derive expressions for $I_{\parallel}(t)$ and $I_{\perp}(t)$ in terms of $G^s(t)$ for our experimental geometry and obtain the two-dimensional, two-body Green's function $G^s(t)$ using Förster dipole-dipole transition rates w_{jk} with the correct orientation dependence [12]. The Experimental Section contains the experimental procedure. In the Data Analysis Section we describe the data treatment, a nonlinear least-squares convolute-and-compare analysis which uses model decay functions derived from the two-body Green's function and which fits the isotropic and anistropic parts of $I_{\parallel}(t)$ and $I_{\perp}(t)$ independently in order to avoid covariance between the isotropic lifetime parameters and the parameters in $G^s(t)$. The results and discussion are presented in the Data Analysis Section, where several factors which specifically influence the

interpretation of surface fluorescence anisotropy measurements are discussed.

Calculation of Fluorescence Components and the Two-Body Green's Function $G^S(t)$

The long-axis polarized $S_1 \leftarrow S_o$ absorption and fluorescence transitions in R3B are assumed to have parallel transition moments which are aligned at a fixed angle θ^* from the surface normal (the z axis), but are randomly distributed in ϕ. The excitation polarization lies in the surface plane (the xy plane) and is parallel to the y axis as shown in Fig. 1; the pumping pulses propagate in the xz plane. The orientational probability distribution for excited state transition moments at time t after laser pulse excitation at t = 0 is [21]

$$W(\theta\phi t) = \int_o^{2\pi} d\phi \int_o^{\pi} d\theta \; G(\theta_o\phi_o|\theta\phi t) \; W(\theta_o\phi_o) \qquad (4)$$

where $G(\theta_o\phi_o|\theta\phi t)$ is a Green's function propagator and $W(\theta_o\phi_o)$ is the initial probability distribution created by electric dipole absorption at t = 0. Since θ is fixed at the adsorption angle θ^*, this becomes

$$W(\phi t) = \int_o^{2\pi} d\phi \; G(\phi_o|\phi t) \; W(\phi_o) \qquad (5)$$

with

$$W(\phi_o) = \frac{1}{\pi} \sin^2\theta^* \cos^2\phi_o \ . \qquad (6)$$

The angles ϕ and ϕ_o are measured from the y axis. The propagator can be expanded in terms of
$\Phi_m(\phi) = (2\pi)^{-1/2}\exp(im\phi)$

$$G(\phi_o|\phi t) = \sum_{m=-\infty}^{\infty} c_m(t)\Phi_m^*(\phi_o)\ \Phi_m(\phi) \qquad (7)$$

and obeys the boundary conditions

$$G(\phi_o|\phi 0) = \delta(\phi - \phi_o) \equiv \sum_{m=-\infty}^{\infty} \Phi_m^*(\phi_o)\Phi_m(\phi) \qquad (8)$$

$$\int_o^{2\pi} d\phi\ G(\phi_o|\phi t) = 1 \ .$$

This requires that $c_o(t) = 1$ and $c_m\ (0) = 1$. Combining Eqs. 5-8 then implies that the orientational probability distribution must evolve as

$$W(\phi t) = \frac{\sin^2\theta^*}{2\pi}[1 + c_2(t)\ \cos\ 2\phi] \ . \qquad (9)$$

The fluorescence components $I_{\parallel}(t)$ and $I_{\perp}(t)$ observed along the z axis are

$$I_{\parallel}(t) = P(t)\int_o^{2\pi} d\phi\ W(\phi t)\sin^2\theta^*\cos^2\phi$$

$$= P(t)\sin^4\theta^* \frac{1}{2}\left[1 + \frac{1}{2}c_2(t)\right] \tag{10a}$$

$$I_\perp(t) = P(t)\int_0^{2\pi} d\phi\, W(\phi t)\sin^2\theta^*\sin^2\phi$$

$$= P(t)\sin^4\theta^* \frac{1}{2}\left[1 - \frac{1}{2}c_2(t)\right] \tag{10b}$$

where P(t) is the isotropic decay law. It may be shown that if all of the fluorescence depolarization proceeds via electronic excitation hopping between stationary dye molecules on the surface, $c_2(t)$ can be identified with $G^S(t)$, the exact probability that the excitation is found on the laser-excited dye molecule at time t. Craver [18] has shown that for the present transition moment adsorption geometry and excitation polarization

$$G^S(t) = 2\,\frac{I_\parallel(t) - I_\perp(t)}{I_\parallel(t) + I_\perp(t)} \tag{11}$$

which is consistent with Eqs. 10. This equation supersedes Eq. 3, which describes fluorescence depolarization in a three-dimensionally random distribution of transition moments. No knowledge of the adsorption angle θ^* is required to extract $G^S(t)$ from the fluorescence components using Eq. 11, provided fluorescence is observed along the surface normal. If the surface were inclined by an angle λ about the y axis, Eq. 11 would be replaced by

$$G^S(t) = 2\,\frac{I_{\parallel}\cos^2\lambda(1 + 2\tan^2\lambda\cot^2\theta^*) - I_{\perp}}{I_{\parallel}\cos^2\lambda + I_{\perp}} \,. \qquad (12)$$

Loring and Fayer [11] derived a self-consistency equation for the Laplace transform of the two-body Green's function $G^S(t)$ in two dimensions in the absence of excitation trapping

$$G^S(\varepsilon) = \left[\varepsilon + \rho\int d\vec{r}_{12}\,\frac{w_{12}}{(1 + 2G^S(\varepsilon)w_{12})}\right]^{-1}. \qquad (13)$$

Here ρ is the surface number density of donor molecules. For simplicity the transfer rate w_{12} was set equal to the orientationally averaged Förster rate $(R_o/r_{12})^6/\tau_D$, leading to

$$G^S(\varepsilon) = \left[\varepsilon + \frac{\pi C}{\tau_D}\left(\frac{4}{27}\right)^{1/2}\left(\frac{2G^S(\varepsilon)}{\tau_D}\right)^{-2/3}\right]^{-1}. \qquad (14)$$

$C \equiv \pi R_o^2\rho$ is the (dimensionless) reduced donor coverage and equals the mean number of donor molecules occupying a circle of radius R_o. Using the correct orientational dependence in w_{12} yields instead the self-consistency equation

$$G^S(\varepsilon) = \left[\varepsilon + \frac{\pi C}{\tau_D}\left(\frac{4}{27}\right)^{1/2}\left(\frac{2G^S(\varepsilon)}{\tau_D}\right)^{-2/3} a^{1/3}\int d\Omega_1 d\Omega_2 |\kappa_{12}|^{2/3}\right]^{-1} \qquad (15)$$

where

$$\kappa_{12} = \hat{d}_1\cdot\hat{d}_2 - 3(\hat{d}_1\cdot\hat{r}_{12})(d_2\hat{\cdot}\hat{r}_{12})$$

$$a = \left[\cos^4\theta^* + \frac{5}{4}\sin^4\theta^*\right]^{-1}.$$

The integral in Eq. 15 is carried out over all orientations Ω_1 and Ω_2 of transition moment pairs randomly distributed on the θ^* cone. Consideration of the anisotropy in w_{12} therefore replaces the reduced coverage C in the two-body Green's function with γC, where

$$\gamma = a^{1/3}\int d\Omega_1 d\Omega_2 |\kappa_{12}|^{2/3} \qquad (16)$$

is a constant which depends on the cone angle θ^*. A similar result is obtained when the anisotropy in w_{12} is incorporated into calculating the two-body, three-dimensional Green's function [13]; in that case, the reduced concentration of donor species becomes multiplied by

$$\gamma = \left[\frac{3}{2}\right]^{1/2}\int d\Omega_1 d\Omega_2 |\kappa_{12}| = 0.846 \ . \qquad (17)$$

This correction brings theoretical fluorescence profiles into excellent agreement with experimental fluorescence components emitted by rhodamine 6G solutions in glycerol [13]. Our reduced dye coverages are far less precisely known than the reduced dye concentrations used in solution

work, since our submonolayer R3B coatings generally exhibit optical densities less than 0.002 at their absorption maximum. We therefore approach comparisons of our experimental profiles with theory by determining to what extent agreement is possible for optimized reduced coverages C in nonlinear least-squares analyses using the two-body, two-dimensional form of $G^S(t)$.

Experimental Section

A Coherent Innova 90 argon ion laser with 5-W plasma tube operated at 26 A was acousto-optically mode-locked by a Harris Corp. H-401 unit driven at 48 MHz. It pumped a cavity-dumped rhodamine 590 dye laser (Coherent CR-599-01 with three-plate birefringent filter), which produced tunable picosecond pulses with ~8-ps fwhm. The cavity dumper combined a Harris Corp. H-100 AOM crystal, an H-102 driver synchronized with the mode-locker driver to provide a 4.8-MHz repetition rate, and optics mounted on Newport Research Corp. beam directors and Line Tool Co. translators. A real-time, rotating-mirror, zero-background autocorrelator [22] provided monitoring and optimization of laser performance.

Rhodamine 3B perchlorate (R3B) was obtained from Eastman Kodak Laser Products, and was used without further purification. Thin-layer chromatography (TLC) of R3B on

Analtech silica gel G plates revealed only one spot with ethanol/acetone, ethanol/acetic acid and 1-propanol/formic acid solvents. The surface substrates were $\lambda/4$ fused quartz. In most experiments, substrates were treated with dichlorodimethylsilane prior to dipping in aqueous R3B solutions with varied concentration (3.7×10^{-9} to 7.4×10^{-7} M), yielding hydrophobic surfaces with macroscopically uniform dye coatings of less than one monolayer. To test for possible effects of adsorption site inhomogeneity of fluorescence properties, some substrates were untreated before dye coating. Untreated substrates yielded visibly less uniform coverage (observed by total fluorescence count rate monitoring during computer-controlled translational surface scanning), but the time-dependent fluorescence profiles were not markedly sensitive to surface pretreatment. Such surface scans identified fluorescence "hot spots" arising from surface scratches or other imperfections, and profile accumulations were limited to uniformly coated areas.

Horizontally polarized dye laser pulses at 575 nm were focused to ~0.1-nm diameter at ~75° incidence on horizontal quartz substrates coated with R3B. Fluorescence was collected vertically with a 5 cm focal length quartz lens and condensed by a 10 cm focal length lens through a variable rectangular aperture onto a Hamamatsu 1564U microchannel plate phototube (MCP) with bialkali

photocathode and borosilicate glass window. The MCP exhibited ~6 x 10^5 gain at 3000 V, 500 nm, and a transit time spread of 76 ps at 3200 V. Three-millimeter Schott filters (two OG-590 and one RG-610) screened 575 nm laser scatter and filter fluorescence from the MCP. The dye laser polarization was purified with a Promaster Spectrum 7 polarizer; an identical polarizer was used as analyzer between the substrate and collecting lens. The differential sensitivity to parallel- and perpendicular-polarized light was less than 2%.

Photocurrent pulses were amplified and inverted with a B&H Electronics AC3011 MIC (3.15 GHz) 21-dB preamplifier and an EG&G IT100 inverting transformer. The amplified pulses were processed in a Tennelec TC455 quad constant-fraction discriminator (CFD) and were used as START pulses in an Ortec 457 time-to-amplitude converter (TAC). The signal from dye laser pulses sampled by an EG&G FOD-100 photodiode in the photoconduction mode was passed through an Ortec 934 quad CFD to provide STOP pulses. TAC output was accumulated in a Canberra Series 30 MCA in the PHA mode, yielding 5.0-, 10.0-, or 20.0-ps channel resolution. Laser pulses scattered from a clean quartz substrate were used for generating instrument functions (~80 ps fwhm) for deconvolution of raw data.

Fluorescence profiles were transferred to a Digital

Equipment Corp. MINC-23 system with dual floppy disk drive operating in an RT-11 environment and analyzed with a Marquardt nonlinear regression [23] program.

Results and Discussion

Details of the convolute-and-compare analysis are given in the Appendix. Following Eq. 10 and the subsequent discussion on the Calculation Section, we use as trial functions for the polarized fluorescence intensities $I_{\parallel}(t)$ and $I_{\perp}(t)$

$$I_{\parallel}(t) = AP(t)[1 + G^{S}(t)/2] \tag{18a}$$

$$I_{\perp}(t) = AP(t)[1 - G^{S}(t)/2] \tag{18b}$$

where $G^{S}(t)$, the two-body, two-dimensional Green's function, is computed as outlined in the Appendix. At this level of approximation, $G^{S}(t)$ depends on the single parameter

$$\alpha = C^{3}/\tau_{D}. \tag{19}$$

Equations 18 imply that the magic analyzing polarizer angle, at which the detected fluorescence profiles will behave as P(t) for our assumed adsorption geometry, is 45° (vs. 54.7° for fluorescence emitted from solutions). Three fluorescence profiles were typically accumulated from each

sample: $I_{\parallel}(t)$, $I_{\perp}(t)$, and a magic-angle profile. Ideally, P(t) should be a single-exponential decay function, and we have in fact obtained excellent single-exponential fits to magic-angle profiles from rhodamine 6G in glycerol in all but the most concentrated solutions, in which excitation trapping by dye dimers distorts the isotropic decay function P(t) [23]. For R3B on quartz, however, single-exponential fits to magic-angle profiles consistently yielded large values of χ^2 (which is defined in the Appendix), even at the lowest R3B coverages. Excellent fits (reduced χ^2 between 0.901 and 1.068) resulted from using a triexponential model function to analyze magic-angle profiles obtained from most of our R3B/quartz samples (Table I). This departure of the isotropic decay function P(t) from single exponentiality can arise from adsorption site inhomogeneity, from dye impurity, or from excitation trapping by adsorbed dye aggregates. The first two causes are unlikely because (i) we obtained results similar to those in Table I for R3B coated onto untreated quartz substrates as well as substrates treated with dichlorodimethylsilane; (ii) the R3B dye purity was verified by TLC (the Experimental Section), and its $-CO_2Et$ functional group cannot produce the carboxylic acid-base equilibrium exhibited by dyes like rhodamine B [16]; and (iii) the nonexponential character of P(t) increases markedly with surface coverage in Table I. In samples 1-3,

Table I. Triexponential fitting parameters for magic-angle profiles

$$N(t) = A_1\exp(-t/\tau_1) + A_2\exp(-t/\tau_2) + A_3\exp(-t/\tau_3)$$

sample	[R3B], M[a]	A_1	τ_1, ns	A_2	τ_2, ns	A_3	τ_3, ns	χ_r^2
1	3.7×10^{-9}	1.0	3.59	19.1	1.86	54.1	4.07	1.068
2	7.4×10^{-9}	1.0	0.194	5.71	2.23	17.0	4.13	0.901
3	3.7×10^{-8}	1.0	0.976	6.27	2.36	17.8	3.95	0.948
4	7.4×10^{-8}	1.0	0.327	4.85	1.65	12.5	3.63	1.031
5	7.4×10^{-7}	1.0	0.186	2.12	1.08	2.88	2.67	1.070

[a]In aqueous coating solution.

the magic-angle profiles are dominated by a long component with lifetime τ_3 = 4.05 ± 0.1 ns; in the two samples with higher coverage, τ_3 decreases to 3.63 and 2.67 ns, and the shorter lifetime components gain more importance. Excitation trapping by aggregates is therefore a major origin of nonexponentiality in P(t) at our higher coverages. This concentration behavior parallels that observed in solution [13, 23] but is more pronounced because dyes form aggregates more readily on surfaces than in alcoholic solution [15].

The experimental $I_{\parallel}$ and $I_{\perp}$ profiles were then deconvoluted using Eq. 19 and 20 with the isotropic lifetime parameters in P(t) fixed as determined in the analyses of the magic-angle profiles. Parameter correlation between P(t) and $G^S(t)$ was thus avoided. $G^S(t)$ itself contains only α (defined in Eq. 21) as an adjustable parameter in the two-body approximation, so $G^S(t)$ contributes very little functional flexibility to $I_{\parallel}(t)$ and $I_{\perp}(t)$. Both of the latter profiles were deconvoluted simultaneously, and their combined χ^2 was minimized using a common, optimized α value [24]. The inverse Laplace transform of Eq. A2 in the Appendix was evaluated numerically [25] in order to compute $G^S(t)$ during deconvolution. Our 80-ps-fwhm instrument function was not wide compared to the 20-ps channel spacing used in most of this work. The convolute-and-compare

algorithm was restricted to integral shift parameters s (Eq. A1), so that choosing M = 1 as the initial channel for computing χ^2 (Eq. A3) produced disproportionate contributions to χ^2 from the sharply rising portions of the fluorescence profiles. Channel M was therefore typically placed on the rising edge at 90% peak counts, and the continuous curves which represent convolutions of the optimized model functions with the instrument function in the figures accompanying this Section all begin with channel M.

The quality of data fits using the model functions in Eq. 18a and 18b can be estimated by evaluating the autocorrelations of residuals [26]

$$A_n = \frac{2N}{N - M} \frac{\sum_{i=1}^{(N-M)/2} Y_i^{1/2}(C_i - Y_i)Y_{i+n}^{1/2}(C_{i+n} - Y_{i+n})}{\sum_{i=1}^{N} Y_i(C_i - Y_i)^2} \quad (20)$$

where N is the number of channels comprising the fluorescence profile. The autocorrelation A_o in channel 0 is unity. For model functions which are indistinguishable from the true decay functions, the autocorrelations A_n in other channels consist of random statistical fluctuations about $A_n = 0$. Such statistical autocorrelations were obtained for all of the triexponential fits to the magic-angle profiles summarized in Table I, meaning that the

triexponential decay model is sufficiently flexible to replicate the observed isotropic decays P(t) to within serve only as phenomenological descriptions of P(t) for deconvolution of the $I_{\parallel}$ and $I_{\perp}$ profiles using variable $G^S(t)$ in Eq. 18a and 18b, and physical interpretations of the preexponential and lifetime parameters in Table I do not enter in the data analysis. Strictly speaking, excitation trapping by aggregates influences the fluorescence anisotropy as well as P(t), and the relationship between the fluorescence components $I_{\parallel}(t)$ and $I_{\perp}(t)$ and the Green's function $G^S(t)$ in Eq. 18 is applicable only in the limit where the donor-donor excitation hopping rate greatly exceeds the rate of excitation trapping. This approximation is more nearly obeyed in samples 1-3 (in which the isotropic decay behavior varies slowly with donor coverage) than in samples 4 and 5, where the long-component lifetime τ_3 in Table I begins to decrease rapidly with increased coverage. Gochanour and Fayer [13] observed isotropic lifetime shortening from 3.1 to ~2.85 ns in their most concentrated rhodamine 6G/glycerol solutions, and they corrected for this effect by using reduced lifetimes in the isotropic decay portion of their three-dimensional analogues to Eq. 18a and 18b. Such corrections are inherent in our procedure of using the least-squares triexponential parameters from Table I in P(t) while varying α in $G^S(t)$ to fit the observed fluorescence anisotropy.

The experimental $I_{\parallel}(t)$ and $I_{\perp}(t)$ profiles are plotted for samples 2-5 in Figure 3; the same spots were irradiated on these surfaces to obtain both these profiles and the magic-angle profiles described in Table I. The continuous curves are convolutions of the model functions in Eq. 18a and 18b with the instrument function, optimized with respect to α and the shift parameters s in Eq. A1. The upper and lower inset plots in each part of Figure 3 show the autocorrelations of residuals (Eq. 20) for $I_{\parallel}(t)$ and $I_{\perp}(t)$, respectively. The time scale in Figure 3 spans ca. 10 ns, or more than $2\tau_D$ for R3B on quartz. At the lowest coverage shown in Figure 3 (sample 2), the fluorescence depolarization is relatively small because $I_{\parallel}/I_{\perp}$ changes comparatively little between t = 0 and $2\tau_D$; much larger depolarizations are evident in samples 3-5.

In Table II, we list the final least-squares fitting parameter α, the reduced χ^2, and the reduced coverage computed from $C = (\alpha\tau_D)^{1/3}$ using τ_D = 4.05 ns, for samples 1-5. The optimized reduced coverage C generally increases with the concentration of R3B coating solution used; a notable exception is the fact that C turns out to be larger for the irradiated point on sample 3 than for that on sample 4. At the highest coverage studied (C = 0.651 for sample 5 in Table II), the mean separation between nearest-neighbor donor molecules is still larger than R_o ~51 Å for R3B on quartz [27]. At and above such coverages, the fluorescence

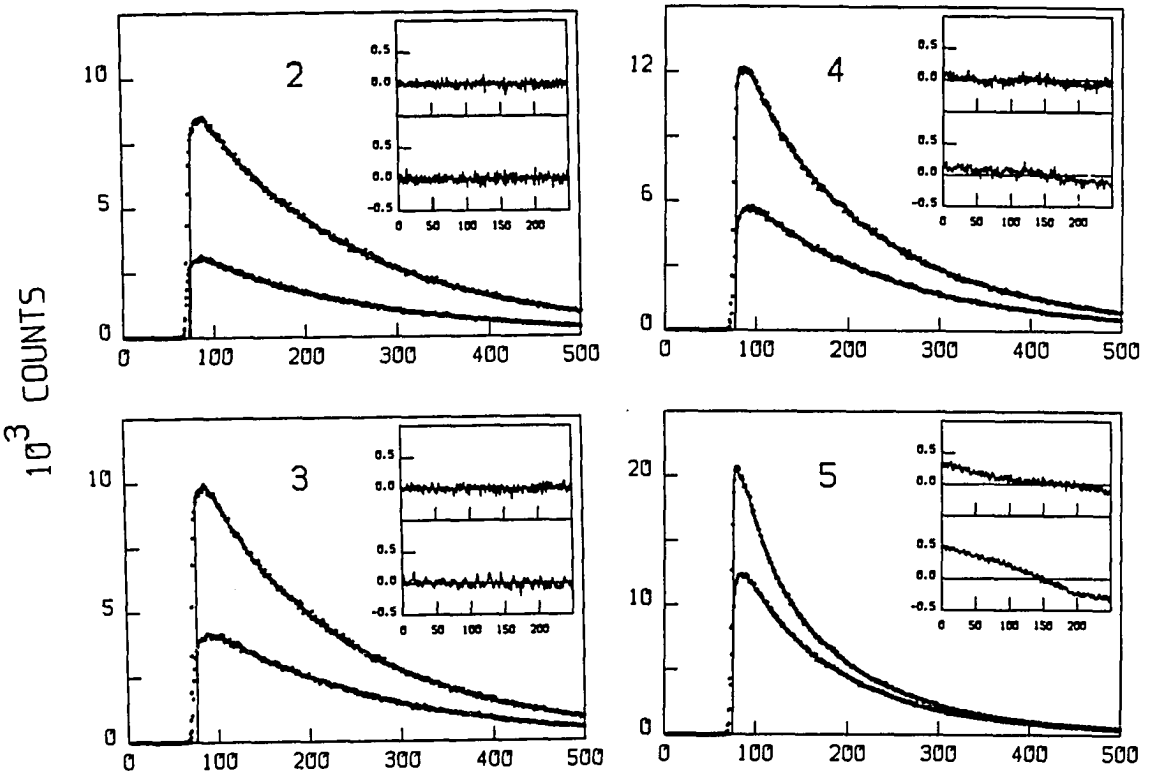

Figure 3. Fluorescence profiles $I_{\parallel}(t)$ and $I_{\perp}(t)$ for sample 2-5 in Table I. Continuous curves are optimized convolutions of the model functions in Eq. 18a and 18b with the instrument function. Upper and lower inset plots show autocorrelations of residuals for $I_{\parallel}(t)$ and $I_{\perp}(t)$, respectively. Time calibration is 20 ps/channel; all fluorescences were excited with in-plane laser polarization

Table II. Fitting parameters for anisotropic fluorescence profiles[a]

$$I_{\parallel}(t) = P(t)\ [1 + \frac{1}{2}G^{s}(t)]$$

$$I_{\perp}(t) = P(t)\ [1 - \frac{1}{2}G^{s}(t)]$$

sample		α, ns^{-1}	Cp[b]	X_r^2
1	$\parallel$	1.29×10^{-4}	0.0805	1.004
	$\perp$			1.119
2	$\parallel$	2.75×10^{-4}	0.104	1.104
	$\perp$			1.055
3	$\parallel$	2.16×10^{-2}	0.444	1.009
	$\perp$			1.046
4	$\parallel$	1.75×10^{-2}	0.414	1.288
	$\perp$			1.229
5	$\parallel$	6.80×10^{-2}	0.651	1.676
	$\perp$			2.155

[a]Triexponential parameters in P(t) fixed at values listed in Table I.

[b]Computed assuming τ_D = 4.05 ns.

count rate decayed noticeably during a typical counting period of ~5 min. Stable count rates were obtained at lower coverages, implying that coverage-dependent photochemistry depleted the surface density of R3B monomers at sufficiently high densities. This photochemistry precluded studying coverages higher than that in sample 5; in the latter case, excitation trapping visibly accelerates the decay in the profiles of sample 5 in comparison to the decay observed in samples 2-4 (Figure 3).

In Figure 4, we plot optimized reduced coverages vs. concentration of aqueous R3B coating solution for triads of profiles obtained by (i) pumping of a given spot, (ii) consecutive pumping of the same spot, and (iii) pumping of a new spot. Photochemistry tends to produce spreads in C values which are largest at the highest coverage, although considerable scatter is also observed at the lowest coverage because in this regime $G^S(t)$ is a weak function of α ($G^S(t) \to 1$ for all t when $\alpha \to 0$). These reduced coverages are not linear in the coating solution concentration, but their locus resembles a Langmuir isotherm in that C levels off at the higher concentrations [28]. The continuous curves are plots of the Langmuir type I isotherm function

$$C = \frac{\alpha M}{1 + \beta M} \qquad (21)$$

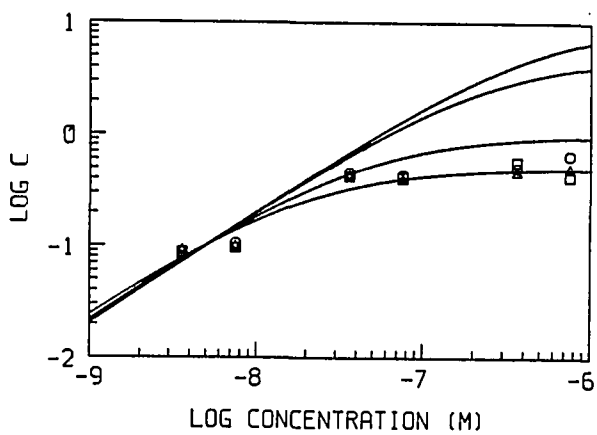

Figure 4. Optimized reduced coverages C for nonlinear least-squares fits to $I_{\parallel}(t)$ and $I_{\perp}(t)$ profiles for samples 1-5, plotted vs. concentration M of R3B coating solution for (O) irradiation of an initial spot, (Δ) consecutive irradiation of the same spot, and (□) irradiation of a new spot on R3B-coated quartz. Continuous curves are Langmuir adsorption functions $C = \alpha M/(1 + \beta M)$ for limiting reduced coverages α/β = 0.5, 1.0, 5.0, and 10.0 (bottom through top), adjusted to pass through C = 0.1 at 5.0×10^{-9} M. The numerical value of γ = 0.837, computed from Eq. 16 with θ^* = 52° [19], was used to adjust the optimized reduced coverages for this figure

for several values of the ratio α/β, which equals the limiting coverage at large coating solution molarities M. Near-Langmuir adsorption behavior has been reported for rhodamine B solution-coated onto SnO_2 and glass [29], and the implications of Figure 4 for the interpretation of our data will be discussed below.

The visual agreement between the optimized convolutions and the fluorescence profiles in Figure 3 is so close that the autocorrelation functions are useful for determining how well Eq. 19 model the decay behavior. The autocorrelations are statistical for the $I_{\parallel}(t)$ and $I_{\perp}(t)$ profiles from samples 1 (not shown), 2, and 3; systematically nonstatistical autocorrelations appear in samples 4 and 5. The latter deviations are not a consequence of modeling artifices in the isotropic decay functions P(t), since our triexponential fits to the magic-angle profiles (Table I) yielded statistical autocorrelations similar to those of sample 2 in Figure 3 in all five samples. Close inspection of the unreduced plots for sample 5 in Figure 3 reveals that the deviations in $I_{\parallel}$ and $I_{\perp}$ anticorrelate, and so they arise from disagreement between the optimized two-body Green's function $G^s(t)$ and the observed anisotropy function $c_2(t)$, which enters with opposite sign in the parallel and perpendicular components of Eq. 10. The two-body Green's function contributes appreciably to the observed decay in $I_{\parallel}(t)$ and $I_{\perp}(t)$ even for C = 0.08 (sample 1), since $G^s(t)$ in

this approximation decays from 1.0 to 0.916 by $t = 2\tau_D$ for this value of C. The nonexponential character in $G^s(t)$ evolves rapidly as C is increased from 0.1 to 1.0 (Figure 5), and it appears remarkable that statistical autocorrelations are obtainable for C as large as 0.444 (sample 3). The quality of any self-consistent approximation to $G^s(t)$ declines as the reduced coverage or concentration is increased [8, 15], and in this context the nonstatistical autocorrelations obtained at the highest coverages in Figure 2 are not surprising.

However, a likelier cause for the larger deviation at higher coverage is excitation trapping. The R3B coverages which are spanned in Figure 4 are all too low for direct spectroscopic measurement of the actual R3B surface number density ρ ($= C/\pi R_o^2$). The optical density of a quartz surface coated with 7.4×10^{-5} M aqueous R3B was determined to be $0.002 \pm .00025$ using a Perkin-Elmer 320 UV-visible spectrophotometer, corresponding to a reduced coverage of $C \sim 9.0$. This fixes a minimum value for $\alpha/\beta \sim 9.0$ in the isotherms of Figure 4 (all of which are adjusted to pass between the sets of points representing samples 1 and 2), if Langmuir adsorption behavior is indeed followed. The isotherms for C = 5.0 and C = 10.0 pass near the points for samples 1-3, but at the higher coverages (sample 4 and 5) the optimized coverages from least-squares fitting of the fluorescence profiles lie far below the isotherms. These

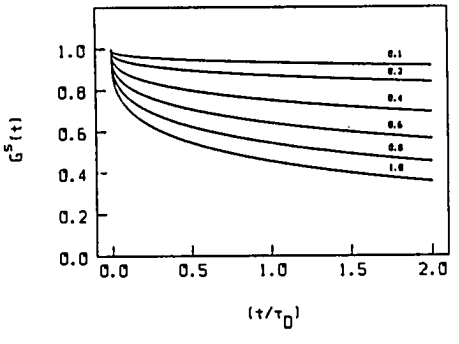

Figure 5. Two-body approximations to the two-dimensional Green's function $G^S(t)$, plotted vs. (t/τ_D) for reduced coverages C = 1.0, 0.8, 0.6, 0.4, 0.2, and 0.1 (bottom through top, respectively)

shortfalls arise physically from the fact that lifetime shortening by excitation trapping interrupts the depolarization process, so that the apparent value of the dynamical parameter C becomes smaller than the actual reduced coverage of donors. It appears certain that the true isotherm in the neighborhood of coating solution concentrations 10^{-7} to 10^{-6} M resembles the plotted isotherm for C = 10.0 more than it resembles the locus of optimized reduced coverages from the fluorescence data, since C must be on the order of 9.0 at 7.4×10^{-5} M. At the highest coverage, then, the optimized reduced coverage is about an order of magnitude too low.

In summary, the model functions which use the two-body Green's function $G^s(t)$ in Eq. 18a and 18b yield optimized convolutions which are statistically indistinguishable from the experimental profiles from the three samples with lowest coverage (1-3). Figure 4 shows that large distortions in the optimized reduced coverage are caused by excitation trapping in the other samples, and poorer autocorrelations are found in those samples. These disagreements do not arise primarily from inaccuracy in the two-body Green's function at these higher coverages; an effective test of the theory for C larger than ~0.4 requires samples in which aggregation and excitation trapping are more completely suppressed than was possible in our systems.

Solution-coated optically flat quartz systems were used

in the present work, because such dye coatings have been more widely studied than, for example, vacuum-sublimed coatings. Systems can be designed to provide better tests of excitation transport theory. Improved surface flatness can be provided in dye-dodecanoic acid layers in N_2-water interfaces [30] or on LiF surfaces, which can be cleaved to within one molecule of flatness. Such systems may also exhibit more uniformity in transition moment geometry. In this work, the presence of aggregation in R3B (as evidenced by excitation trapping at the higher coverages) indicates that the donor distribution is not truly random, so that strictly speaking the surface density ρ cannot be factored out of the integral in Eq. 13. Use of less polar molecules such as tetracene may both mitigate the trapping problem and provide a more disordered spatial distribution. This is of interest, because improved tests of excitation transport theory will require an ability to investigate fluorescence profiles at higher coverages and longer times, where larger divergences between the two-body theory and the exact Green's function can be expected. Such experiments are in progress in this laboratory.

Fedorenko and Burshtein [31] have recently shown that the Laplace transform $\hat{G}^S(\varepsilon)$ can be inverted analytically for the two- and three-body self-consistent approximations in three-dimensional disordered systems. They demonstrated that both approximations to $G^S(t)$ exhibit incorrect long-

time asymptotic behavior for systems in which the trap density greatly exceeds the donor density (the "static quenching limit") by comparing them to the exact $G^s(t)$ [3] for this limit. The three-body Green's function does describe static quenching dynamics rather accurately for $C_T^2(t/\tau_D) \lesssim 5$ [31], where C_T is the reduced trap density. This regime encompasses the limits of most existing time-resolved excitation transport experiments, where the decay kinetics are typically followed for two or three donor lifetimes and $C_T \lesssim 1.5$ No comparison of the three-body $G^s(t)$ with the exact Green's function is possible in the "migration limit" where the donor density is much larger than the trap density, since no exact theory exists for this case. We have recently shown [23] that for depolarized fluorescence profiles obtained from rhodamine 6G in 10-μm-thick glycerol solutions using the present photon counting techniques, the discrepancies between the experimental profiles and optimized profiles calculated from the three-body theory for $0.06<C<1.26$ are dominated by small experimental artifacts (principally self-absorption at the lower dye concentrations), rather than by inaccuracy in the three-body theory. This suggests that the $C^2(t/\tau_D)$ range of applicability for the three-dimensional three-body theory in the migration limit may resemble the $C_T^2(t/\tau_D)$ range of applicability in the static quenching limit and that the three-body theory accurately describes excitation transport

in many physically realizable situations.

Since the differences between exact dynamics and self-consistent theories are likely to be magnified in systems with lower dimensionality and since the exact dynamics are generally unknown in systems of any dimensionality in the migration limit, we were motivated to try the present two-dimensional systems to determine whether systematic errors in $G^s(t)$ calculated from the two-body theory could be identified and measured. Improved sample preparation and characterization will facilitate accomplishment of this goal over a broad range of surface coverages.

Acknowledgements

The Ames Laboratory is operated for the U.S. Department of Energy by Iowa State University under contract No. W-7405-Eng-82. This work was supported by the Office of Basic Energy Sciences. We thank Professor Michael Fayer for helpful discussions.

References

1. Fayer, M. D. Annu. Rev. Phys. Chem. 1982, 33, 63.
2. Förster, Th. Ann. der Physik (Leipzig) 1948, 6, 55.
3. Förster, T. Discuss. Faraday Soc. 1959, 27, 7.

4. Galanin, M. D. Tr. Fiz. Inst. im. P. M. Lebedeva, Akad. Nauk SSSR 1950, 5, 339.

5. Vavilov, S. I. JETP Lett. (Engl. Transl.) 1943, 13, 13.

6. Ore, A. J. Chem. Phys. 1959, 31, 442.

7. Craver, F. W.; Knox, R. S. Mol. Phys. 1971, 22, 385.

8. Gochanour, C. R.; Andersen, H. C.; Fayer, M. D. J. Chem. Phys. 1979, 70, 4254.

9. Loring, R. F.; Andersen, H. C.; Fayer, M. D. J. Chem. Phys. 1982, 76, 2015.

10. Loring, R. F.; Fayer, M. D. Chem. Phys. 1984, 85, 149.

11. Loring, R. F.; Fayer, M. D. Chem Phys. 1982, 70, 139.

12. Miller, R. J. D.; Pierre, M.; Fayer, M. D. J. Chem. Phys. 1983, 78, 5138.

13. Gochanour, C. R.; Fayer, M. D. J. Phys. Chem. 1981, 852, 1989.

14. Fayer, M. D., Dept. of Chem., Stanford University, private communication.

15. Anfinrud, P.; Crackel, R. L.; Struve, W. S. J. Phys. Chem. 1984, 88, 5873.

16. Sadkowski, P. J.; Fleming, G. R. Chem. Phys. Lett. 1978, 57, 526.

17. Faraggi, M.; Peretz, P.; Rosenthal, I.; Weinraub, D. Chem. Phys. Lett. 1984, 103, 310.

18. Craver, F. W. Mol. Phys. 1971, 22, 403.

19. DiLazzaro, P.; Mataloni, P.; DeMartin, F. Chem. Phys. Lett. 1985, 114, 103.

20. Heinz, T. F.; Shen, C. K.; Richard, D.; Shen, Y. R. Phys. Rev. Lett. 1982, 48, 478.

21. Tao, T. Biopolymers 1969, 8, 609.

22. Yasa, Z. A.; Amer, N. M. Opt. Commun. 1981, 36, 406.

23. Anfinrud, P. A.; Hart, D. E.; Hedstrom, J. F.; Struve, W. S. J. Phys. Chem. 1986, 90, 3116.

24. Knutson, J. R.; Beechem, J. M.; Brand, L. Chem. Phys. Lett. 1985, 102, 501.

25. Stehfest, H. Commun. ACM 1970, 13, 47.

26. Grinvald, A.; Steinberg, I. Z. Anal. Biochem. 1974, 59, 583.

27. This value for R_o was evaluated for R3B with Eq. 4 of ref 3 by using measured absorption and fluorescence spectra for R3B adsorbed on quartz.

28. Langmuir, I. J. Am. Chem. Soc. 1916, 38, 2267.

29. Itoh, K.; Chiyokawa, Y.; Nakao, M.; Honda, K. J. Am. Chem. Soc. 1984, 106, 1620.

30. Subramanian, R.; Patterson, L. K. Phys. Chem. 1985, 89, 1202.

31. Fedorenko, S. G.; Burshtein, A. I. Chem. Phys. 1985, 98, 341.

Appendix

Given a trial decay law N(t), the convolute-and-compare analysis computes the convolution C_n in the nth channel of N(t) with the instrument function x(t)

$$C_n = \sum_{i=1}^{n} x(i - s)\, N(n - i) \; . \qquad \text{(A1)}$$

The variable shift parameter s allows for delay variations between profiles evaluated under changing experimental conditions. As trial functions N(t), we use I (t) and I (t)

in Eq. 18a and 18b, where $G^S(t)$, the two-body, two-dimensional Green's function, is given by the inverse Laplace transform of

$$G^S(\varepsilon) = \left[\frac{1}{2\varepsilon} + \frac{1}{4\varepsilon^2} + \frac{0.01637\alpha}{\varepsilon^3}^{1/2}\right]^{1/3} + \left[\frac{1}{2\varepsilon} - \frac{1}{4\varepsilon^2} + \frac{0.01637\alpha}{\varepsilon^3}^{1/2}\right]^{1/3\ 3} . \quad \text{(A2)}$$

The variable parameters s and $\alpha = C^3/\tau_D$ in the convolution C_n are optimized to yield a minimum in

$$\chi^2 = \sum_{i=M}^{N} (C_i - Y_i)^2/Y_i \quad \text{(A3)}$$

where Y_i is the experimental number of counts in channel i and (M,N) is the channel range used in the analysis.

TIME-CORRELATED PHOTON-COUNTING PROBE OF SINGLET EXCITATION TRANSPORT AND RESTRICTED ROTATION IN LANGMUIR-BLODGETT MONOLAYERS

Philip A. Anfinrud, David E. Hart, and Walter S. Struve

Department of Chemistry and Ames Laboratory-USDOE,
Iowa State University, Ames, Iowa 50010

TIME-CORRELATED PHOTON-COUNTING PROBE OF SINGLET EXCITATION TRANSPORT AND RESTRICTED ROTATION IN LANGMUIR-BLODGETT MONOLAYERS

Introduction

Theories for electronic excitation transport in disordered systems frequently deal with singlet excitation migration among randomly situated molecules in a homogeneous d-dimensional system [1-5]. All molecules in the model system are chemically identical, no excitation trapping occurs at dimers or higher aggregates, and the excited state population decays only through unimolecular radiative and/or nonradiative processes. The molecules are typically separated by such large distances that their electronic wavefunctions have minimal overlap. If the ground and lowest excited singlet states S_0 and S_1 are connected by an E1 transition, the transport then occurs by a long-range resonance dipole-dipole mechanism [6].

A primary objective of transport theories is calculation of the time-dependent probability $G^S(t)$ that the excitation resides on the initially pumped molecule. $G^S(t)$ decays from unity at early times, as excitation hops from the initial site to neighboring molecules. However, the excitation can return to the initial site via an infinite variety of pathways, passing through arbitrary sequences of neighbors.

$G^S(t)$ is therefore strictly given by an infinite-order density expansion, which cannot be summed exactly [2,4]. Recent attention has focussed on the question of whether asymptotic expressions for $G^S(t)$ can approximate the transport behavior in real systems. At long times and/or high concentrations, $G^S(t)$ behaves as $t^{-d/2}$ [4]. For 3-dimensional systems in the short time/low concentration regime, Huber and coworkers have shown [1] that

$$G^S(t) \rightarrow \exp\left[-C\left(\frac{\pi t}{2\tau}\right)^{\frac{1}{2}}\right]. \qquad (1)$$

Here τ is the isotropic excited state lifetime, and the dimensionless reduced concentration

$$C = \frac{4}{3}\pi R_o^3 \rho \qquad (2)$$

depends on the molecule number density ρ and on the Förster parameter R_o which characterizes the strength of the resonance dipole-dipole coupling responsible for transport [6,7]. The Huber limit for $G^S(t)$ physically corresponds to ignoring excitation return pathways which pass through more than one neighbor. Baumann and Fayer [5] have extended this "two-particle" theory to 1- and 2-dimensional random systems. In the latter case the 2-particle limit for $G^S(t)$ is

$$G^S(t) \rightarrow \exp[-1.354\ C\ (t/4\tau)^{1/3}] \qquad (3)$$

where C is now the reduced coverage

$$C = \pi R_0^2 \rho \qquad (4)$$

and ρ is now the surface number density of chromophores.

The Green's function $G^S(t)$ can be directly monitored by obtaining time-resolved fluorescence profiles from disordered systems excited by linearly polarized laser pulses. While such profiles do not give an inherently sensitive probe of excitation transport (in the sense that physically dissimilar models for $G^S(t)$ can give nearly congruent calculated fluorescence profiles), the superb S/N ratios afforded by time-correlated single photon counting can be exploited to yield exacting tests of transport theories. We have recently shown that in the absence of orientational correlation [8] and artifacts such as excitation trapping [9] and self-absorption [10], the two-particle theory accurately predicts the fluorescence depolarization for DODCI [8] and rhodamine 640 [11] solutions at concentrations up to several mM and times up to ~5τ. The most probable nearest-neighbor separations are on the order of 40Å at such concentrations, and fluorescence decays to 0.7% of its peak intensity after five lifetimes. The 3-dimensional two-particle theory therefore works well at nearly all concentrations for which interchromophore

interactions are validly expressed by leading terms in the multipole expansion, and for times accessible to current fluorescence measurement techniques.

It is of particular interest to test the corresponding two-particle theory for 2-dimensional random systems, Eq. 3. Two-dimensional transport plays a potentially important role in energy transfer on modified semiconductor surfaces and micelles, and the two-particle theory has provided a basis for extensions of transport theory to Langmuir-Blodgett (LB) bilayer and multilayer assemblies [5]. To our knowledge, no definitive transport study has been performed on any system resembling the idealized 2-dimensional assembly visualized in the two-particle theory. Desiderata for such a system include good surface flatness, good spatial dispersion of chromophores, and avoidance of trapping by aggregates. In an earlier study [12], we obtained polarized fluorescences from rhodamine 3B adsorbed onto $\lambda/4$ fused silica. Trapping severely distorted the isotropic fluorescence profiles at moderate to high dye coverages. Aggregation is often prevalent in LB assemblies of alkylated chromophores dispersedinn visibly transparent fatty acids. Yamazaki et al. [13] identified several excimer and excited dimer fluorescences from 16-(1-pyrenyl)hexadecanoic acid in LB films of stearic acid. In this work, we have obtained excellent dispersion of octadecylrhodamine B (ODRB) chromophores in LB monolayers of dioleoylphosphatidylcholine

(DOL) at air-water interfaces, as evidenced by the nearly constant isotropic fluorescence profiles emitted by these chromophores at reduced coverages up to C≃5. The comparatively short ODRB isotropic lifetime (~2.5ns, similar to that of rhodamine B in alcoholic solvents [14]) precludes excimer formation [15] at these coverages during the measurement time window of ~9ns. Analysis of polarized ODRB fluorescence profiles in terms of theories for $G^S(t)$ requires prior knowledge of (a) the orientational distribution of ODRB transition moments with respect to the interface normal and (b) the nature of these moments' rotational diffusion, which inevitably contributes to depolarization along with transport. These phenomena are characterized in separate experiments at low ODRB density (where negligible transport occurs), and have interesting implications for the microstructure of LB monolayers. We show that when rotational diffusion is properly considered, the two-particle theory for $G^S(t)$ provides an excellent description of the transport dynamics for ODRB reduced coverages between 0.7 and 4.8. Since the latter coverage corresponds to placing an average of 4.8 chromophores in a circle of radius R_0≃45Å for ODRB (the Excitation Transport Section), the range of validity in the two-particle theory appears to be very broad.

Experimental Section

Octadecylrhodamine B was obtained from Molecular Probes, Inc. (Eugene, OR); dioleoylphosphatidylcholine (>99%) was purchased in $CHCl_3$ solution from Avanti Polar Lipids, Inc. (Birmingham, AL). The structures of the chromophore and DOL are shown in Fig. 1. The 18 MΩ water for LB interfaces was deionized by treatment in ion exchange and charcoal columns, and was filtered before use with a 0.2 μm micropore. The LB trough and moveable barrier (Fig. 2) were fashioned from Teflon. The width of the air-water interface was 2.5 cm, and the length could be compressed from a maximum of 5.0 cm using a Newport Research Corporation Model 850-2 linear actuator. The laser beam transmitted at the interface and refracted into the water was passed by a 2.5 cm dia. fused silica window in the bottom of the trough; this minimized laser scatter into the fluorescence detector. The LB monolayer was prepared flush with the top of the trough. The trough was precisely machined to provide smooth, parallel 90° edges, and the barrier was fabricated with a smooth, matching cylindrical edge. These precautions proved critical in preventing leakage of the LB monolayer past the barrier upon compression. The surface pressure Π was monitored in situ during all experiments with a 0.5 cm wide Wilhelmy plate (Whatman #1 Qualitative filter paper) mechanically connected to a Mettler AE100 electronic balance

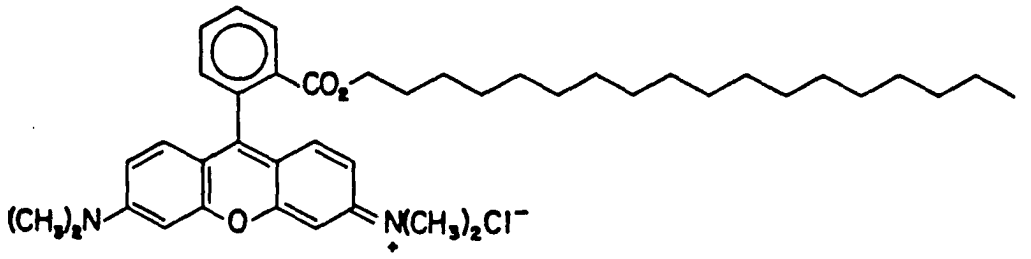

OCTADECYLRHODAMINE B

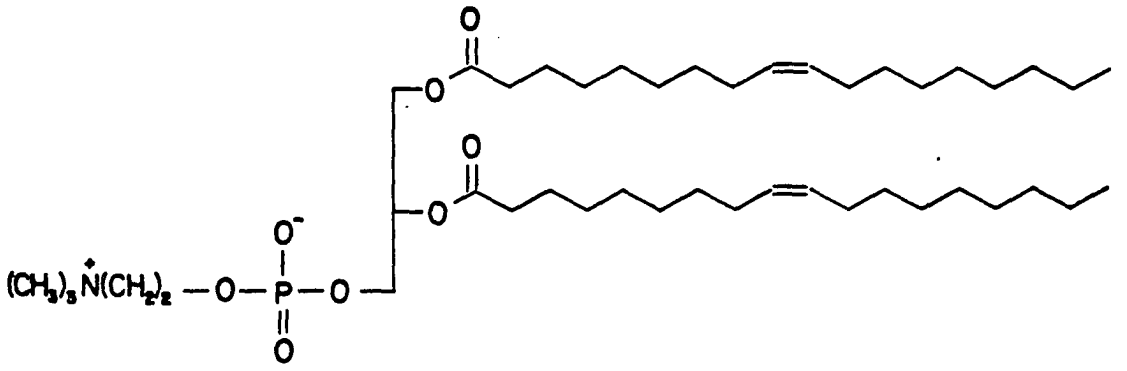

DIOLEOYLPHOSPHATIDYLCHOLINE

Figure 1. Molecular structures of octadecylrhodamine B (ODRB) and dioleoylphosphatidylcholine (DOL)

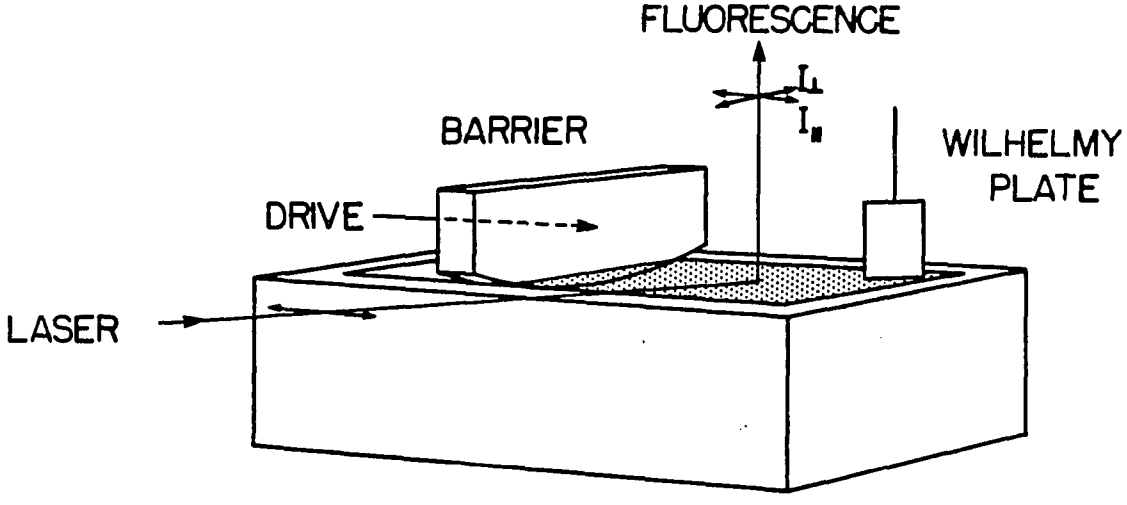

Figure 2. Schematic diagram of Langmuir-Blodgett trough, Wilhelmy plate, and beam geometry

[16,17]. Properly rinsed and prevented from drying, the same Wilhelmy plate could be used indefinitely and reproducibly. By keeping the interface flush with the top of the trough, excessive curvature was avoided near the edges of the assembly, increasing the reliability of surface pressure measurements. Cleanliness of the bare water surface was ascertained prior to monolayer preparation by verifying that the nominal surface pressure remained unchanged to within 0.1 dyne/cm while the surface area was compressed from 12.5 to 1.25 cm^2.

Stock solutions of ODRB were prepared in $CHCl_3$ (Mallinckrodt Nanograde). Aliquots of these solutions were combined with 1.00 cm^3 of the DOL solution (21 mg DOL/cm^3) and diluted to 25 cm^3 with $CHCl_3$. Each ORDB/DOL/$CHCl_3$ mixture was applied to the water surface in a 1.6 μl drop from a 10.0 μl syringe, with the barrier retracted to yield the maximum surface area of 12.5 cm^2. This procedure typically produced no discernible change in Π from that of the bare surface. The barrier was then advanced at a rate of 2 mm/min until Π increased by 0.1 dyne/cm. The advancement rate was then decreased to 0.35 mm/min to achieve near-equilibrium compression of the monolayer. Experiments were conducted at final surface pressures of 5, 15, and 25 dyne/cm (the Rotational Diffusion Section); compression to 25 dyne/cm required some 45 min. The breakdown pressure of LB monolayers of DOL is 44 dyne/cm

[18]. High ambient humidity was required to achieve reproducible compression curves and stable surface films; monolayers with Π stable to ~0.1 dyne/cm over several hours were then readily obtained.

The surface density of ODRB chromophores in LB monolayers may be estimated from the chromophore and DOL molecular weights (M_{ODRB} = 731.5 gm.mol^{-1} and M_{DOL} = 786.15 gm.mol^{-1} respectively), the volume X of the ODRB solution ailquot in cm^3, and the mass Y of the ODRB used per cm^3 of stock solution. The mole ratio of DOL to ODRB in the assembly is then R = 19.54/XY, and the mole fraction of ODRB is $X_{ODRB} = (1+R)^{-1}$. The number density of ODRB chromophores in the monolayer is

$$\rho = \frac{X_{ODRB}}{X_{ODRB}A_{ODRB} + X_{DOL}A_{DOL}} \qquad (5)$$

where A_{ODRB} and A_{DOL} are the areas occupied per molecule of chromophore and lipid, respectively. DOL reportedly occupies ~70Å^2/molecule at Π = 25 dyne/cm [18]. We have evaluated the Π versus A curve at 0.35 mm/min compression speed (which is considerably slower than that in reference [18]), and obtained A_{DOL} = 67Å^2/molecule at 25 dyne/cm. Fatty acids typically fill ~20Å^2/molecule [19]; since the largest ODRB mole fraction in this work was 0.049, the

Table I. Octadecylrhodamine B mole fractions and chromophore densities in Langmuir-Blodgett monolayers at 25 dyne/cm

Monolayer	X_{ODRB}	$\rho(10^{-6}$ Å$^{-2})$
1	0.0496	767
2	0.0321	490
3	0.0254	387
4	0.0163	246
5	0.0129	194
6	0.0082	123
7	0.0065	97

accuracy of this value for A_{ODRB} is not critical to our estimates of ρ. We list in Table I the mole fractions X_{ODRB} and estimated chromophore densities ρ for the LB monolayers used in our transport experiments.

The rhodamine 6G dye laser (synchronously pumped by an acoustooptically mode-locked argon ion laser), optics, and time-correlated single photon counting electronics have been described previously [9,20]. The laser produced linearly polarized 570 nm pulses with ~8 ps FWHM and 4.8 MHz repetition rate. The pulses were incident at 81° from the interface normal with their polarization in the surface plane (Fig. 3). Fluorescence was analyzed using a Promaster Spectrum 7 linear polarizer and detected along the surface normal using a Hamamatsu R1564U microchannel plate phototube (MCP). Two 3mm Schott OG-590 filters discriminated against scattered laser fundamental. The photon counting instrument function (evaluated by scattering laser pulses from a ground glass cover slip 0.15 mm thick) exhibited ~47 ps FWHM.

Appreciable background to the ODRB fluorescence was generated by Raman scattering from the water at the interface. For accurate cancellation of this early-time background from fluorescence profiles, the multichannel analyzer (MCA) was gated ON for a total live time which was proportional to a preset integrated laser intensity, ensuring that profiles could be accumulated with and without LB monolayers with identical background counts. This was

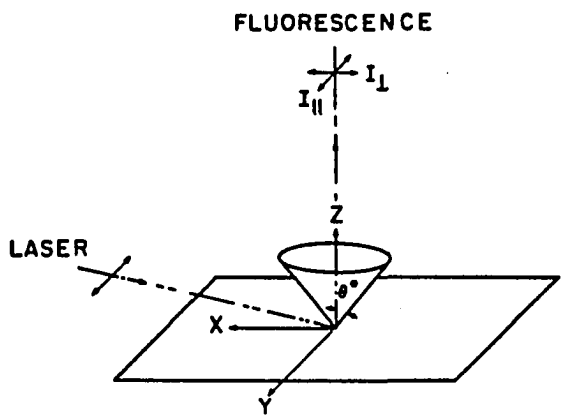

Figure 3. Detailed beam geometry. The Langmuir-Blodgett assembly lies in the xy plane. Laser pulses are y-polarized in most of this work, and fluorescence is observed along the z axis. Laser angle of incidence is 81° from the z axis. For analysis, the dye transition moments are assumed to be randomly distributed on cone of half-angle θ^* (case (b) in text)

achieved by sampling a portion of the laser pulses with an EG&G FOD-100 photodiode, whose output supplied the control voltage to a voltage-controlled oscillator (VCO). The latter oscillated with a frequency (typically 700 kHz) proportional to the laser intensity. The VCO output was enabled only during the live time of the time-to-amplitude converter (TAC), which was itself gated OFF for 125 μs after each true START input in order to eliminate TAC rate dependence for fluorescence counting rates up to 8 kHz [20]. A microprocessor enabled the MCA until a preset number of gated VCO counts was registered. In this way, fluorescence profile accumulation times were scaled to the integrated laser intensities. Such background cancellation was necessary only at the lowest ODRB densities for calibration of rotational diffusion in the absence of excitation transport.

Rotational Diffusion in Langmuir-Blodgett Assemblies

In the absence of excitation transport, the fluorescence intensity components $I_{\parallel}(t)$ and $I_{\perp}(t)$ polarized parallel and perpendicular to the laser polarization are related to the rotational anisotropy function r(t) by

$$I_{\parallel}(t) = P(t)[1 + d_{\parallel}r(t)]$$

$$I_{\perp}(t) = P(t)[1 + d_{\perp}r(t)] \qquad (6)$$

if the chromophore absorption and emission transition moments are parallel. The isotropic decay function P(t), often presumed to be single-exponential in homogeneous systems [9,12], frequently acquires multiexponential character from solvent reorganization and trapping artifacts [8]. The constants $d_{\parallel}$, $d_{\perp}$ depend on the orientational distribution of ODRB transition moments, which is unknown a priori. Conceivable distributions include (a) orientations which are isotropically random over 4π steradians, for which $d_{\parallel} = 0.8$, $d_{\perp} = -0.4$ [21]; (b) moments which are constrained to lie on a cone of fixed half-angle θ^* (Fig. 3), but are random in the azimuthal angle ϕ about the surface normal ($d_{\parallel} = 0.5 = -d_{\parallel}$ [12]); and (c) moments which are randomly oriented inside the cone, with $0 \leqslant \theta < \theta^*$ and $0 \leqslant \phi < 2\pi$. While the isotropic distribution in case (a) appears improbable for ODRB in DOL monolayers, it is specifically considered in our transport data analysis in the Excitation Transport Section. Examples of cases (b) and (c) occur in xanthene dyes adsorbed on fused silica [22] and nonpolar lipid bilayers in vesicles [23], respectively. Apart from influencing the relationship between the rotational anisotropy function and the fluorescence

observables in Eq. 6, the moment distribution controls the magic angle θ_m at which the analyzing polarizer must be aligned in order to isolate the isotropic decay P(t). According to Eqs. 6, θ_m is 54.7° and 45° respectively for cases (a) and (b). In case (c), the magic angle and the constants $d_{\parallel}$, $d_{\perp}$ depend on the cone half-angle θ^*.

The nature of the ODRB rotational diffusion in the DOL monolayers may be appreciated in Fig. 4, which contrasts the polarized fluorescence profiles observed in the limits of high and low chromophore density. Rapid excitation transport occurs at high density in Fig. 4(a), where essentially complete depolarization merges the $I_{\parallel}$ and $I_{\perp}$ profiles within 5 ns after excitation. Negligible transport occurs at the low chromophore density in Fig. 4(b); here the depolarization is governed by the rotational anisotropy function according to Eq. 6. Since r(t) clearly does not tend to zero at long times ($I_{\parallel}$ and $I_{\perp}$ do not converge together), the ODRB rotational diffusion necessarily occurs over a restricted range of azimuthal angles ϕ. An antecedent for restricted rotational diffusion exists on surfaces of micelles, where the chromophore transition moments are free to move inside cones with their symmetry axes parallel to the local surface normals [24]. The anisotropy function is well described in such cases by

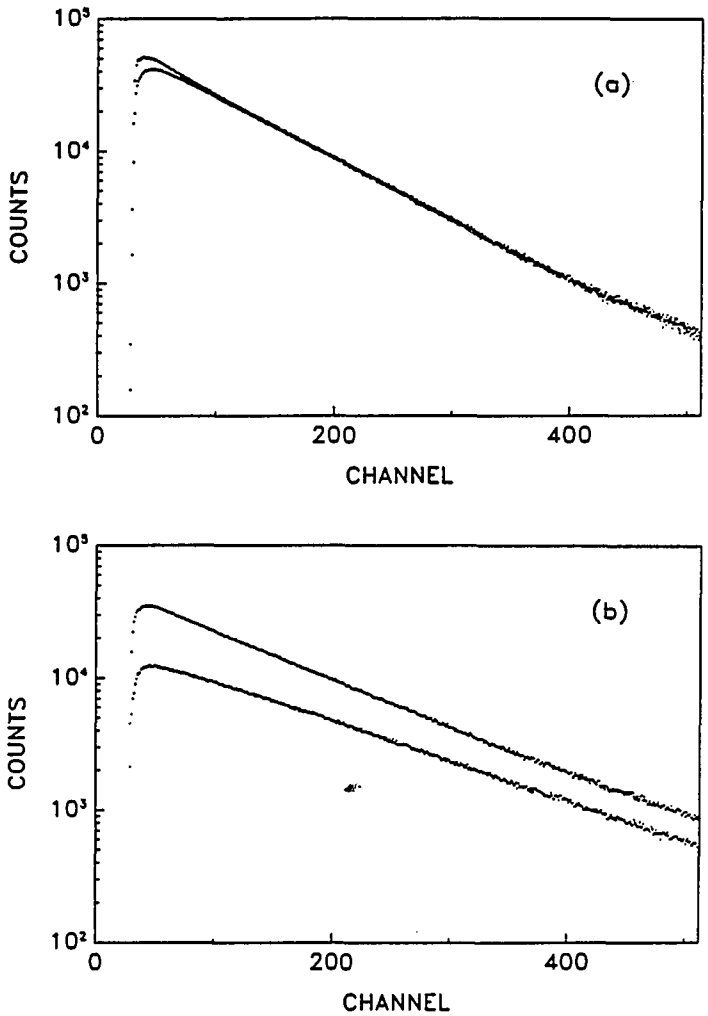

Figure 4. Polarized ODRB fluorescence profiles $I_{\parallel}(t)$, $I_{\perp}(t)$ for chromophore densities 767 x $10^{-6}/Å^2$ (a) and 1.24 x $10^{-6}/Å^2$ (b). The time calibration is 20 ps/channel. In each figure, $I_{\parallel}(t)$ is the upper profile. The counting periods were scaled according to the integrated laser intensities (the Experimental Section), so that these figures accurately represent the relative intensities of $I_{\parallel}(t)$ and $I_{\perp}(t)$

$$r(t) = r(0)\,[a_\infty + (1 - a_\infty)\exp(-Dt)] \qquad (7)$$

where $a_\infty \equiv r(\infty)/r(0)$ is a measure of the restrictedness of the rotational motion and D is a "wobbling" diffusion constant. Lipari and Szabo have shown [24] that a_∞ is related to the cone half-angle θ^* by

$$a_\infty = \langle P_2(\cos\theta)\rangle^2 = 1/4\cos^2\theta^*(1 + \cos\theta^*)^2 \qquad (8)$$

so that in the limit of isotropic diffusion ($\theta^* = \pi/2$), $a_\infty \to 0$. The restricted rotation in our ODRB/DOL systems is physically different from that in micelles in that the air/water interface establishes a single, unique orientation for the cone axis if the moment distribution belongs to either type (b) or (c). The rotational depolarization observed in Fig. 4(b) cannot accompany diffusion over $0 \leqslant \theta < \theta^*$ and $0 \leqslant \phi < 2\pi$ inside the cone surface. Such diffusion processes would produce anisotropy functions r(t) which decay to zero at long times. Restrictions of diffusion to a limited range $\Delta\phi < 2\pi$ is a prerequisite for observation of the rotational anisotropy in Fig. 4(b), since only motion in the azimuthal angle ϕ leads to rotational depolarization in our beam geometry.

To characterize this rotational motion quantitatively, polarized fluorescence profiles $I_\parallel(t)$ and $I_\perp(t)$ were obtained for several surface pressures at a chromophore

density $\rho = 1.24 \times 10^{-6}/\text{Å}^2$, low enough to suppress excitation transport. Magic-angle profiles were obtained with the analyzing polarizer aligned at 45° from the laser polarization. (The impact of this choice for θ_m on our data analysis is examined in the Excitation Transport Section; it is consistent with the moment distribution described in case (b).) Some 35,000 counts were typically accumulated in the peak channel, corresponding to S/N ~190. The magic-angle profiles were fitted with multiexponential functions P(t) using a nonlinear least-squares convolute-and-compare analysis [8,9,20] based on the Marquardt algorithm [25]. All profiles were fitted with biexponential functions; profiles obtained at 25 dyne/cm (the surface pressure used in subsequent transport studies) were also fitted with more accurate triexponential functions. The optimized multiexponential parameters (Table II) are not markedly sensitive to surface pressure, implying that the environmental factors influencing ODRB fluorescence decay change little between 5 and 25 dyne/cm.

The polarized profiles $I_{\parallel}(t)$ and $I_{\perp}(t)$ were analyzed by a linked deconvolution procedure [9,20] using Eqs. 6 with $d_{\parallel} = 0.5 = -d_{\parallel}$ as model functions. The isotropic decay function P(t) was expressed as a multiexponential function at each surface pressure, with parameters fixed at the values listed in Table II. The rotational anisotropy was modeled by the function

Table II. Magic angle fits of ORDB fluorescence profiles,

$$\rho = 1.24 \times 10^{-6}/\text{Å}^2$$

$$P(t) = \sum_i A_i \exp(-t/\tau_i)$$

Π(dyne/cm)	A_1	τ_1,ps	A_2	τ_2,ps	A_3	τ_3,ps	χ_r^2
5	0.884	2542	0.116	1859			1.28
15	0.888	2541	0.112	1934			1.14
25	0.918	2594	0.083	1998			1.44
25	0.903	2597	0.097	1874			1.41
25	0.647	2659	0.107	1779	-0.247	54.8	1.08
25	0.664	2672	0.192	1936	-0.144	95.4	1.65

$$r(t) = a + (1 - a)\exp(-t/\tau_{rot}) \quad (9)$$

where a and τ_{rot} were the only parameters varied (apart from a fluorescence intensity scaling factor) in the convolute-and-compare analyses. The results are given in Table III. Unlike the isotropic fluorescence parameters, the rotational parameters vary considerably with surface pressure. The ODRB diffusion time τ_{rot} becomes dilated as Π increased, presumably due to increased frictional drag from neighboring DOL molecules at higher surface pressure. The a parameter also increases, reflecting more restricted rotation as the monolayer becomes compressed.

The rotational parameters in Table III form a basis for analysis of the polarized fluorescence profiles at higher chromophore densities (the Excitation Transport Section), where excitation transport also contributes to the depolarization. These transport studies were performed at 25 dyne/cm, a surface pressure which affords considerable slewing of the rotational diffusion (thereby casting the transport depolarization into sharper relief) but which is still well below the DOL monolayer breakdown pressure at 44 dyne/cm [18]. For these experiments, rotational parameters were derived by averaging the last two lines in Table III, a = 0.386 and τ_{rot} = 4331 ps.

Table III. Fitting parameters for anisotropic ODRB fluorescence profiles, $\rho = 1.24 \times 10^{-6}/\text{Å}^2$

$$I_{\parallel,\perp} = P(t)[1 \pm 0.5r(t)]$$

$$r(t) = a + (1 - a)\exp(-t/\tau_{rot})$$

Π(dyne/cm)	a	τ_{rot}, ps	$\chi_r^2(^{\parallel}_{\perp})$
5	0.2593	2620	1.44 1.54
15	0.2991	3579	1.22 1.36
25	0.3767	4562	1.62 1.31
25	0.3957	4100	2.79 1.55

If the moment distribution is known to belong to either case (b) or (c), the cone half-angle θ^* can be inferred by measuring the total integrated fluorescence intensity $\int[I_{\parallel}(t) + I_{\perp}(t)]dt$ at low chromophore density for two different laser polarizations. Let I_s and I_p be the total intensities measured for the laser polarization in the surface plane and for the polarization normal to this. It is readily shown that if the moments lie on the cone surface as in case (b), the resulting ratio of integrated intensities is related to θ^* by

$$\theta^* = \tan^{-1}\left[\frac{2\sin^2\lambda}{I_p/I_s - \cos^2\lambda}\right]^{1/2} \qquad (10)$$

where λ is the laser angle of incidence at the surface. The ratio is unaffected by rotational diffusion in case (b). Since the measured ratio I_s/I_p (obtained using the profile integration feature in the MCA) is 1.31 for Π = 25 dyne/cm and $\lambda = 81°$, the inferred cone angle is 58.4°. This value is quite insensitive to λ for λ near 90°: using $\lambda = 90°$ instead of 81° yields $\theta^* = 58.3°$. It is similar to adsorption angles reported [22] for rhodamines on fused silica. (Since the $S_0 \rightarrow S_1$ transition is long axis-polarized in rhodamines [26], these angles are between the chromophore long axis and the surface normal.) For moments randomly distributed inside the cone (case (c)) with $\lambda = 90°$,

$$\frac{I_s}{I_p} = \frac{8(1-\cos\theta^*) - 3\sin^2\theta^* \cos\theta^* \left(\frac{4}{3} + \sin^2\theta^*\right)}{4(1-\cos\theta^*) - 6\sin^2\theta^* \cos\theta^* \left(\frac{1}{3} - \sin^2\theta^*\right)} . \qquad (11)$$

To achieve an intensity ratio of 1.31, the angle θ^* must then be almost 80°, which corresponds to a nearly isotropic distribution. This appears inconsistent with the geometric constraints expected in ODRB chromophores attached to vertical alkyl chains in highly organized monolayers, and these arguments (which are approximate in that Eqs. 10-11 overlook the slow rotational diffusion observed at 25 dyne/cm, Table III) suggest that the moments are in fact distributed on a cone, case (b). This result is not critical to our analysis of transport depolarization in the Excitation Transport Section, and is mentioned here only for its glimpse into the apparent structure of the monolayers.

Excitation Transport in Langmuir-Blodgett Assemblies

In the presence of excitation transport, the fluorescence intensity components are given by

$$I_{\parallel}(t) = P(t)[1 + d_{\parallel} r(t) G^S(t)]$$

$$I_{\perp}(t) = P(t)[1 + d_{\perp} r(t) G^S(t)] \qquad (12)$$

if the chromophore absorption and emission transition moments are parallel and if the laser beam is weak enough to avoid perturbing the orientational distribution of unexcited molecules. A fundamental assumption behind Eqs. 12 is that the ensemble average of the residual polarization $(I_{\parallel} - I_{\perp})/(I_{\parallel} + I_{\perp})$ following a single excitation hop from the initial site is zero [27]. We have analyzed the residual polarization in 2- and 3-dimensional systems [28], and determined that the effects of ignoring it are negligible under present photon counting statistics.

For 2-dimensional transport in which the transition moments are distributed on cones, the constants $d_{\parallel}$, $d_{\perp}$ and θ_m are +0.5, -0.5, and 45°. The anisotropy function r(t) is given by Eq. 9, with the rotational diffusion parameters fixed at a = 0.386 and τ_{rot} = 4331 ps for 25 dyne/cm surface pressure. For each of the monolayers listed in Table I, the $I_{\parallel}$, $I_{\perp}$, and magic-angle profiles were obtained, with typically 50,000 peak channel counts in the $I_{\parallel}$ profile. In several of the data sets, the profiles were accumulated in the order $I_{\parallel}$, magic-angle, $I_{\perp}$, magic-angle, $I_{\parallel}$ in order to check reproducibility. In other data sets, the order of the $I_{\parallel}$ and $I_{\perp}$ profiles was interchanged. The first and last files created in such sequences were always virtually identical, indicating that the ODRB chromophore were stable with respect to laser exposure and oxidation in air over accumulation times of several hours.

The magic-angle profiles were fitted with biexponential expressions for P(t) at all densities but the highest ($767 \times 10^{-6}/Å^2$), where trapping by aggregates considerably distorted the decay. The optimized parameters are listed in Table IV. Trapping causes the magic-angle lifetime to decrease by ~20% between the lowest and highest densities. Nonexponentiality due to trapping becomes evident only at the highest density, where P(t) is simulated by a triexponential decay law in Table IV. This distortion of magic-angle profiles considerably exceeds that observed in dye solutions: the isotropic lifetime of DODCI in glycerol drops by only 6% between 0.012 and 2.49 mM [20]. ODRB in DOL shows far less distortion (for comparable chromophore densities) than rhodamine 3B on silica [12]. Several other alkylated chromophores (e.g., 1, 1'-dihexadecyloxa-dicarbocyanine perchlorate) were tried in monolayers of arachidic acid; aggregation truncated their isotropic lifetimes by at least an order of magnitude from those exhibited by the same chromophore in alcoholic solution. Self-absorption, an important artifact in 3-dimensional systems [10], is of course absent in these monolayer assemblies.

The polarized profiles $I_{\parallel}(t)$, $I_{\perp}(t)$ were fitted with Eqs. 12 using the linked deconvolution algorithm. The parameters in the isotropic decay functions P(t) were fixed at the values in Table IV, and the 2-dimensional two-

Table IV. Magic-angle fits of ODRB fluorescence profiles at high densities[a]

$$P(t) = \sum_i A_i \exp(-t/\tau_i)$$

Monolayer	A_1	τ_1,ps	A_2	τ_2,ps	A_3	τ_3,ps	χ_r^2
1	0.689	1956	0.292	1425	-0.019	228.3	2.86
1	0.686	1966	0.295	1435	-0.020	335.4	2.92
2	0.969	2053	-0.031	185.1			1.69
2	0.965	2041	-0.035	191.1			1.70
3	0.976	2170	-0.024	258.6			2.91
4	0.947	2265	-0.053	146.4			1.61
4	0.955	2264	-0.045	213.5			1.45
5	0.962	2312	-0.038	244.5			1.74
6	0.979	2413	-0.021	242.8			2.94
6	0.985	2405	-0.015	314.3			3.23
7	0.958	2424	-0.042	243.4			2.58

[a] Π = 25 dyne/cm

particle function (Eq. 3) was used for $G^S(t)$. The isotropic lifetime τ in $G^S(t)$ was held at 2650 ps, which approximates the average long-component lifetime of ODRB at low density. (The value of τ pertinent to transport theory is the isolated-molecule lifetime, not the phenomenological lifetimes characterizing the high-density profiles that are distorted by trapping.) Aside from a scaling factor, the only varied parameter in the polarized fluorescence intensities is the reduced coverage C (Eq. 4), which enters in $G^S(t)$. The optimized reduced coverages are given in Table V, and are plotted versus the true chromophore density ρ (Table I) in Fig. 5. The points in this figure should fall on a straight line if the 2-particle theory for $G^S(t)$ is valid. This appears to be very nearly the case. The reduced coverage C in the two-particle theory for $G^S(t)$ is not the true reduced coverage, because the theory is based on an excitation transport probability which is orientationally averaged over 4π steradians. The actual transport rate is proportional to the dipole-dipole orientational factor

$$\kappa^2 = [\hat{d}_i \cdot \hat{d}_j - 3(\hat{d}_i \cdot \hat{r}_{ij})(\hat{d}_j \cdot \hat{r}_{ij})]^2 \qquad (13)$$

where $\hat{d}_i$, $\hat{d}_j$ are unit vectors along the transition moments of chromophores i, j and r_{ij} is their separation. Correct

Table V. Fitting parameters for anisotropic ODRB fluorescence profiles at high densities[a]

$$I_{\parallel,\perp} = P(t)[1 \pm 0.5r(t)G^{s}(t)]$$

$$G^{s}(t) = \exp[-1.354C(t/4\tau)^{1/3}]$$

Monolayer	C	C_D	$\chi^2_r(^{\parallel}_{\perp})$
1	4.38	4.95	4.24 2.81
1	4.07	4.60	3.56 2.31
2	2.74	3.10	1.87 1.77
2	2.71	3.06	2.28 1.74
3	2.07	2.34	4.24 2.65
4	1.47	1.66	2.22 1.65
4	1.48	1.67	2.11 1.62
5	1.12	1.27	2.66 1.85
6	0.76	0.86	4.21 2.45
6	0.73	0.82	4.86 2.76
7	0.66	0.75	4.08 2.23

[a] Π = 25 dyne/cm

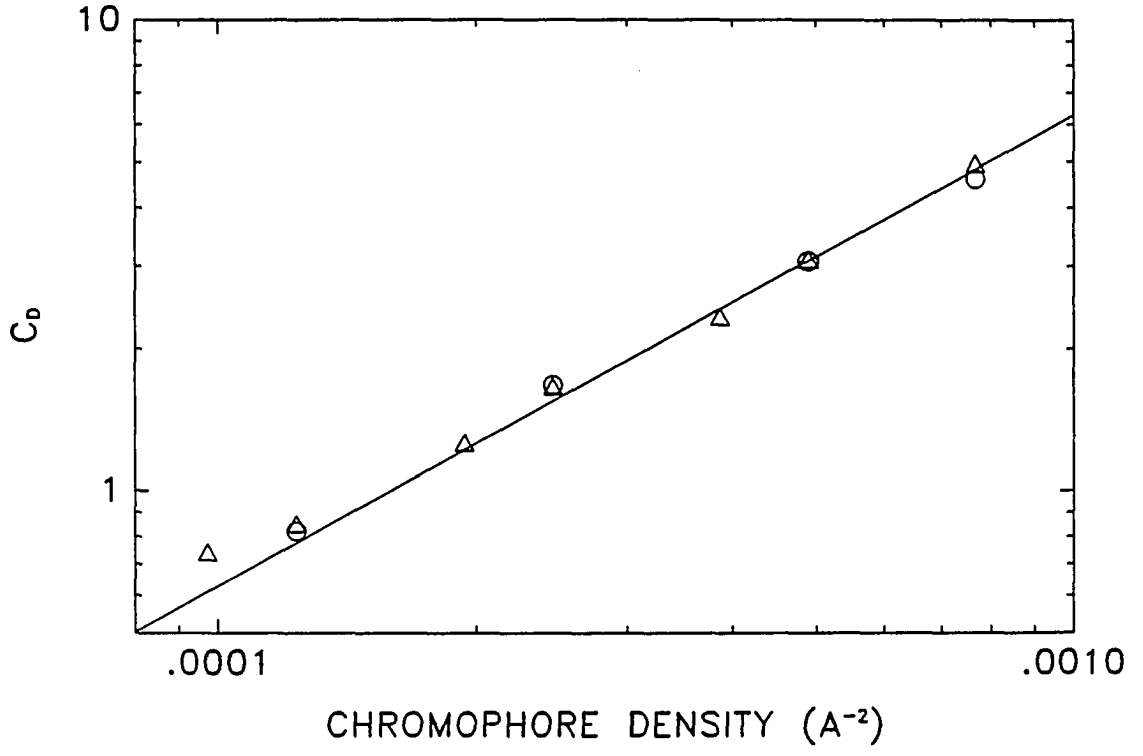

Figure 5. Optimized reduced coverages C_D versus actual ODRB chromophore densities ρ, from linked deconvolutions of $I_{\parallel}$ and $I_{\perp}$ fluorescence profiles using two-particle theory for $G^S(t)$. Straight line gives loci of true reduced concentrations versus ρ for Förster parameter R_O = 44.7Å

averaging of the transport rate over the orientational distribution of moments in the two-particle theory replaces C with the true reduced coverage C_D, where

$$C = C_D\left[\frac{3}{2}\right]^{1/3} \langle\kappa^2\rangle^{1/3} \tag{14}$$

in the dynamic limit where rotational diffusion is rapid compared to transport, and

$$C = C_D\left[\frac{3}{2}\right]^{1/3} \langle|\kappa|^{2/3}\rangle \tag{15}$$

in the static limit of slow rotational diffusion [5]. For moments which are confined to the surface of a cone of half-angle $\theta^* = 58.4°$ (case (b)), the values of $\langle\kappa^2\rangle^{1/3}$ and $\langle|\kappa|^{2/3}\rangle$ are 0.733 and 0.775 respectively. Since the static limit is more appropriate to the ODRB/DOL systems at 25 dyne/cm (Table III), we then take $C = 0.775(3/2)^{1/3}C_D$, or $C_D = 1.13C$. The corresponding values of the "true" reduced coverage (which actually depends on our model for the orientational distribution) are listed in Table V. They are also used for the ordinate in Fig. 5. From the least-squares line which approximates the locus of the points, we derive the value 44.7Å for the Förster parameter R_o. For comparison the value $R_o = 51.5$Å has been inferred

spectroscopically for ODRB in micelles [21]; the difference may reflect environmental effects on R_o.

These conclusions nominally depend on the specific relationships (Eqs. 12) between $G^s(t)$ and the fluorescence observables: our analysis so far has hinged on the assumption that the transition moments are randomly distributed on a cone. We now consider the effects of relaxing this assumption by postulating that while the moments are random in ϕ, the θ-distribution is given by the more general Gaussian function

$$g(\theta) = \exp[-2.77(\theta - \theta^*)^2/\Gamma^2] \tag{16}$$

which has an FWHM of Γ. In the limit $\Gamma \to 0$, $g(\theta)$ becomes proportional to $\delta(\theta - \theta^*)$, as in case (b). When Γ becomes large, the resulting isotropic distribution $g(\theta) = 1$ corresponds to case (a). In the absence of rotational diffusion, the fluorescence intensity components $I_{\parallel}$ and $I_{\perp}$ prior to transport will be proportional to

$$e_{\parallel}^0 = \int_0^{2\pi} d\phi \int_0^{\pi/2} \sin\theta \, d\theta \, g(\theta) \, \sin^4\theta \, \cos^4\phi$$

$$e_{\perp}^0 = \int_0^{2\pi} d\phi \int_0^{\pi/2} \sin\theta \, d\theta \, g(\theta) \, \sin^4\theta \, \sin^2\phi \, \cos^2\phi \tag{17}$$

while the component I_n polarized normal to both $I_{||}$ and $I_{\perp}$ (parallel to the z axis in Fig. 3) will be proportional to

$$e_n^0 = \int_o^{2\pi} d\phi \int_o^{\pi/2} \sin\theta \, d\theta \, g(\theta) \, \sin^2\theta \, \cos^2\theta \, \cos^2\phi. \qquad (18)$$

If complete depolarization accompanies a single excitation hop on the average from the initial site [28], the fluorescence components after one hop will be proportional to

$$\begin{aligned} e_{||}^1 &= \int_o^{2\pi} d\phi \int_o^{\pi/2} \sin\theta \, d\theta \, g(\theta) \, \sin^2\theta \, \cos^2\phi \\ e_{\perp}^1 &= \int_o^{2\pi} d\phi \int_o^{\pi/2} \sin\theta \, d\theta \, g(\theta) \, \sin^2\theta \, \sin^2\phi \qquad (19) \\ e_n^1 &= \int_o^{2\pi} d\phi \int_o^{\pi/2} \sin\theta \, d\theta \, g(\theta) \, \cos^2\theta. \end{aligned}$$

The polarized fluorescence intensities are then given by

$$\begin{aligned} I_{||}(t) &\propto P(t)[e_{||}^0 G^S(t) + Ae_{||}^1(1 - G^S(t))] \\ I_{\perp}(t) &\propto P(t)[e_{\perp}^0 G^S(t) + Ae_{\perp}^1(1 - G^S(t))] \end{aligned} \qquad (20)$$

or equivalently

$$I_{\parallel}(t) = P(t)[1 + d_{\parallel} G^{S}(t)]$$

$$I_{\perp}(t) = P(t)[1 + d_{\perp} G^{S}(t)] \tag{21}$$

with

$$d_{\parallel} = \frac{e^{0}}{Ae^{1}} - 1$$

$$d_{\perp} = \frac{e^{0}}{Ae^{1}} - 1. \tag{22}$$

The normalization constant A in Eqs. 20, 22 may be evaluated from the conservation law

$$e^{0}_{\parallel} + e^{0}_{\perp} + e^{0}_{n} = A(e^{1}_{\parallel} + e^{1}_{\perp} + e^{1}_{n}) \tag{23}$$

so that the constants $d_{\parallel}$, $d_{\perp}$ are uniquely determined by the moment distribution function $g(\theta)$. The magic-angle θ_m is then given by

$$\theta_m = \tan^{-1} [(-d_{\parallel}/d_{\perp})^{1/2}]. \tag{24}$$

In Figure 6, d and d are plotted as functions of the dispersion Γ in the distribution function $g(\theta)$ for $\theta^{*} = 30°$, 60°, and 90°. When $\Gamma = 0$, we obtain the case (b) limit

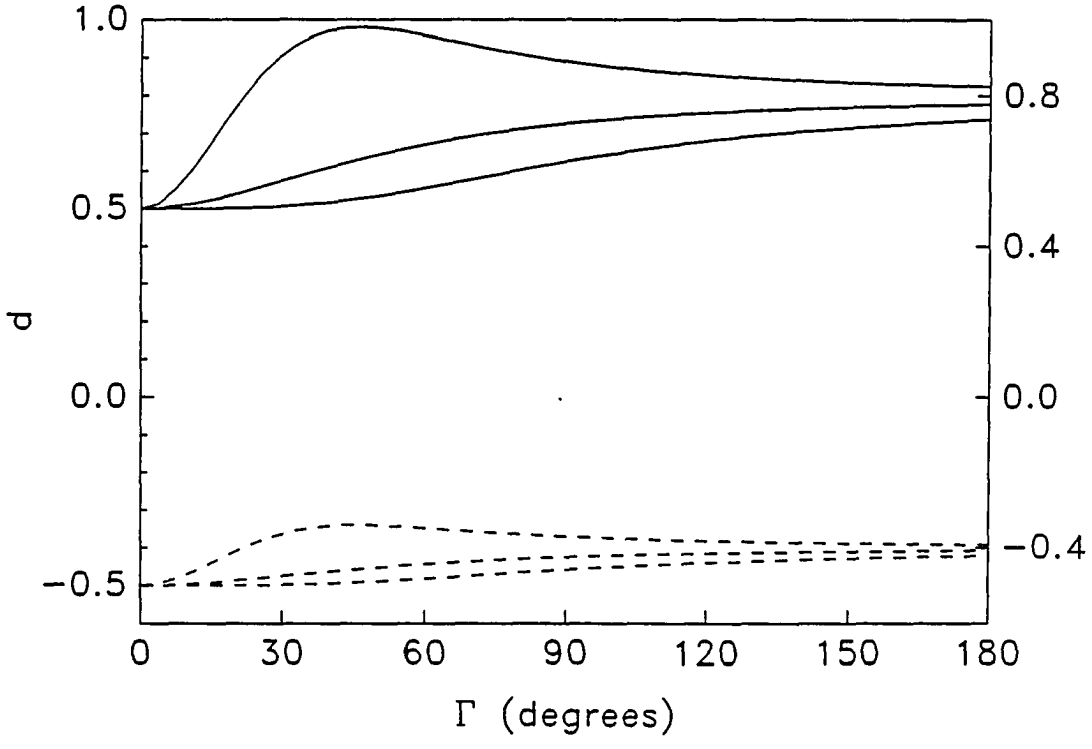

Figure 6. Plots of $d_{\parallel}$ (solid curves) and $d_{\perp}$ (dashed curves) versus the dispersion Γ of the orientational distribution function $g(\theta)$. Values of θ^* in each group of curves are (from top) 30°, 60°, and 90°

$d_{\parallel} = 0.5 = -d_{\perp}$. For large dispersions, the case (a) isotropic limit $d_{\parallel} = 0.8$, $d_{\perp} = -0.4$ is approached. Our measurement of I_S/I_P (the Rotational Diffusion Section) indicate that θ^* is on the order of 60° or larger. For such angles, $d_{\parallel}$ and $d_{\perp}$ increase monotonically with Γ while maintaining the ratio $(d_{\parallel}+ 1)/(d_{\perp}+ 1)$ equal to 3. It is clear in Fig. 6 that $d_{\parallel}$, $d_{\perp}$, and the magic-angle θ_m will be barely affected as the dispersion Γ is increased from 0° to 20°. For such dispersions, the assumption of a case (b) orientational distribution remains valid.

For larger dispersions Γ the use of Eqs. 12 with $d_{\parallel}= 0.5 = -d_{\perp}$ will introduce noticeable errors in the data analysis. In the "worst case" simulation, model fluorescence profiles were generated with the isotropic expressions

$$I_{\parallel}(t) = \exp(-t/\tau_F)[1 + 0.8G^S(t)r(t)]$$
$$I_{\perp}(t) = \exp(-t/\tau_F)[1 - 0.4G^S(t)r(t)]. \quad (25)$$

A magic-angle profile $I_m(t)$ was simulated by

$$I_m(t) = \exp(-t/\tau_F)[1 + 0.4G^S(t)r(t)] \quad (26)$$

and represented the profile which would be observed if the magic-angle were mistakenly taken to be 45° instead of

54.7°. The isotropic lifetime τ_F was taken to be 2600 ps. The rotational anisotropy function was generated using $r(t) = a + (1 - a)\exp(-t/\tau_{rot})$, with $a = 0.350$ and $\tau_{rot} = 4300$ ps. The two-particle expression of Eq. 3 was used to simulate $G^S(t)$ for various C_D, and all profiles were convoluted with an experimental instrument function. Gaussian noise was added to all profiles in order to replicate the S/N ratios characteristic for 50,000 counts in the peak channel of $I_{\parallel}(t)$.

The profiles calculated using $C_D = 0$ were analyzed to obtain the rotational parameters, yielding $a = 0.382$ and $\tau_{rot} = 4713$ ps. These shifts from the simulated values (0.350 and 4300 ps respectively) reflect the errors introduced by assuming a case (b) instead of case (a) orientational distribution. The magic-angle profiles $I_m(t)$ simulated at larger C_D were fitted with biexponential models for P(t), and the polarized profiles were then deconvoluted using Eqs. 12 with $d_{\parallel} = 0.5 = -d_{\perp}$. The results of such analyses are shown in Table VI, which lists the input C_D values used in the simulation and the optimized reduced coverages C obtained in the deconvolutions. In spite of the fact that the isotropic simulated data are incorrectly analyzed in terms of a case (b) distribution in the Table, the true C_D values are recovered to within ~15% in the deconvolutions. Moreover, the percent discrepancies Δ are nearly constant, and the linearity of a plot similar to that

Table VI. Fitting parameters for similated anisotropic ORDB fluorescence profiles

$$I_{\parallel,\perp} = P(t)[1 \pm 0.5r(t)G^{s}(t)]$$

$$G^{s}(t) = \exp[-1.354C(t/4\tau)^{1/3}]$$

C_D	$0.886C_D$[a]	$\Delta(\%)$	$X_r^2(\frac{\parallel}{\perp})$
0.178	0.140	-11.2	1.15 1.06
0.316	0.236	-15.7	0.992 0.982
0.562	0.433	-13.2	1.11 1.01
1.00	0.755	-14.9	1.18 1.14
1.78	1.33	-15.6	1.28 1.21
3.16	2.41	-14.1	1.28 1.08
5.62	4.47	-10.4	1.06 1.18

[a]Static orientational factor for 2-dimensional system with moments randomly distributed on cone with $\theta^* = 58.4°$

in Fig. 5 is hardly affected. Hence, our conclusion that the 2-dimensional two-particle theory for $G^S(t)$ works well for all of the densities shown in Fig. 5 is not sensitive to the model assumed for the orientational distribution of transition moments.

Polarized fluorescence profiles obtained at higher chromophore densities than those shown in Table I show an interesting anomaly in that the fluorescence components $I_{\parallel}$, $I_{\perp}$ do not converge together at long times. At 1511×10^{-6} chromophores/Å^2, the two profiles intersect after ~1 ns, and $I_{\perp}$ decays more slowly than $I_{\parallel}$ at long times. At 2932×10^{-6} chromophores/Å^2, $I_{\perp}$ remains below $I_{\parallel}$ at all times, and the phenomenological decay times are markedly reduced. These ODRB densities are extremely large (the latter density corresponds to packing and average of ~16 chromophore per circle of radius R_o = 44.7Å), and these polarization effects may result from excimer formation.

Acknowledgements

The Ames Laboratory is operated for the U.S. Department of Energy by Iowa State University under Contract No. W-7405-Eng-82. This work was supported by the Office of Basic Energy Sciences. We thank Professors Michael Fayer, Charles Harris, and Larry Patterson for valuable discussions.

References

1. Huber, D. L.; Hamilton, D. S.; Barnett,B. Phys. Rev. B 1977, 16, 4642.

2. Gochanour, C. R.; Anderson, H. C.; Fayer, M. D. J. Chem. Phys. 1979, 70, 4254.

3. Loring, R. F.; and Fayer, M. D. J. Chem Phys. 1982, 70, 139.

4. Fedorenko, S. G.; Burshtein, A. I. Chem. Phys. 1985, 98, 341.

5. Baumann, J.; Fayer, M. D. J. Chem. Phys. 1986, 85, 4087.

6. Dexter, D. L. J. Chem. Phys. 1953, 21, 836.

7. Förster, Th. Discuss. Faraday Soc. 1959, 27, 7.

8. Anfinrud, P. A.; Struve, W. S. J. Chem. Phys. in press.

9. Anfinrud, P. A.; Hart, D. E., Hedstrom, J. F.; and Struve, W. S. J. Phys. Chem. 1986, 90, 2374.

10. Hammond, P. R. J. Chem. Phys. 1979, 70, 3884.

11. Causgrove, T. P.; Bellefeuille, S.; and Struve, W. S. J. Phys. Chem. to be published.

12. Anfinrud, P. A.; Hart, D. E.; Hedstrom, J. F.; and Struve, W. S. J. Phys. Chem. 1986, 90, 3116.

13. Yamazaki, I.; Tamai, N.; and Yamazaki, T. "Ultrafast Phenomena V" Eds. Fleming, G. R.; and Siegman, A. E. Springer-Verlag: Berlin, 1986; p. 444.

14. Sadkowski, P. J.; and Fleming, G. R. Chem. Phys. Letters 1978, 57, 526.

15. Subramanian, R.; and Patterson, L. K. J. Am. Chem. Soc. 1985, 107, 5820.

16. Möbius, D.; Bücher, H.; Kuhn, H.; and Sondermann, J. Ber. Bunsenges. Phys. Chemie 1969, 73, 845.

17. Kleinschmidt, A. Proc. Third Intern. Congr. Surface Activity, Deutscher Ausshuss für grenzflächenaktive Stoffe, Universitätsdruckerei, Mainz, 1961, Vol. II, 138.

18. Tancrede, P.; Parent, L.; Paquin, P.; and Leblanc, R. M. J. Colloid and Interface Sci. 1981, 83, 606.

19. Adamson, A. W. "Physical Chemistry of Surfaces" Fourth Ed., John Wiley & Sons: New York, 1982;

20. Hart, D. E.; Anfinrud, P. A.; Struve, W. S. J. Chem. Phys. 1987, 86, 2689.

21. Ediger, M. D.; Fayer, M. D. J. Phys. Chem. 1984, 88, 6108.

22. Heinz, T. F.; Shen, C. K.; Richard, D.; and Shen, Y. R. Phys. Rev. Lett. 1982, 48, 478. DiLazzaro, P.; Mataloni, P.; and DeMartin, F. Chem. Phys. Letters 1985, 114, 103.

23. Lakowicz, J. R. "Principles of Fluorescence Spectroscopy", Plenum Press: New York, 1983; chapter 5.

24. Lipari, G.; and Szabo, A. Biophys. J. 1980, 30, 489.

25. Marquardt, D. W. J. Soc. Ind. Appl. Math. 1963, 11, 431.

26. Drexhage, K. H. in "Dye Lasers", Ed. F. P. Schäfer Springer-Verlag: Berlin, 1973.

27. Craver, F. W.; Knox, R. S. Mol. Phys. 1971, 22, 385.

28. Anfinrud, P. A.; Struve, W. S. J. Phys. Chem. in press.

SECTION V. PUMP-PROBE SPECTROSCOPY OF DYES ON SURFACES

OPTICAL SHOT-NOISE-LIMITED DETECTION: A SINGLE-SIDEBAND TECHNIQUE WITH FLEXIBLE MODULATION FREQUENCIES

Philip A. Anfinrud and Walter S. Struve

Department of Chemistry and Ames Laboratory - USDOE
Iowa State University, Ames, Iowa 50011

OPTICAL SHOT-NOISE-LIMITED DETECTION: A SINGLE-SIDEBAND TECHNIQUE WITH FLEXIBLE MODULATION FREQUENCIES

Introduction

Optical pump-probe spectroscopy has become well entrenched as a method for studying ultrafast processes. Since pump pulses in sub-picosecond technologies typically contain <1 nJ, the pump-probe signal is often obscured by laser and/or technical noise unless specialized modulation schemes are used to isolate the desired signal. Laser noise spectra in synchronously pumped dye lasers become nearly shot noise limited above ~3 MHz [1]; consequently, successful modulation schemes place the signal content at a rf frequency. Modulation of pump and probe beams at different rf frequencies f_1 and f_2 enable sum- or difference-frequency detection of optical transients [2-4]. Such multiple modulation schemes discriminate effectively against both electrical interference from the optical modulators and scattered pump light.

Bado et al. [2] used a Drake R-7 ham radio receiver tuned to one of the frequencies $f_1 \pm f_2$. A light chopper also modulated the pump beam at an audio frequency. Amplitude modulation (AM) detection of the signal-carrying intermediate frequency (IF) produced an audio-frequency signal, which was synchronously demodulated with a lock-in

amplifier (LIA). AM detection yields nonlinear input signal response; this drawback was averted by Andor et al. [4], who used a single-sideband (SSB) scheme. In SSB detection, the signal-carrying IF is mixed with a reference IF to recover the AF signal, which is subsequently demodulated in a LIA. SSB detection requires phase-locking of the signal-carrying IF to the reference IF. This was accomplished using a frequency synthesis scheme which provided f_1 = 8 MHz and f_2 = 13-13.5 MHz modulation for the probe and pump beams; sum frequency detection was achieved over 21-21.5 MHz with a Drake R-7 receiver. These modulation frequencies are too high for use with cavity-dumped systems, which normally operate at pulse repetition rates of <5 MHz; other modulation frequencies can be obtained in principle by changing the sets of frequency synthesis boards.

We report here a SSB detection scheme, based on a Drake R-7A receiver, which is capable of near shot-noise-limited performance with facile independent control of both modulation frequencies. It provides sum or difference frequency signal detection over the entire tuning range of the receiver (0.01-30 MHz). These features enable efficient, low-cost tailoring of the rf modulation frequencies to the prevailing laser and technical noise spectra.

Frequency Synthesis and Down Conversion

The Drake R-7A receiver translates the input signal frequency to a 50-kHz intermediate frequency (IF) with ~100 dB gain. For effective SSB detection, the signal-bearing 50-kHz IF must be phase locked to an internally generated 50-kHz reference frequency. The detected frequency is given in terms of the voltage-controlled oscillator frequency f_{VCO} and the 40-MHz reference oscillator frequency f_{RO} by

$$\begin{aligned} f_D &= f_{VCO} - (1 + 1/5 + 1/800) f_{RO} \\ &= f_{VCO} - 48.05 \text{ MHz}. \end{aligned} \tag{1}$$

Frequencies f_{VCO} and f_{RO} are available from the receiver; multiple modulation frequencies f_1 and f_2 satisfying $f_D = |f_1 \pm f_2|$ may then be derived from them to ensure the phase-locked condition necessary for SSB detection.

The 48.05-MHz signal must be generated externally to the R-7A receiver. 40-MHz, 8-MHz, and 50-kHz signals were provided by an R-7A reference oscillator board; an R-7A up-converter board was modified for generating the required 48.05-MHz frequency (Fig. 1). The 8-MHz and 50-kHz signals were multiplied in a double balanced mixer (Mini-Circuits SRA-3MH), generating 8.05- and 7.95-MHz signals. These were applied to the rf input on the up-converter board, on which the local oscillator (LO) input was supplied by the 40-MHz

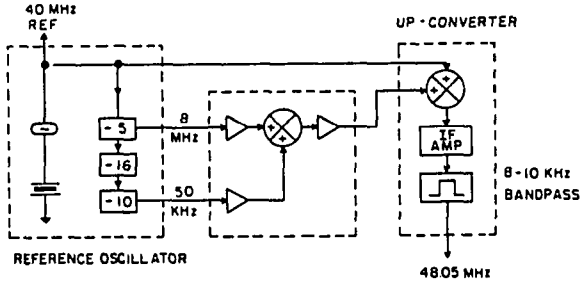

Figure 1. Circuit boards used for synthesizing the 48.05-MHz frequency

reference oscillator. The up-converter board mixed these inputs, passing the resulting signal through crystal filters with 8-10 kHz bandpass centered at 48.05 MHz to remove the unwanted frequencies at 31.95, 47.95, and 32.05 MHz. The 40-MHz frequency was made the master oscillator, and was fed to the external oscillator input of the R-7A.

The f_{VCO} and 48.05-MHz signals were down converted to $f_2 = |f_{VCO} - f_{ext}|$ and $f_1 = |f_{ext} - 48.05\ MHz|$, respectively, by mixing with an external signal f_{ext} from a Harris PRD 7828 frequency synthesizer (Fig. 2). The synthesizer signal, divided in an Anzak HH-107 power splitter with outputs padded by 10-dB attenuators (Mini-Circuits CAT-10), was multiplied by the f_{VCO} and 48.05-MHz signals in Anzak MD-143 mixers. The mixed outputs were amplified (Comlinear CLC-103) and low-pass filtered (Wavetek 3-pole low-pass Chebyshev, with 25-MHz 3-dB point) to eliminate the sum-frequency components. The modulation frequency f_1 is varied by selecting the Harris synthesizer frequency f_{ext}; the other modulation frequency f_2 depends on both f_{ext} and f_{VCO}, where f_{VCO} is controlled by the R-7A tuning dial frequency. The phase-locked detection conditions in Eq. (1) are then satisfied with f_D equal to either the sum or difference frequency $f_D = |f_1 \pm f_2|$.

Mutual isolation between the f_{VCO} and 48.05-MHz signals is critical, since coupling can produce spurious signals at f_D. The power splitter, mixers, and attenuators in Fig. 2

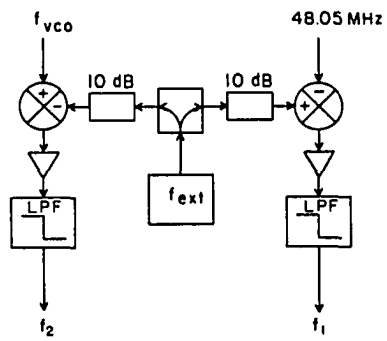

Figure 2. Block diagram of frequency syntheses for f_1 and f_2, the frequencies used for driving the optical modulators. f_{VCO} is tapped from the Drake R-7A receiver, and 48.05 MHz is synthesized by the circuits in Fig. 1. f_{ext} is supplied by a Harris PRD 7828 frequency synthesizer

provide >120-dB isolation; power supply inputs to the amplifiers were filtered with Spectrum Control pi-section EMI/RFI filters. The net isolation of the configuration in Fig. 2 was measured by feeding f_1 or f_2 (~1.5 V p-p) directly into the R-7A antenna input with the receiver at full gain. The 50-kHz signal-bearing IF exhibited noise ~35 dB above the receiver input noise. While the CLC 103 amplifiers were found to contribute to this noise, the largest contribution came from the wings in f_{ext} from the Harris synthesizer. For sum-frequency detection, the lower of the two frequencies f_1, f_2 was therefore low pass filtered, with cutoff between the lower modulation frequency and f_D, at ≥35-dB band stop attenuation. This filtered signal is used to drive the probe beam modulator. (Difference-frequency detection would require a high-pass or low-pass filter, depending on whether the probe beam modulation frequency is higher or lower than f_D.) A 5-pole Cauer-Chebyshev filter was constructed with 500-kHz cutoff and >40-dB attenuation above 800-kHz; with f_D >800 kHz, the low-pass filtered frequency f_1 could be connected to the R-7A antenna input without observable noise level increases in the signal-bearing IF.

Previous detection schemes built around the Drake R-7 or R-7A receiver [2,4] employed an audio-frequency (AF) chopper in the pump or probe beam. The AM or SSB demodulation of the 50-kHz signal-bearing IF generated an AF signal, which

was synchronously demodulated with a LIA. The AF chopper may be obviated by tapping the reference and signal-bearing IF signals from within the R-7A, and demodulating the signal-bearing IF directly with the LIA. These two modes were compared by driving an acousto-optic modulator AOM (Isomet 1206C) with an attenuated signal at f_D (obtained by mixing f_{VCO} and 48.05-MHz). An EG&G FOD-100 photodiode detector, with output directly routed to the R-7A input, detected a transmitted 0.5-mW He/Ne beam, which exhibited 100-nV modulation depth at the antenna input. A 150-Hz AF light chopper was used for SSB detection with AF demodulation, and was removed for direct IF demodulation. LIA response was larger by a factor of 1.6, and the LIA noise level was smaller by a factor of 2.4, in the direct IF demodulation mode; this mode therefore affords an overall sensitivity enhancement of ~3.8 over AF demodulation.

Results and Discussion

The receiver gain, linearity, and stability were characterized by generating a test signal at f_D, obtained by low pass filtering the product of f_{VCO} and 48.05 MHz.

The receiver gain (Fig. 3) for each band in the R-7A tuning range is a property of the switchable filter pass characteristics at the antenna input; optimum system performance clearly requires judicious choice of band as

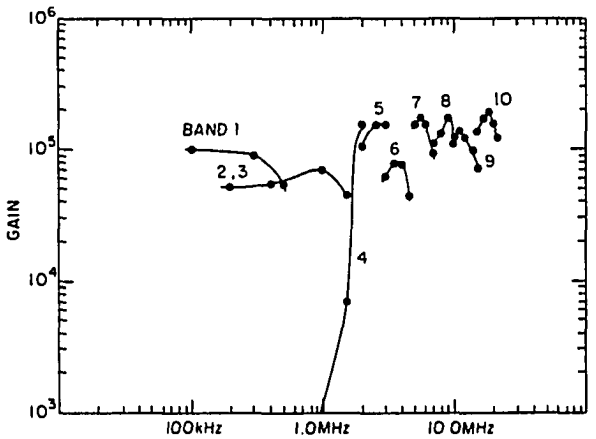

Figure 3. Receiver gain measured for several frequencies in each of bands 1-10 of the Drake R-7A receiver

well as frequency. Receiver linearity and stability were evaluated at 2 MHz in band 4, the lowest frequency with gain $>10^5$; sum detection at this frequency would permit use of multiple modulation with cavity-dumped lasers. A 10-mV rms signal at f_D = 2 MHz was variably attenuated for input to the receiver, and LIA response (Stanford Research Systems SR510) to the signal-bearing IF was monitored. With the receiver set to full gain (without automatic gain control), linear response was found to 3 decades down to the receiver noise floor (Fig. 4). Receiver stability was examined using 10 nV, 100 nV, and 1 μV signals (Fig. 5). A spurious 50-kHz component (magnitude ~25 nV, not necessarily in phase with the signal) resulting from coupling within the receiver can contribute to observable signal drift due to phase drift between reference IF and the signal-carrying IF. The present system phase stability with warmed-up receiver affords measurements to ± 1 nV over 15-min scans. Drift due to phase instability could be eliminated using a two-phase LIA operating in the vector sum mode.

The rms shot noise current I_{rms} is related to the dc current I_{dc} by

$$I_{rms} = \sqrt{2eI_{dc}B}, \tag{2}$$

where B is the detection bandwidth in Hz. For photodetector responsivity of 0.3 A/W at 590 nm, 50-Ω input impedance, and

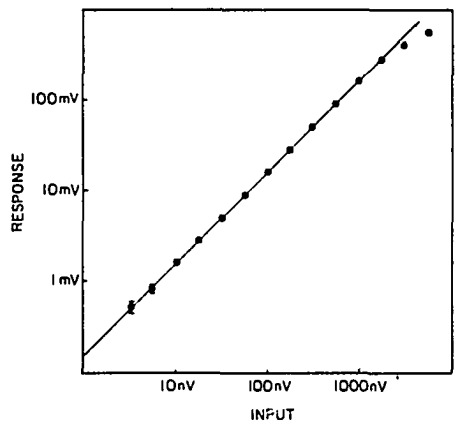

Figure 4. Signal response linearity measured at 2 MHz (band 4), using a Stanford Research Systems SR510 LIA. Error bars show receiver input noise with 0.1-Hz detection bandwidth

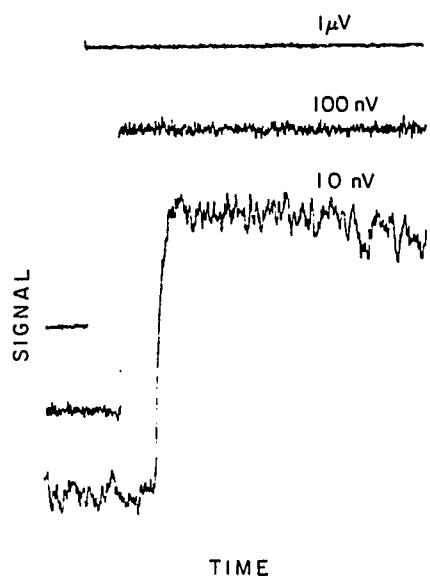

Figure 5. LIA output stability for 1 μV, 100 nV, and 10 nV input signals at 2 MHz (band 4), with RC = 0.1, 1, and 10 s, respectively. Scan time was 17 minutes in each case

1-Hz noise bandwidth, this corresponds to a noise signal of

$$V_{rms} = 15.5\times10^{-9}\sqrt{W}, \qquad (3)$$

where W is the optical power in watts. Our receiver noise is ~1.4 nV at 1-Hz bandwidth, so that near shot-noise-limited performance is predicted with optical powers down to ~8 mW. In practice, 10-mW laser power was found to contribute ~1.2 $nV/Hz^{1/2}$ noise, which agrees within experimental error with the calculated noise.

The present technique by itself cannot differentiate between gain and depletion in the probe beam. This distinction can be made using a calibration scan on a sample with known response. We show in Fig. 6 a picosecond-resolved transient signal (photobleaching of $S_1 \leftarrow S_0$ absorption) obtained in a 2×10^{-7} M aqueous rhodamine 640 solution in a 100-μm cell (~0.0002 optical density at 575 nm), pumped and probed with ~15-ps FWHM pulses from a synchronous Ar^+ -pumped rhodamine 6G laser. The 96-MHz repetition rate 588-nm pump and probe trains each contained ~5 mW average power and were modulated at 6.5 and 0.5 MHz, respectively, using Isomet model 1206C acousto-optic modulators (~80% modulation depth with focused beams). The transmitted probe beam was monitored by an EG&G FOD-100 photodiode, and phase-locked detection was accomplished at 7.0 MHz. The 50-kHz signal-bearing IF was processed in a

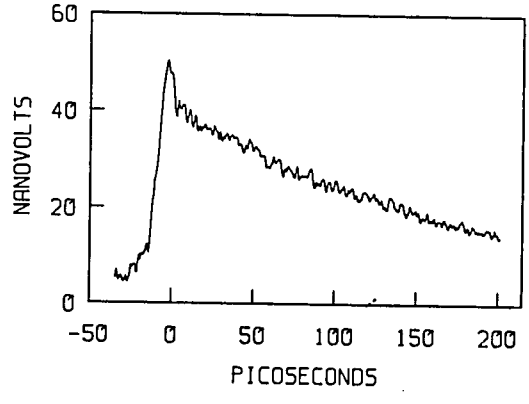

Figure 6. Pump-probe transient signal for aqueous rhodamine 640 solution with ~0.0002 optical density. Pump and probe beams at 588 nm both contained ~5 mW average power, LIA time constant was 1 s (two-pole), and scan rate was 0.5 ps optical delay/s

Stanford Research Systems SR510 LIA. This sample optical density corresponds numerically to the absorption of less than 0.1 monolayer of rhodamine 640 on a surface, and the present technique was motivated by the requirements of doing pump-probe experiments on surface-adsorbed dyes.

In conclusion, the present scheme enables sum or difference frequency detection over the entire tuning range of the Drake R-7A receiver (0.01-30 MHz) with continuously variable modulation frequencies $f_1 = |f_{ext} - 48.05\ MHz|$ and $f_2 = |f_{VCO} - f_{ext}|$ which are controllable via tuning dials on the receiver and on the external frequency synthesizer. Direct LIA demodulation of the 50-kHz signal-carrying IF enhances signal sensitivity while eliminating the need for an AF light chopper. The major components in this technique (radio receiver, frequency synthesis hardware, and external frequency synthesizer) are currently available for less than $8 K.

Acknowledgements

This research was supported by the Office of Basic Energy Sciences, Department of Energy, under Contract No. W-7405-eng-82 at the Ames Laboratory. We have benefited from discussions with George Holland (Ames Laboratory) and David Smith (James Franck Institute, University of Chicago).

References

1. Baer, T. M.; Smith, D. D. "Ultrafast Phenomena IV", Auston, D. H.; Eisenthal, K. B. eds.; Springer: Berlin, 1984; p.96.

2. Bado, P.; Wilson, S. B.; Wilson, K. R. Rev. Sci. Instrum. 1982, 53, 706.

3. Quitevis, E. L.; Gudgin Templeton, E. F.; Kenney-Wallace, G. A. Appl. Opt. 1985, 24, 318.

4. Andor, L.; Lörincz, A.; Siemion, J.; Smith, D. D.; Rice, S. A. Rev. Sci. Instrum. 1984, 55, 64.

PICOSECOND PUMP-PROBE EXPERIMENTS ON SURFACE-ADSORBED DYES: GROUND STATE-RECOVERY OF RHODAMINE 640 ON ZNO AND FUSED SILICA

Philip A. Anfinrud, Timothy P. Causgrove,
and Walter S. Struve

Department of Chemistry and Ames Laboratory - USDOE
Iowa State University, Ames, Iowa 50011

PICOSECOND PUMP-PROBE EXPERIMENTS ON SURFACE-ADSORBED DYES: GROUND-STATE RECOVERY OF RHODAMINE 640 ON ZNO AND FUSED SILICA

Introduction

Solar photochemistry workers have been concerned with the fate of electronic excitation in visibly absorbing dyes adsorbed on wide-band-gap semiconductors. When used in liquid-junction solar cells, single-crystal semiconductors coated with such dyes exhibit low quantum efficiencies ($\lesssim 10^{-2}$) for conversion of dye-absorbed photons into conduction-band electrons [1]. The mechanistic question which arises is whether these low quantum yields are a consequence of efficient back-transfer of electrons to the dye following electron injection into the semiconductor or whether they are due to rapid nonradiative decay of dye excitation into substrate surface modes [2], interband excitation in the semiconductor [3], or surface states.

Time-correlated photon counting was recently used [4] to demonstrate that the fluorescence lifetime of cresyl violet (CV) separated from a TiO_2 single crystal surface by a variable number of organized arachidic acid monolayers depends on the dye-surface separation d for 80Å < d < 509Å in a manner which is consistent with a classical electromagnetic theory for nonradiative excitation decay in

a molecule near a dielectric surface [5]. At such large separations, the theory predicts that the excited state lifetime depends on the substrate's bulk properties largely through the real part n of its refractive index $\tilde{n}$ at the dye fluorescence wavelength. Since both n and d could be characterized for CV above TiO_2 at separations > 80Å, meaningful comparisons between theory and experimental lifetimes were possible at these separations. For directly adsorbed CV ($d \lesssim 5$Å), a controlling parameter in the theoretical lifetime is the imaginary (absorptive) part κ of $\tilde{n}$, a quantity whose order of magnitude is uncertain [6] at visible wavelengths for many wide-band-gap-semiconductors like TiO_2. Since κ and the effective adsorption distance d are unknown for directly adsorbed dye, the ultrafast fluorescence dynamics could not be used to infer the nature of competition between electron injection and nonradiative decay at such small distances.

In this work, ground-state recovery is monitored in rhodamine 640 adsorbed directly onto ZnO using picosecond pump-probe spectroscopy. For radiationless mechanisms involving direct decay of S_1 state dye into ground state dye, the ground state recovery dynamics will be commensurate with dye fluorescence profiles [4] observed on semiconductors. Populations of mobile charge carriers generated in TiO_2 by electron injection from a photoexcited adsorbed dye decay over millisecond timescales [7], and

hence appreciably slower ground-state recovery dynamics can be expected if electron injection is an important excited state decay route. Ground-state recovery on ZnO is contrasted at several coverages with that on $\lambda/4$ fused silica. Photobleaching recovery on ZnO proves to be ultrafast and essentially independent of dye coverage over the studied range. The recovery dynamics on silica are considerably slower; they accelerate with increased dye coverage, because excited state decay on silica is dominated by excitation trapping by dye aggregates whose surface number density increases with coverage. Our results support the occurrence of efficient nonradiative dye → surface excitation decay on semiconductors.

Experimental

Optically flat ($\lambda/4$) silica substrates were precleaned with chromosulfuric acid, and rendered hydrophobic for homogeneous dye coating by treatment with 20% $Si(CH_3)_3Cl$ solution in $CHCl_3$ followed by rinsing in methanol and distilled water. Rhodamine 640 (used as received from Exciton) was adsorbed onto silica from aqueous solution by immersing substrates for 5 - 10 min. Single-crystal ZnO substrates cut and polished normal to the c-axis (Airtron, Morris Plains, NJ) were inherently hydrophobic and were coated similarly. Absorption spectra of aqueous rhodamine

640 solutions obtained on a Perkin-Elmer 320 spectrophotometer at concentrations higher than 10^{-5}M showed, in addition to the monomer $S_1 \leftarrow S_0$ band near 570 nm, a secondary peak at ~540 nm due to dimerization. The dimer peak was not resolved at lower concentrations. The monomer peak position varied with solution concentration: ~572 nm at 10^{-4} and 10^{-5}M and ~565 nm at 10^{-6}M. Since rhodamine 640 (like rhodamine B) exhibits a free carboxyl group, this position shift arises from an acid-base equilibrium [8] between protonated and unprotonated dye. This equilibrium is mirrored in absorption spectra of rhodamine 640 coatings on silica, which closely resemble the aqueous solution spectra apart form spectral shifts (λ_{max} ~ 581 and ~ 572 nm for silica coated with 10^{-5} and 10^{-6}M solutions). On ZnO, the monomer peak position (~ 576 nm) on surfaces coated with solutions over the same concentration range was nearly independent of coverage. Acidic and basic rhodamine B exhibit contrasting fluorescence lifetimes in ethanol (2.48 vs. 3.01 ns [9]). However, ground-state recovery of rhodamine 640 on ZnO proves to be more than an order of magnitude faster than its fluorescence decay in water, and the recovery dynamics are found to be independent of coverage (following section). Hence, the nonradiative decay on ZnO is immaterially influenced by the carboxyl acid-base equilibrium.

Optical densities of coated ZnO and silica surfaces at the dye monomer peak wavelength vary nonlinearly with coating solution concentration between 10^{-6} and 10^{-5}M (Table I). Unlike CV (which dimerizes nearly quantitatively in water and on silica [10]), rhodamine 640 exists predominantly as monomers on both ZnO and silica, and excitation trapping by aggregates is far slower for rhodamine 640 than for CV adsorbed at the same coverage. Adsorption measurements such as those reported in Table I require caution, because dye adsorption onto coating vessel walls and previously coated surfaces can deplete the coating solution concentration below its nominal value, particularly at the lower concentrations. For this reason, the nominal difference between the minimum and maximum coating solution concentrations used in the picosecond transient series on both ZnO and silica is a lower limit to the true difference; the nominal and true solution concentrations can differ by factors up to ~2 at 10^{-6}M and by less at the higher concentrations. The lowest rhodamine 640 optical densities used in pump-probe experiments corresponded to $\lesssim$0.1 monolayer adsorption.

The synchronously pumped rhodamine 6G laser system has been described previously [4,10]; it produced 590 nm pulses with ~12-ps fwhm at 96-MHz repetition rate and ~90-mW average power. The vertical laser polarization was continuously rotatable using a Fresnel double rhomb; the

Table I. Rhodamine 640 adsorption onto ZnO and fused silica

Surface	Coating Solution Concentration, M	Monomer Optical Density at $S_1 \leftarrow S_o$ Peak
Fused Silica	2.0×10^{-7}	0.0017
	4.0×10^{-6}	0.0049
	4.0×10^{-5}	0.0074
ZnO	2.0×10^{-7}	0.0012
	4.0×10^{-6}	0.0036
	4.0×10^{-5}	0.0105

resulting beam was split into orthogonally polarized pump and probe beams of comparable intensity using a calcite Glan-Thompson prism. The two beams were focussed into Isomet Model 1206C acoustooptic modulators operated with ~80% modulation depth at 6.5 and 0.5 MHz respectively.

The pump-probe beam geometry was similar to that of Ippen et al. [11]. The probe beam was subjected to a variable delay using a right-angle BK-7 prism (± 30 arc-s) mounted on a Micro Controle UT10050PP computer-controlled translation stage (0.1 μm/step, 5 cm-range). Both beams were condensed to ~10-μm spot diameter on the dye-coated substrate using a common 7.3 cm f.1. precision-optimized achromatic lens. The average incident laser power at the surface was ~ 10 mW in each beam. The probe beam was detected with an EG&G FOD-100 photodiode, and phase-locked single-sideband detection was achieved at 7.0 MHz in a Drake R-7A radio receiver which was modified and augmented with auxiliary frequency-mixing circuitry to provide flexible modulation frequencies in both beams [12]. At the 7.0 MHz multiple-modulation sum frequency, signal detection was essentially shot noise-limited.

Scattered pump light and dye sample photooxidation introduce more severe complications in surface experiments than in solution work. When parallel pump and probe beam polarizations were used, interference between surface-scattered pump light and the probe beam at the photodiode

surface created a large fluctuating noise signal at 7.0 MHz when the time delay between pump and probe pulses was small enough for their profiles to overlap. Such a spurious signal can arise from spatial inhomogeneity in photodiode response, which enables the fluctuating interference pattern between pump and probe pulses to contribute noise at the sum frequency. This noise was largely eliminated with orthogonally polarized beams. Effects of adsorbed dye photooxidation were minimized by rotating 10 mm × 10 mm ZnO or silica substrates at 12 Hz about the surface normal while translationally cycling them at 1 Hz over a 2 mm range with the laser beam intersection near the sample edge, generating a raster over a 0.4 cm^2 annular region of the surface.

Uncoated ZnO and TiO_2 substrates exhibited a pulse-limited negative-going absorptive transient, which was symmetric about t = 0 and resembled zero-background autocorrelation traces obtained using a Type I KDP crystal rotated 45° about its surface normal from the optimum orientation for SHG for either pump or probe polarization. This transient (which is likely due to two-photon absorption in ZnO) was small on an absolute scale, but it was considerably more intense than the photobleaching transient of dye adsorbed at submonolayer coverage (Fig. 1). The semiconductor transient could be removed by data antisymmetrization [13], but it contributed excessive noise to the antisymmetrized optical density transient near zero

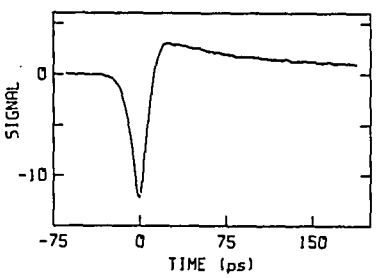

Figure 1. Transient response signal for rhodamine 640 on TiO_2 obtained with rastered surface uniformly covered by dye. Negative-going transient is TiO_2 response; positive-going transient for t>0 is dye photobleaching

delay. Improved S/N ratios were obtained by coating half of the rotating ZnO substrate with dye and by demodulating the resulting 12-Hz signal output from the Drake R-7A receiver using a Stanford Research Systems SR510 lock-in amplifier (LIA) for cancellation of the ZnO transient. (This procedure was unnecessary on silica, which exhibited no such transient.) The LIA output was filtered with ~1 s time constant and routed through a voltage-controlled oscillator to a Canberra Series 30 multichannel analyzer (MCA) operating in the multichannel scaling mode with 1 s dwell time. Since some dye photooxidation occurred despite sample rastering, this dwell time was matched to the 1 Hz raster frequency for signal averaging over the annular region (larger transients were exhibited at the outer edge of the ring, where more rapid sweeping and hence slower photooxidation occurred). The probe pulse delay was translated at 0.5 ps/s.

Raw time-resolved optical density profiles were transferred to a DEC MINC-23 minicomputer system equipped with Winchester disk drive operating in a TSX-Plus multiuser environment. Photooxidation decay caused substantial distortion in the profiles; its kinetics were characterized at all coverages on rastered ZnO and silica substrates by monitoring the real-time dye optical density for fixed 30 ps delay time between pump and probe pulses. A typical calibration profile so obtained for rhodamine 640 adsorbed

with ~0.009 initial optical density at 581 nm on silica is shown in Fig. 2a, where photooxidation caused the optical density to decline ~50% over 480-s sweep time. Such calibration profiles were fitted with biexponential decay laws on silica and with triexponential decay laws on ZnO using a Marquardt nonlinear least-squares program. Raw time-resolved profiles (obtained with probe delay scanned from -66 to +190 ps using identically prepared samples) were then normalized to the fitted calibration profiles, with the result shown in Fig. 2b for the sample whose calibration profile is given in Fig. 2a. The validity of this normalization technique was confirmed by obtaining similar rhodamine 640 ground-state recovery dynamics on ZnO and silica for both directions of probe pulse scanning.

Normalized transient profiles were antisymmetrized using the method of Engh et al. [13] and deconvoluted from the laser autocorrelation function with a nonlinear convolute-and-compare analysis [10] using a biexponential decay law as model function for ground-state recovery.

Results

Antisymmetrized response functions are shown in Fig. 3 for rhodamine 640 coated onto silica using aqueous solutions with 10^{-6} and 10^{-5}M nominal concentrations. The continuous curves are discrete convolutions C_n in channel n of the

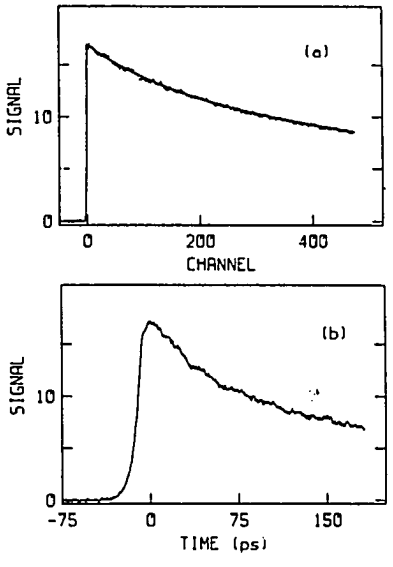

Figure 2. Photooxidation and transient decay curves for rhodamine 640 on a fused silica substrate. (a) Photooxidation decay curve for a sample exposed to pump and probe beams with 30-ps delay, turned on at t=0. Channel calibration is 1.0 s/channel; silica surface is coated with 10^{-5} aqueous dye solution. Continuous curve is fitted biexponential, 0.74 exp(-t/1180s) + 0.26 exp(-t/148s). (b) Transient decay of identically prepared sample, normalized to fitted decay in (a)

laser pulse autocorrelation function x(t) with optimized antisymmetrized biexponential decay functions,

$$C_n = \sum_{i=-\infty}^{n} x(i)A(n-i) \qquad (1)$$

with

$$A(t) = A_1 \exp(-t/\tau_1) + A_2 \exp(-t/\tau_2), \quad t > 0$$
$$= -A_1 \exp(t/\tau_1) - A_2 \exp(t/\tau_2), \quad t < 0 \qquad (2)$$

For $t \gtrsim 15$ ps (i.e., positive times beyond the range of the autocorrelation function), the antisymmetrized response function coincides with the dye photobleaching component of the total response function. The ground-state recovery is clearly more rapid on the silica surface with higher dye coverage, in consequence of excitation trapping by aggregates whose surface number density increases with total dye coverage. This behavior qualitatively parallels the coverage dependence of cresyl violet fluorescence decay on silica [10]. Since rhodamine 640 monomers are the dominant species on the present surfaces, excitation transport typically passes from monomer to monomer several times prior to trapping at an aggregate. Ground-state recovery therefore generally occurs in a monomer other than the photoexcited one. Polarization effects then render the response function decays in Fig. 3 slower than the true ground-state recovery, since excitation transport to monomers with transition moments randomly oriented in the

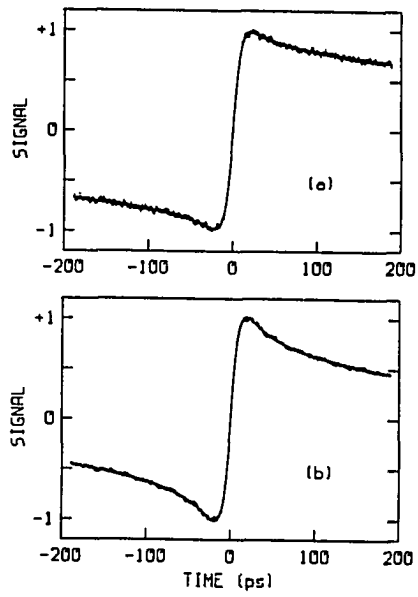

Figure 3. Antisymmetrized response signals for silica coated using (a) 10^{-6} and (b) 10^{-5}M rhodamine 640 solutions. Continuous curves are convolutions of laser autocorrelation function with optimized biexponential decay law in Eqs. 1 and 2

azimuthal angle about the surface normal [14] increases the mean projection of absorption transition moments along the probe pulse polarization when the pump and probe polarizations are orthogonal. These effects can be analyzed to extract the trapping dynamics on silica. We omit such an analysis here because the silica data in Fig. 3 are included primarily for contrast with the ground-state recovery dynamics on ZnO.

Antisymmetrized response functions for rhodamine 640 coated onto ZnO using 10^{-6}, $3x10^{-6}$, and 10^{-5}M solutions are shown in Fig. 4. Similar dye coverages were obtained on ZnO and silica with coating solution concentration over this range (Table I), and the coverages on the first and third ZnO surfaces in Fig. 4 were comparable to those on the first and second silica surfaces in Fig. 3, respectively. The ground-state recovery on ZnO is markedly faster at all coverages than on silica, with antisymmetrized response functions (normalized to 1.0 at the peak observed signal in Figs. 3 and 4) decaying to 0.1 at 200 ps. The decay dynamics on ZnO are very similar at all three coverages; the normalized response functions in Fig. 4 differ primarily in their S/N ratios, which increase with coverage. Optimized biexponential parameters are listed in Table II for fits to the antisymmetrized profiles using Eqs. 1 and 2 for all studied coverages on silica and ZnO. On silica, the decay is dominated by a coverage-dependent long-component lifetime

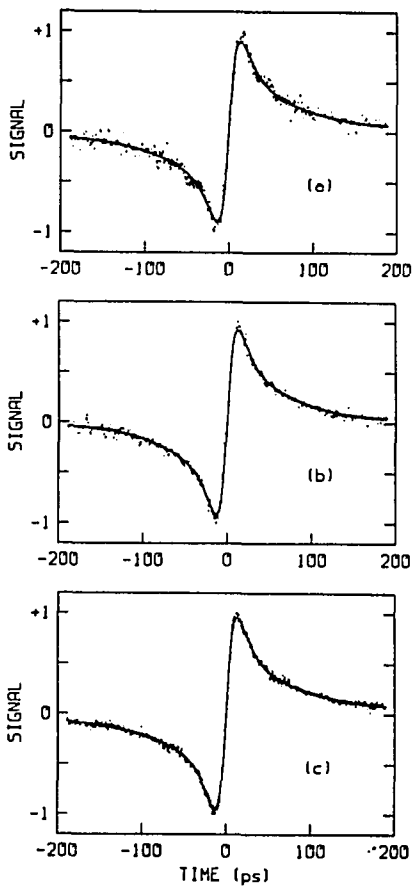

Figure 4. Antisymmetrized response signals for ZnO coated with (a) 10^{-6}M, (b) $3x10^{-6}$M, and (c) 10^{-5}M rhodamine 640 solutions. Continuous curves are convolutions of laser autocorrelation function with optimized biexponential law

Table II. Biexponential fitting parameters for antisymmetrized profiles

Surface	Coating Solution Concentration, M	A_1	τ_1(ps)	A_2	τ_2(ps)
Fused Silica	10^{-6}	0.73	584	0.27	19.7
	10^{-5}	0.62	290	0.38	23.0
ZnO	10^{-6}	0.66	13.3	0.34	78.6
	3×10^{-6}	0.66	9.3	0.34	61.3
	10^{-5}	0.71	12.5	0.29	87.4

in the hundreds of picoseconds; on ZnO, an essentially laser-pulse-limited short-component lifetime (denoted τ_1 in Table II) dominates. Since ground-state recovery is independent of coverage on ZnO, it occurs primarily at the laser-excited site, and polarization effects are unimportant in evaluating the ground-state recovery dynamics from the data in Fig. 4 and Table II. The biexponential decay law in Eq. (2) does not consider the possibility of irreversible photobleaching (e.g., photooxidation and/or electron injection) occurring in parallel with ground-state recovery. The quantum yield $\phi = A(\infty)/A(0)$. An order-of magnitude upper limit for ϕ can be obtained by approximating $A(\infty)$ with the response signal averaged over the last 20 channels in Fig. 4, and by extrapolating the optimized biexponential fit to A(t) back to t = 0 to obtain A(0). This procedure yields $\phi \leq 0.05$, 0.02, and 0.04 for the response signals in Fig. 4 parts a, b, and c. While these estimates are sensitive to errors in fitting the antisymmetrized short-time response function, ϕ is clearly small, and rapid ground-state repopulation occurs efficiently on ZnO. However, ϕ is not negligible, as evidenced by the effects of photooxidation on the real-time transient decay observed on both ZnO and silica.

Discussion

The ground-state recovery on ZnO may be compared with fluorescence profiles of dyes on ZnO. Photon-counting measurements of time-resolved fluorescence from rhodamine 3B adsorbed at low coverage on ZnO [15] indicated that the fluorescence decay is nonexponential; a triexponential fit to a typical rhodamine 3B/ZnO profile yields the optimized fluorescence decay law $I(t) = 0.55 \exp(-t/79\text{ps}) + 0.32 \exp(-t/337\text{ ps}) + 0.13 \exp(-t/1221\text{ ps})$. The dominant short-component lifetime of 79 ps is probably limited by the ~ 80 ps instrument function width of the photon-counting apparatus, in which fluorescence photons are detected by a microchannel plate phototube; similar short-component lifetimes are obtained for rhodamine 3B on TiO_2. Hence, the ground-state recovery of rhodamine 640 on ZnO and the fluorescence decay of rhodamine 3B on ZnO are commensurate in that the dominant short-component dynamics of both measurements are instrument-limited. Since the rate of ultrafast ground-state recovery in Fig. 4 exceeds that of population decay of photogenerated charge carriers in semiconductors [7] by several orders of magnitude, the present experiments furnish strong evidence of rapid, efficient, nonradiative dye → surface excitation decay.

With their comparatively low S/N ratios, our pump-probe results do not elucidate the actual mechanism of the

nonradiative decay. For molecules separated from metal and semiconductor surfaces by distances larger than ~50 Å, the excited state decay appears to be well described [2-4] by the classical electromagnetic theory [5]. The asymptotic behavior of the predicted single-exponential lifetime τ for small d is

$$\frac{1}{\tau} = \frac{3q\lambda^3\theta}{32\pi^3\tau_o} \cdot \frac{n\kappa d^{-3}}{(1 + n^2 - \kappa^2)^2 + 4n^2\kappa^2} \qquad (3)$$

where q is the fluorescence yield, λ is the fluorescence wavelength, τ_o is the isolated-molecule lifetime, and θ = 1(2) for fluorescence transition moments parallel (normal) to the surface. This equation predicts femtosecond decay for visibly fluorescent dyes directly adsorbed on metals like Au ($n = 0.22$, $\kappa = 3.22$ at 6200Å [16]) and considerably slower decay on ZnO ($n = 1.8$, $\kappa \sim 5 \times 10^{-6}$ at 6000Å [17]) owing to the small absorption coefficient of the semiconductor. However, the classical theory breaks down [18] at very short distances. Considerable theoretical (but little experimental) work has focussed on decay of molecules separated from metals by $\lesssim$ 10Å [19, 20]. We are not aware of any theory for excitation decay in molecules adsorbed directly onto semiconductors.

The marked nonexponentiality observed in both our pump-probe transients and photon-counting profiles is difficult to explain on the basis of Eq. 3, even by postulating that

the dye is adsorbed over a distribution of separations d. An alternative decay mechanism is Förster dipole-dipole excitation trapping [21] by bulk impurity or surface states in the semiconductor. Such trapping will be efficient for states with excitation energies which overlap the dye fluorescence spectrum [22] and thus lie significantly below the energies of allowed transitions in the pure bulk semiconductor. When the trap density greatly exceeds the dye number density, averaging of the dipole-dipole transition rate over randomly distributed traps leads to the nonexponential decay law [21]

$$N(t) = N_0 \exp[-t/\tau_0 - \alpha(t/\tau_0)^{d/6}] \qquad (4)$$

where τ_0 is the isolated-molecule lifetime, α is a dimensionless number proportional to the trap density, and d is the dimensionality of the trap distribution. Nonlinear least-squares analysis of photon-counting profiles from rhodamine 3B on ZnO [15] with variable α and τ_0 in Eq. 4 yields excellent fits; τ_0 converges to 2.54 ns and 19.4 ns, respectively for d = 2 and 3. Since the first of these lifetimes is commensurate with those measured in rhodamine 3B solutions and 19.4 ns is unphysically long, the trap distribution appears to resemble a 2-dimensional more than a 3-dimensional one. Similar results have been obtained in fluorescence profiles from rhodamine 3B on TiO_2. The

nonexponentiality in the decay law of Eq. 4 arises from the disorder in the trap distribution, as each excited dye molecule experiences a different set of nearest-trap distances.

Identification of the surface states responsible for trapping requires independent characterization of the surface composition, which is unlikely to have been $Zn_{1.00}O_{1.00}$ prior to coating under our conditions. Auger measurements of oxygen/metal atomic ratios on TiO_2 surfaces untreated by Ar^+ ion bombardment and heating cycles generally yield nonstoichiometric values [23]. The concomitant local variations in surface electronic structure may create surface states. Commonly adsorbed impurities may provide additional trapping sites. Molecular excited-state decay on semiconductors is likely to be sensitive to surface treatment, and experiments on surfaces cleaned under ultrahigh-vacuum conditions may yield results contrasting with those reported here.

Acknowledgements

The Ames Laboratory is operated for the U.S. Department of Energy by Iowa State University under Contract No. W-7405-Eng-82. This work was supported by the Office of Basic Energy Sciences.

References

1. Spitler, M. T. "Proceedings of the Eighth Department of Energy Solar Photochemistry Research Conference", Lake Geneva, WI, June 11-14, 1984.

2. Drexhage, K. H.; Kuhn, H.; Schaefer, F. P. Ber. Bunsen-Ges Phys. Chem. 1968, 72, 329.

3. Whitmore, P. M.; Alivisatos, A. P.; Harris, C. B. Phys. Rev. Lett. 1983, 50, 1092.

4. Crackel, R. L.; Struve, W. S. Chem. Phys. Lett. 1985, 120, 473.

5. Chance, R. R.; Prock, A.; Silbey, R. Adv. Chem. Phys. 1978, 37, 245.

6. Cardona, M.; Harbeke, G. Phys. Rev. 1965, 137, A1467.

7. Fessenden, R. W.; Kamat, P. V. "Proceedings of the Ninth Department of Energy Solar Photochemistry Research Conference", Lake Mohonk, NY, June 2-6, 1985.

8. Faraggi, M.; Peretz, P.; Rosenthal, I.; Weinraub, D. Chem. Phys. Lett. 1984, 103, 310.

9. Sadkowski, P. J.; Fleming, G. R. Chem. Phys. Lett. 1978, 57, 526.

10. Anfinrud, P.; Crackel, R. L.; Struve, W. S. J. Phys. Chem. 1984, 88, 5873.

11. Ippen, E. P.; Shank, C. V.; Bergman, A. Chem. Phys. Lett. 1976, 38, 611.

12. Anfinrud, P.; Struve, W. S. Rev. Sci. Instrum. 1986, 57, 380.

13. Engh, R. A.; Petrich, J. W.; Fleming, G. R. J. Phys. Chem. 1985, 89, 618. See also: Palfrey, S. L.; Heinz, T. F.; Eisenthal, K. B. "Ultrafast Phenomena IV", Auston, D. H.; Eisenthal, K. B., Eds.; Springer-Verlag: Berlin, 1984; Vol. 4, p 216.

14. DiLazzaro, P.; Mataloni, P.; DeMartin, F. Chem. Phys. Lett. 1985, 114, 103.

15. Crackel, R. L.; Anfinrud, P. A.; Struve, W. S. to be published.

16. Johnson, P.; Christy, R. Phys. Rev. B: Solid State 1973, B6, 4370.

17. Burgiel, J. C.; Chen, Y. S.; Vratny,; F. Smolinsky, G. J. Electrochem. Soc. 1968, 115, 729. The absorption spectrum of our ZnO samples was measured on a Perkin-Elmer 320 spectrophotometer.

18. Persson, B. N. J. J. Phys. C 1978, 11, 4251.

19. Maniv, T.; Metiu, J. J. Chem. Phys. 1980, 72, 1996.

20. Waldeck, D. H.; Alivisatos, A. P.; Harris, C. B. Surf. Sci. 1985, 158, 103.

21. Förster, Th. Ann. Phys. (Leipzig) 1948, 6, 55.

22. Förster, Th. Discuss. Faraday Soc. 1959, 27, 7.

23. Vannice, M. A.; Odier, P.; Bujor, M.; Fripiat, J. J. ACS Symp. Ser. 1985, No. 288, 98.

SUMMARY

A fluorescence depolarization study of rhodamine 6G in glycerol spawned a series of publications dealing with excitation transport in 3-dimensional systems (Section III of this dissertation). While this investigation provided the most precise data yet available, it was clear that self-absorption and trapping artifacts were severe enough to prevent a critical commentary on the quality of current excitation transport theories. Self-absorption was minimized and trapping artifacts accounted for (to first order) in a subsequent DODCI in glycerol excitation transport study. Here, severe discrepancies between experiment and current theories (3-body Gochanour-Andersen-Fayer or 2-particle Huber) were observed which could not be explained by any of the following possible artifacts: self-absorption, trapping, solvent reorganization, intrinsic depolarization, 2-dimensional effects (due to the ultrathin sample cell), background emission, or analyzer polarizer misalignment. It was believed that a discrepancy of such severity could not arise from deficiencies in the theories alone. The probable causes for this became evident in our latest 3-dimensional excitation transport study. While the magnitude of the discrepancy was found to be exaggerated by DODCI dimerization and molecular reorientation, the main source is believed to be due to orientational correlation

among DODCI molecules. The correlation apparently arises from 3-dimensional liquid glycerol structure extending to R_0. The discrepancy disappears when ethylene glycol was used as the solvent. Here, excellent agreement between experiment and the 2-particle Huber (or by implication, the 3-body GAF) theory was observed out to reduced concentration ~3.

The first of three 2-dimensional excitation transport studies (Section IV of this dissertation) was conducted with cresyl violet (CV) on fused silica. The CV dimer to monomer ratio was found to be significantly greater on fused silica than in alcoholic solutions; the excitation transport on silica was then dominated by trapping. Indeed, the time-resolved fluorescence decays were well described by the 2-dimensional form of the Förster equation which was augmented with a short component exponential term. The latter term possibly arose from dimer fluorescence. While nonfluorescent in solution, CV dimer might fluoresce if distorted by anisotropic surroundings.

The second 2-dimensional investigation involved rhodamine 3B on fused silica. In contrast to CV, monomer adsorption can be achieved with rhodamine 3B. A conclusive* test of 2-dimensional ET theories could not be achieved, however, because the surface coverages could not be accurately measured spectroscopically ($<<0.1$ monolayer) and because the adsorption isotherm was not known.

Photodecomposition and surface flatness were also a concern. These problems were averted by preparing 2-dimensional systems at an air-water interface with the probe molecule confined to a Langmuir-Blodgett lipid monolayer. Prior knowledge of the area per molecule and the mole ratio enabled accurate determination of the surface concentration. Surface flatness was guaranteed, and photodecomposition was found to be negligible. Here, excellent agreement between experiment and the 2-particle Huber ET theory was obtained up to reduced coverages ~5.

The 2- and 3-dimensional studies (Sections III and IV) revealed that the compact 2-particle Huber expressions provide an excellent description for excitation transport in either dimension. A challenge that remains is to utilize fluorescence depolarization to probe more complicated systems which may ultimately contribute to an understanding of the photosynthetic process.

While Sections III and IV deal with excitation transport in disordered systems, Section V is concerned with the excited state dynamics of dyes on surfaces. The time-resolved fluorescence data obtained via TCSPC was complemented with picosecond pump-probe transient absorption spectroscopy. Submonolayer sensitivity was demanded of either technique in order to isolate the effect of the substrate on the excited state dynamics. A high frequency multiple modulation scheme was developed which achieved near

shot noise limited detection sensitivity with ~10 mW of optical power. This apparatus enabled the pump-probe study of rhodamine 640 on surfaces at submonolayer surface coverages. The ground state recovery on ZnO was fast relative to fused silica for both time-resolved techniques. This implies that the low quantum efficiencies afforded by dye sensitization in photoelectrochemical cells is due to a fast nonradiative excitation decay mechanism which competes effectively with electron injection.

LITERATURE CITED

1. Förster, Th. Annalen der Physik 1948, 2, 55.
2. Förster, Th. Z. Naturforsch. A 1949, 4, 321.
3. Förster, Th. Z. Elektrochem. 1960, 64, 157.
4. Dexter, D. L. J. Chem. Phys. 1953, 21, 836.
5. Craver, F. W.; Knox, R. S. Mol. Phys. 1971, 22, 385.
6. Haan, S. W.; Zwanzig, R. J. Chem. Phys. 1978, 68, 1879.
7. Gochanour, C. R.; Anderson, H. C.; Fayer, M. D. J. Chem. Phys. 1979, 70, 4254.
8. Huber, D. L. Phys. Rev. B 1979, 20, 2307.
9. Silbey, R.; Klafter, J. J. Chem. Phys. 1980, 72, 843.
10. Loring, R. F.; Anderson, H. C.; Fayer, M. D. J. Chem. Phys. 1982, 76, 1982.
11. Fedorenko, S. G.; Burshtein, A. I. Chem. Phys. 1985, 98, 341.
12. Kuhn, H.; Möbius, D.; Bücher, H. in "Physical Methods of Chemistry Part IIIB Optical, Spectroscopic and Radioactivity Methods" Weissberger, A.; Rossiter, B. W. Eds.; Wiley-Interscience: New York, 1972; p. 577.
13. Porter, G.; Tredwell, C. J. Chem. Phys. Lett. 1978, 56, 278.
14. Miller, R. J. D.; Pierre, M.; Fayer, M. D. J. Chem. Phys. 1983, 78, 5138.
15. Hart, D. E.; Anfinrud, P. A.; Struve, W. S. J. Chem. Phys. 1987, 86, 2689.
16. Förster, Th. Z. Elektrochem. 1949, 53, 93.
17. Fayer, M. D. Annu. Rev. Phys. Chem. 1982, 33, 63.
18. Huber, D. L.; Hamilton, D. S.; Barnett, B. Phys. Rev. B 1977, 16, 4642.

19. Sauer, K. Acc. Chem. Res. 1978, 7, 257.

20. Kawski, A. Z. Naturforsch. A 1963, 18, 961.

21. Fleming, G. R. "Chemical Applications of Ultrafast Spectroscopy", Oxford University Press: New York, 1986; chapter 2.

22. Schiff, L. I. "Quantum Mechanics", 3rd ed.; McGraw-Hill: New York, 1968; p. 314.

23. Baumann, J.; Fayer, M. D. J. Chem. Phys. 1986, 85, 4087.

24. Nakashima, N.; Yoshihara, K.; Willig, F. J. Chem. Phys. 1980, 73, 3553.

25. Anfinrud, P. A.; Crackel, R. L.; Struve, W. S. J. Phys. Chem. 1984, 88, 5873.

26. Morgan, J. R.; El Sayed, M. A. J. Phys. Chem. 1983, 87, 2178.

27. Richert, R.; Bässler, H. J. Chem. Phys. 1986, 84, 3567.

28. Ching, W. Y.; Huber, D. L.; Barnett, B. Phys. Rev. B 1978, 17, 5025.

29. Hauser, M.; Klein, K. A.; Gösele, U. Z. Phys. Chem. NF 1976, 101, 255.

30. Knoester, J.; Van Himbergen, J. E. J. Chem. Phys. 1984, 80, 4200.

31. Feofilov, P. P. "The Physical Basis of Polarized Emission", Consultants Bureau: New York, 1961; chapter 1.

32. Lakowicz, J. R. "Principles of Fluorescence Spectroscopy", Plenum Press: New York, 1983; chapter 5.

33. Gochanour, C. R.; Fayer, M. D. J. Phys. Chem. 1981, 85, 1989.

34. Hecht, E.; Zajac, A. "Optics", Addison-Wesley: Reading, 1974; chapter 8.

35. Galanin, M. D. Tr. Fiz. Inst. I. P. Pavlova 1950, 5, 341.

36. Anfinrud, P. A.; Struve, W. S. J. Phys. Chem. in press.

37. Chuang, T. J.; Eisenthal, K. B. J. Chem. Phys. 1972, 57, 5094.

38. Cross, A. J.; Fleming, G. R. Biophys. J. 1984, 46, 45.

39. Hammond, P. R. J. Chem. Phys. 1979, 70, 3884.

40. Birks, J. B. "Photophysics of Aromatic Molecules", Wiley-Interscience: London, 1970; chapter 4.

41. "CRC Handbook of Chemistry and Physics 56th edition", Weast, R. C., Ed.; CRC Press: Cleveland, 1974; p. F-53.

42. Anfinrud, P. A.; Struve, W. S. J. Chem. Phys. in press.

43. Wertz, D. L.; Kruh, R. K. J. Chem. Phys. 1967, 47, 388.

44. Soltwisch, M.; Steffen, B. Z. Naturforsch. 1981, 36a, 1045.

45. Van Koningsveld, H. Rec. Trav. Chim. 1968, 87, 243.

46. Knoester, J.; Van Himbergen, J. E. J. Chem. Phys. 1986, 84, 2990.

47. Knight, H. E. W.; Selinger, B. K. Spectrochimica Acta 1971, 27A, 1223.

48. Heinz, T. F.; Chen, C. K.; Richard, D.; Shen, Y. R. Phys. Rev. Lett. 1982, 48, 478.

49. Di Lazzaro, P.; Mataloni, P.; De Martini, F. Chem. Phys. Lett. 1985, 114, 103.

50. Anfinrud, P. A.; Hart, D. E.; Hedstrom, J. F.; Struve, W. S. J. Phys. Chem. 1986, 90, 3116.

51. Craver, F. W. Mol. Phys. 1971, 22, 403.

52. Kinosita, K. Jr.; Kawato, S.; Ikegami, A. Biophys. J. 1977, 20, 289.

53. Lipari, G.; Szabo, A. Biophys. J. 1980, 30, 489.

54. Kawato, S.; Kinosita, K. Jr.; Ikegami, A. Biochemistry 1977, 16, 2319.

55. Loring, R. F.; Andersen, H. C.; Fayer, M. D. J. Chem. Phys. 1982, 76, 2015.

56. Malmstadt, H. V.; Franklin, M. L.; Horlick, G. Anal. Chem. 1972, 44, 63A.

57. Bevington, P. R. "Data Reduction and Error Analysis for the Physical Sciences", McGraw-Hill Book Co.: New York, 1969.

58. O'Conner, D. V.; Phillips D. "Time-Correlated Single Photon Counting", Academic Press: London, 1984.

59. West, M. A. "Photochemistry" Bryce-Smith, D. Ed.; The Chemical Society: London, 1979; vol. 10, p. 40.

60. Fleming, G. R. Adv. Chem. Phys. 1982, 49, 1.

61. Franken, P. A.; Ward, J. F. Rev. Mod. Phys. 1963, 35, 23.

62. Klann, H.; Kuhl, J.; von der Linde, D. Optics Comm. 1981, 38, 390.

63. Metzger, D. L. "Electronic Components, Instruments, and Troubleshooting", Prentice-Hall: Englewood Cliffs, N. J., 1981, p. 362.

64. May. P. G.; Sibbett, W.; Smith, K.; Taylor, J. R.; Willson, J. P. Optics Comm. 1982, 42, 285.

65. Fork, R. L.; Beisser, F. A. Appl. Opt. 1978, 17, 3534.

66. Harde, H.; Burggraf, H. Optics Comm. 1981, 38, 211.

67. Yasa, Z. A.; Amer, N. M. Optics Comm. 1981, 36, 406.

68. Waldeck, D.; Cross, A. J.; McDonald, D. B.; Fleming, G. R. J. Chem. Phys. 1981, 74, 3381.

69. Yamazaki, I.; Tamai, N.; Kume, H.; Tsuchiya, H.; Oba, K. Rev. Sci. Instrum. 1985, 56, 1187.

70. Bebelaar, D. Rev. Sci. Instrum. 1986, 57, 1116.

71. "Philips Electron Tubes Handbook", Philips: Eindhoven, 1982; Part 9.

72. "Hamamatsu Technical Manual", RES-0795, 1982.

73. "Hamamatsu Technical Data Sheet", T-112, 1987.

74. Rigler, R.; Claesens, F.; Lomakka, G. "Ultrafast Phenomena IV" Auston, D. H.; Eisenthal, K. B., Ed. Springer: New York, 1984; p.472.

75. Coyne, B., Product Development Engineer, Tennelec, Inc., private communication.

76. Coates, D. B. J. Phys. E. 1968, 1, 878.

77. Marquardt, D. W. J. Soc. Indust. Appl. Math. 1963, 11, 431.

78. Grinvald, A.; Steinberg, I. Z. Anal. Biochem. 1974, 59, 583.

79. Knutson, J. R.; Beechem, J. M.; Brand, L. J. Phys. Chem. 1986, 90, 2374.

80. Anfinrud, P. A.; Hart, D. E.; Hedstrom, J. F.; Struve, W. S. J. Phys. Chem. 1986, 90, 2374.

81. Rullière, C.; Declémy, A.; Kottis, Ph. "Ultrafast Phenomena V", Fleming, G. R., Sregman, A. E., Eds.; Springer-Verlag: Berlin, 1986; p. 312.

ACKNOWLEDGEMENTS

I would like to thank my research advisor, Professor Walter Struve, for making my graduate student days (over 2000 of them) enjoyable. He has continually sought to provide me with challenges, direction (redirection when necessary), encouragement, and professional opportunities. I will surely carry many pleasant memories of my association with him.

My colleagues in print, Bob Crackel, John Hedstrom, Dave Hart, and Tim Causgrove deserve much credit for their contributions toward this work.

I would like to thank George Holland of Ames Laboratory and Dave Smith of the James Franck Institute for many profitable discussions about frequency synthesis schemes. In addition, I wish to thank Duane Smith, formerly of Purdue University, for many useful suggestions regarding the technical details of multiple modulation and its applicability to pump-probe spectroscopy.

My wife, Annette, deserves special recognition for her love, patience, understanding, and her willingness to type, edit, and assist in any other way, in pulling this project together in a timely fashion.

I also wish to thank my parents, Arlyn and Verna, for their unfailing encouragement toward academic pursuits. Their support of my whims during High School Science Fair

projects was undoubtedly instrumental in leading me to this point in my career.

To all others who had a part in my research, directly or indirectly; in the spirit of Coaches Orr and Walden, thank you for your support.